



# LUND UNIVERSITY

## Characterisation of mechanical and thermal properties of tungsten for high power spallation target applications

Habainy, Jemila

2018

*Document Version:*

Publisher's PDF, also known as Version of record

[Link to publication](#)

*Citation for published version (APA):*

Habainy, J. (2018). *Characterisation of mechanical and thermal properties of tungsten for high power spallation target applications*. [Doctoral Thesis (compilation), Materials Engineering]. Department of Mechanical Engineering, Lund University.

*Total number of authors:*

1

### General rights

Unless other specific re-use rights are stated the following general rights apply:

Copyright and moral rights for the publications made accessible in the public portal are retained by the authors and/or other copyright owners and it is a condition of accessing publications that users recognise and abide by the legal requirements associated with these rights.

- Users may download and print one copy of any publication from the public portal for the purpose of private study or research.
- You may not further distribute the material or use it for any profit-making activity or commercial gain
- You may freely distribute the URL identifying the publication in the public portal

Read more about Creative commons licenses: <https://creativecommons.org/licenses/>

### Take down policy

If you believe that this document breaches copyright please contact us providing details, and we will remove access to the work immediately and investigate your claim.

LUND UNIVERSITY

PO Box 117  
221 00 Lund  
+46 46-222 00 00



The background of the slide is a grayscale scanning electron micrograph (SEM) showing the surface morphology of a tungsten target. The surface is highly textured, with numerous sharp, angular features and deep, irregular grooves, suggesting a fractured or eroded surface. The lighting creates strong highlights and shadows, emphasizing the three-dimensional nature of the surface.

# Characterisation of mechanical and thermal properties of tungsten for high power spallation target applications

JEMILA HABAINY

DIVISION OF MATERIALS ENGINEERING

DEPARTMENT OF MECHANICAL ENGINEERING | LUND UNIVERSITY



# Characterisation of mechanical and thermal properties of tungsten for high power spallation target applications

Jemila Habainy



**LUND**  
UNIVERSITY

DOCTORAL DISSERTATION

by due permission of  
the Faculty of Engineering, Lund University, Sweden,  
to be defended at lecture hall M: B (M-Building, LTH),  
on 26 October 2018 at 10:00 hrs.

*Faculty opponent*


Prof. Javier Gil Sevillano  
University of Navarra, Spain





Organisation: Division of Materials Engineering, Lund Institute of Technology, Lund University, P.O. Box 118, 22100 Lund	Document name: Doctoral Dissertation	
	Date of issue: October 2018	
Author: Jemila Habainy	Sponsoring organisation: European Spallation Source ERIC, Lund	
Title: Characterisation of mechanical and thermal properties of tungsten for high power spallation target applications		
<p><b>Abstract:</b> The European Spallation Source (ESS), which is currently under construction in Lund, will use pure tungsten as the spallation neutron target. The tungsten will be irradiated by a 2 GeV proton beam, pulsed at a repetition rate of 14 Hz. Each pulse will deposit 357 kJ in the tungsten causing an instantaneous temperature rise of approximately 100 °C, during the 2.86 ms pulse duration. The target is wheel-shaped, 2.6 m in diameter, and will be rotating at 0.39 Hz to distribute the proton beam loads. The tungsten material will consist of nearly 7000 bricks with the dimensions 80×30×10 mm<sup>3</sup>. The bricks are separated by 2 mm wide cooling channels in which helium gas flows at a rate of 2.85 kg/s. The proton beam will be more powerful than the beam used at any other existing spallation neutron facility. Thanks to the high beam power and innovative moderator design, ESS will become the brightest neutron source in the world.</p> <p>However, designing the target is challenging, as its structure should withstand loads from the high beam power. The high intensity proton beam will not only cause cyclic thermo-mechanical loading of the tungsten, but also irradiation damage in the form of displacements of atoms in the microstructure, and production of a wide range of radioactive isotopes such as gaseous transmutation elements, and a significant fraction of solid transmutation elements, which will alter the thermal and mechanical properties of tungsten. Using such a powerful beam requires an optimal design of the target and a good understanding of the complex physical, mechanical, and thermal changes occurring in irradiated tungsten. It is also important to identify and mitigate potential issues and accidental scenarios during operation of the ESS target.</p> <p>The present work aims to characterise thermal and mechanical properties of high-energy proton and spallation neutron irradiated pure tungsten, for the use as a spallation target material. The work includes studies on fatigue properties of unirradiated tungsten from various processing routes, to determine which type of tungsten is the most durable under cyclic loads. The fatigue study served as a basis for setting the maximum acceptable stress of 100 MPa in the tungsten during operation, as well as choosing rolling as the most suitable manufacturing method. The tungsten volume will be contained in a stainless-steel target vessel, which confines the helium gas target-coolant. Tungsten is known to be readily oxidised even at moderate temperatures, which makes even impurity levels of oxygen and water vapour in the helium a potential issue. Therefore, oxidation behaviour of tungsten in mildly oxidising atmospheres and temperatures relevant to ESS operation, was characterised. The results were used to set the upper temperature limit in the tungsten during normal operation, as well as the maximum allowable temperature during off-normal incidents. However, both the temperature and thermo-mechanical stress in the tungsten will alter as the properties of the material change due irradiation.</p> <p>The available data on proton irradiated tungsten is very limited. Therefore, in the present work, concerted efforts have been made for studying tungsten irradiated under similar conditions as the future ESS target material. Specifically, irradiation induced changes in thermal diffusivity, hardness, ductility, and ultimate tensile strength of tungsten irradiated by high power proton beam at Paul Scherrer Institute (PSI), were studied. The results point towards a severe embrittlement of irradiated tungsten. Virtually zero plasticity was found in the specimens tested up to 500 °C, and hardness increased by more than 50%. Thermal diffusivity decreased by 28-51%, depending on the test temperature (25-500 °C). All tested irradiated specimens had lower irradiation damages than the ESS tungsten is expected to accumulate during the 5-year life time of the target.</p> <p>Finally, a concluding study is presented where new calculations of the temperature and maximum stress in the bricks were made, based on the obtained experimental data on the thermal and mechanical properties of irradiated tungsten.</p>		
Keywords: ESS, Tungsten, Spallation target, Mechanical properties, Fatigue, Oxidation, Irradiation effects, Thermal diffusivity.		
Language: English	Number of pages: 266	ISBN: 978-91-7753-844-8 (print), 978-91-7753-845-5 (pdf)

I, the undersigned, being the copyright owner of the abstract of the above-mentioned dissertation, hereby grant to all reference sources permission to publish and disseminate the abstract of the above-mentioned dissertation.

Signature  Date 2018-09-26



# Characterisation of mechanical and thermal properties of tungsten for high power spallation target applications

Jemila Habainy



Division of Materials Engineering  
Department of Mechanical Engineering  
Lund University, Sweden  
October 2018

Cover photo by Jemila Habainy,  
showing a fatigue fracture surface of forged tungsten.

© Jemila Habainy  
Division of Materials Engineering  
Department of Mechanical Engineering  
Lund University, Sweden  
ISBN 978-91-7753-844-8 (print)  
ISBN 978-91-7753-845-5 (pdf)

Printed in Sweden by E-husets Tryckeri, Lund University  
Lund, September 2018



# Table of Contents

Populärvetenskaplig sammanfattning .....	i
Abstract .....	v
Acknowledgements .....	ix
List of publications and author's contribution .....	xi
Glossary .....	xii
List of abbreviations .....	xiii
List of figures .....	xiv
List of tables .....	xvii
1. Outline .....	1
2. Objectives .....	3
3. Background .....	5
3.1 Tungsten .....	5
3.1.1 From mineral to finished product .....	7
3.1.2 Past and current research on tungsten properties .....	14
3.2 European Spallation Source .....	15
3.2.1 Neutron scattering .....	17
3.2.2 The ESS design .....	18
3.2.3 The spallation target .....	19
3.2.4 Target material issues .....	21
3.3 Radiation types .....	24
3.4 Radiation damage in metals .....	26
3.4.1 Migration and annihilation of defects .....	28
3.5 Irradiation of tungsten .....	29

3.5.1 Tungsten as plasma-facing material for fusion applications .....	30
3.5.2 Proton and spallation neutron irradiation .....	31
<b>4. Materials and Methods .....</b>	<b>35</b>
4.1 Research plan .....	35
4.1.1 Fatigue studies.....	36
4.1.2 Oxidation studies .....	39
4.1.3 Thermal diffusivity of irradiated tungsten.....	43
4.1.4 Mechanical properties of irradiated tungsten .....	44
4.1.5 Cyclic loading by pulsed heavy ion irradiation .....	46
4.2 Specimens .....	50
4.2.1 Irradiated tungsten .....	51
4.2.2 Unirradiated tungsten .....	56
4.3 Characterisation techniques .....	58
4.3.1 Microscopy .....	58
4.3.2 Thermal analysis.....	61
4.3.3 Hardness measurements .....	63
4.3.4 X-ray diffraction – XRD.....	64
<b>5. Results and Discussion .....</b>	<b>65</b>
5.1 Fatigue studies.....	65
5.1.1 Forged vs. rolled.....	66
5.1.2 Rolled vs. HIPed.....	74
5.2 Oxidation study.....	82
5.2.1 TGA studies of the larger specimens.....	82
5.2.2 DSC-STA studies of the smaller foil specimens .....	85
5.2.3 In situ ESEM studies of the smaller foil specimens .....	86
5.2.4 XRD observations .....	87
5.2.5 AES observations.....	89
5.2.6 EDS observations .....	90
5.2.7 Tungsten alloys .....	92
5.3 Thermal diffusivity studies.....	93
5.4 Mechanical properties of irradiated tungsten .....	99
5.5 Pulsed heavy ion irradiation.....	104

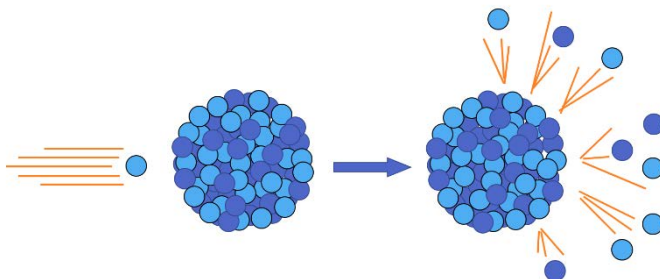


5.5.1 Hardness measurements .....	105
5.5.2 Dynamic response and fatigue.....	108
5.5.3 Radiation damage and thermal diffusivity .....	110
5.5.4 Oxide layer and the pulsed beam.....	111
5.5.5 Implications of the results on the ESS target.....	113
<b>6. Conclusions .....</b>	<b>117</b>
6.1 Fatigue .....	117
6.2 Oxidation.....	120
6.3 Thermal diffusivity.....	122
6.4 Mechanical properties .....	123
6.5 Modelling the thermal stress.....	124
6.6 Future work .....	125
<b>References.....</b>	<b>127</b>



## Populärvetenskaplig sammanfattning

Inom ett par år kommer det nya materialforskningscentret ESS, The European Spallation Source, att stå färdigbyggt. Det kommer då vara det mest avancerade forskningsinstitutet i sitt slag och leverera upp till 30 gånger fler neutroner än någon annan neutronkälla i världen. En av de viktigaste komponenterna på ESS är det s.k. strålmålet som består av nästan 7000 bitar av det metalliska grundämnet volfram. Volframets enda, och för ESS helt avgörande uppgift, är att ge ifrån sig så många av sina neutroner som möjligt. Neutronerna produceras i den s.k. spallationsprocessen som går ut på att skjuta protoner med hög hastighet mot volfram för att på så sätt slå ut dess neutroner.



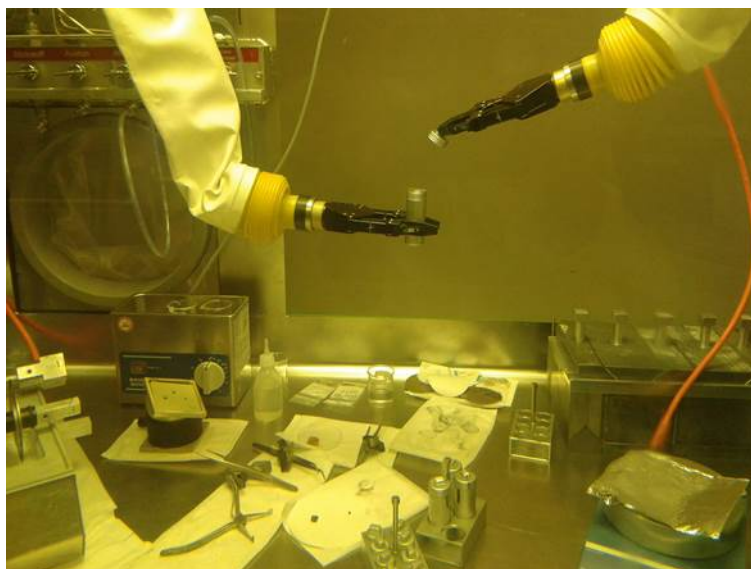
**Spallationsprocessen.** Ljusa kulor är protoner, mörka är neutroner. När en proton skjuts med tillräckligt hög fart mot volframatomen kommer den att överföra en del av sin energi till partiklarna i kärnan, som då blir fria.

Protonstrålen levererar 14 pulser i sekunden och är mycket kraftfull. Energin från protonerna som träffar volframet motsvarar energin som krävs för att stoppa en Mercedes-Benz S-klass som kör i 250 km/h – varje sekund. Varje puls kommer att öka temperaturen i volframet med ca 100 °C, vilket innebär att volframet får utstå höga cykliska termiska och mekaniska belastningar. Volframet kommer även att få strålskador av

Hantering av radioaktiva volframprover är mycket komplicerad och begränsad till särskilda laboratorier med s.k. hotcells, där proverna bearbetas med hjälp av robotarmar. På grund av svårigheten att dels producera, dels hantera radioaktivt volfram finns det i nuläget väldigt begränsad kunskap om hur materialet påverkas av strålning. Det är svårt att förutsäga hur väl det bestrålade volframet kommer att stå emot de kraftiga protonpulserna.

ii

av bestrålning, bl.a. försämras värmeledningsförmågan vilket leder till ännu högre temperaturer som i sin tur leder till ännu högre spänningar. Dessutom blir bestrålat volfram extremt sprött, och risken för utmattning som följd av den cykliska belastningen ökar kraftigt.



**Bearbetning av volfram i en hotcell.**

I den här avhandligen presenteras studier gjorda på både bestrålat och obestrålat volfram. Med hjälp av olika experiment kartläggs materialegenskaperna med särskilt fokus på volframets roll som neutronproducerande strålmål. Oxidationsstudier resulterade i ett förslag på 500 °C som maxtemperatur. Utmattningsstudier visade att valsat volfram är överlägset bäst och att den högsta tillåtna spänningen borde sättas till 100 MPa. Mätningar av hårdhet, brottgräns och termisk diffusivitet av bestrålat volfram gav svar på hur strålning förändrar materialegenskaperna. Hårdheten ökade med mer än 50% och den termiska diffusiviteten minskade med 28-51%, beroende på testtemperaturen. Proverna blev extremt spröda och bröts utan några

tecken på föregående deformation. Den experimentella datan användes för att simulera hur temperaturen och spänningen i volframet påverkas av de nya materialegenskaperna. Resultatet har använts för att förbättra designen av strålmålet.

**Nyckelord:** ESS, Volfram, Spallation, Mekaniska egenskaper, Utmattning, Oxidation, Strålningseffekter, Termisk diffusivitet.

## Abstract

The European Spallation Source (ESS), which is currently under construction in Lund, will use pure tungsten as the spallation neutron target. The tungsten will be irradiated by a 2 GeV proton beam, pulsed at a repetition rate of 14 Hz. Each pulse will deposit 357 kJ in the tungsten causing an instantaneous temperature rise of approximately 100 °C, during the 2.86 ms pulse duration. The target is wheel-shaped, 2.6 m in diameter, and will be rotating at 0.39 Hz to distribute the proton beam loads. The tungsten target consists of nearly 7000 bricks with dimensions  $80 \times 30 \times 10 \text{ mm}^3$ . The bricks are separated by 2 mm wide cooling channels in which helium gas flows at a rate of 2.85 kg/s. The proton beam will be more powerful than the beam used at any other existing neutron spallation facility. Thanks to the high beam power and innovative moderator design, ESS will become the brightest neutron source in the world.

However, designing the target is challenging, as its structure should withstand loads from the high beam power. The high intensity proton beam will not only cause cyclic thermo-mechanical loading of the tungsten, but also irradiation damage in the form of displacements of atoms in the microstructure, and production of a wide range of radioactive isotopes such as gaseous transmutation elements, and a significant fraction of solid transmutation elements, which will alter the thermal and mechanical properties of tungsten. Using such a powerful beam requires an optimal design of the target and a good understanding of the complex physical, mechanical, and thermal changes occurring in irradiated tungsten. It is also important to identify and mitigate potential issues and accidental scenarios during operation of the ESS target.

The present work aims to characterise thermal and mechanical properties of high-energy proton and spallation neutron irradiated pure tungsten,



for the use as a spallation target material. The work includes studies on fatigue properties of unirradiated tungsten from various processing routes, to determine which type of tungsten is the most durable under cyclic loads. The fatigue study served as a basis for setting the maximum acceptable stress of 100 MPa in the tungsten bricks during operation, as well as choosing rolling as the most suitable manufacturing method. The tungsten volume will be contained in a stainless-steel target vessel, which confines the helium gas target-coolant. Tungsten is known to be readily oxidised even at moderate temperatures, which makes even impurity levels of oxygen and water vapour in the helium a potential issue. Therefore, oxidation behaviour of tungsten in mildly oxidising atmospheres and temperatures relevant to ESS operation, was characterised. The results were used to set the upper temperature limit in the tungsten target during normal operation, as well as the maximum allowable temperature during off-normal incidents. However, both temperature and thermo-mechanical stress in the tungsten will alter as the properties of the material change due irradiation.

The available data on proton irradiated tungsten is very limited. Therefore, in the present work, large efforts have been made for studying tungsten irradiated under similar conditions as the future ESS target material. Specifically, irradiation induced changes in thermal diffusivity, hardness, ductility, and ultimate tensile strength of tungsten irradiated by a high power proton beam at Paul Scherrer Institute (PSI), were studied. The results point towards a severe embrittlement of irradiated tungsten. Virtually zero plasticity was found in specimens tested up to 500 °C, and the hardness increased by more than 50%. Thermal diffusivity decreased by 28-51%, depending on the test temperature (25-500 °C). All tested irradiated specimens had lower irradiation damages than the ESS tungsten is expected to accumulate during the 5-year life time of the target.

Finally, a concluding study is presented in which new calculations of temperature and the maximum stress in the bricks were made, based on the obtained experimental data on the thermal and mechanical properties of irradiated tungsten.

**Keywords:** ESS, Tungsten, Spallation target, Mechanical properties, Fatigue, Oxidation, Irradiation effects, Thermal diffusivity.



## Acknowledgements

The work presented in this thesis has been carried out under the supervision of Prof. Srinivasan Iyengar at the Division of Materials Engineering at Lund University, Dr. Yongjoong Lee, Head of the Materials Group at the Target Division of the European Spallation Source, and Dr. Yong Dai, Head of the Advanced Nuclear Materials group of the Laboratory of Nuclear Materials at Paul Scherrer Institute. Their guidance and support are gratefully acknowledged.

I am thankful for the opportunity to work at these institutes. In each group I developed different skills and gained knowledge by learning from experts in materials engineering, nuclear materials, and spallation target development. I am fortunate to have had many colleagues in both Switzerland and Sweden, who helped me and generously shared their knowledge and advice. Today they are some of my closest friends. Thank you all for your support during these years, both professional and personal.

I would especially like to thank the following people: Dr. Kumar Babu Surreddi, Dr. Hossein Sina, Dr. Vladimir Krsjak, Dr. Barbara Horvath, Mr. Wei-Neng Hsu, Mr. Rikard Hjelm, Mr. Zivorad Zivkovic, Dr. Monika Hartl, Ms. Sofie Borre, Dr. Erdzan Hodzic, Ms. Lijuan Cui, Mr. Roger Brun, Mr. Matteo Ferrari, Mr. Johan Wendel, and Dr. Elizabeth Di Geronimo.



## List of publications and author's contribution

This thesis is based on the following papers:

- Paper I J. Habainy, S. Iyengar, Y. Lee, Y. Dai, Fatigue behaviour of rolled and forged tungsten at 25°, 280° and 480 °C, J. Nucl. Mater. 465 (2015) 438-447.
- Paper II J. Habainy, A. Lövberg, S. Iyengar, Y. Lee, Y. Dai, Fatigue properties of tungsten from two different processing routes, J. Nucl. Mater. 506 (2018) 83-91.
- Paper III J. Habainy, S. Iyengar, K. B. Surreddi, Y. Lee, Y. Dai, Formation of oxide layers on tungsten at low oxygen partial pressures, J. Nucl. Mater. 506 (2018) 26-34.
- Paper IV J. Habainy, Y. Dai, Y. Lee, S. Iyengar, Thermal diffusivity of tungsten irradiated with protons up to 5.8 dpa, J. Nucl. Mater. 509 (2018) 152-157.
- Paper V J. Habainy, Y. Dai, Y. Lee, S. Iyengar, Mechanical properties tungsten irradiated with high energy protons and spallation neutrons, submitted to J. Nucl. Mater., July 2018.
- Paper VI J. Habainy, Y. Lee, K. B. Surreddi, A. Prosvetov, P. Simon, S. Iyengar, Y. Dai, M. Tomut, A study of heavy ion beam induced damage in tungsten for high power target applications, submitted to Nucl. Instrum. Methods Phys. Res. B, August 2018.

In the papers listed above, the author has made major contributions in planning and executing the experimental work, analysis of data and preparing the manuscript for publication.

# Glossary

## **Beam trip**

When the beam intensity drops to less than 50% of the target operational value, for more than one minute. The beam is then considered unavailable.

## **Cross-section (in particle physics)**

Probability of a collision between two particles, followed by a certain reaction.

## **Differential Thermal Analysis**

Temperature difference measurement between the sample and a reference material during heating.

## **Half-life**

Time required to reduce a quantity to half of its original value by decay of a radioisotope.

## **Helium ash**

Alpha particles (helium nuclei) produced by fusion reactions in the deuterium-tritium plasma.

## **Sinks**

Locations to which (radiation) defects migrate and annihilate. E.g. free surfaces and phase boundaries.

## **Spallation**

Break-up of a nucleus bombarded by an energetic proton.

## **Thermogravimetry**

Measurement of mass changes during heating.



## List of abbreviations

AES	Auger Electron Spectroscopy
appm	Atomic Parts Per Million
BCC	Body centred cubic
BSE	Back-Scattered Electrons
DBTT	Ductile-to-brittle Transition Temperature
DSC	Differential Scanning Calorimetry
DTA	Differential Thermal Analysis
dpa	Displacement Per Atom
EBS	Electron Backscatter Diffraction
EDM	Electrical Discharge Machining
EDS	Energy Dispersive X-ray Spectroscopy
ESEM	Environmental Scanning Electron Microscope
ESS	European Spallation Source
FIB	Focused Ion Beam
ITER	International Thermonuclear Experimental Reactor
LDV	Laser Doppler Vibrometer
LFA	Laser/Light Flash Apparatus
P/M	Powder Metallurgy
PKA	Primary Knock-on Atom
PSI	Paul Scherrer Institute
SEM	Scanning Electron Microscope
STA	Simultaneous Thermal Analysis
TGA	Thermogravimetric Analysis
UTS	Ultimate Tensile Strength
XRD	X-ray Diffraction

# List of figures

Figure 1	A schematic view of the ESS facility. Copyright Henning Larsen Architects.	p.16
Figure 2	Made to scale model of one of the 36 segments of the target wheel.	p. 20
Figure 3	The inside of a hotcell.	p. 23
Figure 4	A schematic representation of the max, min, and mean stress.	p. 38
Figure 5	Sample holder. A) Frontside with copper spring washers, B) backside with reflective tape, C) luminescence target showing the beam spot.	p. 47
Figure 6	Experimental setup at GSI for irradiation with pulsed heavy ion beam.	p. 48
Figure 7	Temporal development of maximum temperature of the uranium irradiated 3 mm thick tungsten specimen.	p. 50
Figure 8	One-dimensional configurations of the dpa values per single ion.	p. 50
Figure 9	Fluence of protons and fast spallation neutrons as a function of distance to the Gaussian shaped beam centre.	p. 53
Figure 10	Photograph taken after the extraction of irradiated tungsten and a drawing of the disk and bend bar specimens cut from larger pieces.	p. 54
Figure 11	Geometries of (a) room temperature and (b) high temperature tensile and fatigue test specimens. All dimensions are in mm.	p. 57
Figure 12	Micrographs of polished forged and rolled specimens: (a) HFP, (b) RLP, (c) RTP, (d) HLP.	p. 67
Figure 13	Tensile data for rolled and forged specimens at 25 °C.	p. 68
Figure 14	Tensile data for polished rolled and forged specimens at different temperatures.	p. 69
Figure 15	Wöhler diagram for rolled and forged specimens tested at 25 °C	p. 71
Figure 16	SEM images of fatigue fracture surfaces. (a) RLP 25 °C, (b) RTP 25 °C, (c), RLU 25 °C, (d) RLP 280 °C	p. 72
Figure 17	SEM images of fracture surfaces of forged specimens. (a) FU 25 °C, (b) FU 280 °C.	p. 73
Figure 18	Fracture surfaces of (a) FP 25 °C, (b) FP 280 °C, (c) FP 480 °C, (d) RLU 480 °C.	p. 74
Figure 19	Gauge sections of SH and RA specimens.	p. 75
Figure 20	Microscopic images of etched SH and RA specimens.	p. 76
Figure 21	Triplanar micrograph of a rolled specimen.	p. 76

Figure 22	Monotonic tensile test results of SH and RA specimens.	p. 77
Figure 23	Wöhler diagram for SH and RA tungsten.	p. 78
Figure 24	Crack propagation in the RA specimen, b) and c) show large cracks and delamination, the arrows point in the rolling direction, and d) illustration of the serrated wedge grips.	p. 79
Figure 25	Stress-strain relationship during the initial and later stages of strain-controlled cyclic testing.	p. 80
Figure 26	Strain-controlled testing of an RA specimen showing completely elastic response.	p. 81
Figure 27	Fractographs of an SH and an RA fatigue tested specimen.	p. 82
Figure 28	Oxidation of tungsten in a He-0.5%O <sub>2</sub> gas mixture.	p. 83
Figure 29	Specimens after oxidation for 2h in a He-0.5%O <sub>2</sub> gas mixture.	p. 84
Figure 30	Oxidation of tungsten in He-Ar-H <sub>2</sub> O gas mixture, with a p <sub>H<sub>2</sub>O</sub> of 790 Pa.	p. 85
Figure 31	Tungsten foils oxidised in argon gas (max. 5 ppm O <sub>2</sub> ).	p. 86
Figure 32	SEM images of tungsten at various temperatures during in situ oxidation in a hot stage, at a p <sub>H<sub>2</sub>O</sub> of 100 Pa.	p. 87
Figure 33	XRD of tungsten foils oxidised in pure argon (max. 5 ppm O <sub>2</sub> ).	p. 88
Figure 34	XRD of tungsten disks oxidised in air for 24 h.	p. 88
Figure 35	Tungsten oxide scale thickness measured by AES.	p. 89
Figure 36	EDS analysis at different positions on the oxide scale.	p. 91
Figure 37	Oxidation of pure and alloyed tungsten.	p. 92
Figure 38	Thermal diffusivity of unirradiated tungsten.	p. 93
Figure 39	Thermal diffusivity of irradiated tungsten.	p. 94
Figure 40	Thermal diffusivity of irradiated and annealed tungsten.	p. 96
Figure 41	Results from 3-point bend tests.	p. 99
Figure 42	Microhardness of irradiated tungsten.	p. 101
Figure 43	SEM images of fracture surfaces of unirradiated tungsten, tested at 25 °C (a, c, e) and at 450 °C (b, d, f).	p. 102
Figure 44	Fractographs of specimens irradiated to 1.3 dpa (a, c) and 3.5 dpa (b, d), tested at 25 °C.	p. 103
Figure 45	Fractographs of specimens irradiated to 1.4 dpa and tested at 450 °C (a, c), and 3.5 dpa and tested at 500 °C (b, d).	p.104

Figure 46	Microhardness of uranium ion irradiated tungsten. Horizontal bars show the indentation, vertical bars represent the standard deviation.	p. 105
Figure 47	Illustration showing the side view of the irradiated specimen. The yellow layer represents the irradiated area. Hardness measurements were performed on the plane marked with a black line.	p. 106
Figure 48	Nanohardness over the cross-section of an irradiated specimen. The dotted line represents the average hardness at depths beyond the reach of the heavy ions.	p. 107
Figure 49	Calculated stress in the centre of the irradiated specimen after a 150 $\mu$ s long beam pulse with the intensity $7.5 \times 10^9$ ions/cm <sup>2</sup> /pulse.	p. 108
Figure 50	Snapshot of the specimen at time = 2.245 ms after the start of a 150 $\mu$ s long beam pulse. Shown here is the maximum and minimum von Mises stress.	p. 109
Figure 51	Relative change in thermal diffusivity of tungsten as a function of fluence.	p. 111
Figure 52	Oxidised tungsten. The darker area appeared after irradiation and corresponds to the shape and size of the beam spot.	p. 112
Figure 53	SEM images of the oxidised specimen before and after irradiation.	p. 113
Figure 54	Model representing the middle section of an ESS target segment (left) and the beam profile used for heat deposition calculations (right).	p. 114
Figure 55	Calculated maximum temperatures in a brick. Comparison between unirradiated and irradiated tungsten with 20% lower thermal conductivity.	p. 115

# List of tables

Table 1	Properties of tungsten.	p. 6
Table 2	Spallation neutron sources and their key parameters. Design values are shown in brackets [12].	p. 16
Table 3	Main design parameters of ESS.	p. 19
Table 4	Beam conditions, in-situ monitoring (ISM), and post irradiation examination (PIE).	p. 49
Table 5	Summary of UTS values.	p. 67
Table 6	Replication rates and number of specimens used in each set.	p. 70
Table 7	Endurance limits and maximum stress amplitudes at runout.	p. 70
Table 8	EDS analysis of positions 1-6 on the oxide scale.	p. 90
Table 9	Reference data for unirradiated tungsten.	p. 98
Table 10	Thermal conductivity of irradiated tungsten.	p. 98
Table 11	Radiation damage effect on operational temperature and maximum von Mises stress in an ESS tungsten brick.	p. 116



# Part I

## Introduction





# 1. Outline

The aim of this work has been to characterise thermal and mechanical properties of pure tungsten under conditions of relevance to the European Spallation Source (ESS). The role of tungsten at ESS is to produce neutrons for scattering experiments. This is done via a process called spallation, which involves high-energy protons colliding with tungsten. During the spallation process, the tungsten is exposed to radiation and thermo-mechanical cycling, which could lead to fatigue failure. The radiation, in particular, is a serious concern as it severely deteriorates the properties of the material. The present work was carried out to get a better understanding of tungsten behaviour under these conditions. This was achieved by studies on both irradiated and unirradiated tungsten. Properties such as thermal diffusivity, ultimate tensile strength, fatigue life, oxidation resistance, and hardness, were characterised.

The present thesis consists of two parts in which the first part serves as an introduction to the papers included in the second part. *Objectives* of the present work are given in the second chapter of Part I. Chapter 3, *Background*, focuses on literature studies, basic theory of radiation damage in materials and the spallation process, background information on the design of the tungsten spallation target at ESS, and different

methods of tungsten production and processing and their effect on the mechanical properties. Chapter 4, *Materials and Methods*, presents the test specimens, equipment and methods of characterisation as well as the data analysis method. The fifth chapter, *Results and discussion*, gives an overview of the most important findings, summarises the appended publications and presents implications of the results on the design and operation of the ESS tungsten target. Lastly, in Chapter 6, *Conclusions*, concluding remarks are given and future work is suggested.

## 2. Objectives

Pure tungsten has been chosen as the spallation material at ESS due to its high atomic mass, high density, high melting temperature, and commercial availability in large amounts. The spallation target consist of 6696 bricks of tungsten with dimensions  $80 \times 30 \times 10 \text{ mm}^3$ . The 2 GeV pulsed proton beam, with a pulse length of 2.86 ms and a repetition rate of 14 Hz, will deliver 357 kJ per pulse to the tungsten bricks. During the 5-year lifetime of the target, it will be exposed to a high flux proton and spallation neutron irradiation which will cause a maximum displacement damage of 10 dpa. In addition, the target material will be subjected to thermo-mechanical cycling caused by beam pulses and occasional beam trips. The design of the ESS facility includes unique features that have not been used before on such a large scale. One of them is the pulsed proton beam which will be several times more powerful than the beams used in other leading spallation sources. Another feature is the unprecedentedly large target, which is rotating and is cooled by a large helium flow.

Although tungsten has many attractive properties, it is also known for its low ductility, low DBTT, poor high-temperature oxidation resistance, and severe irradiation induced embrittlement. There is no previous experience

of using pure, unprotected tungsten in such a demanding environment. Further, data on thermal and mechanical properties of high energy proton and spallation neutron irradiated tungsten is very limited. It is expected that the risk of target failure due to cyclic thermo-mechanical loading is increased by the displacement damage and transmutation products caused by irradiation. The full extent of the changes in tungsten as a spallation material is, however, still unknown. The objective of the present work was therefore to study the changes in physical, mechanical, and thermal properties of pure tungsten induced by high-energy, high-flux proton beam irradiation. The outcome of this work is not only important for ensuring a reliable operation of the ESS target, but also produces data useful for other, present and future, high power spallation sources using tungsten as the target material.

## 3. Background

Chapter 3 summarises theoretical aspects and gives background information on the topics discussed in this work. The focus areas are tungsten production, the European Spallation Source, and the effect of radiation damage on metallic materials. This chapter is based on reviews of literature on tungsten and ESS.

### 3.1 Tungsten

Tungsten is a metallic transition element with nuclei containing 74 protons and 84-116 neutrons [1]. It has a body centred cubic (BCC) crystal structure. The naturally occurring tungsten isotopes are  $^{184}\text{W}$  (30.67%),  $^{186}\text{W}$  (28.6%),  $^{182}\text{W}$  (26.3%), and  $^{183}\text{W}$  (14.3%). The most important tungsten minerals are wolframite (Fe, Mn)  $\text{WO}_4$ , scheelite  $\text{CaWO}_4$ , hübnerite  $\text{MnWO}_4$ , and ferberite  $\text{FeWO}_4$  [2]. Table 1 summarises some of the most important properties of tungsten, determined at room temperature [1, 3].

**Table 1 Properties of tungsten**

Properties of pure tungsten at room temperature			
Crystal structure		BCC	
Atomic number	Z	74	
Young's modulus	E	390-410	GPa
Poisson's ratio	$\nu$	0.280-0.3	
Density	$\rho$	19.3	g/cm <sup>3</sup>
Melting temperature	$t_m$	3422	°C

The main characteristics of tungsten are the exceptionally high melting point of 3422 °C [1] and the high theoretical density of approximately 19.3 g/cm<sup>3</sup>. In addition, it has a high Young's modulus, high ultimate tensile strength, good thermal stability, low vapour pressure, and high creep resistance. This makes tungsten a favourable material for applications in areas such as nuclear and high energy physics, in commercial products, and for military and aeronautical use. Due to its high melting point, tungsten is widely used in high temperature applications, especially as a coating material, as filaments for electric lamps, and as a source of electrons in electron microscopes. It is also one of the main sources for X-ray targets. However, just like other refractory metals, tungsten is easily degraded in oxidising atmospheres, even at moderately low temperatures. This restricts the use of pure, unprotected tungsten to lower temperatures or non-oxidising high-temperature atmospheres [4]. The density, which is approximately 70 % higher than that of lead, makes it a suitable candidate for applications such as weights and counter-balances, as well as missiles and bullets. As an alloying element, tungsten is very often used in metal working tools, such as high-speed steel tools, cutting tool bits, and drill bits.

### 3.1.1 From mineral to finished product

#### **Production of tungsten powder**

Tungsten is extracted from ore concentrates, which are first processed to get oxides which are then reduced to metal in powder form. Due to the high melting temperature of tungsten, it is almost exclusively shaped through powder metallurgy (P/M). Typically, the ore has an initial average concentration of 0.5 wt.%  $WO_3$ . Tungsten bearing scrap is recycled and added to the ore as it goes through the enrichment process. Depending on the type of mineral, different techniques such as gravity methods and flotation are employed to increase the  $WO_3$  concentration to 60-70%. Once the ore and the tungsten rich scrap mixture has reached this concentration, it is treated with chemicals. Wolframite is treated with NaOH and Scheelite with  $Na_2CO_3$ , which leads to the formation of the water-soluble sodium tungstate  $Na_2WO_4$ . This is followed by a set of purification steps ending in APT, Ammonium Para Tungstate. APT is then heated to between 400 °C and 900 °C to remove water and ammonia via evaporation. The remaining substance after this step is tungsten oxide. If the process is carried out in an oxygen rich environment the oxide formed will be the yellow  $WO_3$ . Less oxygen leads to the formation of a slightly reduced oxide,  $WO_{3-x}$ , which is blue in colour. The last step of the powder production is the reduction of oxides to tungsten by flowing hydrogen gas. This proceeds according to the following reaction:



Depending on the type of furnace used for the reduction, and by controlling parameters such as the temperature and oxide powder layer thickness in the furnace, the particle size of the metallic tungsten powder can be controlled. Thicker the powder layer, larger is the resistance to diffusion and slower is the removal of the reaction product ( $H_2O$ ). The humidity is naturally always higher at the bottom of the layer than at the



top. Therefore, since the local humidity determines the nucleation and growth of the metal particles, the height of the powder layer is directly proportional to the size of the particles. This also means that the powder layer thickness is directly affecting the distribution of the particle sizes. Increasing layer thickness results in a broader distribution. The final particle size of tungsten depends on a combination of several parameters. In general, small particles form at low temperatures, dry hydrogen, small powder layer heights, high layer porosity, and low oxide feed. Similarly, using the opposite parameters produces large particles.

Tungsten powder can be produced as 0.1-100  $\mu\text{m}$  sized particles. Pure tungsten is normally produced in the size range 2-6  $\mu\text{m}$ . Larger particles may lead to incomplete sintering, and smaller may inhibit the evaporation of trace impurities due to a much higher sintering activity [1]. Not only the particle size can and should be controlled, the shape and agglomeration of the particles are important properties as well. Good agglomeration of the tungsten powder leads to less porosity and better mechanical properties in the final product. If the reduction is performed at low temperatures and in dry environments, the powder will form very fine particles that agglomerate and transform into metal sponges. In very humid and high temperature conditions, individual tungsten particles can be formed over relatively large distances as they are aided by the chemical vapour transport (CVT) of the volatile species  $\text{WO}_2(\text{OH})_2$ . The particles formed under such conditions are well-faceted, partly intergrown, and about 10  $\mu\text{m}$  in diameter. These micron-sized facets are sometimes visible on fracture surfaces of some tungsten specimens. Electron microscopic images of these faceted grains can be found in the attached Papers II and V. The latter includes a discussion on the effect of the well-faceted grains on the fracture of the specimen.

## **Compaction and sintering of the powder**

Powder metallurgy, or P/M, is a method for forming metal parts by compacting the powder and heating it to a temperature much below the melting point. This is the standard manufacturing process for refractory metals due to their high melting points. Each step in the process, i.e. powder production, compaction, sintering, and post-sintering operations, has a strong influence on the quality and performance of the finished product. In general, lower the porosity, higher is the quality of the product. The particle size of the powder also has a major impact on the properties of the finished piece.

Once the tungsten powder is produced, it is usually pressed and sintered at temperatures of 1900-2300 °C [5]. This first step should increase the density to about 92-98% [1]. In the sintering process, the high surface area of the compact is decreased by diffusional flow of atoms into the pore volume, driven by capillary forces. As individual particles grow together, the surface area decreases, and the free energy is lowered. During sintering, the densification process is driven by grain boundary diffusion. When high levels of density are reached, the process is controlled by lattice diffusion instead. Tungsten is always sintered in a reducing atmosphere, such as in dry and high-purity hydrogen. Vacuum or inert gas is not enough to protect the material. Even very small amounts of oxygen and moisture will affect the mechanical properties of tungsten, especially the ductility. Since sintering is performed at very high temperatures, the tungsten undergoes several changes. Besides grain growth, strains are relieved and recrystallisation occurs, i.e. new strain-free grains with low dislocation density are formed. When sintering is completed, the part is further processed by e.g. forging or rolling, to reach its final shape as a near fully dense product.

## **Densification methods and other post-sintering operations**

There are several densification methods suitable for tungsten products and the choice depends on factors such as cost, availability, shape, size, thickness, complexity of the part, requirements on surface roughness, properties of the material, and tolerances. Generally, processes which create grains elongated in the deformation direction lead to a stronger material (in this direction) and are preferable over annealing or recrystallisation. Lower working temperatures result in greater work hardening, although, the temperature should not be too low, as the risk of fracture during the process increases with decreasing temperature. Besides eliminating residual porosity, primary working during ingot breakdown improves the workability for subsequent cold forming, through grain size reduction. The temperature range for forming tungsten is limited at the lower end by its low temperature brittleness, and at the higher end by the recrystallisation temperature.

Hot Isostatic Pressing (HIP) is a method in which the material is contained in a pressure-tight, sealed container and is subjected to a high isostatic gas pressure at an elevated temperature. HIPing causes plastic deformation of the powder which closes the pores and increases the density. For tungsten parts, the temperature during this process is approximately 1700 °C. Argon, nitrogen, and helium gases are commonly used, and the pressure can vary between 20 MPa and 300 MPa. HIPed products tend to have a fine microstructure with equiaxed grains which leads to isotropic physical and mechanical properties. Similarly, machinability is improved due to the uniform and fine grained microstructure. Often, the HIPing process can be preceded by sintering, especially for tungsten and its alloys. The combined sintering and HIP method starts with a partially dense, already compacted piece, which is sintered while pressure is applied during the HIPing phase [6].

Another common method for compaction of tungsten powder is forging. Forging involves simultaneous application of heat and pressure in a die that gives shape to the final product. Forging is performed on high-speed presses, resulting in high deformation rates and large plastic flow. This breaks up oxide layers on the particles and enhances bonding. The amount of oxygen in the part is determined by the oxidising gases in the environment during sintering of the preform. The presence of oxides in the forged specimen disturbs the bonding between particles, and affects the fatigue properties [7].

Rolling of tungsten is an excellent densification method. In general rolling results in higher densities than forging and HIPing, which means better mechanical properties. However, the material becomes highly anisotropic. The orientation of the final tungsten part relative to the direction of the applied stress is very important in rolled materials. The grains become very elongated, and if cross-rolled, the diameter of the pancake shaped grain can reach the size of millimetres. If the material is rolled heavily, delamination of the layers can occur. This phenomenon was observed in both the rolled tensile and fatigue specimens, as well as the rolled thin foils, used in this work. This issue is discussed further in the attached Paper II, as well as in the result section of this thesis. Another issue with rolled tungsten is the variation in hardness throughout the thickness of the plate. Typically, the surface will be harder compared to the part well inside the bulk material.

### **Customising properties through additions of rhenium**

As mentioned earlier, tungsten suffers from severe low-temperature brittleness. This is one of the main problems in using pure tungsten at moderate temperatures. There is a range of temperature in which this behaviour changes, and tungsten becomes ductile. The mean temperature in this region is called the ductile-to-brittle transition temperature, or

DBTT for short. The DBTT is an important characteristic, especially for tungsten, as it is several hundred degrees above room temperature. This limits the usefulness and fabrication possibilities for tungsten at lower temperatures. The brittleness of polycrystalline tungsten below the DBTT is believed to be caused by weakness of the grain boundaries, leading to crack initiation in both wrought and recrystallised samples. Pure single crystal tungsten is known to be ductile, even at a temperature of 20 K [1], which strengthens this interpretation.

To a certain extent, the DBTT can be controlled. It can be modified by various mechanical, chemical, and microstructural factors. Parameters such as the amount and distribution of the impurities, the grain size, surface roughness, sample size, strain rate, and type of applied stress (tensile, compressive, shear), will cause a shift of the DBTT. In general, the DBTT is lowered by plastic deformation. Higher the degree of plastic deformation, lower is the DBTT. Annealing, on the other hand, increases it. The highest transition temperature is therefore found in recrystallised tungsten samples.

Adding rhenium is a common way to increase the ductility of tungsten products. As rhenium has a hexagonal closed packed (HCP) crystal structure, rather than a body centred cubic (BCC) like tungsten, it does not exhibit a DBTT. Annealed rhenium is, unlike tungsten, very ductile. Tungsten-rhenium alloys have very good mechanical properties. Not only is the DBTT significantly lowered, but the high-temperature strength is even higher than that of pure tungsten. In fact, the tungsten-rhenium alloy is the only important tungsten-based solid-solution alloy today [1]. Rhenium additions also stabilise the grain structure and increase the recrystallisation temperature. The improved ductility of tungsten-rhenium alloys is attributed to the increased solubility of elements such as nitrogen, carbon, oxygen, sulphur, and phosphorus, which otherwise would have migrated to low-energy positions such as the grain boundaries

and dislocations, thus weakening the material. Rhenium causes re-distribution of the impurities as clusters within the lattice, which improves the grain-boundary fracture toughness.

The effect naturally depends on the amount of rhenium added. In general, tungsten-rhenium alloys can be separated into three groups depending on their rhenium content. These are W-(3-5)Re, W-10Re, and W-(25-26)Re. Higher the rhenium content, higher is the ductility. Peak ductility is reached just below the maximum solid solubility limit of rhenium in tungsten, which is approximately 27 wt.% Re. A rhenium content of 26 wt.% results in an increase in hardness of around 20% [1]. Tungsten-rhenium alloys with lower rhenium content have high creep strength, good workability, better welding properties, and are extremely resistant against thermal stresses.

Unfortunately, none of the benefits of alloying tungsten with rhenium can be used utilised at ESS. The environment which the tungsten will be in, once the facility is up and running, will be harsh and introduces complex issues. The most important problem, and one which is still not very well understood, is the expected radiation induced change in tungsten alloys. There have been studies showing that tungsten-rhenium alloys lose their beneficial mechanical and thermal properties on irradiation. The attached papers IV and V contain more information on this topic.

### **Metal forming**

Tungsten and its alloys are difficult to machine and require special fabrication techniques. Mechanical working should be performed below the recrystallisation temperature, but above the DBTT. As the solubility for carbon, nitrogen, oxygen, and hydrogen, is very low (<0.1 ppm) [1], there is a significant risk of grain boundary embrittlement if the impurity levels are not kept to a minimum. This is, however, very difficult to

achieve. Instead, it is easier to control the microstructure during fabrication, to ensure a reasonably low DBTT [4].

Cutting tungsten at room temperature is difficult and the risk of fracture is high. A suitable method for this is electrical discharge machining (EDM). This method was the only one that could be used successfully on the extremely brittle irradiated tungsten specimens used in this work. Details of the sample preparation technique is discussed in Chapter 4 as well as in the attached Papers IV and V.

### 3.1.2 Past and current research on tungsten properties

Much of the early understanding of tungsten and its alloys comes from research conducted around the time of World War II. Two of the most important applications during the war were armour-piercing projectiles and high-speed tool steels made of tungsten carbide [8]. A few decades later, tungsten became a material of increasing interest once again. The National Aeronautics and Space Administration (NASA) has conducted many studies on tungsten during the past decades, focusing mainly on the high temperature behaviour of the material. Recently, much of the research on tungsten has been done by the fusion and neutron spallation community. The attached papers provide summaries of the available literature on tungsten and its properties, both irradiated and unirradiated. Other very useful sources of tungsten data are the ASM Handbooks (American Society for Metals), a book on tungsten and its properties published by Erik Lassner and Wolf-Dieter Schubert in 1999 [1], a comprehensive literature review published by NASA in 1969 [9], and of course, many journal publications by researchers in various fields.

## 3.2 European Spallation Source

The European Spallation Source (ESS), is a European Research Infrastructure Consortium (ERIC), currently under construction in Lund, located in southern Sweden. It is one of the largest and most prestigious science and technology infrastructure project being built today. The research facility will be based on the world's most powerful proton linear accelerator and brightest neutron source, which will enable scientific breakthroughs in various fields such as materials, life sciences, energy, environmental technology, cultural heritage, and fundamental physics. ESS is a joint European project with 15 founding members and 38 in-kind partners, working together on designing and building the facility. The construction started in 2014 and full power operation is expected by 2025, with the first beam on target in 2021 [10].

The ESS facility consists of a proton linear accelerator, a target station, many scientific instruments, and various laboratories, sample preparation rooms, workshops and offices. Figure 1 shows a schematic view of the facility, made by Henning Larsen Architects. The start of the linear accelerator is seen in the bottom left. The target is located approximately 600 meters away from the ion-source and surrounded by laboratories and experimental halls. Also seen here is future Science Village and beyond that MAX IV, a synchrotron radiation facility.

The planning of ESS started already 20 years ago, when the Organisation for Economic Co-operation and Development (OECD), strongly recommended that North America, Asia, and Europe, each should build a new generation of high-intensity neutron source in the MW-class [11]. The United states was the first to commission its neutron source. Oak Ridge National Laboratory (ORNL) in Tennessee, US, started its Spallation Neutron Source (SNS) in 2006. Japan followed in 2009 with the Japan Spallation Neutron Source (JSNS) at the Japan Proton



Accelerator Research Centre (J-PARC) in Tokai. Besides ESS, SNS, and JSNS, there are a few other spallation sources around the world. These are summarised in table 2. The following section describes the scientific purpose of a spallation neutron source, namely neutron scattering experiments.



**Figure 1. A schematic view of the ESS facility. Copyright Henning Larsen Architects.**

**Table 2 Spallation neutron sources and their key parameters. Design values are shown in brackets [12].**

Facility	Beam Power [MW]	Pulse energy [kJ]	Target	Location
ESS	(5)	(357)	W	Sweden
JSNS	0.5 (2)	20 (80)	Hg	Japan
SNS	1.4 (2)	23 (33)	Hg	USA
SINQ	1.2	-	Pb	Switzerland
ISIS	0.16	3.2	W	UK
CSNS	(0.1)	(6)	W	China
LANCE	0.1	5	W	USA
ISIS TS2	0.05	5	W	UK

### 3.2.1 Neutron scattering

Neutron scattering is a well-developed and extensively used method for determining the relative positions and motion of atoms in a bulk sample. It is a means of characterising fundamental properties of physical materials as well as biological matter. Neutrons have excellent characteristics for use in probes. As they are electrically neutral, they do not interact with the electrons in the matter. The distance between two nuclei is significantly larger than the size of a nucleus, which means neutrons can easily travel large distances without being scattered or absorbed. They penetrate matter far better than charged particles. If they do strike a nucleus, they will be scattered, leaving the sample distributed over many directions and velocities. Analysing the distribution of the scattered neutrons provides the desired information on the structure and dynamics of the atoms in the specimen. The relatively small interaction rate of neutrons can be compensated by using a high flux of the particles. The higher the flux, the brighter the image of the examined sample becomes. The vast number of neutrons needed for a scattering measurement can only be provided by large scale facilities.

A wide range of different instruments have been developed for scientific purposes using neutron scattering. Each instrument focuses on resolving only certain details while ignoring others in order to maintain sufficient intensity for a meaningful measurement. The neutron scattering technique can be further separated into different methods according to the information they provide. Neutron diffraction is used to characterise the atomic arrangement in a material, while inelastic neutron scattering measures the vibration of atoms. Larger structures such as polymers, can be studied using small-angle neutron scattering (SANS). Reflectometry provides information about layered materials and interfaces, and magnetic properties of matter are examined using polarised neutron beams, as well as magnetic neutron scattering.

The wavelength of the incoming neutron is important, and as it is inversely proportional to the speed of the particle, it can be controlled. In scattering experiments, a wavelength of 0.1-1 nm is often used as it corresponds well to the interatomic distance in matter. For this reason, neutrons in the slow energy range are particularly useful [13]. The neutrons produced at ESS will initially have much higher energies than is suitable for neutron scattering experiments. They will, therefore, first be moderated, i.e. slowed down to useful speeds.

### 3.2.2 The ESS design

The main purpose of ESS is to deliver a high flux of neutrons at a high brightness, with energies suitable for neutron scattering experiments. The facility must first be able to produce a high flux of neutrons, moderate them to appropriate energies, and then guide them to the scientific instruments. Each part of the facility has been carefully designed to meet the goal of delivering the brightest neutron beam in the world. Compared to similar existing facilities, there are some features of the ESS design that are unique. The volume of the neutron producing target is much bigger than in other spallation sources. It is also rotating and cooled with helium, whereas most other facilities use a fixed, water cooled target. The beam power is also much higher at ESS, which is a necessity for producing an unprecedentedly large number of neutrons. Some of the most important design parameters of the ESS proton linear accelerator are summarised in table 3.

The ESS facility can be separated into several major sections: the proton linear accelerator, the target building, the experimental halls, and the laboratories, workshops and offices. The focus of this thesis is the neutron producing tungsten target. Its function, design, and potential failure risks are discussed in the next section.

**Table 3 Main design parameters of the ESS proton linear accelerator.**

Parameter	Value
Average beam power	5 MW
Proton beam energy	2 GeV
Pulse repetition rate	14 Hz
Pulse length	2.86 ms
Energy per pulse	357 kJ

### 3.2.3 The spallation target

The ESS spallation volume is composed of 6696 bricks of pure tungsten, contained within 36 segments of a horizontally positioned wheel. A made to scale model of one of these segments is presented in figure 2. The tungsten bricks are of the dimension  $80 \times 30 \times 10 \text{ mm}^3$ , and arranged standing side by side, separated by 2 mm wide channels where the helium cooling gas flows. The spallation volume and coolant are confined within the wheel-shaped target vessel made of stainless steel. The diameter of the wheel is 2.6 m, and it will be rotating with a frequency of 0.39 Hz.

The target is one of the most important components of the facility. The neutrons are produced here, in the tungsten. The process in which this occurs is called spallation. It requires a high-energy impinging particle and a target atom preferably belonging to a heavy element. At ESS, the particle used to initiate spallation is a proton and the element used as the target is a tungsten atom. As the proton strikes the tungsten atom, it will transfer some of its energy to several nucleons (protons and neutrons) which are knocked out of the nucleus and scattered. The heavier the target element, and the more energetic the incoming particle is, more neutrons will be produced. The liberated neutrons are moderated and sent to the scientific instruments.

The protons at ESS are accelerated nearly to the speed of light, in the 600 m long linear accelerator. With a power of 5 MW, the proton beam delivers a kinetic energy of 357 kJ per pulse to the spallation volume. The entire process of spalling, moderating, and delivering neutrons at the right energy and in the right direction, is extremely inefficient. Each 2 GeV proton incident on the tungsten will liberate about 56 neutrons. Only a fraction of these neutrons will enter the cold and thermal moderators, and even a smaller fraction of these will exit the moderator in the right direction, towards the neutron scattering instrument. On an average, 10 000 protons are required to create 1 useful neutron [12].

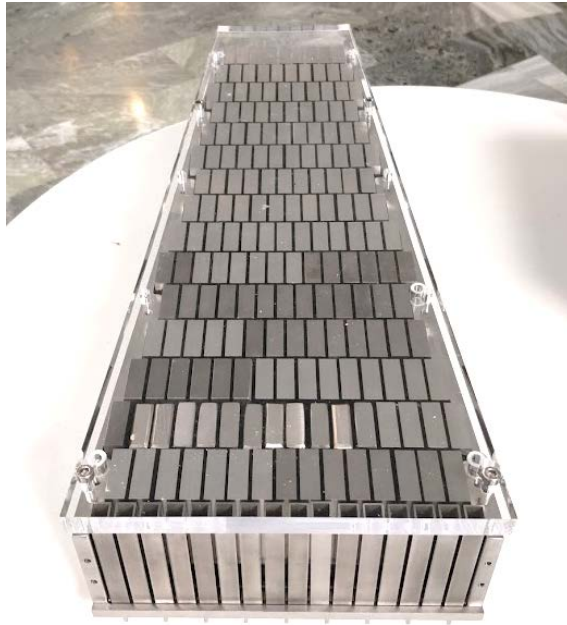


**Figure 1** Made to scale model of one of the 36 segments of the target

The protons are pulsed at 14 Hz, with a pulse length of 2.86 ms. In order to distribute the energy delivered by the proton beam in the spallation volume, the target is designed to rotate in synchronisation with the beam pulse. This way, the heat and damage caused by the beam can be distributed more uniformly over a larger volume. Each pulse will raise the temperature of tungsten instantaneously by approximately 100 °C. Without the rotation of the target, the temperature in the tungsten bricks would increase by more than 1000 °C in a second, leading to immediate catastrophic failure.

The choice of tungsten as spallation material was based on several factors. Most importantly, tungsten provides a high neutron production yield thanks to its high density and high atomic mass, and it is commercially available. In addition, it has a high melting point and high thermal conductivity, which makes it a very good candidate for high power spallation targets. Other spallation neutron sources have targets made of liquid mercury, lead, or tungsten clad with tantalum. The tantalum cladding extends the lifetime of the target as it protects tungsten from catastrophic failure due to irradiation induced embrittlement, and corrosion by the heavy water coolant. The cladding is however not necessary at ESS as the coolant is gaseous. The other options, lead and mercury, present environmental issues. Also, targets using liquid mercury are known to have issues with cavitation-induced erosion of the vessel containing mercury [14].

### 3.2.4 Target material issues

The designed lifetime of the ESS target is 5 years. During this time, the tungsten bricks will have to endure dynamic thermo-mechanical loading due to beam pulses and occasional beam trips. The tungsten will be subjected to nearly 10 million cycles per year. In addition, the proton

beam also causes severe irradiation damage in tungsten. Irradiation with protons causes displacement of tungsten atoms from their lattice positions, creating vacancies, interstitials and other microstructural defects. The irradiation also produces gaseous transmutation products, trapped in the microstructure as bubbles, making tungsten even more brittle and shifting the DBTT over the target operation temperature. The spallation neutrons produced by the proton beam also contribute to the irradiation damage. Thermal and cold neutrons mainly from the moderators will be captured and incorporated in the nuclei of tungsten, creating radioactive isotopes. Together with the protons, the fast spallation neutrons and slow neutrons create solid and gaseous transmutation products. Some of these elements cause a severe deterioration of the thermal and mechanical properties of tungsten. There is also a risk of oxidation of tungsten. The maximum temperature in the tungsten during operation is limited to 500 °C, to avoid the formation of a rapidly growing oxide. It has been shown in the attached Paper III, that even small amounts of oxygen impurity in the inert gas is enough to oxidise tungsten at ESS relevant temperatures.

Another concern, in fact the most serious one, is the risk of fatigue failure of the bricks due to the thermo-mechanical loading caused by the pulsed beam. Although tungsten is not a structural material, failure of a brick might lead to a partial blockage of the 2 mm wide cooling channel, resulting in a hot spot in the target which could jeopardise its structure. This could also increase the rate of diffusion driven release of radioactive isotopes. The stress response in a tungsten brick during a pulse is a function of its material properties. The fatigue life is determined by the magnitude of the stress as well as the mechanical properties of the brick. Both these factors change with irradiation. Thermal diffusivity has been observed to decrease significantly in irradiated tungsten in the present work, which results in larger thermal stresses in the target bricks, as

discussed in attached Papers IV and VI. Irradiation will increase the hardness and decrease the ductility in tungsten, which also affects the fatigue limit, see attached Papers I and II.

Tungsten is currently, and has been for many years, used as spallation target material at a few other facilities. Despite this, the understanding of the combined effect of high power, pulsed proton and spallation neutron irradiation on tungsten is limited. One obvious reason is the difficulty of obtaining proton and spallation neutron irradiated tungsten specimens with a high damage dose. The second issue is the extreme brittleness of the specimens which complicates mechanical testing. And lastly, high residual radioactivity of the samples requires handling of the material in specially equipped laboratories with so called hotcells, where the specimens can be prepared for mechanical testing. Often the material is very radioactive and requires remote handling. The inside of one such hotcell, located in the nuclear laboratory at the Paul Scherrer Institute (PSI) in Switzerland, is shown in figure 3 below. The image shows a polishing and cutting set-up behind thick leaded glass. Most of the irradiated tungsten specimens used in this work were prepared and examined at PSI.

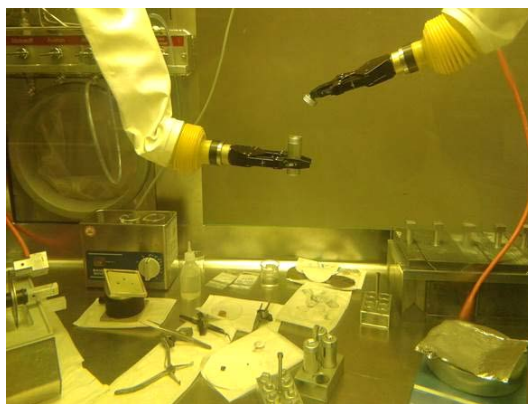


**Figure 3** The inside of a hotcell.



### 3.3 Radiation types

Radiation is mainly divided into two classes, ionising and non-ionising. The non-ionising radiation, e.g. UV-light, microwave radiation or radio waves, carries enough energy to excite an electron to a higher energy state, but not enough to ionise atoms, i.e. completely remove the electron. The ionising radiation can be potentially lethal and cause great material damage. This class of irradiation is further divided into two categories, directly and indirectly ionising. Among the directly ionising are alpha and beta radiation, and in the indirectly ionising group are gamma and neutron radiation.

Alpha radiation consists of alpha particles which are identical to a helium nucleus, i.e. two protons and two neutrons. These particles are highly ionising but with a low penetration depth, they can easily be stopped by a sheet of paper. A beta particle is an electron or positron moving with high speed and energy. These particles are produced by beta decay of atomic nuclei.  $\beta^-$  represents the emission of an electron and  $\beta^+$  the emission of a positron. Beta decay usually occurs in neutron-rich fission by-products produced in nuclear reactors. If a nucleus is unstable due to an excess of neutrons it can undergo  $\beta^-$  decay where a neutron is converted into a proton, an electron and antineutrino. The path for the incoming beta particle is very torturous as compared to the path of the much heavier alpha particle. Because of the low mass, the beta particle changes its direction very easily in a collision. In some cases, the  $\beta^-$  particle, the electron, will deflect so greatly that it will turn back around and be emitted from the material, as in so called back scattering which is used in electron microscopes. More information of electron microscopes can be found in section 4.3.1.

Gamma radiation is electromagnetic radiation of high frequency and high energy per photon. It is most commonly produced by the decay from high energy states of atomic nuclei. Every photon has a probability of vanishing when passing through matter. The probability depends on the energy of the radiation and on the properties of the matter that it passes, but is completely independent of how far the ray has penetrated the material. The intensity of the gamma rays decreases exponentially with the absorber's thickness, but unlike charged particles gamma rays do not have a definite range. No matter how thick the absorber is, some of the radiation, albeit a very small amount, will pass through and each of these particles will have the same energy as they did while entering the material.

Neutrons are electrically neutral and as such have a very high penetration depth, higher than that of alpha, beta and sometimes even gamma radiation. The neutrons can easily enter a nucleus and if they do, there is a good chance that they will remain there. Neutrons are not affected by electrons in the matter and can only lose energy through direct collisions with the nuclei, although the probability for this is low. If a free neutron hits and reacts with a nucleus a new isotope will form, which in turn may produce radiation through neutron activation, e.g. the extra neutron is transformed into a proton under the emission of an electron. So, although the neutron radiation does not ionise the atoms in the same way as the protons or electrons, the neutron interactions are largely ionising.

When shielding from this type of radiation, care must be taken to avoid using materials with nuclei which undergo fission or neutron capture that results in radioactive decay of the nuclei while producing gamma rays. Neutrons can easily pass through most material, but the interaction is enough to cause biological damage. Water and concrete are the most effective shielding materials.  $B_4C$ , boron carbide, is also commonly used as shielding material in nuclear reactors.

Neutrons are usually divided into separate groups depending on their energy level. These are termed cold, thermal, epithermal, slow, fast, and high energy neutrons – with energies ranging from lowest to highest. Cold neutrons have energies up to about 0.025 eV. Both scattering and absorption can occur at these energies. Thermal neutrons have kinetic energies that are in equilibrium with the atoms in the surrounding matter. Slow neutrons have energies up to 0.5-1 MeV. Fast neutrons have energies ranging from 0.5 to 20 MeV, and high energy neutrons have energies above 20 MeV [15]. At ESS, neutrons produced from the target and moderators are in the energy range from cold to GeV.

### 3.4 Radiation damage in metals\*

The fundamental process that drives the radiation induced changes in metals is the displacement of atoms from their lattice sites. The consequences of irradiation include changes in shape and volume, severe embrittlement, reduced ductility, increased hardness, and increased susceptibility to environmentally induced cracking. The radiation damage event can be described in several steps. First, there is the interaction between the lattice atom and an energetic incident atom, whose kinetic energy is transferred to the lattice atom. This creates a primary knock-on atom (PKA). The PKA is displaced and while moving through the lattice, it produces additional knock-on atoms. The group of point defects created by the PKA is called a displacement cascade. The radiation damage event is concluded when the PKA comes to rest as an interstitial.

Once the displacement cascade reaches its final state, agglomeration and diffusion of defects begin. Stable lattice defects are formed either as point defects or defect clusters. Some defects are mobile and escape the cascade

---

\* Largely based on *Fundamentals of Radiation Materials Science* by G. S. Was [16]

region through thermally activated diffusion. This process can last nanoseconds or months, depending on the temperature and irradiation conditions. When all the mobile lattice defects have left the region, the final microstructure is formed. The distribution and number of the remaining defects make up the basis for the observable effects of irradiation damage.

Depending on the type of irradiation particle, the extent and type of the damage varies. Proton irradiation produces small and widely spaced cascades, and many isolated Frenkel defects, i.e. atoms displaced from their original lattice positions, becoming interstitials while leaving a vacancy behind. Neutrons and heavy ions, on the other hand, produce dense cascades with substantial recombination during the radiation damage event. Irradiation with electrons leads to a few widely spread Frenkel defects with low probability of recombination. To facilitate comparisons between diverse types of irradiation damage, the term dpa, displacements per atom, was established. The dpa value gives an estimate of the ratio of displaced atoms in a specimen. The dpa number is often correlated to changes in thermal, mechanical and physical properties, but should be used with caution. The dpa value does not give any information on the chemical changes in a material. Some irradiation conditions lead to the production of substantial amounts of transmutation products. This aspect may be more important to consider than the actual dpa value. Next section focuses on the migration of defects and its consequences on material properties.

### 3.4.1 Migration and annihilation of defects

Vacancies and interstitials tend to migrate to locations where they can annihilate. These positions in the microstructure are called sinks and include areas such as the free surface, grain and phase boundaries. The absorption rate depends on the diffusion coefficient of the defect and the difference in its concentration at the sink relative to the bulk.

Interstitials tend to find the sinks first, followed by vacancies. A high recombination rate between interstitials and vacancies leads to a high irradiation damage recovery. However, if the sink density is high, there will be a competition between the annihilation of interstitials at sinks and the recombination of interstitials with vacancies. Temperature also plays a significant role. For a certain particle type and dose rate, there is a temperature at which the damage production and the recovery rate are equal. Below this temperature, the damage production rate is dominating, and the material can become amorphous.

Isolated point defects can migrate to sinks and form new clusters or interact with the existing ones. They can also gather at grain boundaries which can lead to radiation-induced segregation (RIS). This is a very important issue, especially for structural materials irradiated at elevated temperatures. RIS occurs if one of the elements in the material has a higher diffusion rate than the others. This element is then depleted at the grain boundaries because the flow of vacancies to the grain boundaries is balanced by an equal flow of atoms in the opposite direction. RIS causes changes in the microstructure and gives rise to problems such as intergranular corrosion and stress corrosion cracking.

Low temperature irradiation of most metals leads to formations of clusters of vacancies and interstitials bound by dislocations. During irradiation, the cluster either grows by absorption of defects of the same kind or shrink by absorption of defects of the opposite type. At higher temperatures,

clusters of vacancies may also grow into voids. Voids are normally formed at temperatures between 30% and 50% of the melting temperature. Below this temperature the vacancies are not mobile enough to reach voids before annihilating with migrating interstitials. In this temperature range, insoluble gases formed by transmutation, such as helium, have a strong stabilising influence on voids by turning the voids into gas filled bubbles. Voids and bubbles have a profound effect on material properties. They cause severe embrittlement and even volumetric swelling of the material by tens of percent. Irradiation-induced hardening is also caused by voids, bubbles and other defects such as defect clusters, dislocation lines and loops, and precipitates.

Hardening can be separated into two contributions, source hardening and friction hardening. The former is the increase in stress required to start a dislocation movement. Once the dislocation is moving, it can be hindered by natural or radiation-produced obstacles, and this resistance to the motion of the dislocation is called friction hardening. For BCC metals, there exists an additional hardening mechanism referred to as radiation anneal hardening. Annealing post irradiation enables the migration of interstitials to defect clusters and thereby strengthening them in their role as barriers to dislocation mobility.

### 3.5 Irradiation of tungsten

This section summarises issues relevant to tungsten irradiation studies and its applications. The section is divided into two parts, the first covering tungsten from a fusion point of view, i.e. under neutron irradiation and plasma exposure, and the second discussing tungsten from a spallation aspect, where the tungsten is irradiated with high energy protons and spallation neutrons.

### 3.5.1 Tungsten as plasma-facing material for fusion applications

A clear majority of the most recent papers about irradiated tungsten have been written as a part of the research behind the ITER project. ITER, the International Thermonuclear Experimental Reactor, is a nuclear fusion project aiming to make the transition from experimental studies of plasma physics to full-scale electricity producing fusion power plants. The ITER divertor, one of the main components, will extract heat, helium ash, and other impurities from the plasma, and protect other components from thermal and neutronic loads. It consists of two main parts, a supporting stainless-steel structure and the plasma-facing component made of tungsten.

The thermal requirements on a plasma-facing material are very high, it needs to withstand heat loads of up to  $20 \text{ MW/m}^2$  [17]. With advantages such as a high melting point, high thermal conductivity, high sputtering threshold, low sputter yield (which minimises impurity generation), and low tritium retention, tungsten is considered the most plausible material for the divertor [18-20]. However, there are some issues associated with the use of tungsten in this environment. Plasma-facing materials in fusion reactors suffer mainly two types of damage; surface damage including erosion, fuzz formation, cracking, sputtering and blistering caused by bombardment of deuterium, tritium, helium, and other impurities in the plasma, and displacement damage caused by 14 MeV neutron irradiation. During the past few decades, the effects of plasma exposure of tungsten have been studied quite extensively, as well as the effect of neutron irradiation on the mechanical and thermal properties of tungsten [21-23].

Depending on the irradiation conditions, different changes in the microstructure can occur. One of the key issues is the formation of helium bubbles, which are sometimes believed to cause other microstructural changes as well. Helium in metals has a fast thermal migration through

the lattice and a very strong attractive interaction with defects such as vacancies, vacancy clusters, impurity atoms, and other helium atoms. The helium recombines at defect locations or along grain boundaries, and form bubbles. The helium bubbles induce significant hardening and reduction of thermal conductivity, which enhances erosion under high heat loads [24]. In a study where computer simulations were used to investigate the synergistic effects of helium plasma exposure on microstructural evolution induced by neutron irradiation, it was shown that vacancies formed by neutron irradiation trap helium in helium-vacancy clusters, which then suppress the helium diffusion deeper into the material. These helium-vacancy clusters accumulate within a few microns of the irradiated surface. The formation of clusters changes the neutron irradiation effects and lead to blistering, void swelling, and irradiation hardening [25]. The blister formation is, however, dependent on the manufacturing process of tungsten. It has been suggested that the layered structure formed in cold-rolled tungsten facilitates blistering [26].

### 3.5.2 Proton and spallation neutron irradiation

There is far less data on the irradiation effects of high-energy protons on tungsten. To this date, only a few studies have been published. One of the reasons for this is the difficulty to obtain irradiated samples and even more so, to handle the highly radioactive specimens. Tungsten, once irradiated, becomes activated due to the decay of the many transmutation products formed. Several of these radioisotopes have very long half-lives, for example, Ti-44 with a half-life of 59 years [27]. The proton irradiated tungsten specimens which were studied in the present work, were irradiated in a spallation target at PSI, nearly a decade ago. Recent gamma spectrum measurements performed on these specimens showed the presence of Tm-172, Hf-182, Os-182, and Co-58, among others. The radioisotopes with the highest activity were Hf-172 and Lu-172, with



half-lives of 1.87 years and 6.70 days, respectively. The relatively short half-lives of these nuclides, found in the tungsten many years after the irradiation campaign was concluded, point towards a long and complex chain of radioactive decay taking place in the irradiated tungsten [28].

Depending on the particle type and its energy, the effect on the microstructure of the irradiated material varies. That is why fully relevant information cannot be obtained by using e.g. ion or neutron irradiation to foresee the effects of proton irradiation, even if the displacement damage is comparable. The cross-section for displacement of a certain atom, i.e. the probability that the incident particle will displace this atom, depends on the incident particle energy. It has been shown that above a particle energy of about 20 MeV, the displacement cross-sections of neutrons and protons are virtually the same [29]. The energy of the incident particle does not only determine the displacement, but also the character of the affected zone. Low particle energy irradiation, i.e. less than 100 eV, will cause mostly single Frenkel defects. Higher energies tend to create cascades, where a cluster of vacancies are surrounded by interstitials. The size of the cascade increases with increasing energy, until reaching a certain threshold energy, where the cascade starts to split and form sub-cascades. The threshold energy for sub-cascade formation depends on the mass of the target atoms, which for tungsten is 160 keV [30].

Spallation targets are exposed to a mixture of high-energy protons and spallation neutrons created by the protons. It is also exposed to thermalized neutrons from water coolants and moderators. The neutrons contribute to the irradiation damage as well. Radioisotopes, and both solid and gaseous transmutation products are formed. The transmutation elements with the highest production cross-sections are hydrogen and helium. Other common transmutation products in proton and neutron irradiated tungsten are various isotopes of tungsten, rhenium, osmium,

hafnium, lutetium, tantalum, and thulium. These elements are all located near tungsten in the periodic table. Rhenium and osmium have higher atomic numbers than tungsten, whereas the rest of the elements mentioned have lower ones. Due to the relatively high atomic mass of tungsten (and the existence of impurity elements), many radioisotopes are formed during irradiation. These isotopes continue to decay and transform into other elements, even after the irradiation is discontinued. The matter of understanding the full chain of reactions is complicated by the different reactions that can occur both during and after the irradiation itself. The long-term residual decay heat of the target material is, however, primarily due to thermal neutron capture. Since neutrons have no electric charge, they can enter a nucleus easily. The main solid transmutation product in the ESS spallation material is expected to be rhenium, which is produced in tungsten by thermal neutron capture ( $n, \gamma$ ) followed by beta decay ( $\beta^-$ ). In this process, the neutron collides with the nucleus of the target atom, becomes absorbed and forms the next higher isotope. The new isotope, now being in an excited state, de-excites by emitting a gamma ray. Then, the previously absorbed neutron transforms into a proton by emission of an electron and an electron antineutrino, and the atom becomes the next higher element. The probability of neutron capture is termed neutron absorption cross-section and is highly dependent on the energy of the incident neutron. In the low energy range, corresponding to thermal neutrons, the neutrons are slower and have more time to interact with the target nuclei. In this region, the neutron absorption cross-section is inversely proportional to the incident neutron energy. At higher energies, i.e. in the fast neutron region, the cross-section is much lower and decreases with increasing incident energy [31].



## 4. Materials and Methods

This chapter describes the materials and methods used in the present work. The overall research plan is presented first, followed by several subsections, each focusing on research methods for studying specific tungsten properties and behaviour. After this, the test specimens and the type of tungsten used for these studies are presented. This part is divided into two sub-sections, irradiated and unirradiated tungsten.

### 4.1 Research plan

The plan was to study tungsten systematically under conditions of relevance to ESS. The aim was to characterise thermal and mechanical properties of tungsten which were still not fully covered by existing literature. There was a lack of fatigue data on pure tungsten, and scarce information on the behaviour of tungsten in low-oxygen gaseous atmospheres. Both topics were studied during the initial stages of the work, where the focus was on the unirradiated tungsten material. The results were published in three papers; two on fatigue behaviour (Paper I and II), and one on oxidation (Paper III). The later stages of the work

focused on the properties of irradiated tungsten. Tungsten, irradiated in a spallation source at PSI, Switzerland, provided invaluable data which elucidated the potential irradiation induced changes occurring in tungsten due to high energy proton irradiation. Thermal diffusivity was also studied, as it is an important property determining the temperature evolution in the material after each beam pulse. The findings were published in Paper IV. The ultimate tensile strength, the DBTT, and hardness were also determined. These results are summarised in Paper V. Lastly, a study was taken up in which some of the observed (pulsed) irradiation induced effects were combined to present an estimated increase in the maximum thermal stress of an ESS tungsten brick. Paper VI presents the results.

#### 4.1.1 Fatigue studies

In the early stages of the project, the focus was on characterisation of properties of unirradiated tungsten. A review of the existing literature on the fatigue properties of pure tungsten revealed that there are very few studies on this topic. Many publications deal with the mechanical properties of tungsten [32-35], on the causes of the DBTT shift [36-38], and on the effects of various alloying elements [39-40]. To the best of the author's knowledge, prior to the present work, there existed only one publication on the fatigue properties of unalloyed tungsten. It was published in 1981 by Schmunk and Korth [41], who studied the tensile and low-cycle fatigue properties of cross-rolled tungsten, both as-received and recrystallised. Their experiments were performed at room temperature and at 815 °C. The room temperature tests could not be carried out under strain control as they were too brittle.

Due to the risk of fatigue failure of the ESS target, there was a critical need to understand the fatigue behaviour of various types of tungsten under cyclic loading. Setting design parameters such as maximum allowed

stress in the ESS tungsten target required a systematic gathering of experimental data which could serve as a basis for the decision. The objective of the fatigue study was to answer questions such as: how large is the difference in quality between the manufacturers; which processing route produces the best suited tungsten for spallation target applications; what is the impact of the choice of surface finishing technique; how is the fatigue life affected by temperatures similar to the ESS target operating temperature; and most importantly, to set the maximum allowed stress in the ESS target material. Several types of tungsten specimens, from different manufacturers, were obtained for studying the fatigue behaviour. The specimens varied in size, surface roughness, and manufacturing techniques.

Fatigue can be explained as a localised damage process occurring in materials subjected to cyclic loading. This typically leads to failure at nominal stresses below the yield stress of the material. During the process, cracks form at high stress concentration sites and their lengths increase with the number of load cycles, until the material fails. In the present work, stress-controlled fatigue testing was chosen. Strain-controlled tests require a certain amount of ductility, which tungsten specimens tested at room temperature did not have. It was decided to perform the fatigue testing in the most conservative way possible, i.e. in full tension, as explained by figure 4. Generally, cracks propagate during tension, not compression of the material. The minimum stress for the tungsten specimens was set to +5 MPa (0.1 kN), so that compressive stresses would be avoided. Accordingly, the mean stress was approximately the same as the stress amplitude. The initial stress level was set based on results from tensile testing of the specimen; it was set to 60% of the experimentally determined ultimate tensile strength (UTS). These tensile tests were performed according to ASTM E8/E8M standards [42], with displacement rates in the range 0.6-2 mm/s. The load reversal frequency

was in the interval 25-30 Hz, and the runout limit was set to  $2 \times 10^6$  cycles without failure. Typically, a runout limit of  $10^7$  cycles is more commonly used, but it could not be employed here due to time constraints. Nearly five days would be required for a specimen to reach  $10^7$  cycles at 25 Hz, instead of the 22h to reach  $2 \times 10^6$  cycles. Similarly, a slightly higher frequency than the 14 Hz used at ESS, was chosen to shorten the experimental time.

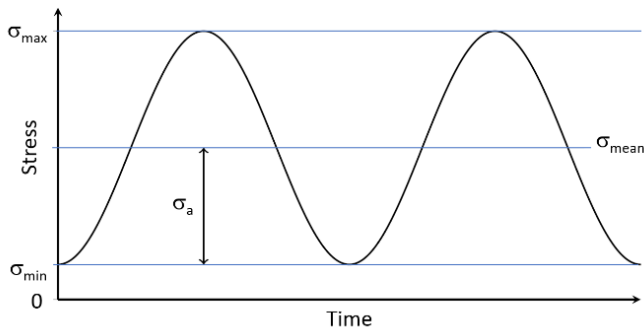


**Figure 4 A Schematic representation of the max, min, and mean stress.**

The fatigue limit was determined using the so-called staircase method, also known as the up-and-down method [43-44]. If the specimen fails at a certain stress level, the next specimen will be tested at a stress level one step below. If the specimen is a runout then the next test will be done at one step higher stress level. The step size should be constant and is chosen based on the number of available specimens and the desired accuracy of the fatigue limit. Or it can be set as 0.5-2 times the standard deviation [44], but this of course requires either previous experience of testing the same material, or a very good guess. The staircase data is evaluated using the maximum likelihood method [45-46].

### 4.1.2 Oxidation studies

The initial stages of this research project also included studies of oxidation behaviour of unirradiated tungsten at low oxygen partial pressures. As the 5 MW proton beam at ESS delivers 357 kJ/pulse to the target, the temperature in the tungsten brick will rise instantaneously by 100 °C. Pure, unprotected tungsten is known to oxidise readily at elevated temperatures, and there are many publications on this topic. However, most of these publications deal with the oxidation of tungsten at very high temperatures and in steam / oxygen-rich atmospheres. These conditions do not apply to the target environment at ESS.

The tungsten target at ESS is confined in a helium gas environment. Helium gas flows into the target at the rate of 2.85 kg/s and a pressure of 1.0 MPa [12]. It enters the target at a temperature of 40 °C and leaves it at around 240 °C. Helium is contained in a loop where it is filtered, purified and recirculated. However, there is a risk that even very low levels of oxygen and water vapour may lead to oxidation.

The temperature rise in the tungsten bricks depends on the size of the beam footprint. Before the beam hits the target, it is expanded by fast-switching magnets, rastering the beam within a certain area. The size of this area, the so-called beam footprint, is a compromise between the maximum tolerable temperature rise in the tungsten, and the neutron production yield. The maximum tolerable temperature in the tungsten is set according to two important criteria; the thermo-mechanical cyclic stress should be much below the fatigue limit, and the maximum temperature should not cause significant oxidation.

Aiming at completely avoiding the oxidation of tungsten is unrealistic. Instead, a temperature should be chosen where the rate of oxide formation and its growth is low, and the oxide formed is protective and adhesive.



The objectives of this oxidation study were to characterise the oxidation behaviour of tungsten at low oxygen partial pressures and temperatures of relevance to ESS, identifying the temperature at which the oxide scale loses its protective nature, and comparing the oxidation rates at different oxygen partial pressures. The work focused on acquiring oxidation data in the temperature range 400-900 °C, in inert gas mixtures with additions of small amounts of oxygen or water vapour. Several oxygen and water vapour levels were used in the inert gas atmosphere, these ranged from  $p_{\text{O}_2}$  of 0.5 Pa to 5.1 kPa, and  $p_{\text{H}_2\text{O}}$  of 100 Pa to 790 Pa. Even though commercially pure helium gas is considered inert, it may still contain small amounts of oxygen and moisture. The lower oxygen partial pressure used in this study simulates the effect of an impurity level of oxygen. The higher partial pressure was used to study off-normal operation conditions, such as a leak in the helium loop or target vessel. The temperature range of 400-900 °C was chosen to cover various scenarios during target operations, as well as to characterise the behaviour of the oxides at higher temperatures, especially above the volatilisation temperature of tungsten oxide. The onset temperature of volatilisation depends on the amount of water vapour in the environment, the oxygen content of the gas, the gas flow rate, and the thickness of the oxide scale [47-50]. The lowest reported onset temperature is between 700 °C and 800 °C [49].

The oxidation of tungsten is rather complex. Two stoichiometric oxides,  $\text{WO}_3$  and  $\text{WO}_2$ , and a wide range of non-stoichiometric oxides corresponding to the formula  $\text{WO}_{3-x}$  where  $0 < x < 1$ , can be found in the W-O system [51]. The most common oxides are  $\text{WO}_2$ ,  $\text{WO}_{2.72}$  ( $\text{W}_{18}\text{O}_{49}$ ),  $\text{WO}_{2.9}$  ( $\text{W}_{20}\text{O}_{58}$ ), and  $\text{WO}_3$  [52-53], with colours ranging from violet for the lowest oxide, to dark blue, black, green, and yellow, as the oxygen content increases.

Tungsten begins to oxidise at relatively low temperatures [54]. Around 600 °C, the rate becomes significant [55], and volatilisation starts at temperatures above 700 °C. The oxidation of tungsten proceeds through several steps, each governed by different mechanisms. The very first step is phase boundary controlled, i.e. there are no diffusional effects yet. The growth rate for this initial oxide layer follows the logarithmic law until it becomes a few nanometres thick [56]. At temperatures above 400 °C and slightly thicker layers, the oxide begins to grow according to the parabolic law. At this stage, the oxide is still very thin, adhesive and protective. The growth rate here is limited by the diffusion of  $O^{2-}$  ions through the oxide scale.

The next stage takes place at temperatures between 500 °C and 700 °C. This stage includes the growth of the dark, protective layer, as well as the formation and growth of a bright-yellow, porous layer consisting of  $WO_3$ , which is found in the outermost layer of the oxide scale where the oxygen content is the highest. The last stage begins when the protective oxide layer is fully covered by the  $WO_3$ . There is a significant volume change in the oxide scale as  $WO_3$  forms. This type of oxide has a Pilling-Bedworth ratio of 3.6 [57], which creates high stresses in the scale leading to crack formation. As the cracks expose fresh surfaces to the oxidising atmosphere, the protective nature of the oxide scale is lost, and oxidation proceeds according to a linear growth rate.

Keeping in mind the harsh environment in the ESS target, it is important to retain the normal operation temperature in the tungsten bricks below the onset temperature for rapid growth of the porous, poorly adhesive  $WO_3$ . More importantly, the absolute maximum temperature in the tungsten must be designed to never reach the onset temperature of volatilisation of the oxide. As tungsten will be highly radioactive after irradiation, it is imperative to avoid erosion of the oxide scale as well as the formation of highly volatile radioactive tungsten hydroxides, which

can potentially be released to the surrounding environment under accidental conditions.

The oxidation studies in the present work were carried out in different setups. Most of the experiments were conducted using a thermogravimetric analysis (TGA) unit, in which the specimens were oxidised under isothermal conditions for a duration of 2h per experiment. The specimens were suspended from the bottom hook of a Shimadzu AUW120D microbalance, with an accuracy of  $\pm 0.01$  mg, into a Carbolite STF 15/75/450 vertical furnace. The compositions of the oxidising gas mixtures were the following: He-5%O<sub>2</sub>, He-0.5%O<sub>2</sub>, He (max. 5 ppm O<sub>2</sub>) and He-Ar-H<sub>2</sub>O (p<sub>H<sub>2</sub>O</sub> 790 Pa). The last-named gas mixture was created by passing pure argon gas with a flow of 50 ml/min, through distilled water at room temperature, and mixing with dry helium flowing at 150 ml/min. The rest of the gas mixtures were supplied by AGA gas company, Stockholm. Some of the tests were carried out in a Netzsch STA 449 F3 Jupiter Simultaneous Thermal Analysis (STA) unit, in which data from differential scanning calorimetry (DSC) and thermogravimetry could be collected simultaneously. The gas flow rate here was 70 ml/min.

In addition, some experiments were carried out in a hot stage mounted inside an environmental scanning electron microscope (ESEM). The specimen was heated in a low pressure environment of water vapour at a pressure of 100 Pa. After the oxidation studies, the specimen surfaces were examined using SEM and light optical microscopy. The oxides were characterised using X-ray diffraction (XRD), Energy-dispersive X-ray spectroscopy (EDS), and Auger Electron Spectroscopy (AES). The results from this study served as a basis for determining the highest operation temperature of the tungsten material in the ESS target.

### 4.1.3 Thermal diffusivity of irradiated tungsten

The temperature and equivalent stress in the target material during operation were previously calculated using thermo-mechanical data of unirradiated tungsten. The calculated maximum temperature is 445 °C, and the largest equivalent stress 110 MPa [58]. Using correct thermal conductivity data is critical as it determines the development of the temperature and secondary thermal stresses in the tungsten bricks. However, sufficient data on irradiation induced degradation of thermal properties of tungsten in spallation target environment, is not available.

The tungsten at ESS will mainly be irradiated by high-energy protons and fast neutrons produced in the spallation process. Some of these neutrons will be thermalized by the surrounding hydrogen-rich moderators and water coolants, and therefore contribute to the formation of rhenium as a transmutation product. In addition, there will be a displacement damage of maximum 2 dpa per year in the tungsten. Based on data from experiments in neutron reactors, it is assumed that thermal diffusivity of tungsten irradiated at ESS will follow a similar trend of irradiation induced decrease in thermal properties. The extent is, however, not fully understood.

Data from reviewed neutron irradiation studies point towards a decrease of thermal diffusivity in the range 15-50%, with a clear dependence on the amount of rhenium present [21,59]. Even without irradiation, a rhenium addition of only 5% causes the thermal diffusivity to drop by nearly 50% at room temperature [22]. Hasegawa et al. [21] irradiated tungsten specimens to 1 dpa, in a fast reactor (JOYO) and in a mixed spectrum reactor (HFIR), which resulted in specimens with different amount of rhenium as the transmutation product, but the same amount of displacement damage. The high flux of thermal neutrons at HFIR led to higher rhenium production rates. The composition of the specimens was expected to change to W-5Re-0.5Os, whereas the specimens

irradiated at JOYO were expected to produce less than 0.03% rhenium. Before and after the irradiation, electrical resistivity measurements were made. The results showed a difference in the increase of electrical resistivity between the different specimens, of nearly 50%. The increase of electrical resistivity can partly be related to the decrease of thermal conductivity via Wiedemann-Franz law. The law applies to metals and states that the ratio of the electronic contribution of the thermal conductivity  $\lambda$ , to the electrical conductivity  $\sigma$ , is proportional to the temperature  $T$  through the proportionality constant  $L$ , also known as the Lorenz number.

$$\lambda/\sigma = LT \quad (2)$$

Results from thermal diffusivity measurements of neutron irradiated tungsten and tungsten alloys, by Fujitsuka et al. [22], showed that the addition of 5-25% rhenium significantly lowers the thermal diffusivity of all the alloys compared to that of pure tungsten, also after irradiation.

The measurements in the present study were made on two tungsten specimens, irradiated by protons and spallation neutrons to different doses. Using a commercial Netzsch LFA 467 Light Flash apparatus, with a xenon lamp and an InSb IR-detector, their thermal diffusivities could be determined in the temperature range 25 °C to 500 °C.

#### 4.1.4 Mechanical properties of irradiated tungsten

Despite being used in spallation targets for many years, data on mechanical properties of proton and spallation neutron irradiated tungsten is very limited, owing mainly to the difficulties of both obtaining and handling irradiated tungsten, as well as to the brittle nature of the material which makes mechanical testing difficult. The present study was taken up to obtain data on the effect of high-energy proton irradiation on the mechanical properties and fracture behaviour of tungsten. The data is

of great value in the design of the ESS target, where the tungsten is expected to experience temperature and stress variations of maximum 100 °C and 70 MPa, respectively. Although tungsten is not a structural material, it is important to maintain the mechanical integrity of the bricks to keep the 2 mm wide helium cooling channels free and retain the radioactive transmutation elements.

Pure tungsten, from the same irradiation campaign as the specimens in the thermal diffusivity study, was tested in 3-point bending at temperatures of 25 °C to 500 °C. 3-point bend testing is an attractive method of determining the mechanical properties of irradiated specimens, as it does not require large material volumes. The flexure strength (maximum stress prior to fracture) can be determined using the following relationships where  $\sigma$  is the fracture stress (MPa),  $F$  is the maximum load (N) prior to fracture,  $L$  is the support span (mm),  $b$  is the specimen width (mm),  $d$  is the specimen thickness (mm),  $D$  is the deflection (mm), and  $\varepsilon$  is the strain.

$$\sigma = \frac{3FL}{2bd^2} \quad (3)$$

$$\varepsilon = \frac{6Dd}{L^2} \quad (4)$$

The specimen preparation is described in section 4.2.1. In short, the irradiated tungsten material was cut into bend bars using electro-discharge machining, and polished. The specimen size was 1×2×8 mm<sup>3</sup>. Some specimens were smaller, 1×2×4 mm<sup>3</sup>. These were prepared from the fractured pieces of the larger specimens, to collect more data over a wider temperature range. The doses and test temperatures of the larger test pieces were: 1.8 dpa (350 °C), 2.1 dpa (400 °C), and 1.4 dpa (450 °C). The corresponding values for the smaller pieces were: 1.3, 2.1, and 3.5 dpa (25 °C), 1.8 dpa (350 °C), 2.1 dpa (400 °C), 1.4 dpa (450 °C), and 2.6 dpa (500 °C).

Hardness of the specimens was determined prior to the 3-point bend test. A Vickers hardness tester with a load of 0.5 kg and 15 seconds dwell time was used. The 3-point bend tests were done on a Zwick universal testing machine with a load capacity of 10 kN. The crosshead travel speed during the tests was 0.1 mm/min. After the 3-point bending tests, the fracture surfaces were observed using scanning electron microscopy.

#### 4.1.5 Cyclic loading by pulsed heavy ion irradiation

In this study, specimens were irradiated with a pulsed heavy ion beam, with the purpose of studying changes in thermal and dynamic response properties of tungsten, as a function of progressive irradiation damage, as well as the adhesion of a tungsten oxide scale under a pulsed beam. Irradiation with heavy ions does not create the same type of damage as high-energy protons would, however, the advantage of using heavy ions is that the irradiated material does not become activated and can be manually handled already within a day. The chosen ion beam energy is below the Coulomb barrier and does not induce any nuclear reactions in the tungsten atoms. It may be noted that the tungsten material irradiated at PSI required a cooldown period of nearly a decade before the specimens irradiated to the lowest doses could be examined. The low energy ion irradiation campaign was useful in making a focused study on the atomic displacement damage effect on the properties of tungsten. In addition, the 4.8 MeV/nucleon pulsed beam caused stresses and temperatures in the tungsten comparable to those expected in the ESS bricks. The dynamic mechanical response was analysed using a transient mechanical and thermal simulation software.

Irradiation with heavy ions was carried out at GSI Helmholtz Centre for Heavy Ion Research, in Darmstadt, Germany. The specimens, 20 mm wide disks with thicknesses 3 mm or 26  $\mu\text{m}$ , were mounted on aluminium

sample holders and fixed with copper spring washers. The holder is shown in figure 5. The black line on the specimens is graphite paint used for the online infrared (IR) temperature measurements. The small piece of reflective tape visible on the back of the specimens was used for measurements of beam pulse induced dynamic vibrations, using a laser doppler vibrometer (LDV). The insert in the image shows a luminescence target with a  $1 \times 1 \text{ cm}^2$  beam spot.

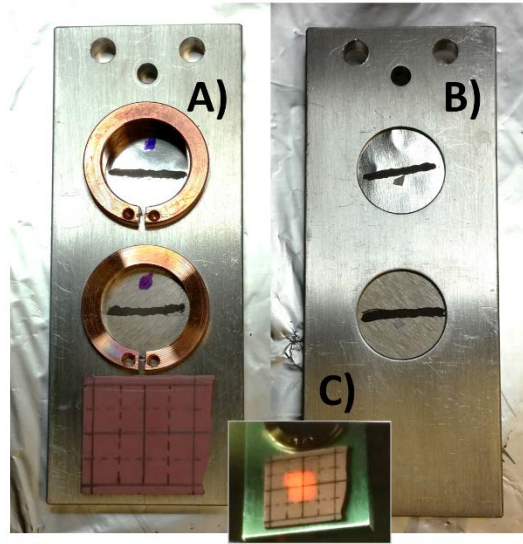


**Figure 5 Sample holder. A) Frontside with copper spring washers, B) backside with reflective tape, C) luminescence target showing the beam spot.**

The experimental setup is shown in figure 6. The specimen is placed in the middle of the chamber, with two mirrors on each side. The mirrors are positioned at an angle such that the infrared camera can read the temperature on both sides of the specimen simultaneously. The LDV is directed towards the back of the specimen, relative to the beam upstream side, and measures the vibration of the specimen during the pulsed irradiation.



The dynamic response of tungsten was studied using a pulsed uranium beam with a kinetic energy of 4.8 MeV/nucleon, repetition rate of 1 Hz, and pulse length of 150  $\mu$ s. The intensity of each pulse was  $7.5 \times 10^9$  ions/cm<sup>2</sup>/pulse. Some specimens were irradiated with gold ions instead. The kinetic energy of the gold ion beam was 4.8 MeV/nucleon as well, and the time averaged ion flux was  $5 \times 10^9$  ions/cm<sup>2</sup>/s. A summary of the irradiated specimens, beam conditions, in-situ monitoring (ISM), and post irradiation examinations (PIE) is presented in table 4. The specimen IDs with the name “thick” are of 3 mm thickness, while the “thin” specimens are of 26  $\mu$ m thickness. Specimen ID Thick\_Ox\_U refers to the pre-oxidised specimen used for tungsten oxide adhesion studies.

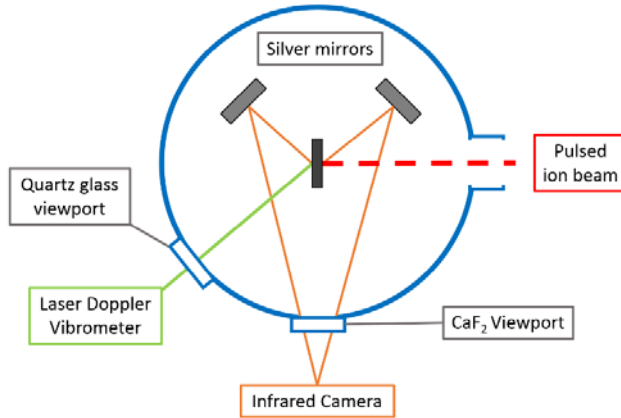


**Figure 6 Experimental setup at GSI for irradiation with pulsed heavy ion**

Prior to the experiment, the quasi-static thermal and mechanical loads in the thicker tungsten specimen, induced by the pulsed uranium ion beam, were calculated using ANSYS [60]. The particle transport code FLUKA [61-62], was used to calculate the heat deposition in the specimen. A beam spot of  $1 \times 1$  cm<sup>2</sup> with a uniform distribution of the beam current was assumed in the simulated model. Figure 7 presents the resulting temporal development of the maximum temperature of the uranium

irradiated tungsten specimen, at a flux of  $7.5 \times 10^9$  ions/cm<sup>2</sup>/pulse. The resulting maximum von Mises stress in the same model was 122 MPa at the peak of the 20<sup>th</sup> pulse. The maximum temperature difference is 54 °C. These values are comparable to the maximum operational stress and temperature range per each pulse in the ESS tungsten, at 5 MW full power operation. The temperature and stress differences in a tungsten brick in the ESS target are in the range of 74 °C and 56 MPa. respectively. This suggests that the pulsed beam at GSI simulates the dynamic loads on tungsten at 5 MW beam operation at ESS reasonably well.

**Table 4 Beam conditions, in-situ monitoring (ISM), and post irradiation examination (PIE).**

Specimen ID	Ion type	Fluence [ions/cm <sup>2</sup> ]	ISM	PIE
Thick_U	Uranium	$7.5 \times 10^{13}$	IR/LDV	AES/Hardness/SEM
Thick_Ox_U	Uranium	$5 \times 10^{12}$	IR/LDV	AES/SEM
Thin_U	Uranium	$7.5 \times 10^{13}$	IR/LDV	SEM
Thin_Au_1	Gold	$1 \times 10^{11}$	-	LFA
Thin_Au_2	Gold	$1 \times 10^{12}$	-	LFA
Thin_Au_3	Gold	$5 \times 10^{12}$	-	LFA
Thin_Au_4	Gold	$2 \times 10^{13}$	-	LFA

The expected displacement damage in the tungsten irradiated at GSI was calculated using FLUKA. The calculation shows that the damage caused by the 4.8 MeV/nucleon beam is confined within a depth of 20 µm from the irradiated surface. The maximum displacement damage in the thicker specimen, irradiated by uranium, is 0.06 dpa. The corresponding values for the thin specimen, irradiated by gold ions to the highest fluence, is 0.04 dpa. Figure 8 shows the one-dimensional configurations of the dpa values per single ion, for the uranium and gold ions beam cases.

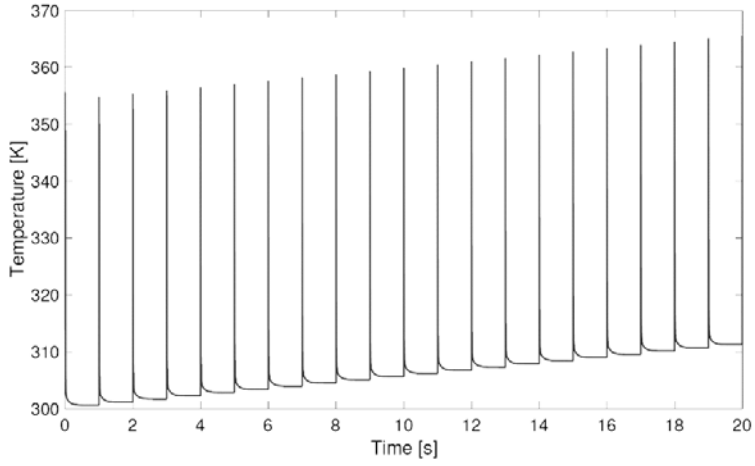


**Figure 7** Temporal development of maximum temperature of the uranium irradiated 3 mm thick tungsten specimen.

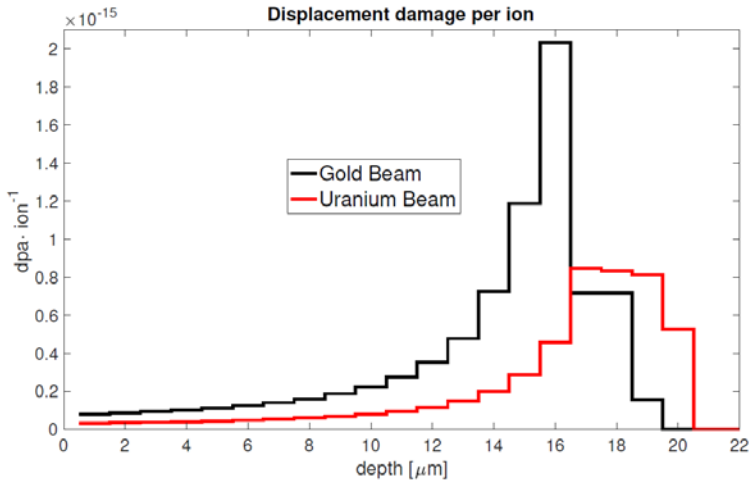


**Figure 8** One-dimensional configurations of the dpa values per single ion.

## 4.2 Specimens

Tungsten used in this work came from several different suppliers, in various shapes and sizes, from diverse processing routes, and with varying surface treatments. Some specimens were tested as-received, other had been irradiated to a range of different doses by either two different heavy ions, or by high energy protons and spallation neutrons.

### 4.2.1 Irradiated tungsten

The irradiated material can be divided into two groups: high energy proton and spallation neutron irradiated, and heavy ion irradiated. The effects of the two types of irradiation are very different and gives an opportunity to study various materials related issues.

#### **Irradiation by high energy protons and spallation neutrons**

All the examined specimens irradiated by protons and spallation neutrons originate from the same piece of irradiated tungsten. This was a commercially pure (99.9%), cross-rolled plate with the average grain size 25, 20 and 17  $\mu\text{m}$ , in its three directions. The original dimensions of the plate were  $1\times 10\times 60\text{ mm}^3$ . The plate was irradiated in the Swiss Spallation Neutron Source (SINQ), at the Paul Scherrer Institute (PSI). The irradiation was part of the fifth campaign of the SINQ Target Irradiation Program (STIP-V) which lasted two years, 2007-2008. In the STIP irradiation campaigns, some of the spallation material in the SINQ target were replaced by specimens for research purpose. The Swiss spallation target is about 50 cm long and made up of an array of lead rods, enclosed in zircaloy tubes [63]. The Gaussian shaped proton beam hits the target from below, which means the that rods in the target will be exposed to varying energies and fluxes of the protons and spallation neutrons, depending on the position of the rod relative to the beam centre. This

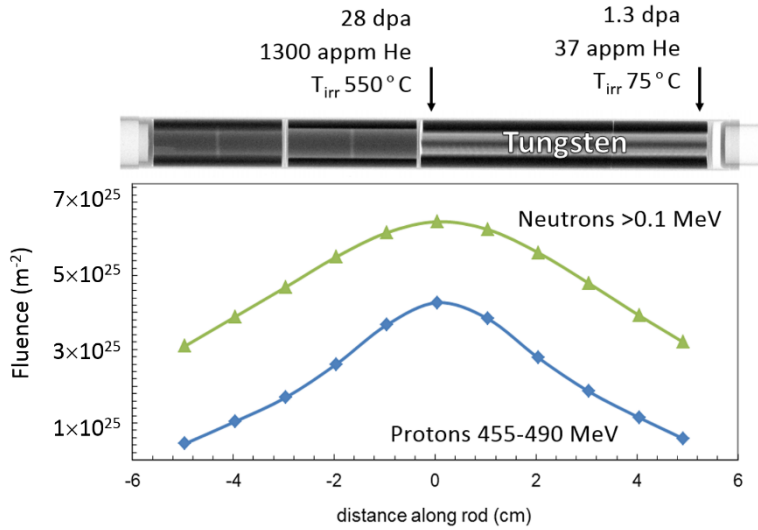
also leads to position specific irradiation temperatures and transmutation product production rates, even within the same rod.

Figure 9 illustrates the fluence of protons and fast neutrons according to the distance of the tungsten plate from the beam centre. The tungsten plate is positioned in the right half of the rod. The centre of the Gaussian shaped beam coincides with the left end of the plate. This part of the tungsten material received a total dose of 28 dpa with 1300 appm He and 7200 appm H, at an average irradiation temperature of 550 °C. The corresponding values for the right end of the plate are 1.3 dpa, 37 appm He, 310 appm H and 75 °C. The irradiation doses for STIP specimens were calculated using MCNPX codes, and the irradiation temperatures simulated with ANSYS [64-65].

Immediately after the irradiation, the radioactivity of the tungsten was very high. The rod was opened inside a hotcell and the tungsten plate extracted. During this procedure the plate broke into several smaller pieces. Figure 10 shows a photograph taken by the PSI hotcell operator during the unpacking of the plate. With careful planning, a total of 31 specimens could be obtained from the tungsten pieces, using electro-discharge machining (EDM) inside the hotcell. The specimens include several miniature bend bars, tensile specimens, and five 6 mm disks. The irradiation doses were ranging from 1.3 to 28 dpa.

Unfortunately, nearly ten years after the irradiation, most of the tungsten specimens are still too radioactive for manual handling and testing. So far, only a few of the lowest dose specimens could be studied. These include two 6 mm disks, and six bend bars with the dimension  $1 \times 2 \times 8 \text{ mm}^3$ . All the specimens were prepared and tested in the nuclear laboratory (Hotlab) of PSI. They were mechanically polished in a lead-shielded fume hood, specially equipped for active samples. The specimens were polished on both sides in several steps, finishing with standard colloidal silica

suspension. Prior to any testing, the entire procedure is simulated with inactive reference tungsten. Because the irradiated tungsten is so precious, and the mechanical testing destructive, there is only one chance to make a successful measurement. Therefore, EDM cutting, polishing and mechanical testing was carefully planned and practised. As the sample preparation is performed outside the hotcell, great care must be taken to do the work safely, carefully, and quickly. This tungsten material was used for 3-point bending tests, measurements of thermal diffusivity and hardness, and microscopy.



**Figure 9 Fluence of protons and fast spallation neutrons as a function of distance to the Gaussian shaped beam centre.**

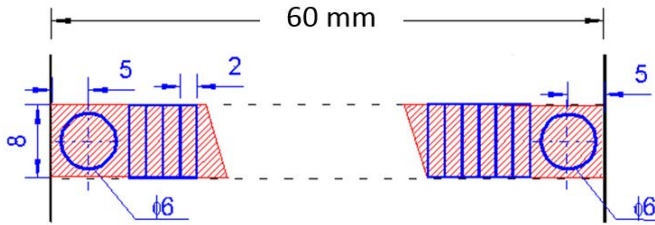
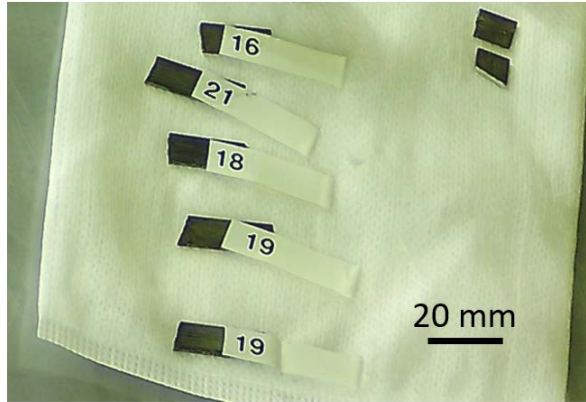


**Figure 10** Photograph taken after the extraction of irradiated tungsten, and a drawing of the disk and bend bar specimens cut from the larger pieces.

The rhenium content in the PSI irradiated tungsten was estimated as it known that even a small amount of this transmutation product changes the properties of tungsten. Rhenium is produced in tungsten by thermal neutron capture ( $n, \gamma$ ) followed by beta decay ( $\beta^-$ ). The two most common stable tungsten isotopes are W184 (30.7%) and W186 (28.6%). Thermal neutrons with a typical kinetic energy of 0.025 eV, have a ( $n, \gamma$ ) cross-section of 1.62 barn for W184, and 37.9 barn for W186. With a calculated maximum thermal neutron flux of  $1.5 \times 10^{13}$  n/cm<sup>2</sup>/s/mA in the SINQ target [66], and an accumulated beam charge of 9.83 Ah, the rhenium fraction in the PSI irradiated tungsten material is approximated to 2%.

### **Irradiation by pulsed heavy ion beam**

Two types of tungsten specimens were irradiated with heavy ions at the M3-beamline of the UNILAC facility at GSI Helmholtz Centre for Heavy Ion Research. The purpose was to study the behaviour of tungsten under dynamic beam loads comparable to those at ESS, as well as the irradiation induced degradation of thermal diffusivity. The material was pure tungsten in the shape of a disk with a 20 mm diameter. One type was 3 mm thick and the other was a foil of 26  $\mu\text{m}$  thickness, both types were rolled tungsten. The thick disk was fabricated by Beijing Tian-Long Tungsten & Molybdenum Co, Ltd., China\*, and the thin foil by Plansee Metall GmbH, Austria.

The irradiation was done using pulsed gold and uranium ion beams with a kinetic energy of 4.8 MeV/nucleon. The repetition rate of the uranium beam was 1 Hz, the pulse length 150 ms, and the ion intensity  $7.5 \times 10^9$  ions/cm<sup>2</sup>/pulse. The uranium beam was used to study the dynamic response of tungsten while the gold beam, with the time averaged ion flux  $5 \times 10^9$  ions/cm<sup>2</sup>/s, was used to study the effect on thermal diffusivity as a function of increasing fluence. The displacement damage in the specimens, calculated by FLUKA, was 0.06 dpa for a thick disk irradiated with uranium, and 0.04 dpa for a foil irradiated with gold. After the irradiation the specimens were hardness tested and studied using various microscopy techniques, such as SEM, AES, and EBSD.

---

\* *Beijing Tian-Long Tungsten & Molybdenum Co.* will hereafter be referred to as *Tian-Long* for short.



## 4.2.2 Unirradiated tungsten

There are two categories of the unirradiated tungsten used in this work: reference specimens for the irradiation damage studies, and specimens used for fatigue and oxidation experiments. The reference material was prepared in the same way as the irradiated one and will not be covered here. The remaining unirradiated tungsten material can be further classified according to the type of study it was used in.

### **Oxidation behaviour**

Mainly disk shaped rolled tungsten with a minimum purity of 99.97%, was used for the oxidation studies. The specimens were 20 mm in diameter and 3 mm thick, electro-polished, and manufactured by Tian-Long, China. In addition, experiments with four different tungsten alloys were conducted for comparison purposes. The alloys had the following alloying elements: **D176** – 5% Ni, 1% Fe; **D185** – 2% Ni, 1% Fe; **IT170** – 7% Ni, 2.5% Cu; and **IT180** – 3.5% Ni, 1.5% Cu. Some experiments were carried out with the rolled, 26  $\mu\text{m}$  thick tungsten foil from Plansee. These specimens were 5.5 mm in diameter.

### **Fatigue properties**

One of the objectives of the fatigue studies was to investigate the difference in fatigue properties of tungsten from different processing routes. In Paper I, all specimens were tested as-received and were made of unalloyed, commercially pure tungsten, by Tian-Long. This paper focused on fatigue testing of rolled and forged tungsten at temperatures 25 °C, 280 °C, and 480 °C. The specimens were either electro-polished or unpolished, and the rolled specimens were oriented either along the rolling direction or in the transverse direction. Totally six types of tungsten specimens were tested. The dimensions of the high temperature specimens were designed to fit the special high temperature grips. Figure 11 shows both the room and high temperature specimen geometries.

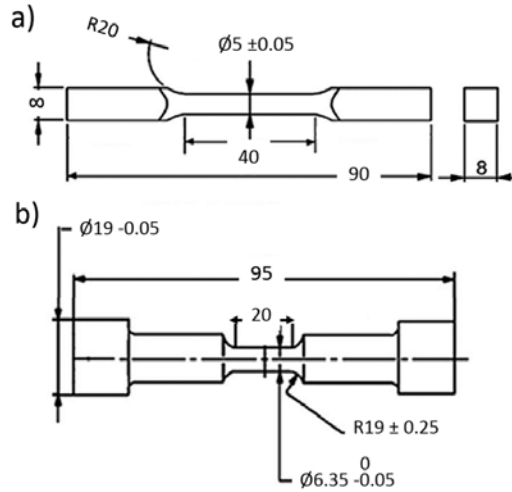


**Figure 11 Geometries of (a) room temperature and (b) high temperature tensile and fatigue test specimens. All dimensions are in mm.**

The rolled room temperature specimens were manufactured from sheets rolled five times at a temperature of 1450-1650 °C. The bigger high temperature specimens were prepared from a 20 mm thick sheet, rolled four times with a 20-25% reduction in each step. The rolling temperature was 1500-1650 °C. The forged specimens were machined from a plate reduced in three forging steps, from 150 mm thickness to 90 mm, at a temperature range of 1550-1700 °C. The porosities of the rolled and forged specimens were determined to be 0.1 and 1.92%, respectively. In Paper II, fatigue properties of rolled & annealed, and sintered & HIPed specimens were compared. The specimens were made of commercially pure tungsten manufactured by Plansee Metall GmbH and tested in the as-received condition. The dimensions were like those of the room temperature specimens in Paper I. The rolled specimens were oriented in the rolling direction. The surface roughness in the gauge section was maximum 1.6  $\mu\text{m}$ , according to the supplier. The porosity of the sintered & HIPed tungsten was approximately 4.28%, while that of the rolled tungsten was about 0.48%.

## 4.3 Characterisation techniques

The most important techniques and equipment used for characterisation of the specimens are presented in the following subsections. Light optical and electron microscopes are covered briefly and their use in this work is described. This is followed by an introduction to the various equipment used for thermal analysis, including a short section on the basic function of a light flash apparatus (LFA). Techniques used for hardness measurements are presented, and lastly, a short description of the X-ray powder diffraction technique (XRD) is given.

### 4.3.1 Microscopy

Microscopic techniques have been used extensively in this project. They offer a powerful method for characterising the microstructure of the specimens. In addition, various types of microscopes have been used to gather different kinds of information on the structural, chemical, and physical attributes of the observed material. Light optical microscopy (LOM) was used to characterise the grain size distribution in the different types of tungsten used in e.g. the fatigue study. By etching with Murakami's reagent, the grain boundaries became observable in the LOM. Murakami's reagent works quite well on tungsten, it consists of one-part  $\text{K}_3\text{Fe}(\text{CN})_6$ , one-part KOH and ten-parts  $\text{H}_2\text{O}$ . In some cases, LOM was also used to estimate the porosity of the material, in particular, the forged and HIPed type. The LOM most frequently used in this work is a LEICA DMRME optical microscope with Qwin application software. A LOM provides only a two-dimensional image of relatively low resolution, but over a comparably large area.

For images of higher resolution, a scanning electron microscope (SEM) was used. The SEM most frequently used in this work is an environmental scanning electron microscope (ESEM), of the model Philips XL-30. It is based on a LaB<sub>6</sub> electron source and has an ultimate resolution of 3.5 nm. The specimen chamber can be used either in high vacuum or in the environmental mode in which the specimens can be examined in an atmosphere of up to 1333 Pa of water vapour, oxygen, or any other non-corrosive gas. The ESEM mode was used in the oxidation study, where tungsten was oxidised in a hot stage, in situ, in an atmosphere of water vapour at low pressure.

The main components of an SEM are the electron source, the apertures and lenses, the specimen chamber, and the detector. The electron source is heated and produces electrons which are guided through the lenses, focused and directed towards the specimen in the chamber. The electron beam is highly focused and scanned across the surface of the specimen. As the electrons interact with the material, a signal is generated by the detector which subsequently translates into an image of the specimen. Different types of signals can be used to gather information about the specimen. Backscattered electrons (BSE) are especially useful when the specimen is made of elements with significant differences in atomic number. The contrast will be very good as elements with high atomic numbers give rise to more backscattered electrons compared to elements of low atomic numbers. In addition, the intensity of the backscattered electrons is sensitive to the orientation of the grains, and topology of the specimen. Secondary electrons (SE) are detected when the electrons from the beam collide with the electrons in the observed material. These are then ejected from their orbits, scattered, and detected. Majority of the images acquired using electron microscopy in this work, were taken in the SE-SEM mode.

Transmission electron microscopy (TEM) can provide even higher resolutions than SEM, as well as both image and diffraction information. And, as opposed to SEM, TEM gives information not only on the surface of the specimen. However, the specimen preparation is significantly more challenging. As the electrons must be able to penetrate the specimen, it must be transparent. For tungsten specimens, this translates into a typical thickness of a few hundred nanometres. The specimen preparation is even more challenging when the material is radioactive; thinning of the radioactive tungsten at the laboratories of PSI, Switzerland, was only possible using focused ion beam (FIB) milling. Chemical thinning could not be utilised due to issues of disposing radioactive chemical waste. TEM specimens of irradiated tungsten were first cut out in sizes of a few microns, using the FIB, then milled down to the desired shape and thickness, which was about 200 nm, and lastly electropolished to TEM transparency. This preparation method was perfected by Dr. Barbara Horvath during her research on irradiated tungsten, conducted at PSI [67]. In the present work, the TEM technique was used to study the specimens irradiated by heavy ions.

Electron microscopy is also an extremely useful tool for gathering information on the observed material. High energy electrons cause emission of characteristic X-rays as they interact with electrons in the specimen. The X-rays can be characterised by an energy dispersive spectrometer (EDS), which provides quantitative data of the composition in the observed area. This technique was used extensively in the present work; it was used on the oxide scales of the oxidised specimens, and on the specimens irradiated by heavy ions – both in an SEM and TEM. The method in which the energy of the emitted electrons is measured is called Auger electron spectroscopy (AES). Auger electrons are normally emitted from a surface layer of several atoms thickness, which is why this method is used for studying the chemical composition of thin layers or surfaces of

solids. Combined with an argon ion gun which removes thin layers of material, AES can be used for depth profiling. This technique was utilised in the oxidation study of this work, where the depth profile gave an estimation of the oxide scale thickness. The equipment was a PHI 700 Scanning Auger Nanoprobe with 4 kV Ar<sup>+</sup> ion sputtering. Typically, a sputter rate of 55 nm/min was used. The rate was calibrated using a Ta<sub>2</sub>O<sub>5</sub> reference standard, under the same sputtering conditions.

An SEM can also make use of the electron backscatter diffraction (EBSD) attachment, which provides information about the microstructure and crystallographic texture of the specimen. EBSD maps are produced by scanning the electron beam across a well-polished specimen surface. The backscattered electrons are detected by scintillator screens which are positioned close to the specimen, and tilted at an angle of 60-70° relative to the SEM incident beam. The specimen is also tilted. It is normally positioned at an angle of 60-80° relative to the detector. Careful specimen preparation is vital. The EBSD pattern is formed from surface layers of tens of nanometres thickness, therefore, the surface must have a mirror-like finish. In the present work, EBSD was used to examine various types of specimens; this method gave a good indication of the grain size and orientation, and it was useful in discovering substructures in some of the specimens.

#### 4.3.2 Thermal analysis

Thermal analysis refers to the measurement of certain predetermined properties of a specimen, as a function of temperature. In this work, two types of thermal analyses were used, namely thermogravimetric analysis (TGA) and differential scanning calorimetry (DSC). Both techniques were used to study the oxidation behaviour of tungsten in a wide range of temperatures and atmospheres. The TGA setup comprised of a large

vertical furnace positioned below a microbalance from which the specimen was hung. The mass change was recorded continuously during the experiment. Some of the oxidation experiments were conducted in the DSC instead. The machine that was used for these experiments was in fact a simultaneous thermal analyser (STA) of model Netzsch STA 449 F3 Jupiter. STA refers to the simultaneous application of thermogravimetry and differential scanning calorimetry. The basic principle of DSC is based on keeping two specimen crucibles at the exact same temperature during the entire experiment. One of the crucibles is always empty, the other contains the material to be studied. The difference in heating rates between the crucibles will reveal potential phase transformations of the specimen and show heat effects during the oxidation of tungsten. As the machine is equipped with a highly sensitive balance, it can also measure mass changes of the specimen during the heating or cooling cycle.

Another type of characterisation equipment used in this work, is the light (or laser) flash apparatus (LFA). A Netzsch LFA 467 Light Flash apparatus was used for determining thermal diffusivities of irradiated tungsten specimens. The principle of the machine is to send out a short duration, high intensity energy pulse towards a specimen, and measure the subsequent temperature raise on the rear surface of the specimen. The flash source is a Xenon lamp, and InSb is the detector. The thermal diffusivity of the specimen is obtained from the specimen thickness  $L$  and  $t_{0.5}$ , which is the time required for the rear surface to reach half of the maximum temperature. For adiabatic conditions, thermal diffusivity  $\alpha$  ( $\text{m}^2/\text{s}$ ) can be expressed using the following relationship [68]:

$$\alpha = \frac{0.138785 L^2}{t_{0.5}} \quad (5)$$

The relationship above has been modified since it was first presented in 1961, to consider heat losses, porosity of the material, transparency and radiative heat transfer within the specimen. Different models can be chosen in the accompanying Netzsch software Proteus [69] and used to automatically fit the thermograms describing the heat propagation through the specimen. The quality of the results is highly dependent on the specimen surface preparation. During the thermal diffusivity study, it was noticed that the specimens should be coated with graphite only very lightly. The graphite coating is necessary to increase the absorption of the flash energy, homogenise the surfaces of the test specimen and the reference specimen, and to improve the emission of infrared radiation to the detector. Applying the graphite coating too generously led to completely wrong thermal diffusivity values. The same issue was noticed by Akiyoshi et al. [70] who used a graphene nanoplatelets containing agent instead. They emphasise the importance of a very thin, sparsely coated surface, especially when the specimen is thinner than recommended.

### 4.3.3 Hardness measurements

Hardness measurements were performed on nearly all types of tungsten studied in this work. Large fatigue and tensile specimens were microhardness tested with a Knoop diamond indenter mounted on a Leica light optical microscope, and with a Sematic Durometer which measured the HRC Rockwell macrohardness. Hardness of the proton and spallation neutron irradiated tungsten was measured with a Vickers microindenter using loads of 0.5 kg and a dwell time of 15 s. Specimens irradiated with heavy ions were only damaged on the surface as the penetration depth of the ions was approximately 20  $\mu\text{m}$ . The hardness of these specimens was measured using two methods; microhardness from the top straight onto the irradiated surface, and nanohardness on the



cross-section which gave the irradiation damage dependent hardness. Nanohardness was determined using a Berkovich indenter and a load of 50 mN, resulting in an average displacement of 500 nm into the material.

The Knoop indenter is a rhombic-shaped indenter with a 7:1 axial ratio, suitable for testing brittle or anisotropic materials, and for coatings or thin films which require a shallow depth of impression. In general, the pyramid-shaped Vickers indenter is the most frequently used. It is suitable for materials of a wide range of hardness and requires no complicated calculations as the hardness is independent of the size of the indenter.

#### 4.3.4 X-ray diffraction – XRD

The X-ray powder diffraction technique is the most widely-used characterisation method for phase analysis and the determination of crystal structures. The method usually employs monochromatic radiation (for example, Cu-K $\alpha$ ) to characterise the sample. An important feature of the X-ray powder diffraction method is to provide qualitative and quantitative information regarding crystalline phases present in an unknown sample. The identification of phases is based on a comparison of the diffractogram obtained, with the standard powder diffraction files in crystallographic databases.

In the present study, X-ray powder diffraction has been used to characterise the tungsten oxides. This was done using a vertical Stoe Stadi X-ray apparatus with a germanium monochromator and a detector set in the reflection mode.

## 5. Results and Discussion

Main results from each study are presented in the following sections. The findings are grouped according to the topics outlined in Chapter 4. More details can be found in the attached papers. Conclusions are summarised in Chapter 6.

### 5.1 Fatigue studies

#### **Papers I and II**

The fatigue behaviour of unalloyed unirradiated tungsten was studied using tungsten specimens from several different manufacturers with diverse production methods. Being a powder metallurgy product, the material properties of tungsten specimens from different production routes can vary widely. The fatigue studies discussed in the present work aim at creating a better understanding of the correlation between the microstructure and the endurance of the material.

The work was done in two parts. In the first part, rolled and forged specimens from Tian-Long were tested at temperatures ranging from 25 °C to 480 °C. In the second part, rolled and HIPed specimens from Plansee were tested. The experimental setup and the runout limit were the same in both studies. The results are presented and discussed according the outlines in the attached Papers I and II.

### 5.1.1 Forged vs. rolled

The specimens in this study were tested at 25 °C, 280 °C, and 480 °C, and were either rolled or forged, and polished or unpolished. The rolled specimens were oriented either across or along the rolling direction. To distinguish between the specimens, the following abbreviations were used: F – forged, R – rolled, L – longitudinal, along the rolling direction, T – transverse, across the rolling direction, P – polished, U – unpolished, and H – high temperature adapted specimen geometry.

Hardness of the specimens was determined on both macro and micro scale. The average macrohardness was just above 40 HRC for all types of specimens, except for the FP (forged, unpolished) ones, which was on average 35.8 HRC. The FP type had the largest scatter, the lowest minimum value, and lowest average macrohardness, which indicates that the surface was relatively rough. Microhardness values for all types of specimens were in the range 460-583 KHN. Microscopic examination of the specimens prior to testing revealed cracks, pores, and machining marks in all the specimens. The electropolished surfaces were relatively smoother, but the variation in quality of the polishing was large. Figure 12 shows four examples of surfaces in the gauge section. The micrographs show electro-polished specimens, one forged (a) and three rolled (b, c, d).

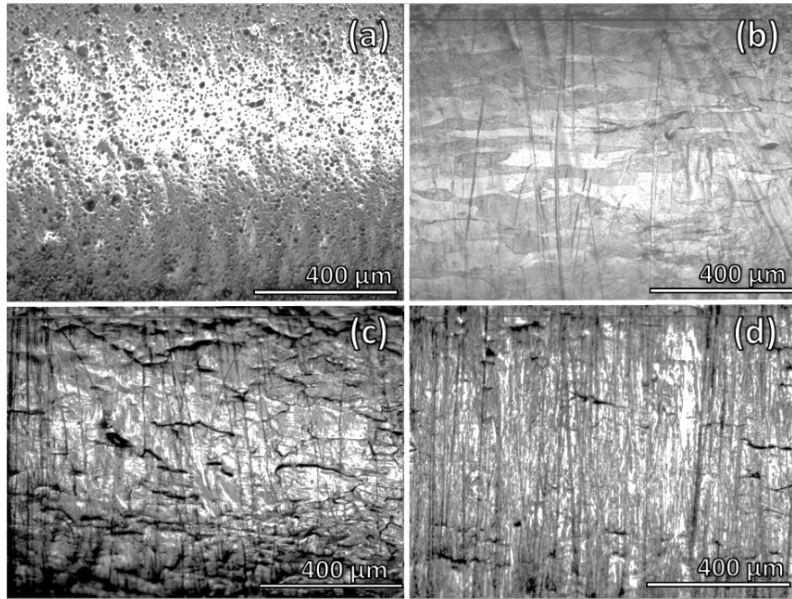


Figure 12 Micrographs of polished forged and rolled specimens: (a) HFP, (b) RLP, (c) RTP, (d) HLP.

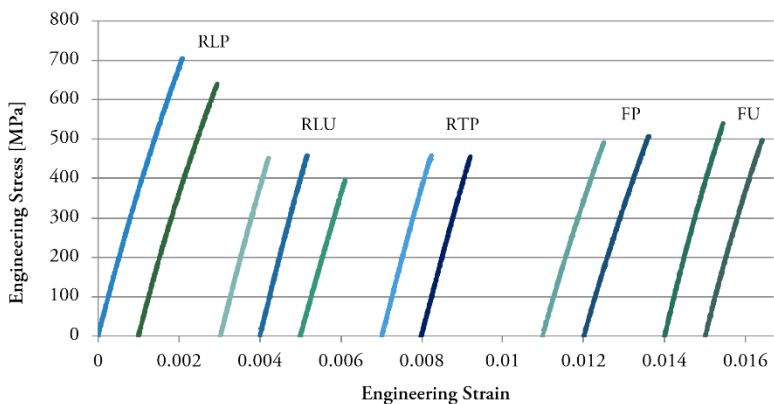
### Tensile testing

Stress-strain data from the tensile tests are plotted in figure 13. A summary of the UTS values is presented in table 5. The results are grouped according to the testing temperature and type of specimen.

Table 5 Summary of UTS values

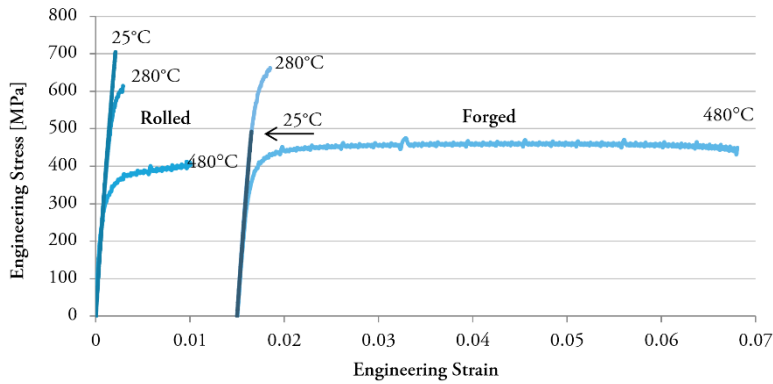
Mean Ultimate Tensile Strength [MPa]							
		25°C		280°C		480°C	
		U	P	U	P	U	P
R	L	503 (397-571)	673 (640-705)	588 (495-681)	593 (571-615)	447	450
	T	-	458 (456-459)	633	522	475	481
F		519 (498-540)	500 (493-507)	507 (472-542)	540 (537-542)	550	525 (363-537)

Figure 13 shows the tensile data for the rolled and forged specimens tested at 25 °C. They were, as expected, very brittle. There is little difference in the UTS between the forged specimens due to the rough surface of the polished specimen. Examination of the surfaces showed no significant difference in roughness between the polished and unpolished forged tungsten. Mean values of UTS and Young's modulus for the forged specimens tested at 25 °C, were determined to be 510 MPa and 340 GPa, respectively. The rolled specimens showed a significant difference in tensile strength depending on specimen orientation relative to the rolling direction. Polished rolled specimens oriented in the longitudinal direction showed the highest UTS values of all specimens. The longitudinally oriented specimens reached a mean UTS value of 673 MPa, whereas the transversely oriented specimens was 458 MPa. Therefore, only the longitudinally oriented rolled specimens were fatigue tested in the next step of the study.



**Figure 13 Tensile data for rolled and forged specimens at 25 °C**

Figure 14 shows a comparison of the stress-strain curves between polished forged and polished rolled tungsten at the three temperatures. The rolled specimens are oriented in the rolling direction. It is evident that the specimens are still relatively brittle at 280 °C. The DBTT seems to be between 280 °C and 480 °C.



**Figure 14 Tensile data for polished rolled and forged specimens at different temperatures.**

As this study was conducted before determining the mechanical properties of the irradiated tungsten, there was uncertainty regarding the ductility of the ESS tungsten during operation. It was decided to test the specimens at three different temperatures. The room temperature test results represent the fatigue behaviour of brittle tungsten. Tests were also conducted at 480 °C as it is close to the maximum operation temperature of the ESS target. Since then, it has been shown that tungsten will have virtually zero ductility when it is irradiated by the proton beam, see Paper V. For this reason, the high temperature tensile test results presented in Paper I will not be discussed in detail here.

### **Stress-controlled fatigue testing**

The number of specimens of each type varied. In total 12 sets of stress-controlled experiments were conducted, one for each type of specimen. In some of the sets the number of specimens was not enough to ensure statistical reliability, therefore only data from sets with more than six specimens were used. The minimum number of specimens required for various types of tests is specified in ASTM E739-10 [71]. Table 6 shows

the replication rates for the specimens used in the stress-controlled fatigue experiments.

**Table 6 Replication rates (%) and number of specimens used in each set**

	25°C						280°C				480°C	
	RLU	RLP	FU	FP	RTP	RTU	RLP	RLU	FP	FU	RLU	FP
Stress levels	13	7	5	5	3	3	6	2	7	11	6	6
Specimens	22	16	12	12	3	3	9	2	9	12	6	9
Replication	41	56	58	58	0	0	33	0	22	8	0	33

Table 7 gives a summary of the endurance limits and the maximum stress amplitudes at a runout, i.e. completion of  $2 \times 10^6$  cycles without specimen failure.

**Table 7 Endurance limits and maximum stress amplitudes at runout**

Stress amplitude [MPa]					
Sample		Endurance limit	No. of tests	Highest runout	
25°C	T	U	150.0	3	150.0
		P	137.5	3	137.0
	R	U	150.0	22	337.5
		P	237.5	16	300.0
	F	U	175.0	9	200.0
		P	125.6	12	170.6
280°C	R L	U	300.0	2	300.0
		P	252.5	12	290.0
	F	U	242.5	12	300.0
		P	212.5	9	250.0
480°C	R L	U	150.0	6	150.0
	F	P	175.0	9	187.5

The RLU specimens tested at 25 °C show large scatter in the data. This type had the highest runout stress amplitude (337.5 MPa) as well as one of the lowest endurance limits (150 MPa). The polished counterpart, RLP, had less scatter and much higher endurance limit, in fact about half

of the tested specimens failed at stress amplitudes between 237.5 MPa and 312.5 MPa. Again, the FP specimens did not perform well, the endurance limit of 125.6 MPa is the lowest of all, even lower than that of the FU specimens. The FU specimens showed relatively less scatter. The polishing of the forged specimens seems to have been performed less carefully than that of the rolled specimens; the difference in endurance limit between RLP and RLU is almost 90 MPa, whereas the polishing of the forged specimens seems to have damaged them rather than improved them. The fatigue behaviour is difficult to predict in such a sensitive material as tungsten. Some of the tested specimens would result in both runout and instantaneous failure, at the same stress amplitude, while originating from the same set of specimens. This highlights the importance of careful surface treatment and good quality control. To some extent, defects in the specimen surface are inevitable, but this must be kept to a minimum by choosing the optimal manufacturing and surface finishing methods. A visualisation of the scatter at 25 °C is presented in a Wöhler diagram in figure 15. For high temperature stress-controlled data as well as results from strain-controlled fatigue experiments, the reader is referred to the attached Paper I.

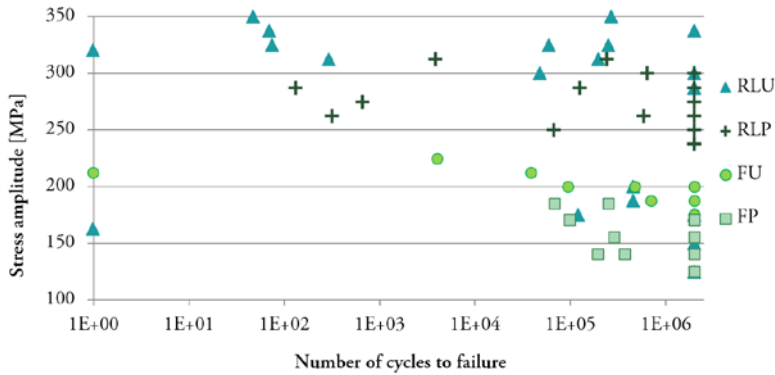
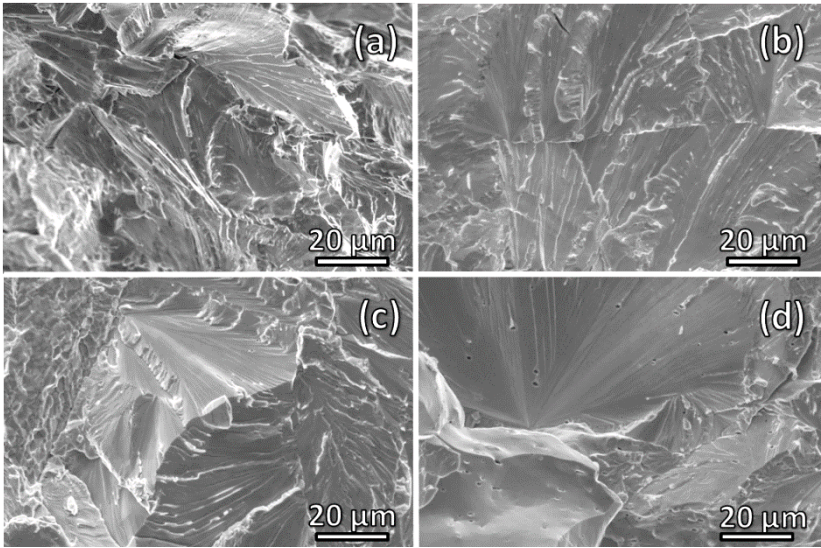


Figure 15 Wöhler diagram for rolled and forged specimens tested at 25 °C.



## Fractography

Eighteen specimens were chosen for SEM observations after fatigue testing. Fracture surfaces of different types of specimens, tested at various loads and temperatures, were studied. Figure 16 shows fractographs of a few rolled specimens: (a) RLP, tested at 25 °C and a stress amplitude of 175 MPa, failed at cycle 120841; (b) RTP, tested at 25 °C and a stress amplitude of 163 MPa, failed at cycle 136219; (c) RLU, tested at 25 °C and a stress amplitude of 200 MPa, failed at cycle 448951; and (d) RLP, tested at 280 °C and a stress amplitude of 302.5 MPa, failed at cycle 25.



**Figure 16** SEM images of fatigue fracture surfaces. (a) RLP 25 °C, (b) RTP 25 °C, (c), RLU 25 °C, (d) RLP 280 °C.

Images (a)-(c) show brittle failures with the characteristic chevron pattern and ridges. The transversely oriented specimen (b) seems to have fractured in an even more brittle manner compared to the longitudinally oriented one (a), crack propagation should have occurred easier in this specimen. The RLU specimen (c) is associated with more ductility and some

contribution from intergranular fracture. Also shown in the fractograph is a faceted structure, which could possibly be subgrains. At 280 °C, there seems to be some ductility in the specimen (d), although, the fracture surface is dominated by transgranular cleavage.

Two fracture surfaces of forged and unpolished specimens are shown in figure 17. The SEM images reveal porous microstructures and brittle failures in both specimens, but also very different fracture modes. The FU specimen tested at 280 °C (b) does not resemble any other observed fracture surface. The grains seem to be smaller ( $\sim 30\text{ }\mu\text{m}$ ) compared to the FU tested at 25 °C (a) and poorly attached. Some grains look like loose gravel, which suggests that problems occurred during sintering or the subsequent forging. This specimen failed soon after loading and did not show any signs of fatigue.

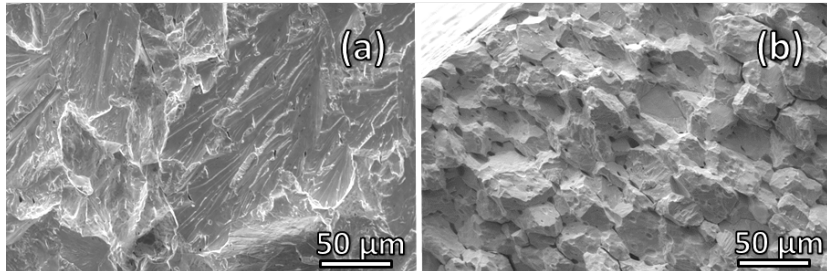


**Figure 17** SEM images of fracture surfaces of forged specimens. (a) FU 25 °C, (b) FU 280 °C.

Figure 18 shows a few different types of fracture surfaces. All the specimens, except the FP (a), were tested at higher temperatures and display some ductility. The FP (a) specimen failed in a mixed inter- and transgranular fracture, as did the FP (b) specimen tested at 280 °C but this surface is characterised by smoother grains and some plastic deformation. Images (c) and (d) compare the fracture surfaces of an FP and an RLU specimen tested at 480 °C. Both areas show relatively large

amounts of plasticity. The rolled specimen (d) has clearly visible elongated grains with large amounts of delamination. The surface of the forged specimen (c) is dominated by transgranular fracture.

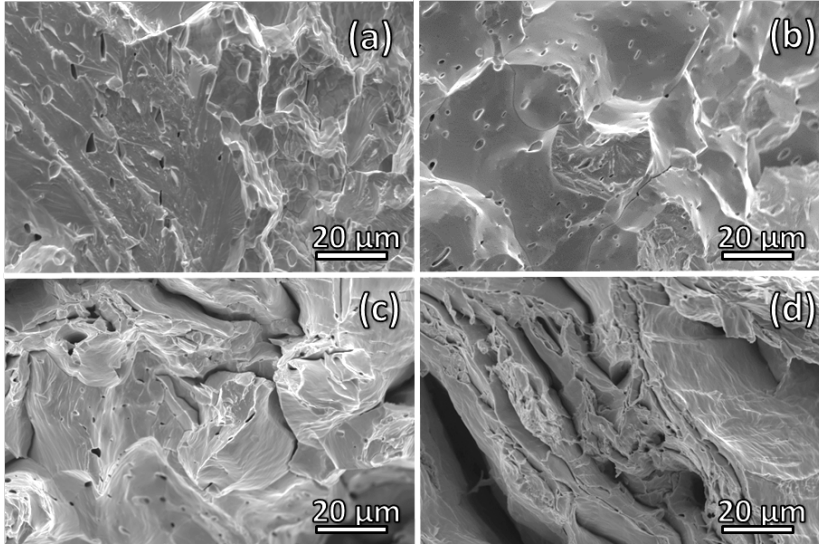


**Figure 18** Fracture surfaces of (a) FP 25 °C, (b) FP 280 °C, (c) FP 480 °C, (d) RLU 480 °C.

### 5.1.2 Rolled vs. HIPed

The second fatigue study focused on the behaviour of rolled and annealed versus sintered and HIPed tungsten. With experience from the first study the experiments performed in the second could be improved. One of the most important points was to not only chose polished specimens, but also specify the maximum tolerable surface roughness. This time, no unpolished specimens and no rolled specimens oriented in the transverse direction were tested. The specimens were provided by Plansee, and only one type of specimen dimension was used. All the tests in this work were performed at room temperature.

According to specifications from Plansee, the surface roughness in the gauge section was maximum 1.6  $\mu\text{m}$ . The surfaces were observed to be of reasonably good quality, with only few visible surface defects. The HIPed specimens (SH) were typically more porous than the rolled ones (RA), which resulted in a rougher surface. Figure 19 shows a comparison of two typical gauge sections.

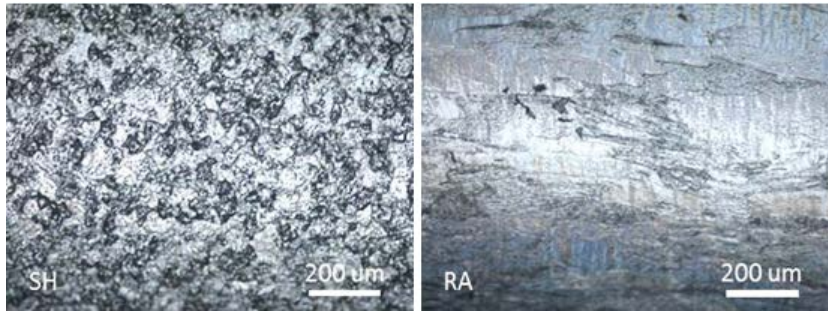


**Figure 19 Gauge sections of SH and RA specimens.**

The porosity of the SH material was estimated to about 4.3%, with uniformly distributed pores in the microstructure, which corresponds well to the reported 4% porosity of HIPed tungsten [72]. The average porosity of the RA specimen was 0.5%. The grain size of the SH material was in the range 10-85  $\mu\text{m}$ , with an average around 30  $\mu\text{m}$ . The RA specimen had very large, thin and interlocking grains. Some grains were as long as 1 mm, and clearly visible to the naked eye once the surface was polished and etched. Micrographs of an SH and RA are shown in figure 20. The surface of the RA specimen, etched with Murakami's reagent, displays details within the larger grains which could indicate presence of a subgrain structure.

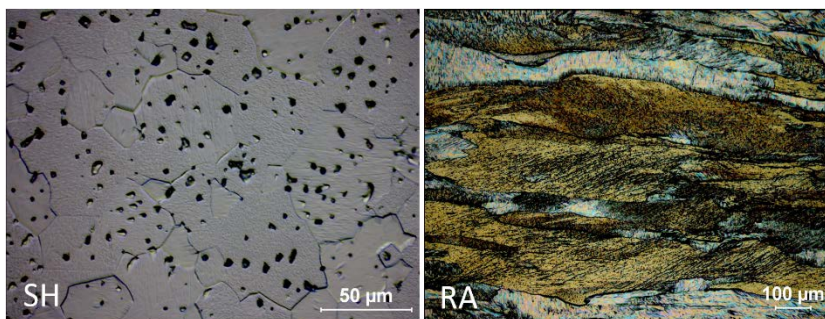


**Figure 20** Microscopic images of etched SH and RA specimens.

The effect of rolling is visible in figure 21 which presents a triplanar micrograph. The top view of the micrograph represents the rolling plane. A difference in hardness was observed between the two types of specimens; the average Vickers microhardness for RA was 508 HVN, and 389 HVN for SH, using a load of 0.4 kg.

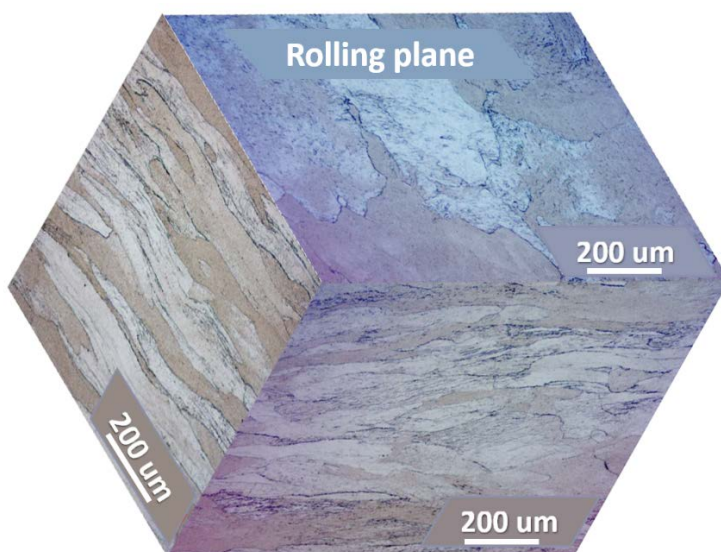


**Figure 21** Triplanar micrograph of a rolled specimen.

## Tensile testing

As the number of specimens was limited, only one RA and two SH specimens were used for the tensile tests. Engineering stress-strain diagrams based on the monotonic tensile response of the specimens are shown in figure 22. As in the previous study, specimens tested at room temperature display negligible plastic deformation. The average UTS of the SH material is much below that of the RA. In addition, there is a difference in Young's modulus, which can be explained by the difference in porosity between the two types of specimen [73].

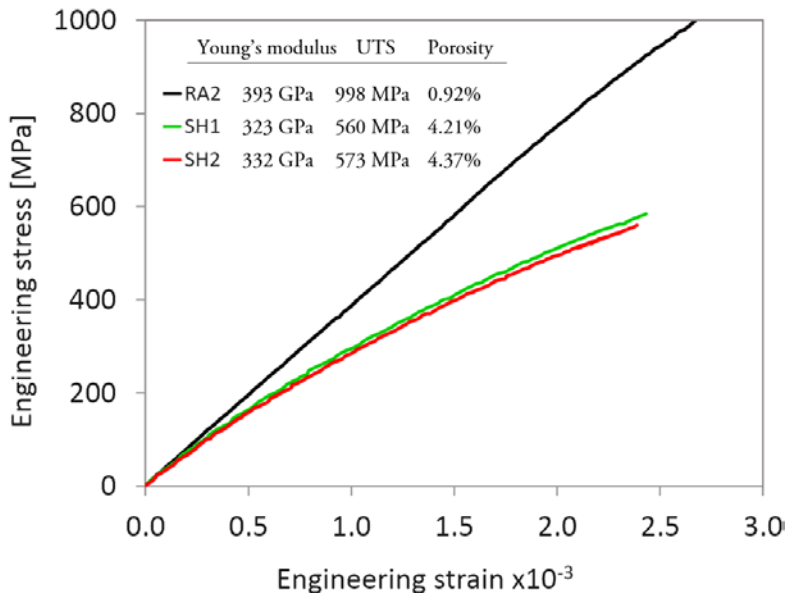


Figure 22 Monotonic tensile test results of SH and RA specimens.

## Stress-controlled fatigue testing

As in the first fatigue study, all stress-controlled tests were performed in the tensile regime with a minimum stress of 5 MPa, i.e. in a fluctuating stress mode. The results are plotted in a Wöhler diagram with the stress

amplitude  $S_a$  plotted against number of cycles to failure,  $N$ . The runout limit is set at  $2 \times 10^6$ . Figure 23 presents fatigue data.

The first RA and SH specimens were used to quickly find the appropriate starting stress amplitude. The SH specimen was initially tested at an amplitude of 180 MPa, which resulted in a runout. The same specimen was then reused at progressively increasing stress amplitudes until it failed at 250 MPa. This way the number of specimens used for determining the endurance limit could be minimised. A similar approach was used for the RA specimens. The initial stress amplitudes were chosen based on the results from the first fatigue study.

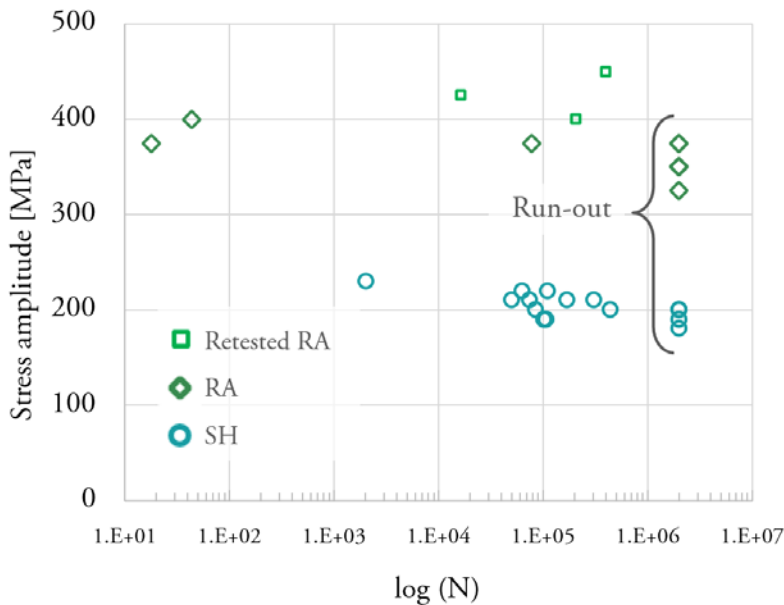


**Figure 23 Wöhler diagram for SH and RA tungsten.**

For reused runout specimens, only the very first test results were included in the staircase data. Some of the RA runout specimens were also retested at higher stress amplitudes. This was done in order to get an idea of the fatigue behaviour at higher stresses. These data were not used for



determining the endurance limit. Due to negligible plasticity and large scatter, a regression analysis of the fatigue data for the RA specimens could not be performed. For analysis of the SH data, the reader is referred to the attached Paper II. Nevertheless, a one-sided confidence band could be calculated for the fatigue limit of both types. The mean fatigue limit and standard deviation for the SH specimens were 185 MPa and 26.4, respectively. The corresponding data for the RA specimens were 371 MPa and 13.3, respectively. In accordance with guidelines by ASTM [74], the replication rate of fatigue data is 62.50% for the SH type and 55.55% for RA, which means SH is in the range for allowable data for design, while RA is in the research and development stage.

During testing there were problems associated with mounting of the RA specimens. Many of the specimens were very brittle and would fail already while being mounted in the grips of the testing device. Images of typical cracking in a specimen are presented in figure 24.

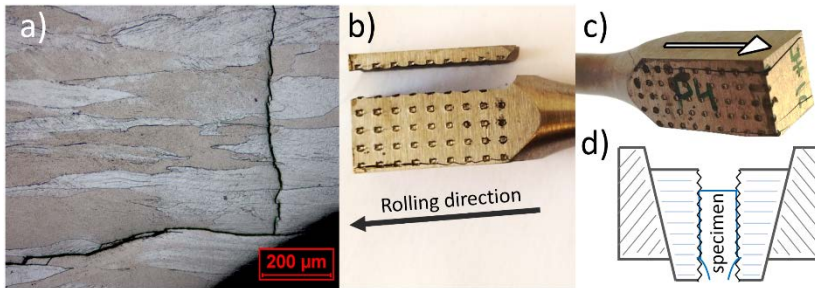


**Figure 24 a) Crack propagation in the RA specimen, b) and c) show large cracks and delamination, the arrows point in the rolling direction, and d) illustration of the serrated wedge grips.**

It was found that choosing the right orientation of the specimen could reduce the risk of failure in the grip section. When gripped in the plane perpendicular to the rolling direction, the indentation from the wedge grips would initiate cracks which propagated along the grain boundaries



of the specimen, and in the worst case, cause delamination throughout the entire grip area. Mounting the specimens so that the grips were attached in the same plane as the rolling direction resulted in fewer immediate failures. All RA specimens were sensitive to the grips and showed damage to varying extents. No such issue was found with the SH specimens. A summary of the staircase test data with the stress amplitudes and number of cycles to failure for each tested specimen can be found in the attached Paper II.

### Strain-controlled fatigue testing

The SH specimen showed rapid hardening during the first 20 cycles of fully reversed straining at  $\pm 0.15\%$  and a strain rate of  $10^{-3}/s$ . After a short period of saturation, the specimen continued to harden gradually until failure at cycle 90. Figure 25 compares the stress response during the first cycle with the stress response of a cycle at saturation. It should be noted that the strength in tension (400 MPa) during the first cycle is significantly lower than in compression (490 MPa).

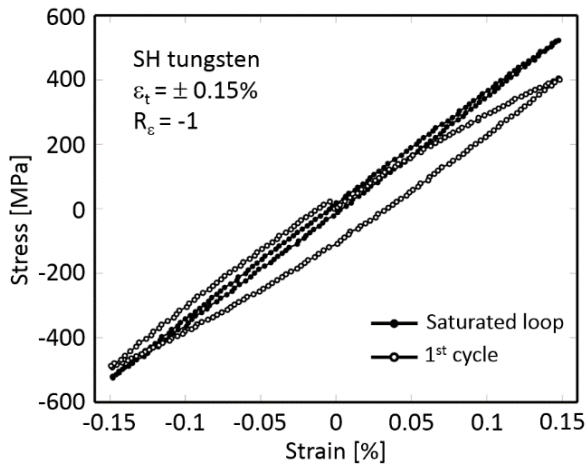
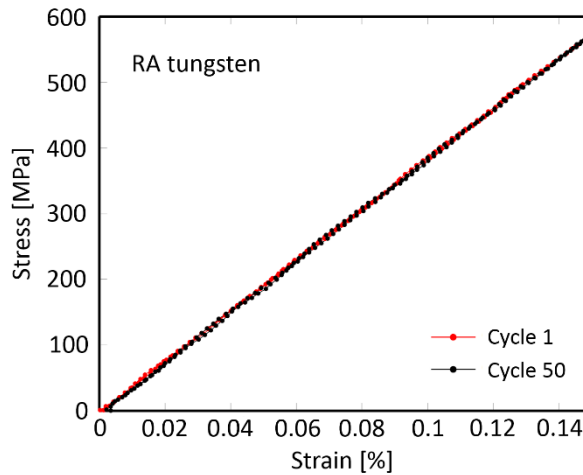


Figure 25 Stress-strain relationship during the initial and later stages of strain-controlled cyclic testing.

Strain-controlled testing of the RA specimen did not result in any changes of the stress response. The specimens were too brittle. Testing resulted in purely elastic response where the 1<sup>st</sup> and 50<sup>th</sup> cycle behave essentially the same. The elastic response of an RA specimen is shown in figure 26.



**Figure 26 Strain-controlled testing of an RA specimen showing completely elastic response.**

### Fractography

The SH specimens fractured in a predominantly intergranular mode, where larger grains were cleaved and smaller left intact. The large fraction of pores likely contributed to fatigue failures. Catastrophic failure has been shown to occur because of coalescence and growth of microcracks, which tend to initiate at pores and inclusions [75]. The RA specimens were typically very brittle with a pronounced anisotropic behaviour. Typical fracture surfaces of both types of specimens are shown in figure 27. All RA specimens failed in transgranular fracture mode during fatigue as well as tensile testing. Intergranular fracture is unlikely due to the long grains ( $\sim 1$  mm) of the RA material. The fracture surfaces of RA specimen showed no signs of local deformation.

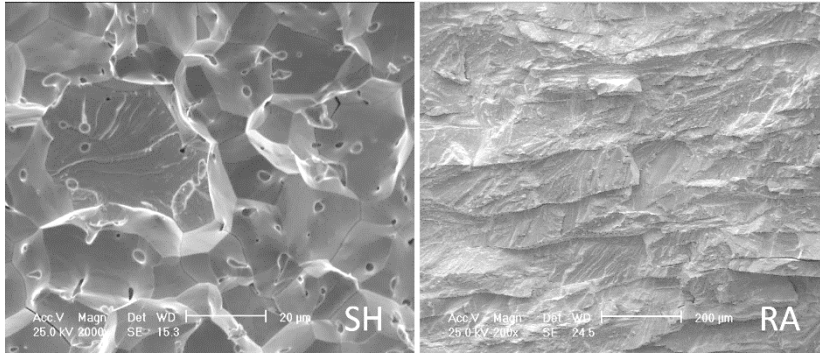


**Figure 27** Fractographs of an SH and an RA fatigue tested specimen.

## 5.2 Oxidation study

### Paper III

The surfaces of the oxidised specimens were examined with several different techniques. The results are presented in sub-sections based on the experimental setup and the oxide characterisation method. First, results from TGA, DSC-STA, and in situ ESEM studies will be discussed, followed by the XRD, AES, and EDS observations, and lastly, results from the tungsten alloy study will be presented.

### 5.2.1 TGA studies of the larger specimens

Pure unirradiated cross rolled tungsten specimens of 3 mm thickness and 20 mm diameter, where oxidised isothermally for 2h in two different gas mixtures. The mass of the specimen was monitored continuously during the experiment. The mass change as a function of temperature for the specimens oxidised in a He-0.5%O<sub>2</sub> gas mixture is shown in figure 28.

Below 500 °C, the mass change is marginal, but the oxidation rate increases drastically with temperature. At 907 °C the increase is nearly 18 mg/cm<sup>2</sup> after 2h. The mass change of the specimen oxidised at 811 °C shows signs of suddenly increased growth rate after approximately 50 min, indicating cracking of the oxide scale which leads to easier access for oxygen to the bare tungsten.

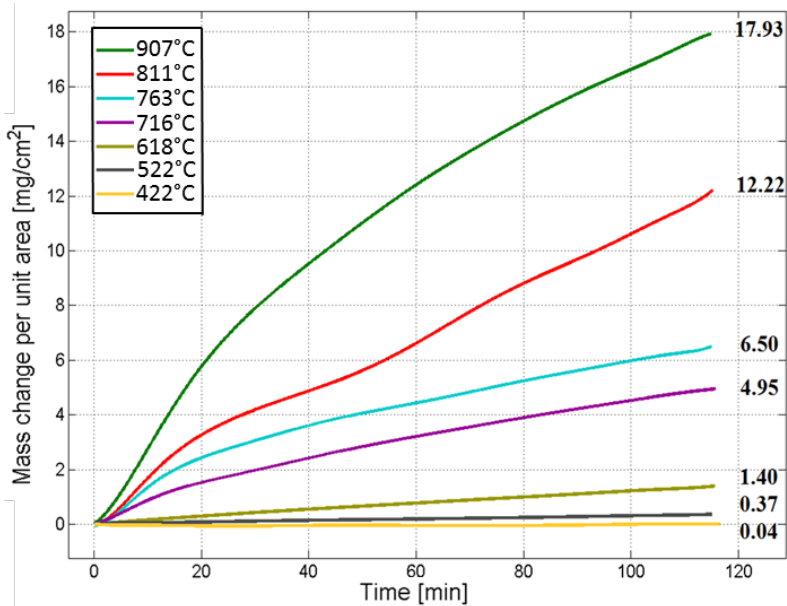


**Figure 28 Oxidation of tungsten in a He-0.5%O<sub>2</sub> gas mixture.**

Images of the specimens after the 2h oxidation in He-0.5%O<sub>2</sub> are shown in figure 29. The oxide layer formed at the lowest temperature is very thin, appearing more like a thin coat of metallic paint. The next specimen shows a thin black oxide layer with full coverage. The oxide is very adherent. At 618 °C, the oxide scale looks similar with the addition of a very thin layer of the porous type of oxide. There is a significant change in the appearance of the oxide scale as the temperatures reaches 716 °C, which can be correlated to the increased oxidation rate as seen in the previous

figure. The oxide scale is significantly thicker, owing mainly to the growth of the green porous oxide type. The specimens oxidised at the two highest temperatures display a thick layer of the green oxide, which is believed to consist of mainly  $\text{WO}_3$ . The  $\text{WO}_3$  is bright yellow in its pure form, but changes colour even at the slightest oxygen deficiencies, e.g.  $\text{WO}_{2.98}$  is blue although the crystal structure is the same. Other lower tungsten oxides tend to shift in colours of red, violet, and blue [76].

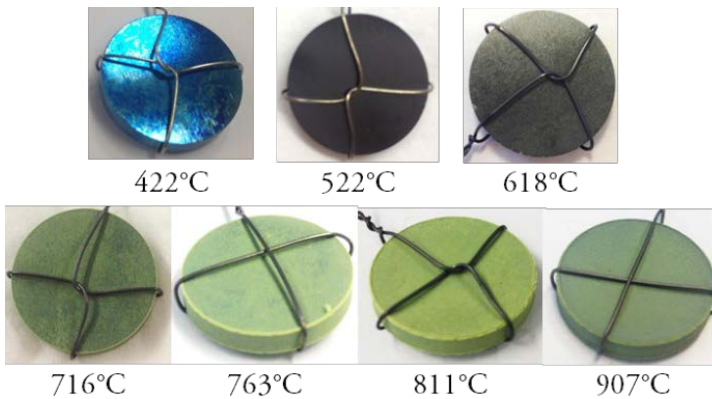


**Figure 29 Specimens after oxidation for 2h in a He-0.5%O<sub>2</sub> gas mixture.**

Results from the oxidation experiments carried out in a He-Ar-H<sub>2</sub>O gas mixture are presented in figure 30. The mass change is relatively less pronounced, yet still significant. The partial pressure of the water vapour was 790 Pa, which seems to be enough to oxidise tungsten. This is an important observation as it shows the necessity of keeping the helium cooling gas at ESS as free from moisture as possible. The appearance of the specimens at different temperatures were similar to those presented above, but with slightly thinner oxide scales.

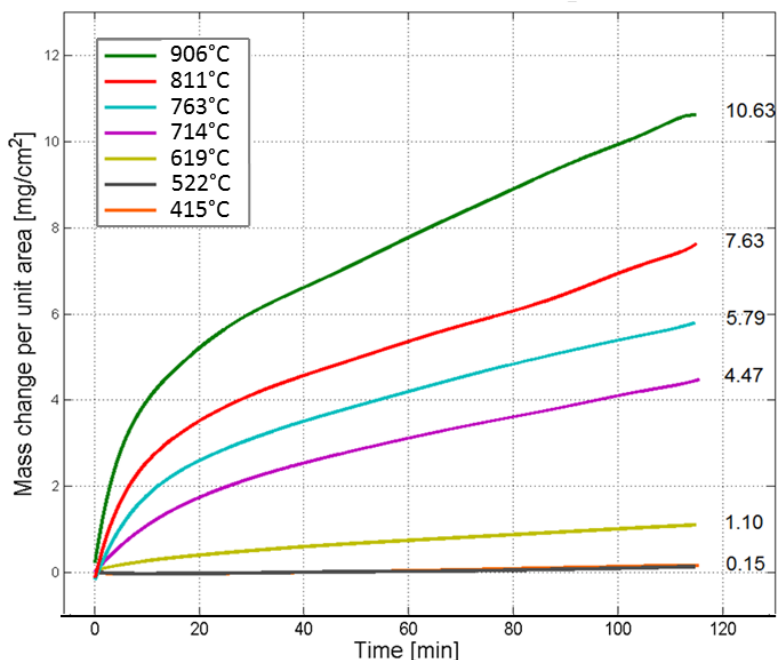
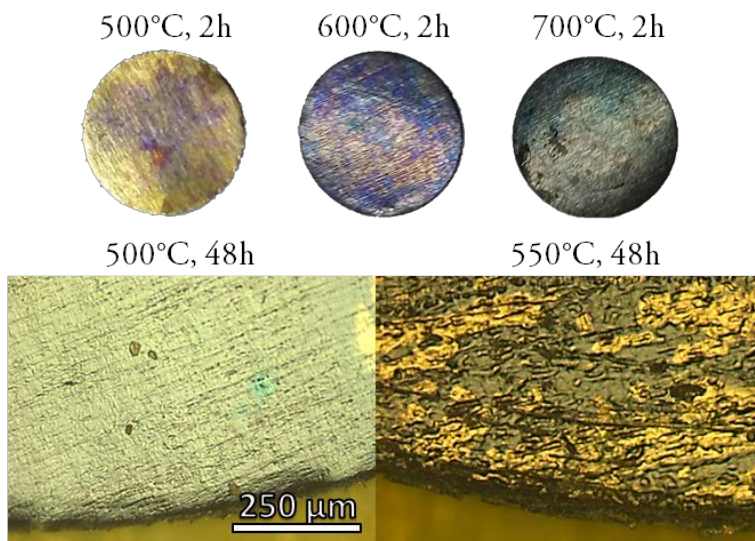


Figure 30 Oxidation of tungsten in He-Ar-H<sub>2</sub>O gas mixture, with a p<sub>H<sub>2</sub>O</sub> of 790 Pa.

### 5.2.2 DSC-STA studies of the smaller foil specimens

Specimens of 26  $\mu\text{m}$  thickness and 5.5 mm diameter were oxidised in pure and dry argon which contained oxygen as an impurity. The oxygen partial pressure was less than 5 ppm. The oxidation was carried out at atmospheric pressure for up to 48 h. Figure 31 presents images of the specimens after oxidation. It appears as if there is an oxide layer on all specimens, even the one oxidised at 500 °C in commercially pure argon gas. The results show that over a long period of time, there is a possibility of oxide formation on tungsten even at relatively low temperatures and impurity levels of oxygen. The specimens were further examined using XRD and these results are presented in section 5.2.4.



**Figure 31** Surface images of tungsten foils oxidised in argon gas (max. 5 ppm O<sub>2</sub>).

### 5.2.3 In situ ESEM studies of the smaller foil specimens

The specimens were placed in an ESEM at a water vapour partial pressure of 100 Pa, then slowly heated while simultaneously observing the changes on the surface. Below 600 °C, no significant changes were observed. As the temperature is increased, the oxide begins to form. At 800 °C, the surface appears to be nearly covered by the oxide. The images from this experiment are presented in figure 32.

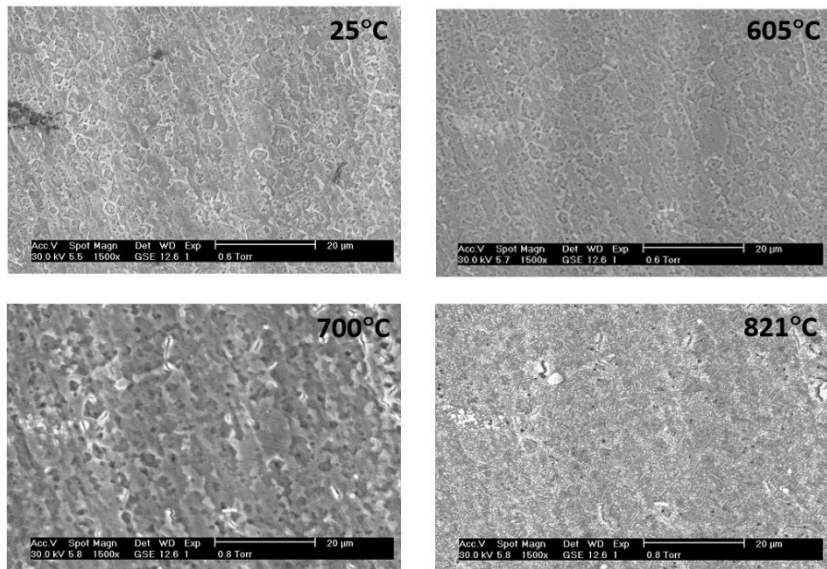


**Figure 32** SEM images of tungsten at various temperatures during in situ oxidation in a hot stage, at a  $p_{\text{H}_2\text{O}}$  of 100 Pa.

### 5.2.4 XRD observations

XRD was used to identify the oxides formed on the tungsten foils oxidised in commercially pure argon ( $p_{\text{O}_2} \leq 5$  ppm) at 600 °C and 700 °C, as well as on thicker disk specimens oxidised at 500 °C and 600 °C in air. The diffractograms are shown in figures 33 and 34. Oxides were detected in all the specimens. Both foils and the disk specimen oxidised at the lower temperature were covered by mainly  $\text{W}_{18}\text{O}_{49}$ . The surface of the disk specimen oxidised at 600 °C showed the presence of  $\text{WO}_3$ .



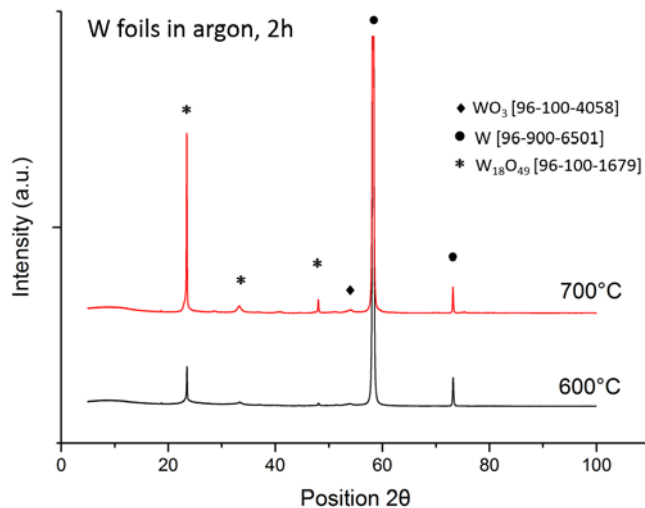


Figure 33 XRD of tungsten foils oxidised in pure argon (max. 5 ppm  $\text{O}_2$ ).

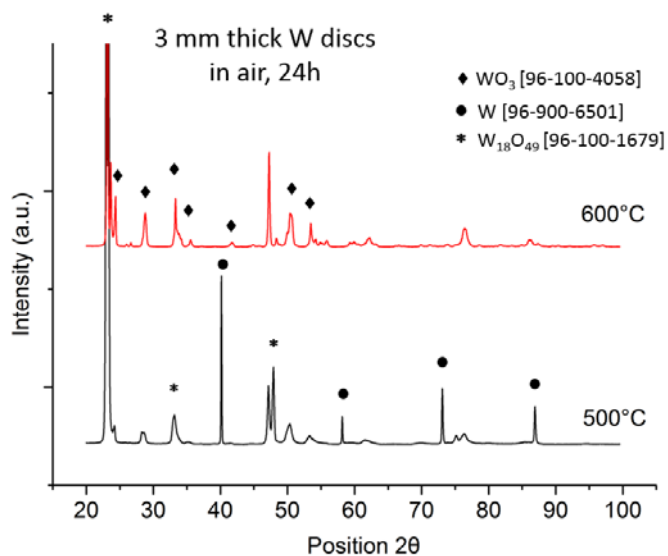
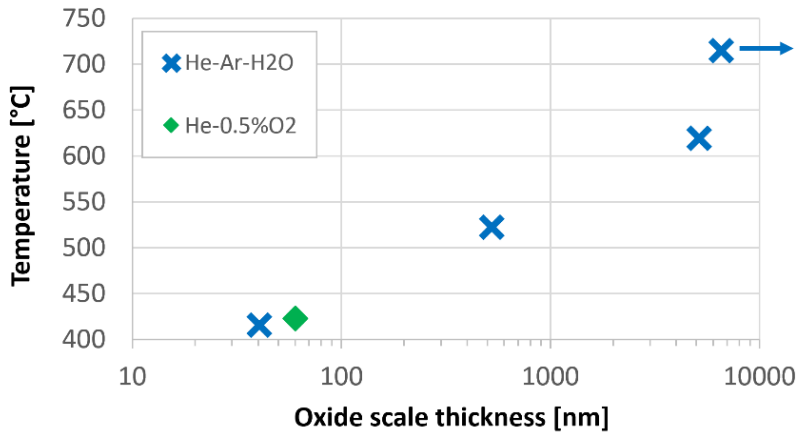


Figure 34 XRD of tungsten disks oxidised in air for 24 h.

### 5.2.5 AES observations

Some of the oxidised 3 mm disk specimens were further characterised using Auger electron spectroscopy. The thickness of the oxides could be measured and a depth profile with elemental analysis was acquired. As AES is a technique used mainly for studying thin layers, only the specimens with the smallest mass gain could be studied, i.e. specimens oxidised for 2h at 400 °C, 500 °C, and 600 °C. Data from the AES observations are presented in figure 35. The 700 °C specimen had to be discontinued due to its very thick oxide layer. Only one of the specimens oxidised in He-0.5%O<sub>2</sub> was observed with the AES as the oxide layers of the remaining specimens were too thick.



**Figure 35 Tungsten oxide scale thickness measured by AES.**

The average oxide thickness of the specimen oxidised at 415 °C in He-Ar-H<sub>2</sub>O is 35 nm, while that of the He-0.5%O<sub>2</sub> oxidised at a similar temperature is 60 nm. The oxide scales of the 500 °C and 600 °C He-Ar-H<sub>2</sub>O specimens are approximately 0.5 µm and 5 µm, respectively. SEM images of the sputtered surfaces and the depth profiles acquired by AES can be seen in the attached Paper III.

### 5.2.6 EDS observations

Energy-dispersive X-ray spectroscopy was used to analyse the specimen surface oxidised at 714 °C in the He-Ar-H<sub>2</sub>O gas mixture. Several positions in the thick oxide scale were chosen for observation. Figure 35 shows SEM images of the positions marked 1-6. The orange box marks the area of the measurement for position number 6. Measurements 1-5 were made within this box. The second SEM image shows the same area at a higher magnification. Data from the EDS measurements are presented in table 8. It confirms that the oxide scale of tungsten consists of a range of oxide stoichiometries, from WO<sub>2</sub> to WO<sub>3</sub>.

**Table 8 EDS analysis of positions 1-6 on the oxide scale**

Position	at.% O*	at.% W**	O/W
1	73.06	26.94	2.71
2	67.23	32.77	2.05
3	75.36	24.64	3.06
4	70.24	29.76	2.36
5	71.75	28.25	2.54
6	71.96	28.04	2.57

\*K-lines, \*\*M-lines

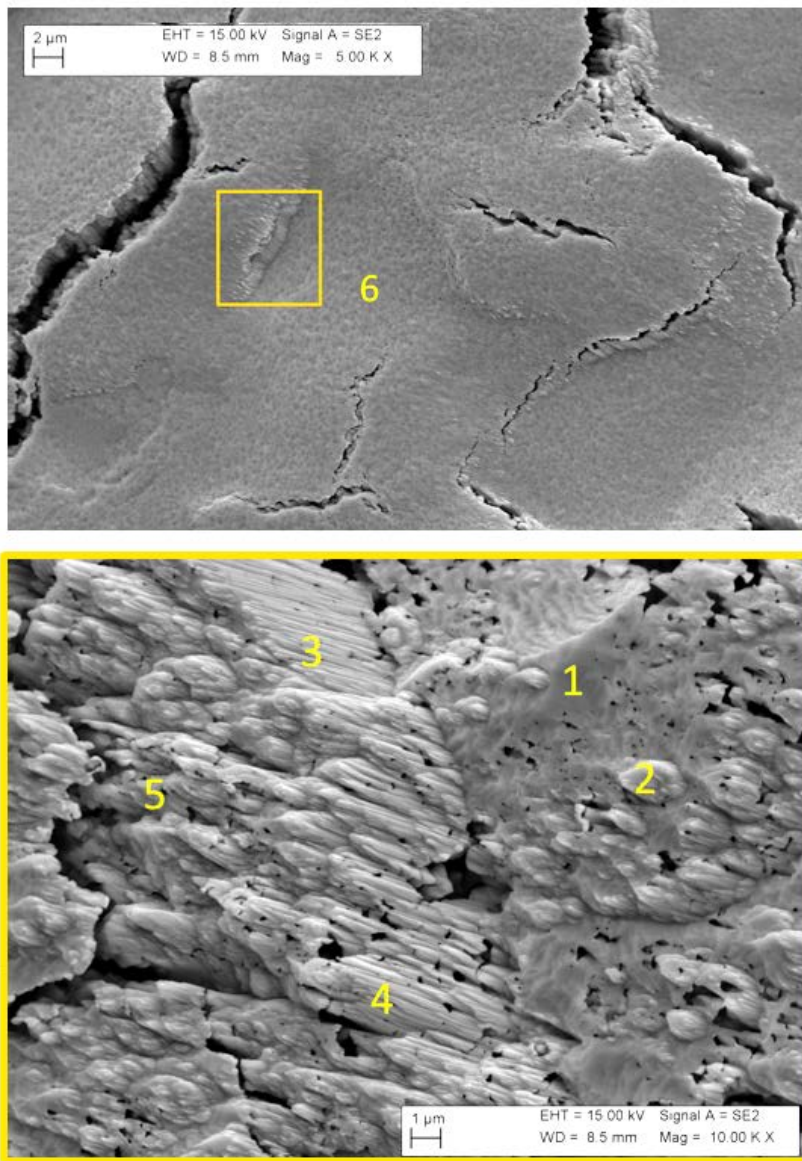


**Figure 36 EDS analysis at different positions on the oxide scale.**

### 5.2.7 Tungsten alloys

For purposes of comparison, oxidation behaviour of four different tungsten alloys was studied at slightly higher oxygen partial pressures. The oxidising gas mixture was He-0.5%O<sub>2</sub> and the duration of the test 2h. The results acquired with the TGA setup are shown in figure 37. The graph compares the mass change during 2h between unalloyed tungsten and the alloy D176, at 800 °C, 900 °C and 1000 °C. The alloy is much more prone to oxidation at all temperatures, which can be attributed to the presence of 5% nickel and 2.5% iron in the alloy. The comparison between the remaining three alloys can be seen in the attached Paper III. The results show that the alloy with the lowest fraction of alloying elements (D185) oxidised the least.

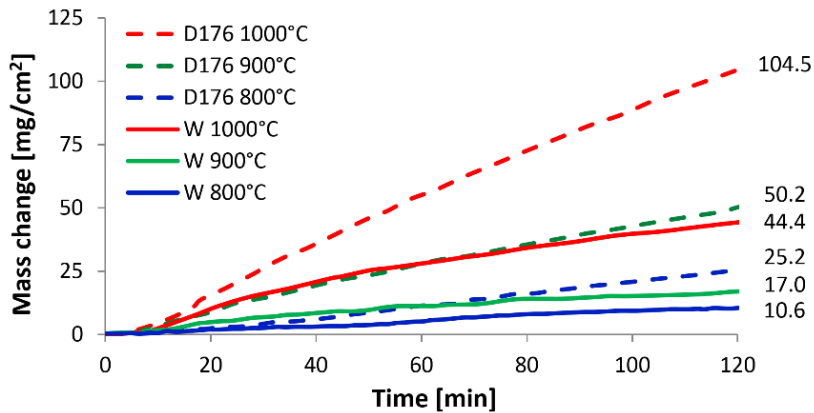
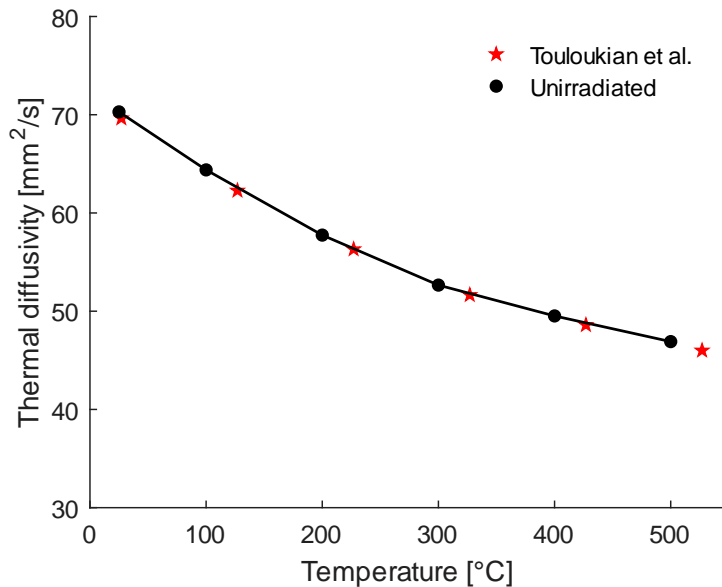


Figure 37 Oxidation of pure and alloyed tungsten.

## 5.3 Thermal diffusivity studies

### Paper IV

Results from thermal diffusivity measurements of unirradiated tungsten specimen were compared to reference data reported by Touloukian et al. [77]. This reference is also used by Netzsch in the Proteus software, used with the LFA. Experimental thermal diffusivity values correspond very well to the reference data, as can be seen in figure 38. The results are plotted as a function of the testing temperature.



**Figure 38 Thermal diffusivity of unirradiated tungsten.**

Data for thermal diffusivity of unirradiated tungsten in the range 25-500 °C, can be expressed using the polynomial fit given below, where thermal diffusivity ( $\alpha_{ref}$ ) is expressed in mm²/s. and the temperature (T) in °C.

$$\alpha_{ref} = 72.625 - 9.3617 \times 10^{-2}T + 1.0392 \times 10^{-4}T^2 - 3.8694 \times 10^{-8}T^3 \quad (6)$$

A molybdenum specimen was tested simultaneously and showed very good agreement with reported standard thermal diffusivity values. This confirms that the preparation of the specimens, the measurement, and the data analysis were performed correctly.

Data for the two irradiated specimens are presented in figure 39. The irradiation at SINQ significantly reduced thermal diffusivity of both specimens. There is little difference in thermal diffusivity between the specimens, despite their different irradiation doses. The average thermal diffusivity at room temperature is approximately 35 mm<sup>2</sup>/s for both specimens, which is only half the value of the unirradiated tungsten. At 500 °C, thermal diffusivity of the unirradiated specimen decreases to 47 mm<sup>2</sup>/s, while those of the irradiated specimens remain at approximately 35 mm<sup>2</sup>/s.

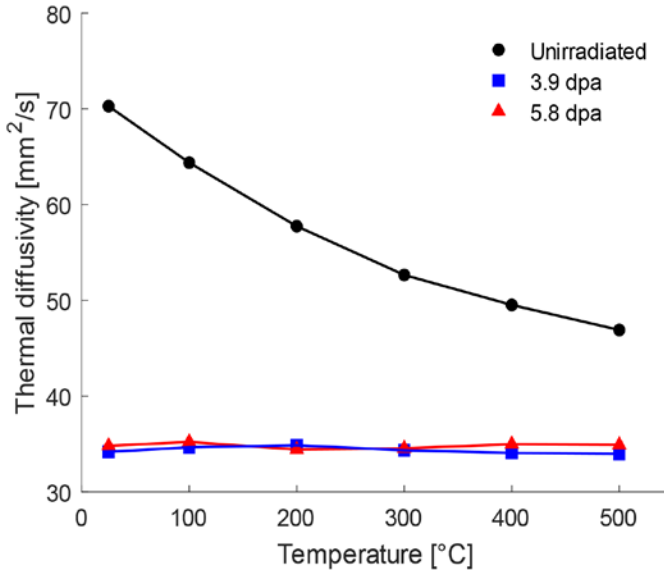


Figure 39 Thermal diffusivity of irradiated tungsten.

This type of temperature independent thermal diffusivity has also been reported by Tanabe et al. [59], but for unirradiated tungsten-rhenium alloys. Thermal diffusivity of a W-9.8%Re alloy, measured in the temperature range 27-500 °C, was nearly constant at around 25 mm<sup>2</sup>/s. The corresponding values for a W-5.3%Re alloy was in the range 30-34 mm<sup>2</sup>/s. Relative to the pure tungsten specimen tested at room temperature, these values are 48-62% lower.

As mentioned in the introduction, irradiation induced degradation of thermal diffusivity of tungsten is attributed to both displacement damage and compositional changes in the form of transmutation products. It has been shown that already 5% of rhenium in tungsten lowers thermal diffusivity at room temperature by 50%, even without irradiation [21]. Other studies show that the thermal diffusivity of a W-1%Re alloy is 10-20% lower in the temperature range 25-200 °C. The corresponding values for a 2% rhenium addition are 20-30% lower compared to pure tungsten in the same temperature interval [78].

To get a better understanding of the separate contributions to the decrease of thermal diffusivity, the irradiated 3.9 dpa specimen was annealed and remeasured. The annealing was done at 1000 °C, for 1 h, in a vacuum of 1 Pa. Tantalum foil wrapping was used as additional protection against oxidation. The second measurement was made together with the molybdenum standard specimen and the unirradiated reference specimen which had also been annealed. The test temperatures were 25 °C, 300 °C, and 500 °C. The results are presented in figure 40.



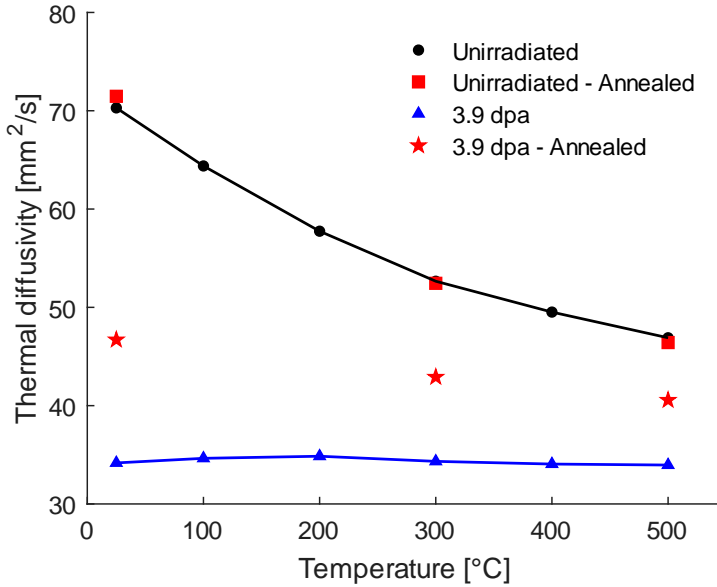


**Figure 40 Thermal diffusivity of irradiated and annealed tungsten.**

Both unirradiated specimens showed values consistent with the first measurement. The thermal diffusivity of the irradiated and annealed specimen showed partial recovery. At 25 °C thermal diffusivity had increased to 47 mm<sup>2</sup>/s, and at 500 °C to 41 mm<sup>2</sup>/s, which is an increase of 37% and 19%, respectively.

In a study by Horvath et al. [67], specimens from the same piece of irradiated tungsten as was used in the present work, were examined with transmission electron microscopy (TEM). The effect of post-irradiation annealing at different temperatures, on the microstructure of the specimens was presented. The microstructure of unirradiated tungsten was characterised by dislocations up to tens of microns in length, and a dislocation density of approximately  $1.6 \times 10^{13} \text{ m}^{-2}$ . The irradiated specimens, with doses 1.4 and 3.5 dpa, contained mainly defect clusters

and dislocation loops of a few nanometres. Annealing the irradiated specimens at 900 °C for 1 h, resulted in a reduction of the number of defect clusters and dislocation lines by factors of 6 and 2, respectively. The average size of the defect clusters increased from 2 nm to 5 nm. In addition, 1-2 nm sized cavities appeared after annealing. The cavities are believed to have grown from invisible helium-vacancy clusters, which together with the small defect clusters are thought to be responsible for the reduction in thermal diffusivity of irradiated tungsten. Annealing can largely recover this part of the reduction.

The obtained thermal diffusivity data were used to calculate thermal conductivity  $\lambda$  ( $\text{Wm}^{-1}\text{K}^{-1}$ ) of irradiated tungsten. The following relationship was used, where  $\alpha$  ( $\text{m}^2/\text{s}$ ) is the measured thermal diffusivity,  $\rho$  ( $\text{kg}/\text{m}^3$ ) the mass density, and  $C_p$  ( $\text{Jkg}^{-1}\text{K}^{-1}$ ) the specific heat.

$$\lambda = \alpha \times \rho \times C_p \quad (7)$$

Unfortunately, as experimental data on the density and specific heat capacity of irradiated tungsten is not available, thermal conductivity was calculated assuming that neither property is significantly changed by irradiation. The assumption regarding the density is partly justified by the TEM study made by Horvath et al. [67], which showed no signs of irradiation induced swelling. In addition, neutron irradiation induced swelling in tungsten has been reported to reach less than 0.22 vol% at a temperature of 430 °C [79]. Using unirradiated tungsten density data to calculate the thermal conductivity of the irradiated tungsten is therefore not expected to cause any significant errors. Specific heat capacity of tungsten irradiated by neutrons to doses of 0.2 and 0.6 dpa, was measured by Roedig et al. [80] using a differential scanning calorimeter. The publication mentions a change in the specific heat capacity with irradiation, but does not present the data nor specify the magnitude of this change. It is however mentioned that the decrease of thermal

diffusivity is relatively more distinct and has a larger contribution to the total irradiation induced degradation of thermal conductivity.

Density data of unirradiated tungsten were taken from Hurd et al. [81] and adjusted to the 1% porosity of the specimens. The specific heat capacity data were taken from Lee et al [82]. These and other reference data are presented in table 9.

**Table 9 Reference data for unirradiated tungsten**

<b>Temp.</b> (°C)	<b>Density</b> [81] (g/cm <sup>3</sup> )	<b>Spec. heat capacity</b> [82] (J·kg <sup>-1</sup> ·K <sup>-1</sup> )	<b>Ther. diffusivity</b> [77] (mm <sup>2</sup> /s)	<b>Ther. conductivity</b> [82] (W·m <sup>-1</sup> ·K <sup>-1</sup> )
25	19.297	129.13	69.8	172.29
100	19.279	131.56	64.3	164.75
200	19.254	134.74	57.9	155.53
300	19.229	137.85	52.8	147.21
400	19.204	140.89	49.4	139.76
500	19.178	143.86	46.7	133.11

The calculated thermal conductivity of the irradiated tungsten based on reference data for density and specific heat capacity of pure unirradiated tungsten is summarised in table 10.

**Table 10 Thermal conductivity of irradiated tungsten**

Thermal conductivity (Wm <sup>-1</sup> K <sup>-1</sup> )				
Temp. (°C)	Unirr.	3.9 dpa	5.8 dpa	3.9 dpa - Annealed
25	173	84	86	115
100	162	87	88	-
200	148	90	88	-
300	138	90	91	113
400	133	91	94	-
500	128	93	95	111

## 5.4 Mechanical properties of irradiated tungsten

### Paper V

This section presents results obtained in the study of the mechanical properties of irradiated tungsten. The work is based on 3-point bend tests and microhardness measurements of unalloyed tungsten material irradiated in a target of SINQ at PSI. Data obtained from the 3-point bend tests were converted into engineering stresses and strains and plotted in the diagram shown in figure 41. The results are grouped according to the testing temperature, where the distance of each section on the x-axis corresponds to a total strain of 5%. Results from the unirradiated reference specimens are plotted in black, while the coloured curves represent specimens irradiated to different doses.

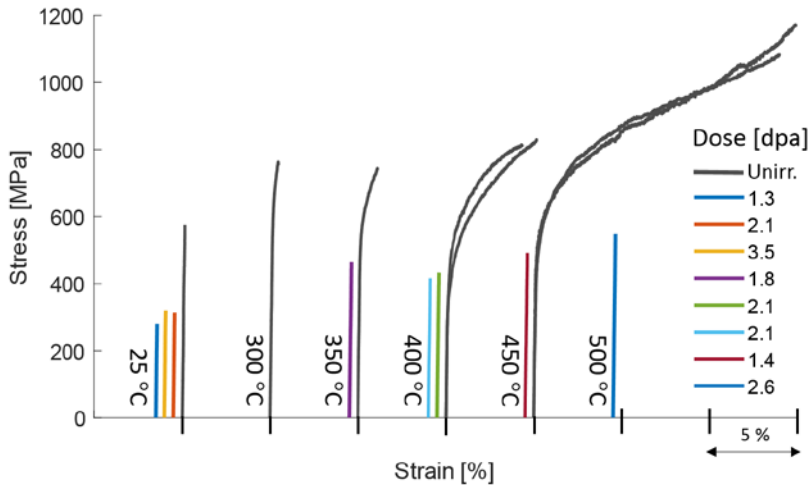


Figure 41 Results from 3-point bend tests.

The strain and fracture stress of the unirradiated tungsten increased with increasing temperature. At 25 °C, the specimen fractured already at 570 MPa in the elastic regime. The fracture stress for the specimen tested at

450 °C was 1171 MPa, which is more than double in comparison. The strain at this temperature was approximately 15%. The DBTT is around 350 °C.

The irradiated specimens on the other hand, do not show any ductility, regardless of testing temperature and irradiation dose. All irradiated specimens fractured in the elastic regime. Three irradiated specimens were tested at 25 °C, resulting in an average fracture stress of 304 MPa. The fracture behaviour among the three specimens does not seem to be significantly influenced by the difference in irradiation dose, which ranged from 1.3 to 3.5 dpa. Instead, the fracture stress increases with increasing temperature. At 500 °C, the 548 MPa fracture stress of a 2.6 dpa specimen, has nearly reached the fracture stress of unirradiated tungsten tested at room temperature. This implies that the tungsten used in the target of ESS, operated at maximum 500 °C, is most likely to have even less ductility and lower fracture stress than unirradiated pure tungsten at room temperature.

Specimens irradiated to doses of 1.3, 1.4, 2.1, and 3.5 dpa were used for hardness measurements. The results are compared to the 400 HV hardness of the unirradiated reference tungsten, and to similar data presented by Maloy et al. [83]. The comparison can be viewed in figure 42. The work done by Maloy et al. includes microhardness tests of pure tungsten irradiated by 800 MeV protons in the temperature range 50-160 °C, with a helium production of 50-320 appm. Their hardness is slightly lower in comparison.

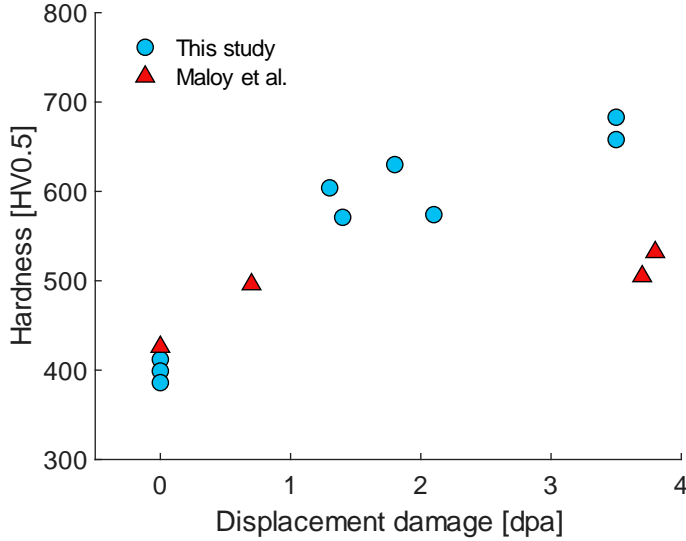


**Figure 42 Microhardness of irradiated tungsten.**

After the 3-point bend test, some of the fracture surfaces of the specimens were observed in an SEM. Figure 43 compares fractographs of two unirradiated specimens, tested at 25° and 450 °C, respectively. As expected, the specimen tested at the lower temperature (Fig. 43 a, c, e) does not show any sign of plasticity. The specimen tested at the higher temperature (Fig. 43 b, d, f), above the DBTT, displays a significant amount of plastic deformation. Numerous cracks and slip bands are seen in the side view (Fig. 43 d). This specimen fractured mainly in an intergranular mode (Fig. 43 f), while the 25 °C specimen fractured in a mixed trans- and intergranular mode (Fig. 43 e).

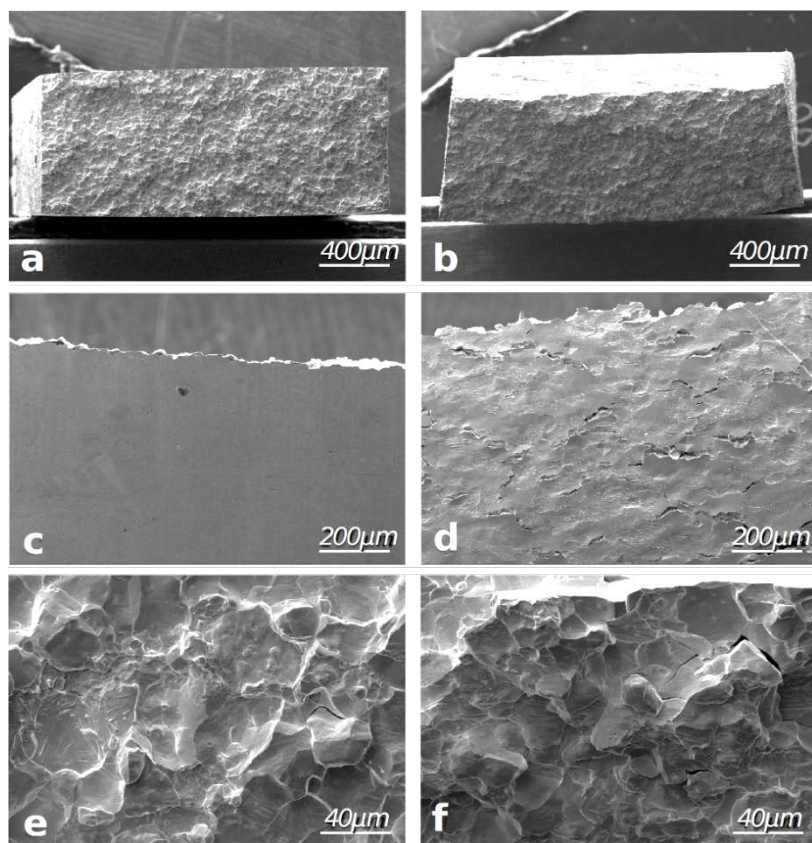


**Figure 43** SEM images of fracture surfaces of unirradiated tungsten, tested at 25 °C (a, c, e) and at 450 °C (b, d, f).

Fractographs of irradiated specimens are presented in figure 44. The figure shows two specimens with irradiation doses 1.3 and 3.5 dpa, tested at 25 °C. The fracture surface of the 1.3 dpa specimen (Fig. 44 a, c) is similar to that of the unirradiated specimen tested at the same temperature. It failed in a mixed fracture mode dominated by transgranular cleavage. The fracture surface is relatively smooth, compared to the surface of the high dose specimen (Fig.44 b, d), which has many small facets. The latter specimen also failed in a mixed trans- and intergranular fracture mode.

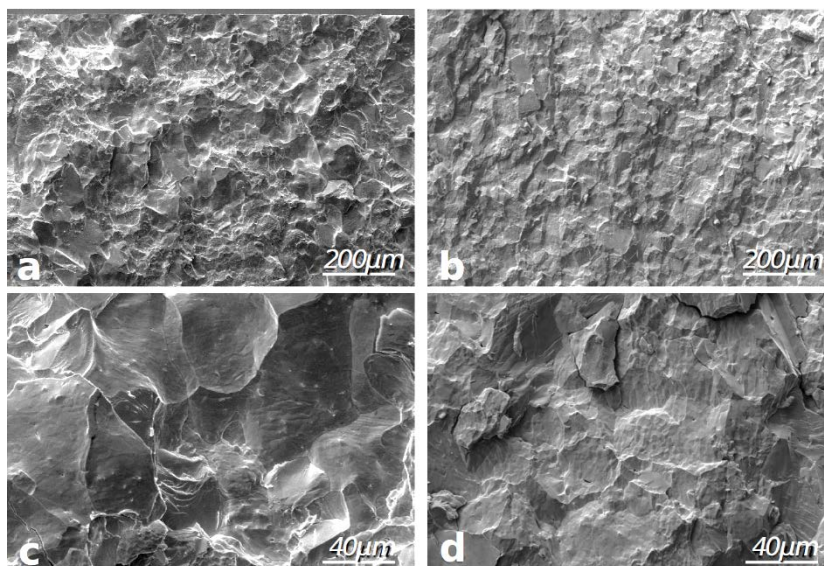


**Figure 44** Fractographs of specimens irradiated to 1.3 dpa (a, c) and 3.5 dpa (b, d), tested at 25 °C.

Figure 45 shows fractographs of irradiated specimens tested at elevated temperatures. Fig. 45 (a, c) presents the fracture surface of the 1.4 dpa specimen tested at 450 °C, and Fig. 45 (b, d) presents the 2.6 dpa specimen tested at 500 °C. Both surfaces look similar to the surface of the irradiated specimen tested at 25 °C. The fracture mode is mixed and there is no sign of ductility. There are however some differences. The 1.4 dpa specimen (a, c) exhibits numerous slip bands on the grains, and the 2.6 dpa specimen shows many tiny facets on the larger grains (d). The lower magnification SEM image of the 2.6 dpa specimen (b) gives the impression that the rather flat fracture surface is a result of a high degree of transgranular fracture mode. However, the higher magnification image (d) reveals an intergranular mode with many very small facets, as shown in the insert in the image. These are believed to be subgrains.



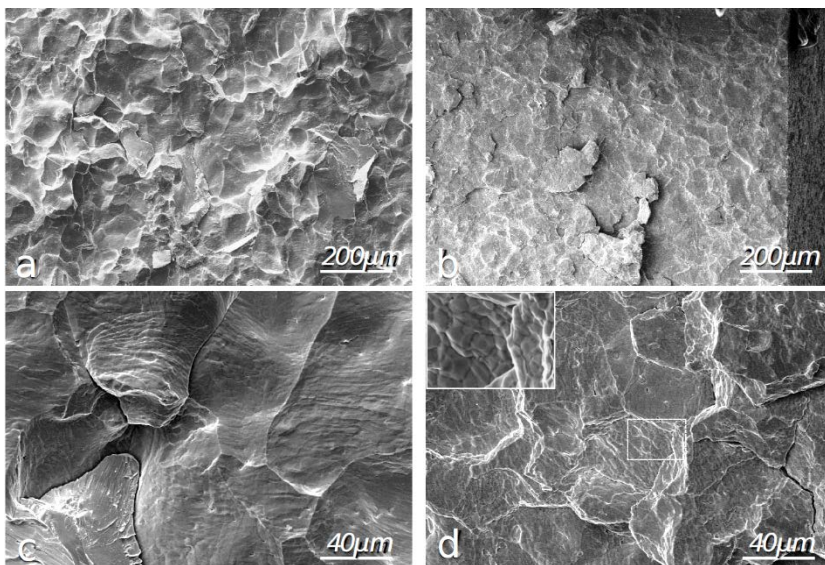


**Figure 45** Fractographs of specimens irradiated to 1.4 dpa and tested at 450 °C (a, c), and 3.5 dpa and tested at 500 °C (b, d).

## 5.5 Pulsed heavy ion irradiation

### Paper VI

In this study, pulsed heavy ion irradiation was used to observe the behaviour of tungsten under dynamic beam conditions. The specimens were irradiated at the M3-beamline of the UNILAC facility at GSI Helmholtz Centre for Heavy Ion Research, using gold and uranium ions. The effect of irradiation on the hardness and thermal diffusivity was determined and used as input data to simulate the changes of operational temperature and mechanical stress in the ESS target material.

### 5.5.1 Hardness measurements

Hardness was measured on the uranium irradiated 3 mm thick specimen using two different methods. First, microhardness was measured on the top surface, in- and outside the irradiated area. Auger electron spectroscopy was used to sputter away material in three areas. The depths of the three spots were 6, 9, and 12  $\mu\text{m}$ . Microhardness was subsequently measured in the spots with a Micro Combi Tester using a load of 500 g. The results are shown in figure 46, where the hardness is presented as horizontal bars according to the penetration depth of the indenter. Ten measurements were made at each depth.

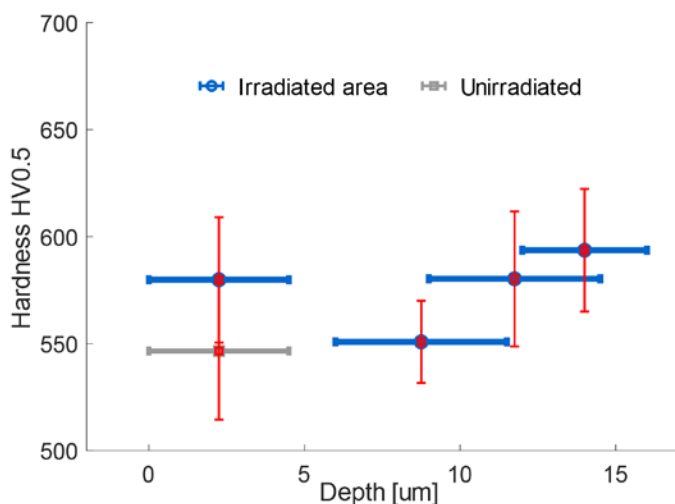


**Figure 46** Microhardness of uranium ion irradiated tungsten. Horizontal bars show the indentation, vertical bars represent the standard deviation.

After the microhardness tests, the specimen was sectioned and polished at an angle. A schematic illustration of the sectioning can be viewed in figure 47. The irradiation damaged zone was only around 20  $\mu\text{m}$  deep, which complicated the indenting along the cross-section. By polishing the specimen at an angle more data could be collected. This way,

nanohardness measurements could be made on the extended cross-section, giving the hardness as a function of depth and therefore, also as a function of irradiation damage.

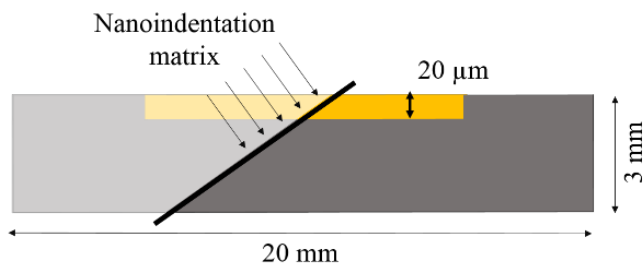


**Figure 47** Illustration showing the side view of the irradiated specimen. The yellow layer represents the irradiated area. Hardness measurements were performed on the plane marked with a black line.

Hardness was measured with a Berkovich nanoindenter, at depths 3.5 to 51.5 μm, using a load of 50 mN which resulted in a displacement of around 500 nm into the material. Eight rows of indentations were made, each containing ten measurements. The rows were placed at least 15 μm apart. The resulting hardness as a function of depth, can be seen in figure 48.

Both methods indicate irradiation induced hardening resulting from the uranium ion beam. It is also seen in both hardness graphs that the surface hardness is slightly higher compared to the hardness a few microns deeper into the material. This could perhaps be explained by the rolling procedure used during specimen manufacture. The deformation and thus also hardness, is greater in the outermost layers of the specimens. There could also be residual stresses in this top layer. Microhardness data also show a difference between the irradiated and non-irradiated top surface.

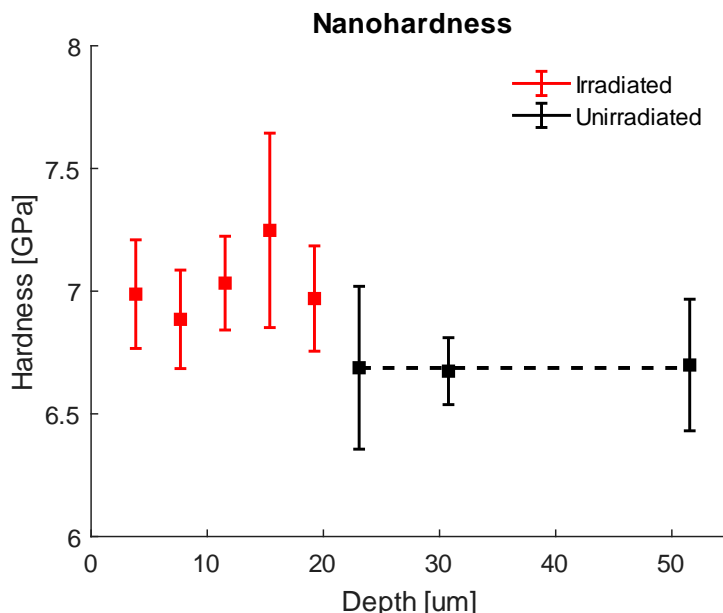


**Figure 48 Nanohardness over the cross-section of an irradiated specimen. The dotted line represents the average hardness at depths beyond the reach of the heavy ions.**

The microhardness on the surface increased from an average of 550 to approximately 580 HV0.5 due to irradiation. The nanoindentation measurements show a similar tendency of increasing hardness with increasing depth. The maximum nanohardness is at a depth which corresponds well to the calculated depth of the maximum ion irradiation damage. Data from the hardness measurements were used to estimate the stiffness of the material [84] in the irradiated zone. The irradiation induced stiffness increase was estimated to approximately 15%.

### 5.5.2 Dynamic response and fatigue

Irradiation of the 26  $\mu\text{m}$  thin specimen with the pulsed uranium beam induced vibrations in the specimen. An attempt was made to model these vibrations in ANSYS. Due to limitations of computational power the specimen was modelled as a quarter of a symmetric disk, therefore, no non-symmetric vibration modes were resolved. The time step of the dynamic simulation was set to 5  $\mu\text{s}$ , which suppressed vibration modes with frequencies higher than 200 kHz. Figure 49 shows the calculated maximum and minimum principal stresses at the centre of the specimen, resulting from a 150  $\mu\text{s}$  long beam pulse with a uranium ion intensity of  $7.5 \times 10^9$  ions/ $\text{cm}^2$ /pulse. Figure 50 displays a snapshot of the von Mises stress in the specimen 2.245 ms after the start of the beam pulse.

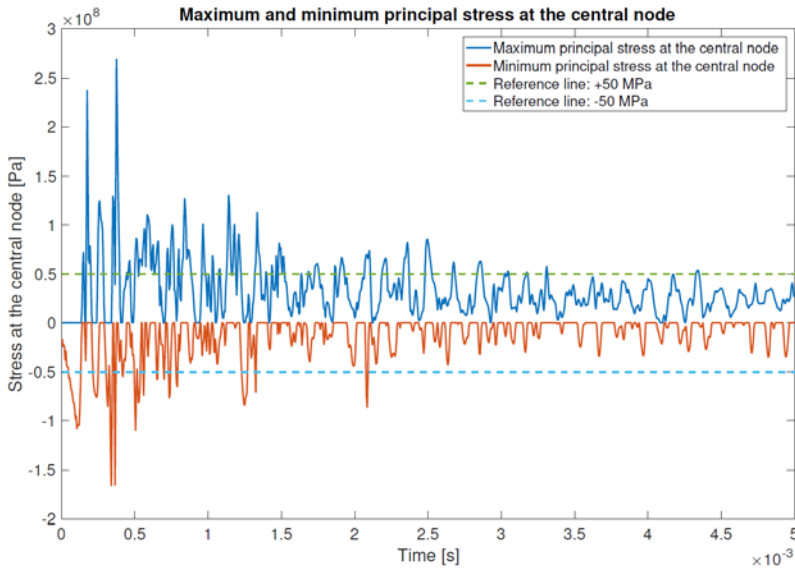


**Figure 49** Calculated stress at the centre of the irradiated specimen after a 150  $\mu\text{s}$  long beam pulse with the intensity  $7.5 \times 10^9$  ions/ $\text{cm}^2$ /pulse.

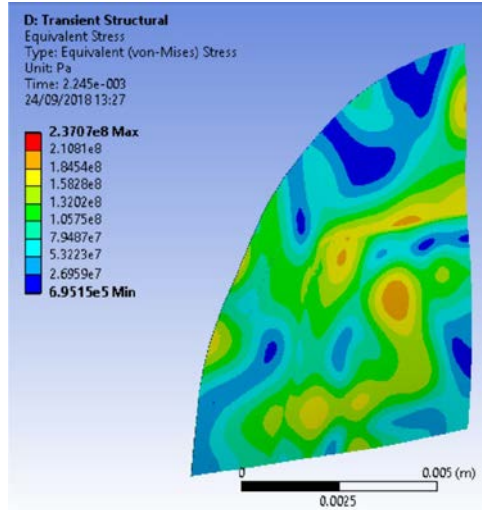


**Figure 50** Snapshot of the specimen at 2.245 ms after the start of a 150  $\mu\text{s}$  long beam pulse. Shown here is the maximum and minimum von Mises

The initial plan was to compare the experimental results obtained during the irradiation using a laser doppler vibrometer (LDV), to the results obtained from the simulation. Unfortunately, due to the relatively rough surface of the specimen and an insufficient data collection frequency, the experimental data could not be used for comparison with the simulated data. Still, the LDV measurement gave useful information of the time scale of the stress wave damping after each pulse. In the beginning of the irradiation, at a fluence level of  $5 \times 10^{11}$  uranium ions/ $\text{cm}^2$ , the velocity amplitude of the vibration was damped after 5 ms. After some time, at the higher fluence of  $4 \times 10^{13}$  uranium ions/ $\text{cm}^2$ , there was no damping observed. A possible explanation for this behaviour is the gradual loosening of the specimen holder with progressive irradiation. In the beginning of the irradiation experiment, the specimen holder is still tightly fixed, and the stress wave induced by the beam pulse is damped by the surrounding structure. As the irradiation continues and fluence is accumulated, the vibrations from the beam pulse are assumed to loosen

the specimen holder which caused the stress wave to propagate solely within the specimen geometry, with its edge providing a virtual free vibration condition.

The vibration mode with a frequency of approximately 7 kHz provided the largest stress variation according to the simulation. Assuming an average stress wave damping time scale of 15 ms and a 7 kHz vibration frequency, the centre of the irradiated specimen experiences about 100 cycles per pulse with a stress variance of 100 MPa, as shown by the simulation. The irradiated specimen received a total of 10,000 pulses, which corresponds to  $1 \times 10^6$  fatigue cycles with a stress amplitude of 50 MPa. The specimen was observed in the SEM after the irradiation experiment and was found to be intact, which agrees with the fatigue data presented in this work.

### 5.5.3 Radiation damage and thermal diffusivity

Four tungsten specimens of 26  $\mu\text{m}$  thickness were irradiated with gold ions to fluences  $1 \times 10^{11}$ ,  $1 \times 10^{12}$ ,  $5 \times 10^{12}$ , and  $2 \times 10^{13}$  ions/ $\text{cm}^2$ , respectively. Thermal diffusivities of the specimens were measured at room temperature using a laser flash apparatus (LFA) and an in-plane specimen holder. A thin layer of graphite was applied on the surface of the specimens to increase and homogenise the amount of absorbed energy. The obtained results were compared to the thermal diffusivity of the unirradiated reference specimen. The data is plotted in figure 51. Up to a fluence of  $1 \times 10^{11}$  ions/ $\text{cm}^2$ , no change is seen in thermal diffusivity. As the fluence increases, the relative thermal diffusivity decreases. The highest fluence resulted in a lowering of thermal diffusivity by approximately 12%, relative to the unirradiated tungsten.

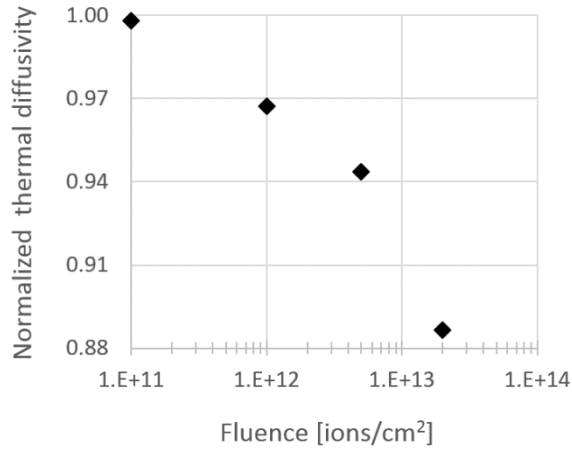


**Figure 51 Relative change in thermal diffusivity of tungsten as a function of fluence.**

#### 5.5.4 Oxide layer and the pulsed beam

A pre-oxidised tungsten specimen was irradiated to study the tungsten oxide adhesion under a pulsed beam. An image of this specimen after irradiation is seen in figure 52. The specimen was oxidised at 500 °C in air prior to the experiment, leading to the formation of tungsten oxides with varying stoichiometries, ranging from  $\text{WO}_2$  at the metal-oxide interface to  $\text{WO}_3$  at the surface. The former oxide is thin, adherent, and dark, while the latter is porous, thick, and yellow. After the irradiation with the pulsed ion beam, there is a clear mark in the centre of the specimen, corresponding to the shape and size of the beam spot. The colour shift indicates a removal of the outermost oxide layer, exposing the more adherent oxide underneath.



Before the irradiation, the surface of the oxidised specimen was examined using SEM. The entire area in the centre of the specimen was observed. After the irradiation, images in the same positions were taken for comparison. They revealed a very damaged oxide layer, as seen in figure 53, containing before and after images. The images show large flakes of oxide which appear to have been blown off due to the pulsed beam.

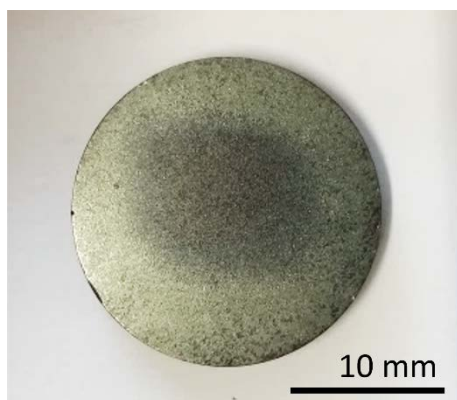


**Figure 52 Oxidised tungsten. The darker area appeared after irradiation and corresponds to the shape and size of the beam spot.**

The specimen was further studied with AES. Argon ion sputtering was used to characterise the remaining oxide scale in the irradiated area. The thickness of the scale was estimated by depth profiling. The depth of the oxide in the unirradiated area of the specimen was estimated to 2.4  $\mu\text{m}$ , while the oxide thickness in the centre of the beam spot was approximately 1.3  $\mu\text{m}$ . This indicates that more than 1  $\mu\text{m}$  of the oxide scale was removed by the pulsed beam. Results from the elemental analysis and the depth profile can be found in the attached Paper VI.

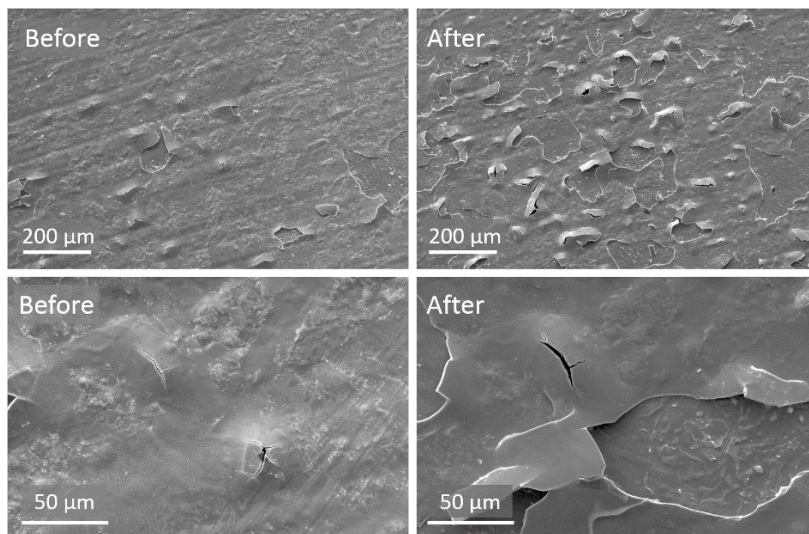


**Figure 53 SEM images of the oxidised specimen before and after irradiation.**

### 5.5.5 Implications of the results on the ESS target

Heat deposition calculations using FLUKA were made together with coupled flow, thermal and structural simulations using ANSYS Workbench. The results were used to assess the impact of the observed radiation induced material hardening and thermal diffusivity degradation on the operational conditions of the ESS target. The heat deposition calculations were made using a full model. These data were used as an input in the ANSYS simulations, which were made on a smaller scale model representing only a quarter radial fraction of a middle section of one segment of the target. The ANSYS model is shown in figure 54, together with the beam profile on target, which was used for the heat deposition calculations.

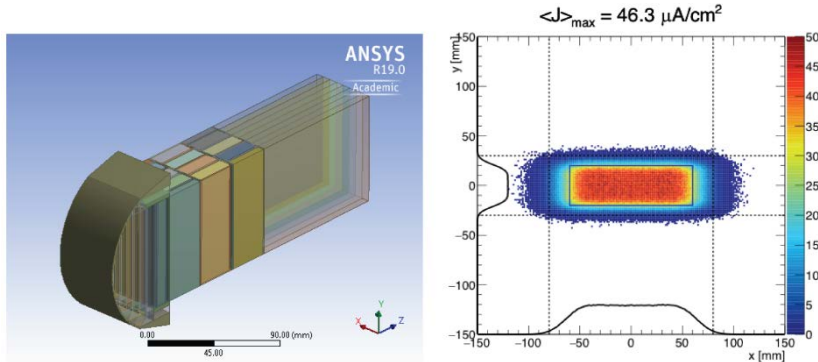


**Figure 54** Model representing the middle section of an ESS target segment (left) and the beam profile used for heat deposition calculations (right).

The mass flux of the helium coolant is adjusted correspondingly. The flux for this model becomes 19.79 g/s, with an inlet temperature of 400 K. The heat exchange between the tungsten and the helium is calculated using a shear stress transport model and a fine boundary layer mesh resolution. A steady state simulation is solved first, and subsequently used as the initial condition for the transient simulation of eight beam pulses. Several scenarios with varying conditions were simulated. These include a tungsten brick at the start of irradiation, i.e. data for unirradiated tungsten were used, an irradiated tungsten brick with a 20% reduction in thermal conductivity, and an irradiated tungsten brick with a 20% increase in stiffness as well as a 20% decrease in thermal conductivity. The increase stiffness is based on the hardness measurements performed on the ion irradiated 3 mm thick specimen. The estimated increase in stiffness was 15%, but a higher value of 20% was used in the simulations to obtain more conservative results.

Figure 55 shows the maximum temperature for one the bricks in the model, using material data for unirradiated tungsten and material data which was adjusted to account for an estimated 20% decrease in thermal conductivity. The 12% decrease in thermal diffusivity of the ion

irradiated tungsten in this work was measured in a specimen irradiated to 0.06 dpa, which is much lower than what is expected at ESS. Therefore, a more realistic value for ESS of 20% was used instead.

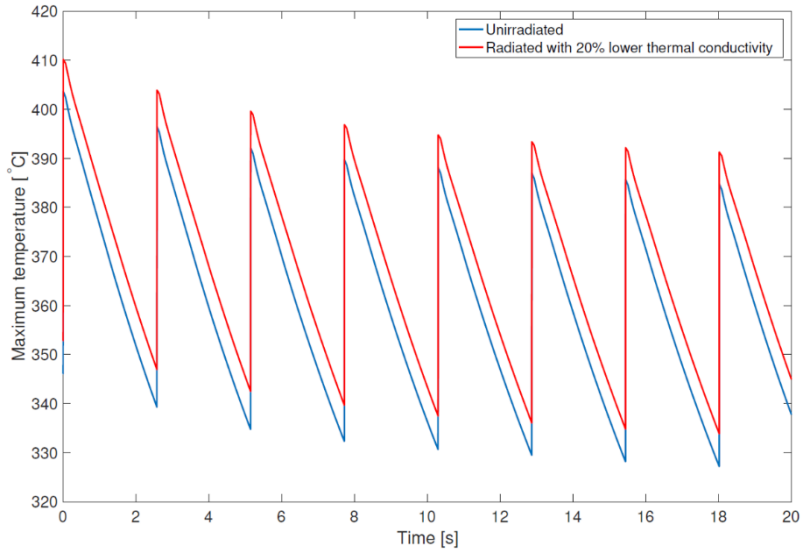


**Figure 55** Calculated maximum temperatures in a brick. Comparison between unirradiated and irradiated tungsten with 20% lower thermal conductivity.

The combined effects of radiation induced degradation of thermal and mechanical properties, as observed in this study, were simulated in quasi-static structural analyses. Cases were set up around the time just before (pre-pulse) and immediately after (post-pulse) the eighth pulse. Material data for the unirradiated tungsten brick was collected from the ESS Materials Handbook [82]. Materials data for the irradiated tungsten brick was adjusted with a 20% increase in stiffness and a 20% decrease in thermal conductivity. The results of the simulation are summarised in table 11.

According to the simulation, the irradiation induced increase in temperature is about 8 °C. The increase in maximum stress is however more significant. The combination of higher stiffness and lower thermal conductivity could cause an increase of maximum thermal stress of more than 20%, which could be an issue since the tungsten is expected to remain completely brittle due to the irradiation. A study on irradiated tungsten showed that the tensile stress of a 2 dpa specimen was 150 MPa [85], which is close, but still above the expected thermal stress in the irradiated ESS tungsten. Nevertheless, brittle tungsten is known to show largely scattered statistics, and with nearly 7000 bricks of tungsten in the ESS target, there is a risk of failure for at least some of these bricks.

**Table 11 Radiation damage effect on operational temperature and maximum von Mises stress in an ESS tungsten brick.**

	Time	Max. temp [°C]	Max. stress [MPa]
Unirradiated	Pre-pulse	321.3	26.6
	Post-pulse	395.4	82.7
	Difference	74.1	56.1
Irradiated	Pre-pulse	329.3	40.7
	Post-pulse	403.2	107.9
	Difference	73.9	67.2

## 6. Conclusions

Summaries and main conclusions from the different studies are presented in this chapter. The sections are arranged as in previous chapters with conclusions from studies performed on unirradiated tungsten first, i.e. the fatigue and oxidation projects, followed by conclusions from studies on irradiated tungsten, i.e. the thermal diffusivity, mechanical properties, and heavy ion irradiation works. Lastly, recommendations for future work are given.

### 6.1 Fatigue

Various types of unalloyed unirradiated tungsten specimens were used in the fatigue and tensile property studies. These included forged, rolled, and HIPed specimens, polished and unpolished surfaces, stress- and strain-controlled testing, and testing in ambient and elevated temperatures. For nearly all types of tungsten specimens, the resulting data showed wide scatter. This is in part attributed to the brittle nature of tungsten, but even more so the differences in surface condition, volume fraction porosity, grain orientation, and specimen production technique.

All specimens failed in a brittle manner when tested at room temperature. Majority of the specimens did not show any sign of plastic deformation on the fracture surfaces. The fatigue properties were slightly improved at 280 °C and most of the specimens were observed to be in the ductile regime. At 480 °C, the specimens behaved even more ductile. In general, the rolled specimens showed higher endurance limits, higher density, and higher average hardness compared to the forged specimens. The rolled specimens were however, highly anisotropic. Specimens oriented across the rolling direction were of significantly lower quality. RLP specimens, i.e. rolled, oriented in the rolling direction and polished, showed the best fatigue properties. The endurance limits were 237.5 MPa at 25 °C and 252.5 MPa at 280 °C. The lowest endurance limit, 125.6 MPa, belonged to the polished forged specimen type.

The UTS values of the rolled and forged specimens from Tian-Long were in the range 397-705 MPa, at room temperature. These values are relatively low compared to UTS values of tungsten reported in other studies, but it could be explained by the differences in size and quality of the specimens. As a brittle powder metallurgy product, tungsten is extremely notch sensitive. When it comes to tungsten in general, the smaller the test specimen, the lower is the probability of failure. For comparison, Foster and Stein [86] reported UTS values of 793-1630 MPa, using specimens of 0.5 mm thickness with a gauge less than 10 mm wide. In the present work, room temperature elongation of the specimens oriented in the rolling direction was in the range 0.11-0.21%, while a value of 1.5% was reported in a study of ultrafine-grained tungsten. The specimen size was however not mentioned [87].

The scarcity of fatigue data on pure tungsten makes it difficult to compare the obtained results to those of other studies. The most relevant study to date, was published by Schmunk et al. [39] in 1981. In their work, tensile

and low-cycle fatigue tests were performed on cross-rolled tungsten at room temperature and at 815 °C. The room temperature fatigue experiments were run under fully reversed load control at 1 Hz. Two tests were terminated after 500 000 cycles without failure, in the stress ranges  $\pm 206.8$  MPa and  $\pm 275.7$  MPa, respectively. In comparison, the tests in the present work were terminated after 2 million cycles and loaded only in tension.

The second fatigue study in the present work, benefited from experience gained during the first. The surfaces of the specimens had relatively fewer visible defects, and the study could focus on testing only the best type of rolled specimens. In the second fatigue study, fatigue and tensile response of rolled and annealed (RA) tungsten was compared to sintered and HIPed (SH). The tests were performed at room temperature and the specimens were manufactured by Plansee.

Once again, rolled tungsten proved to have superior fatigue properties while simultaneously displaying a highly brittle behaviour and strong anisotropy. The RA tungsten used in the second fatigue study was characterised by very large, elongated and interlocking grains of 1 mm length with an approximate width to length ratio of 1:10. The ultimate tensile strength was nearly 1000 MPa, and the mean fatigue strength 371 MPa. The grains of the SH specimens were on average 30  $\mu\text{m}$ . The material was characterised by a relatively large fraction of porosity (4.3%) and slightly higher ductility as compared to the RA specimens. The average ultimate tensile strength was 567 MPa, and the mean fatigue strength 185 MPa. Further, SH specimens were softer (389 VHN) than the RA specimens (508 VHN) and displayed cyclic hardening in the strain-controlled tests.

To summarise, rolled tungsten shows far better fatigue properties, surviving much higher stress amplitudes than both the forged and the



HIPed tungsten. It is extremely important to make sure that the surface is of high quality with a minimum of defects and machining marks. Rolled tungsten has nearly zero room temperature ductility and is highly anisotropic, which means that the orientation of the ESS bricks with respect to the proton beam need to be carefully considered. The recommendation to ESS is to use cross rolled tungsten with a maximum surface roughness of 10  $\mu\text{m}$ . The post-pulse maximum stress should be below 100 MPa, and the post-pulse peak stress amplitude should be lower than 50 MPa, which is one third of the fatigue stress amplitude for the Tian-Long rolled tungsten at room temperature.

## 6.2 Oxidation

This study focused on the oxidation behaviour of unirradiated tungsten in inert gas atmospheres with small amounts of oxygen and water vapour. The temperature range of 400-900 °C was chosen to reflect both normal operation of the ESS target as well as potential off-normal situations such as e.g. overheating caused by an over-focused proton beam. The gas mixtures were chosen with the same intention. The commercially pure inert gases contained oxygen impurities of maximum 5 ppm, which turned out to be enough to oxidise tungsten at temperatures similar to the normal operation temperature of the target. Some of the tests were performed with slightly higher oxygen partial pressures. 5% oxygen was added to the helium gas, which could represent an incident of a leakage in the helium loop or air ingress into the target vessel.

The oxidation experiments were monitored using TGA and STA-DSC. The experiments where only pure inert gas was used were performed in the latter setup, using small tungsten foil specimens. In argon gas with max. 5 ppm oxygen, a very thin and adherent oxide layer was observed

already at 500 °C. XRD analysis of the surface confirmed the presence of  $W_{18}O_{49}$ . Analysis of specimens oxidised in air suggest that a transition from the  $W_{18}O_{49}$  oxide to  $WO_3$  occurred between 500° and 600 °C. EDS studies on one of the thicker oxide scales (He-Ar- $H_2O$ , 700 °C) showed the presence of a range of oxides, varying in stoichiometry between  $WO_2$  to  $WO_3$ . The non-isothermal in situ experiments performed in a hot stage inside an ESEM at a water vapour pressure of 100 Pa, showed that oxidation becomes noticeable above 600 °C. Isothermal TGA experiments with two different gas atmospheres, He-0.5% $O_2$  and Ar-He- $H_2O$ , showed that the oxidation rate is relatively low below 600 °C, but increases rapidly above this temperature. AES was used to measure the oxide scale thickness of some He-Ar- $H_2O$  specimens. Between 415 °C and 619 °C, the thickness increased approximately by a factor of ten with each 100 °C increase in temperature.

The implication of these results is that the temperature of the tungsten in the ESS target is recommended to be kept below 500 °C under normal operation conditions. It is not feasible to aim at completely avoiding oxidation, but it is important to note that tungsten does oxidise at this temperature even in an environment of inert gas. It is very important to monitor the impurity levels of oxygen and water vapour during operation, as well as designing a top-quality purification system for the helium loop. If the temperature in the tungsten can be kept below 500 °C there is a possibility that the oxide formed will consist of mainly the thin and adherent oxide type. Temperatures and environments where the tungsten oxide transforms into the porous type must be avoided. The risk of erosion of the oxide scale, caused by the helium gas flowing at 2.85 kg/s at 1 MPa, will increase significantly if the oxide type changes from the protective to the porous one. There is also a concern that the beam pulse and beam trip induced thermal cycling will lead to spalling of the oxide

layer. To minimise such risks, it is important to design the target so that the temperature in the tungsten is kept as low as reasonably possible.

## 6.3 Thermal diffusivity

Thermal diffusivity of proton and spallation neutron irradiated tungsten was measured in the temperature range 25-500 °C. The specimens were irradiated at PSI in the SINQ facility, to displacement damage doses of 3.9 and 5.8 dpa. Thermal diffusivity of both irradiated specimens was approximately 35 mm<sup>2</sup>/s, independent of irradiation dose and test temperature. This value is 51% lower than the thermal diffusivity of the unirradiated reference specimen tested at 25 °C, and 28% lower compared to the value at 500 °C.

The irradiation induced decrease in thermal diffusivity is attributed to a combination of displacement damage and compositional changes due to transmutations. Both specimens showed similar thermal diffusivity values despite being irradiated to two different doses. This implies that the rhenium content, which is expected to be similar in both specimens, is responsible for the main contribution of the degradation. This theory is strengthened by studies on thermal diffusivity of unirradiated tungsten-rhenium alloys in which even minor rhenium additions causes a significant decrease of thermal diffusivity.

To investigate this further, the irradiated tungsten was annealed at 1000 °C for 1h and remeasured. The heat treatment should have caused partial recovery of the irradiation induced displacement damage. The test results showed that the thermal diffusivity did increase after the annealing. At 25 °C it was 47 mm<sup>2</sup>/s, and at 500 °C it was 41 mm<sup>2</sup>/s, which is an increase by 37% and 19%, respectively.

## 6.4 Mechanical properties

Cross rolled, commercially pure tungsten was irradiated in SINQ Target 7 at PSI, Switzerland, during the period 2007-2008. The irradiation was part of STIP-V (SINQ Target Irradiation Program), where specimens are placed in the spallation target for irradiation experiments. The tungsten material was exposed to high-energy protons and spallation neutrons causing a displacement damage in the range of 1.3-28 dpa, and a production of helium as transmutation product in the range of 37-1300 appm. Nearly a decade later many of the high dose specimens were still too radioactive for manual handling, therefore only a few of the lowest dose specimens have been tested so far. In this study, specimen with irradiation doses of 1.3-3.5 dpa were examined. The fracture behaviour of the irradiated specimens was investigated with 3-point bend tests at temperatures 25-500 °C. In addition, irradiation induced hardness was studied, and the fracture surfaces of the tested specimens were observed with an SEM. The results showed that all irradiated specimens, regardless of irradiation dose and test temperature, fail in the elastic regime. The tungsten has virtually zero ductility and fails at stress levels much below those of the unirradiated reference specimens. The hardness measurements demonstrate a strong irradiation induced hardening effect in all specimens.

Unirradiated and low dose specimens (1.3-1.4 dpa) fail in a mixed trans- and intergranular mode. The intergranular fracture mode becomes more dominant at higher temperatures. At 450 °C, both the unirradiated specimen and the 1.4 dpa specimen display a fracture surface with slip bands visible on the grain surfaces, which indicated some amount of plastic deformation taking place inside the grain. Specimens irradiated to higher doses, 2.6 and 3.5 dpa, exhibit a rather flat fracture surface, which indicates a very brittle cleavage fracture, with the crack propagating in a

transgranular mode. However, fractographs of higher magnification revealed tiny facets in the grains, which were determined to be a substructure with small grains. Similar facets were found in other tungsten specimens, and EBSD analysis of their fracture surfaces demonstrated that this structure consists of 0.5-2  $\mu\text{m}$  sized grains with grain boundaries angles of more than  $10^\circ$ . This implies that the fracture of the 2.6 and 3.5 dpa specimens was caused by crack propagation along the subgrain boundaries, i.e. through the intergranular fracture mode.

The results from this study also show that high-energy proton and spallation neutron irradiated specimens, tested at temperatures similar to the operating temperature of the ESS target, fail at fracture stresses above 200 MPa. This is higher than the expected stress of 44-110 MPa in the ESS tungsten, but as tungsten is known to be brittle, with highly scattered fatigue data, there is still a risk of failure of some of the 7000 bricks in the ESS target.

## 6.5 Modelling the thermal stress

Pure tungsten specimens of diameter 20 mm and thicknesses 3 mm or 26  $\mu\text{m}$ , were irradiated with a pulsed beam of gold or uranium ions with energies of 4.8 MeV/nucleon. The beam pulse induced stress in the specimen reached 122 MPa in the thick one and 270 MPa in the thin one. The values are comparable to the expected maximum stress of 83 MPa in the ESS target material. The thin specimen was fatigue tested using the pulsed beam. The specimen was tested up to approximately 10 000 pulses, which corresponds to roughly  $1 \times 10^6$  cycles with a stress amplitude of about 50 MPa. The specimen did not show any signs of fatigue.

Irradiation induced increase in hardness and decrease in thermal diffusivity was confirmed by micro- and nanohardness measurements as well as thermal diffusivity tests using an LFA. The data were used in coupled flow, thermal and mechanical simulations of the maximum temperature and stress in the ESS tungsten brick after irradiation. The calculated results for an irradiated tungsten brick show an increase of more than 20% of the maximum thermal stress, which is above the maximum stress design value of 100 MPa. In fact, the simulated maximum stress of 108 MPa is close to the reported UTS of irradiated tungsten [85].

Lastly, this work involved studies on the oxide adhesion under a pulsed beam. SEM imaging and AES characterisation of the oxide scale confirmed loss of more than 1  $\mu\text{m}$  thickness in the irradiated region. The scale was considerably damaged. The implication is that the oxide scale formed during the operation of the target will eventually be released into the helium cooling loop. Therefore, the design of the target cooling loop purification system at ESS assumes the complete loss of oxide layer on the tungsten bricks during operation [81].

## 6.6 Future work

The mechanism behind irradiation induced degradation of thermal diffusivity in tungsten is still not fully understood. There is a need for further testing of tungsten specimens with a wider range of transmutation production rates and displacement damages. Characterisation of the changes in microstructure, before and after irradiation and subsequent annealing studies would lead to a better understanding of the phenomenon. Another important factor is the effect of temperature and it would be valuable to collect data at higher temperatures as well and identify the contributions to thermal conductivity from electron and phonon transport. It would be interesting to study the formation,

transformation, and decay of the many radionuclides formed as transmutation products. As even small amounts of rhenium affect the properties of tungsten significantly, there is a need to determine the fraction of rhenium in the irradiated tungsten used in the present work, more precisely. An attempt was made to study the role of transmutation elements rhenium, osmium, and tantalum in the PSI proton irradiated tungsten, by using extended X-ray absorption fine structure (EXAFS) spectroscopy in combination with microprobe analysis. The experiment was performed at the MicroXAS beamline of the Swiss Light Source (SLS at PSI) and its purpose was to determine the clustering behaviour and local structure of the transmutation elements in irradiated tungsten. The analysis of the work is still ongoing, and the results are therefore not included in this thesis.

# References

- [1] E. Lassner, W-D. Schubert, *Tungsten properties, chemistry, technology of the element, alloys, and chemical compounds*, New York: Kluwer Academic/Plenum Publishers, 1999.
- [2] The mineralogy of tungsten, Hudson Institute of Mineralogy, online source, available at <https://www.mindat.org/element/Tungsten>, accessed 31-July-2018.
- [3] D. R. Lide, ed., CRC Handbook of Chemistry and Physics, 90<sup>th</sup> Edition (Internet version 2010), CRC Press/Taylor and Francis, Boca Raton, FL.
- [4] J. B. Lambert, J. J. Rausch, Refractory Metals and Alloys, ASM Handbook, 10<sup>th</sup> edition, vol. 2, Metals Handbook, American Society for Metals, Metals Park, Ohio, pp. 557-565, 2012.
- [5] B. Lux, B. Zeiler, Production of Refractory Metal Powders – Production of Tungsten and Tungsten Carbide Powders, ASM Handbook, 10<sup>th</sup> edition, vol. 7, Metals Handbook, American Society for Metals, Metals Park, Ohio, pp.188-196, 2011.
- [6] J. J. Conway, F. J. Rizzo, Hot Isostatic Pressing of Metal Powders, ASM Handbook, 10<sup>th</sup> edition, vol. 7, Metals Handbook, American Society for Metals, Metals Park, Ohio, pp. 605-607, 2011.
- [7] H. A. Kuhn, Forging and Hot Pressing, ASM Handbook, 10<sup>th</sup> edition, vol. 7, Metals Handbook, American Society for Metals, Metals Park, Ohio, pp. 633-637, 2011.



- [8] M. G. Andrews, *Tungsten, the story of an indispensable metal*, The tungsten institute, 1757 K Street, N. W., Washington, D. C., 1955.
- [9] V. Y. Ivanov, Y. P. Nechiporenko, L. N. Yefimenko, M. I. Yurchenko, High temperature oxidation protection of tungsten (NASA Technical Translation), National Aeronautics and Space Administration, Washington, D. C., 1096.
- [10] The European Spallation Source, Mission Statement, online source, available at <https://europeanspallationsource.se/about>, accessed: 4-August-2018.
- [11] D. Richter, T. Springer, A twenty years forward look at the neutron scattering facilities in the OECD countries and Russia, Technical report, European Science Foundation, Organisation for the Economic Co-operation and Development, Megascience forum, 1998.
- [12] R. Garoby et al. The European Spallation Source design, Phys. Scr. 93 (014001) (2018) 1-121.
- [13] R. Pynn and L. Liang et al. (eds.), Neutron Applications in Earth, Energy and Environmental Sciences – Neutron Scattering Applications and Techniques, Chapter 2: Neutron Scattering – A Non-destructive Microscope for Seeing Inside Matter, Springer Science+Business Media, 2009.
- [14] D. A. McClintock, B. J. Vevera, B. W. Riemer, F. X. Gallmeier, J. W. Hyres, P. D. Ferguson, Post-irradiation tensile properties of the first and second operational target modules at the Spallation Neutron Source, J. Nucl. Mater. 450 (2014) 130-140.

- [15] L. Heilbronn, Neutron properties and definitions, online source, posted 2015-09-07, available at [https://three.jsc.nasa.gov/articles/heilbronn\\_neutron\\_supplement.pdf](https://three.jsc.nasa.gov/articles/heilbronn_neutron_supplement.pdf), accessed 2018-08-30.
- [16] G. S. Was, Fundamentals of Radiation Materials Science – Metals and Alloys, ISBN 978-3-540-49471-3, Springer-Verlag Berlin Heidelberg, 2007.
- [17] ITER Divertor, online source, available at <https://www.iter.org/mach/divertor>, accessed 12-July-2018.
- [18] O. El-Atwani, M. Efe, B. Heim, J. P. Allain, Surface damage in ultrafine and multimodal grained tungsten materials induced by low energy helium irradiation, *J. Nucl. Mater.* 434 (2013) 170-177.
- [19] R. A. Pitts, S. Carpentier, F. Escourbiac, T. Hirai, V. Komarov, S. Lisgo, A. S. Kukushkin, A. Loarte, M. Merola, A. Sashala Naik, R. Mitteau, M. Sugihara, B. Bazylev, P. C. Stangeby, A full tungsten divertor for ITER: Physics issues and design status, *J. Nucl. Mater.* 438 (2013) S48-S56.
- [20] T. Hirai, F. Escourbiac, V. Barabash, A. Durocher, A. Fedosov, L. Ferrand, T. Jokinen, V. Komarov, M. Merola, S. Carpentier-Chouchana, N. Arkhipov, V. Kuznetsov, A. Volodin, S. Suzuki, K. Ezato, Y. Seki, B. Riccardi, M. Bednarek, P. Gavila, Status of technology R&D for the ITER tungsten divertor monoblock, *J. Nucl. Mater.* 463 (2015) 1248-1251.
- [21] A. Hasegawa, T. Tanno, S. Nogami, M. Satou, Property change mechanism in tungsten under neutron irradiation in various reactors, *J. Nucl. Mater.* 417 (2011) 491-494.

- [22] M. Fujitsuka, B. Tschhiya, I. Mutoh, T. Tanabe, T. Shikama, Effect of neutron irradiation on thermal diffusivity of tungsten-rhenium alloys, *J. Nucl. Mater.* 283-287 (2000) 1148-1151.
- [23] S. Kajita, W. Sakaguchi, N. Ohno, N. Yoshida, T. Saeki, Formation process of tungsten nanostructure by the exposure to helium plasma under fusion relevant plasma conditions, *Nucl. Fusion* **49** 095005, 2009.
- [24] N. Yoshida, H. Iwakiri, K. Tokunaga, T. Baba, Impact of low energy helium irradiation on plasma facing metals, *J. Nucl. Mater.* 337-339 (2005) 946-950.
- [25] Q. Xu, N. Yoshida, T. Yoshiie, Accumulation of helium in tungsten irradiated by helium and neutrons, *J. Nucl. Mater.* 367-370, Part A, (2007) 806-811.
- [26] J. H. Evans, The role of implanted gas and lateral stress in blister formation mechanisms, *J. Nucl. Mater.* 76-77 (1978) 228-234.
- [27] I. Ahmad, J.P. Greene, E. F. Moore, S. Ghelberg, A. Ofan, M. Paul, W. Kutschera, Improved measurement of the  $^{44}\text{Ti}$  half-life from a 14-year long study, *Phys. Rev. C* **74** 065803, 2006.
- [28] J. Habainy, Y. Dai, Y. Lee, S. Iyengar, PIE program of STIP-V tungsten specimens for ESS target engineering, presented at the 6<sup>th</sup> High Power Targetry Workshop (HPTW), Oxford, April 2016.
- [29] P. Jung, Radiation effects in structural materials of spallation targets, *J. Nucl. Mater.* 301 (2002) 15-22.
- [30] A. De Backer, A. E. Sand, K. Nordlund, L. Luneville, D. Simone, S. L. Dudarev, Subcascade formation and defect cluster size scaling in high-energy collision events in metals, *EPL* **115** 26001, 2016.

- [31] R. Pampin, Tungsten transmutation and resonance self-shielding in PPCS models for the study of sigma-phase formation, EURATOM/UKAEA Fusion, UKAEA FUS 525, 2005.
- [32] A. S. Wronski, A. C. Chilton, The effects of temperature and pressurization on the tensile and compressive properties of polycrystalline cast tungsten, *Scr. Mater.* 3 (1969) 395-400.
- [33] F. F. Schmidt, H. R. Ogden, DMIC Report 191: The Engineering Properties of Tungsten and Tungsten Alloys, 1963.
- [34] D. Rupp, S. M. Weygand, Loading rate dependence of the fracture toughness of polycrystalline tungsten, *J. Nucl. Mater.* 417 (2011) 477-480.
- [35] V. Krsjak, S. H. Wei, S. Antusch, Y. Dai, Mechanical properties of tungsten in the transition temperature range, *J. Nucl. Mater.* 450 (2014) 81-87.
- [36] K. Farrell, A. C. Schaffhauser, J. O. Stiegler, *J. Less-Common Met.* 13 (1967) 141-155.
- [37] A. Giannattasio, S. G. Roberts, Strain-rate dependence of the brittle-to-ductile transition temperature in tungsten, *Philos. Mag.* 87 (2007) 2589-2598.
- [38] Y. Zhang, A. V. Ganeev, J. T. Wang, J. Q. Liu, I. V. Alexandrov, Observations on the ductile-to-brittle transition in ultrafine-grained tungsten of commercial purity, *Mater. Sci. Eng. A* 503 (2009) 37-40.
- [39] P. L. Raffo, Yielding and fracture in tungsten and tungsten-rhenium alloys, *J. Less-Common Met.* 17 (1969) 133-149.

- [40] H. Braun, K. Sedlatschek, On the influence of small additions of non-metals and metals on the sintering, working and the mechanical properties of tungsten, *J. Less-Common Met.* 2 (1960) 277-291.
- [41] R. E. Schmunk, G. E. Korth, Tensile and low-cycle fatigue measurements on cross-rolled tungsten, *J. Nucl. Mater.* 103-104 (1981) 943-948.
- [42] ASTM E8/E8M-13a, Standard Test Methods for Tension Testing of Metallic Materials, ASTM International, West Conshohocken, PA, 2013. [www.astm.org](http://www.astm.org).
- [43] R. Pollak, A. Palazotto, T. Nicholas, A simulation-based investigation of the staircase method for fatigue strength testing, *Mech. Mater.* 38 (2006) 1170-1181.
- [44] S-K. Lin, Y-L. Lee, M-W. Lu, Evaluation of the staircase and the accelerated test methods for fatigue limit distributions, *Int. J. Fatigue* 23 (2001) 75-83.
- [45] K. A. Brownlee, J. Hodges Jr., M. Rosenblatt, The up-and-down-method with small samples, *J. Am. Stat. Assoc.* 48 (1953) 262-277.
- [46] W. J. Dixon, A.M. Mood, A method for obtaining and analysing sensitivity data, *J. Am. Stat. Assoc.* 43 (1948) 109-126.
- [47] E. A. Gulbransen, W. S. Wysong, Thin oxide films on tungsten, *Met. Technol.* XIV (1947) 611-627.
- [48] G. A. Greene, C. C. Finfrock, Generation, transport, and deposition of tungsten-oxide aerosols at 1000 °C in flowing air/steam mixtures, *Exp. Therm. Fluid Sci.* 26 (2002) 917-929.

- [49] G. A. Greene, C. C. Finfrock, Vaporization of tungsten in flowing steam at high temperatures, *Exp. Therm. Fluid Sci.* 25 (2001) 87-99.
- [50] J. L. Sabourin, R. A. Yetter, High-temperature oxidation kinetics of tungsten-water reaction with hydrogen inhibition, *J. Propul. Power* 27 (2011) 1088-1096.
- [51] H. A. Wriedt, The O-W (Oxygen-Tungsten) system, *Bull. Alloy Phase Diagr.* 10 (1989) 368-384.
- [52] P. E. Blackburn, K. F. Andrew, E. A. Gulbransen, F. A. Brassart, Oxidation of tungsten and tungsten based alloys, WADC TR 59-575 Part II, Arlington, 1961.
- [53] J. P. Bonnet, J. Nowotny, M. Onillion, I. Sikora, Surface electrical properties of tungsten oxides in equilibrium with the gas phase, *Oxid. Met.* 13 (1979) 273-282.
- [54] A. Warren, A. Nylund, I. Olefjord, Oxidation of tungsten and tungsten carbide in dry and humid atmospheres, *Int. J. Refract. Met. Hard Mater.* 14 (1996) 345-353.
- [55] E. A. Kellett, S.E. Rogers, The structure of oxide layers on tungsten, *J. Electrochem. Soc.* 110 (196) 502-504.
- [56] N. Birks, G. H. Meier, F. S. Pettit, Introduction to the high-temperature oxidation of metals, second ed., Cambridge University Press, New York, 2006.
- [57] A. Mozalev, M. Bendova, F. Gispert-Guirado, Z. Pytlíček, E. Llobet, Metal-substrate-supported tungsten-oxide nanoarrays via porous-alumina-assisted anodization: from nanocolumns to nanocapsules and nanotubes, *J. Mater. Chem. A*, 4 (2016) 8219-8232.

- [58] J. Aguilar, L. Mena, M. Mancisidor, J. L. Martinez, Equipment Specification Document: Spallation Material, Report No. ESS-0058358, September 16, 2016.
- [59] T. Tanabe, C. Eamchotchawalit, C. Busabok, S. Taweethavorn, M. Fujitsuka, T. Shikama, Temperature dependence of thermal conductivity in W and W-Re alloys from 300 to 1000 K, *Mater. Lett.* 57 (2003) 2950-2953.
- [60] ANSYS, Inc., ANSYS® Academic Research Workbench, Release 19.0.
- [61] A. Ferrari, P. R. Sala, A. Fasso, J. Ranft, Fluka: a multi-particle transport code, Tech. Rep. CERN-2005-10, INFN/TC\_05/11, SLAC-R-773 (2005).
- [62] T. T. Böhlen, F. Cerutti, M. P. W. Chin, A. Fasso, A. Ferrari, P. G. Ortega, A. Mairani, P. R. Sala, G. Smirnov, V. Vlachoudis, The Fluka code: Developments and challenges for high energy and medical applications, *Nuclear Data Sheets* 120 (2014) 211-214.
- [63] SINQ Facility – Spallation Target, online source, available at <https://www.psi.ch/bsq/spallation-target>, accessed: 6-August-2018.
- [64] Y. Dai and G.S. Bauer, Status of the first SINQ Irradiation Experiment, STIP-I, *J. Nucl. Mater.* 296 (2001) 43-53.
- [65] Y. Dai, X. Jia, R. Thermer, D. Hamaguchi, K. Geissmann, E. Lehmann, H. P. Linder, M. James, F. Gröschel, W. Wagner, G. S. Bauer, The Second SINQ, Target Irradiation Program, STIP-II, *J. Nucl. Mater.* 343 (2005) 33-44.
- [66] L. Zanini, A. Aiani, A neutron booster for the SINQ neutron source using thin fissile layers, No. INIS-xa-09N0647, International Atomic Energy Agency (IAEA), 2009.

- [67] B. Horvath, Y. Dai, Y. Lee, Annealing effect on the microstructure of the tungsten irradiated in SINQ target, *J. Nucl. Mater.* 506 (2018) 19-25.
- [68] W. J. Parker, R. J. Jenkins, C. P. Butler, G. L. Abbott, Flash method of determining thermal diffusivity, heat capacity, and thermal conductivity, *J. Appl. Phys.* 34 (1963) 1909-1913.
- [69] Netzsch-Proteus LFA-software, Version 7.1, Software Help Manual.
- [70] M. Akiyoshi, R. Kasada, Y. Ishibashi, L. M. Garrison, J. W. Geringer, W. D. Porter, Y. Katoh, Validation of miniature test specimens for post-irradiation thermal diffusivity measurement, *Fusion Eng. Des.* (2018) <https://doi.org/10.1016/j.fusengdes.2018.03.008>.
- [71] ASTM E739-10, Standard practice for statistical analysis of linear or linearized stress-life (S-N) and strain-life ( $\epsilon$ -N) fatigue data, ASTM International, West Conshohocken, PA, 2010.
- [72] B. Gludovatz, S. Wurster, T. Weingärtner, A. Hoffmann, R. Pippan, Influence of impurities on the fracture behavior of tungsten, *Philos. Mag.* 91 (22) (2011) 3006-3020.
- [73] K. K. Phani, S. K. Niyogi, Young's modulus of porous brittle solids, *J. Mater. Sci.* 22 (1987) 257-263.
- [74] ASTM, American Society for Metals, *ASM Handbook, Mechanical Testing* vol. 8, 1985.
- [75] G. S. Upadhyaya, *Powder Metallurgy Technology*, Cambridge International Science Publishing, Cambridge, 1997.



- [76] G. R. Smolik, R. J. Pawelko, R. A. Anderl, D. A. Petti, Oxidation and volatilization from tungsten brush high heat flux armor during high temperature steam exposure, Technical report INEEL/EXT-2000-00390, Idaho National Engineering and Environmental Laboratory, May 2000.
- [77] Y. S. Touloukian, C.Y. Ho, Thermophysical properties of matter – the TPRC data series, in Thermal diffusivity, vol. 10, Purdue University, 1974.
- [78] F. Hofmann, D. R. Mason, J. K. Eliason, A. A. Maznev, K. A. Nelson, S. L. Dudarev, Non-contact measurement of thermal diffusivity in ion-implanted nuclear materials, *Sci. Rep.* 5 (2015) 16042.
- [79] J. Matolich, H. Nahm, J. Moteff, Swelling in neutron irradiated tungsten and tungsten-25 percent rhenium, *Scripta Metall.* 8 (1974) 837-842.
- [80] M. Roedig, W. Kuehnlein, J. Linke, D. Pitzer, M. Merola, E. Rigal, B. Schedler, E. Visca, Post irradiation testing of samples from the irradiation experiments PARIDE 3 and PARIDE 4, *J. Nucl. Mater.* 329-333 (2004) 766-770.
- [81] D. T. Hurd, “Tungsten” in *Metals Handbook, Properties and selection of metals*, vol.1, American Society for Metals, Metals Park, Novelty, Ohio, 1061.
- [82] Y. Lee, M. Hartl, *Materials Handbook*, Technical Report ESS-0028465, European Spallation Source ERIC, July 28, 2017.
- [83] S. A. Maloy, M. R. James, W. Sommer Jr., G. J. Willcutt Jr., M. Lopez, T. J. Romero, M. B. Toloczko, The effect of 800 MeV proton irradiation on the mechanical properties of tungsten at room temperature and at 475 °C, *J. Nucl. Mater.* 343 (2005) 219-226.

- [84] W. C. Oliver, G. M. Pharr, Measurement of hardness and elastic modulus by instrument indentation: Advances in understanding and refinements to methodology, *J. Mater. Res.* 19 (1) (2004) 3-30.
- [85] H. Ullmaier, F. Carsughi, Radiation damage problems in high power spallation neutron sources, *Nucl. Instrum. Methods Phys. Res. B* 101 (1995) 406-421.
- [86] L. R. Foster, Jr., B. A. Stein, Tensile properties and sheet-bending fatigue properties of some refractory metals at room temperature, NASA Tech. Note D-1592, January 1963.
- [87] Y. Zhang, A. V. Ganeev, J. T. Wang, J. Q. Liu, I. V. Alexandrov, Observations on the ductile-to-brittle transition in ultrafine-grained tungsten of commercial purity, *J. Mater. Sci. Eng. A*, 503 (2009) 37-40.



Part II

Appended Papers

(I-VI)



# PAPER I

J. Habainy, S. Iyengar, Y. Lee, Y. Dai

**Fatigue behaviour of rolled and forged tungsten  
at 25°, 280° and 480 °C**

*Journal of Nuclear Materials*, vol. 465, 2015, pp. 438-447

Reproduced with permission from Elsevier





# Fatigue behavior of rolled and forged tungsten at 25°, 280° and 480 °C



J. Habainy<sup>a</sup>, S. Iyengar<sup>a,\*</sup>, Y. Lee<sup>b</sup>, Y. Dai<sup>c</sup>

<sup>a</sup> Division of Materials Engineering, Lund University, Box 118, 22100 Lund, Sweden

<sup>b</sup> European Spallation Source ESS AB, Box 176, 22100, Lund Sweden

<sup>c</sup> Paul Scherrer Institute, Laboratory for Nuclear Materials, 5232 Villigen PSI, Switzerland

## ARTICLE INFO

### Article history:

Received 17 March 2015

Received in revised form

12 June 2015

Accepted 14 June 2015

Available online 20 June 2015

### Keywords:

Fatigue properties

Tungsten target

Spallation source

## ABSTRACT

Pure tungsten has been chosen as the target material at the European Spallation Source facility in Lund. Calculations show that the target temperature can reach 500 °C momentarily during the spallation process, leading to thermal fatigue. Target life estimations require fatigue data at different temperatures and this work focuses on generating such data for pure, unirradiated, rolled and forged tungsten in the range 25°–480 °C.

For specimens oriented in the rolling direction, tensile tests at room temperature indicated Young's modulus values in the range 320–390 GPa, low levels of plasticity (<0.23%) and UTS values in the range 397 MPa (unpolished) and 705 MPa (Polished). UTS for forged specimens were around 500 MPa.

Stress-controlled fatigue tests were conducted in the tensile regime, with a runout limit of  $2 \times 10^6$  cycles. At 25 °C, unpolished specimens had fatigue limits of 150 MPa (rolling and transverse direction), and 175 MPa (forged). For polished specimens in the rolling direction, fatigue limits were higher at 237.5 MPa (25 °C) and 252.5 MPa (280 °C). The forged specimens showed slightly better fatigue properties and marginal cyclic hardening at 480 °C.

© 2015 Elsevier B.V. All rights reserved.

## 1. Introduction

Neutron scattering methods offer a powerful tool for characterizing materials and their behavior under controlled conditions. In this context, the need for a large scale neutron facility has led to the European Spallation Source which is currently under construction in Lund. In this facility [1], the neutrons are produced through a spallation process in tungsten which has a high neutron production density due to its high atomic number and density. The proton beam driving the spallation process is associated with energy and power levels of 2 GeV and 5 MW, respectively. The proton beam is pulsed at 14 Hz with a pulse duration of 2.86 ms and each beam pulse carries 357 kJ to the spallation volume. Beam pulses and beam trips during the operation introduce thermal fluctuations in the target, with temperatures reaching 775 K momentarily. Thermal fatigue is thus a distinct possibility and may cause target failure. In addition, the target is also subjected to high beam power as well as radiation damage. The life of the target is thus affected by a combination of these factors. In order to estimate the target life, it

is essential to have reliable data on the mechanical properties of tungsten, both in the unirradiated and irradiated conditions. The following section presents a review of the studies on unirradiated tungsten.

### 1.1. Review of literature

Studies on tungsten have been mainly concerned with characterizing and improving its strength, ductility and fracture behavior at different temperatures. Tungsten is known to be brittle at ambient temperatures and exhibits ductility above the ductile to brittle transition temperature (DBTT). However, processing conditions affect DBTT and irradiation is also known to push it to higher temperatures.

Schmidt and Ogden [2] compiled data on the ultimate tensile strength (UTS), ductility, DBTT and other engineering properties of pure tungsten and its alloys, as a function of temperature. Foster and Stein [3] studied fully dense tungsten sheet specimens (0.5 mm thick) in bending at room temperature and reported a fatigue limit of 772 MPa under conditions of complete stress reversal and UTS values in the range 793–1630 MPa.

Beardmore and Hull [4] tested single crystals of tungsten in tension and observed ductility at low temperatures (–196° to

\* Corresponding author.

E-mail address: [srinivasan.iyengar@material.lth.se](mailto:srinivasan.iyengar@material.lth.se) (S. Iyengar).



22 °C), indicating that tungsten is extremely notch-sensitive and not necessarily inherently brittle. Discontinuous yielding was observed along [110], which may be attributed to the lower rate of dislocation multiplication in the vicinity of this direction [5].

Wronski and Chilton [6] did not observe any significant change in the tensile and compressive properties of polycrystalline cast tungsten due to pressurization at 1400 MPa. At 420 °C, they noted an elongation of 20% for tungsten, which became negligible at lower temperatures.

Braun and Sedlatschek [7] studied the effect of small alloying additions on the sintering, working and mechanical properties of tungsten. An addition of 0.01% thorium led to a 32% higher ductility, while chromium and vanadium additions showed the opposite effect. Raffo [8] studied the mechanical properties of vacuum arc-melted tungsten and tungsten–rhenium alloys in the temperature interval –196° to 537 °C. Even at low concentrations (1 at%), Rhenium was effective in lowering the DBTT of tungsten, attributed to increased dislocation mobility.

Farrell et al. [9] observed that the DBTT in bending for tungsten sheets (wrought and powder metallurgical products) were the lowest at 70 °C. This increased to 225 °C after primary recrystallization at 1150 °C. DBTT after secondary recrystallization was in the range 235°–280 °C. Intergranular fracture was observed in specimens after primary recrystallization, which changed to transgranular cleavage after secondary recrystallization. In a following study [9], yield point inflections were noted during bending tests of sheet specimens above DBTT and the temperature dependence of yield and tensile strengths were similar. They observed a deviation from the classical Hall–Petch relationship and attributed it to the annealing treatment.

Forster and Gilbert [10] conducted 3-point bend tests on 99.9% pure tungsten wire specimens recrystallized at different temperatures to produce a range of grain structures. They found that fine-grained specimens had a lower DBTT (257–307 °C) relative to the coarse-grained specimens (297–657 °C). However, coarse grained materials withstand greater pre-yield strain before the initiation of fracture in the brittle regime.

Schmunk and Korth [11] studied tensile and low cycle fatigue properties of cross-rolled tungsten (DBTT–300 °C) at room temperature as well as at 815 °C. At both temperatures, a smaller strain interval was observed for recrystallized tungsten specimens compared to the as received material. Predictions from the universal slopes equation [12] were in agreement with fatigue data on the as received material at room temperature. At 815 °C, the average yield strength and UTS were 415 and 426 MPa respectively for the as received material, 115 and 240 MPa for recrystallized tungsten.

The dynamic recrystallization of potassium-doped tungsten during the rolling process was studied by Briant and Hall [13]. They observed high angle grain boundaries at low levels of deformation, with many dislocation-free grains and low angle grain boundaries at higher levels of deformation. Annealing the rolled material in the temperature range 1275°–1950 °C showed abnormal grain growth, which emphasizes the need for close grain size control during the production of the target material.

Giannattasio and Roberts [14] investigated the strain-rate dependence of the brittle to ductile transition in single crystal and polycrystalline tungsten specimens. They found an Arrhenius relationship over a large strain rate interval, with an activation energy of 1.05 eV. As this value suggests double-kink formation on screw dislocations, the authors concluded that dislocation motion controls the transition.

Using micro hardness measurements, Zhang et al. [15] studied commercially pure ultrafine-grained tungsten and observed the DBTT to decrease from 483° to 350 °C as the grain size decreased

from 10 to 0.9  $\mu\text{m}$ .

Rupp and Weygand [16] studied the fracture toughness of polycrystalline rolled tungsten in the brittle and semi-brittle regime, considering the crack orientation with respect to the rolling direction. With increase in temperature (–150° to 350 °C), the fracture toughness improved for all types of specimens, with understandably better properties in the longitudinal direction. Fractographic studies showed that the longitudinal specimens were associated with transcrystalline cleavage at room temperature and intercrystalline failure at elevated temperatures. The authors have also developed a model which predicts the transition between the two fracture modes [17].

Using Auger electron spectroscopy and scanning electron microscopy, Gludovatz et al. [18] found that grain boundary impurities like phosphorus and oxygen did not affect the fracture behavior of tungsten materials. They concluded that factors such as size and shape of the grains, the extent of deformation and dislocation density have a greater impact on fracture.

Reiser et al. [19] carried out tensile tests on specimens made from commercially produced tungsten plates, rolled to 1 mm thickness. At room temperature, specimens oriented in the rolling direction and at 45° had high yield strengths (1350–1380 MPa) and surprisingly good ductility (1.5% strain in the rolling direction and 1% at 45°), while the transverse specimens showed no ductility. The authors also reported isotropic behavior of the tungsten specimens at 600 °C and a tensile strength of about 700 MPa.

Yan et al. [20] investigated the effect of hot working and found that swaged and rolled tungsten had the highest relative density (99.1%) and a bending strength of 2180 MPa. They also noted that the properties could be improved by the addition of 1%  $\text{La}_2\text{O}_3$ .

Gaganidze et al. [21] studied the influence of anisotropic microstructure on the fracture behavior of polycrystalline tungsten up to 1000 °C. Intergranular fracture dominated in longitudinally oriented specimens up to 600 °C and transgranular cleavage in others at low temperatures.

Krsjak et al. [22] studied the fracture properties of rolled and hot isostatically pressed (HIP) tungsten and found that the DBTT for both materials were similar and in the range 180°–230 °C, while the flexural strength at room temperature was much higher for rolled tungsten (1050 MPa) than for the HIPed material (440 MPa).

Zhang et al. [23] determined the texture evolution during the rolling of tungsten. After annealing at 1800 °C for 2 h, full recrystallization was observed in 60% and 90% rolled tungsten. Goss and  $\theta$ -fiber textures were predominant in 80% rolled tungsten which was considered to have the best irradiation resistance.

Wurster et al. [24] reviewed the progress in the development of tungsten alloys for divertor structural and plasma facing materials. They have considered several approaches to increase ductility and fracture toughness as well as to decrease the DBTT by alloying additions and the use of fine-grained materials. The main challenge is in extending the excellent ductile properties of thin foils to bulk materials and to ensure optimal irradiation resistance in the material.

## 1.2. Present work

Most of the studies on the mechanical properties of tungsten reviewed in the previous section used nearly fully dense, miniature sized or thin specimens. As tungsten has been found to be extremely notch sensitive, it is important to note the production method and specimen size while characterizing its mechanical properties. Further, fatigue data are very important in applications such as the design of the spallation target at ESS. However, published data on the fatigue behavior of pure bulk tungsten are limited to a few studies based on bend tests [3] and a low cycle

fatigue study on cross-rolled tungsten subjected to fully reversible stresses [11]. Hence, the present study was taken up to obtain fatigue and tensile data for unirradiated, polycrystalline, bulk tungsten specimens obtained from powder metallurgical processing. Keeping in mind the temperatures relevant to the ESS project, tensile and fatigue tests on tungsten were carried out at 25°, 280° and 480 °C.

## 2. Materials and methods

Table 1 presents the impurity content of rolled and forged tungsten specimens used in this work. Most of the rolled specimens were oriented along the rolling direction, with a few oriented in the transverse direction. In order to determine the variation in fatigue strength due to surface quality, both unpolished and electropolished tungsten were tested. The specimen geometries used for room and high temperature tests are shown in Fig. 1. All the specimens were supplied by Beijing Tian-Long Tungsten & Molybdenum Co. and tested in the as received condition. The rolled high temperature samples were manufactured from a 20 mm thick sheet which had been rolled four times in the temperature interval 1500°–1650 °C, with a 20–25% reduction in each step. The smaller room temperature samples were machined from sheets rolled 5 times at a temperature of 1450°–1650 °C. The forged fatigue and tensile specimens were prepared from a tungsten plate hot forged in the temperature interval 1550°–1700 °C. This enabled a reduction in thickness from 150 mm to 90 mm achieved in a 3-step forging operation, during which the tungsten block was held in position on its sides under slight pressure.

In order to get an idea about the porosities in the samples, the densities were determined using the Archimedes principle. Mechanical testing was carried out using an MTS machine equipped with a Digital Electronic system supplied by Instron. For the high temperature tests, a furnace was installed and the grips were changed. The reported temperatures were measured at the surface of the specimen using a chromel–alumel (type K) thermocouple.

The tensile testing followed the standards set in ASTM E8/E8M [25], and the displacement rates were in the range of 0.6–2 mm·s<sup>−1</sup>. The stress-controlled fatigue testing was performed according to ASTM E739 [26] and only in the tensile regime. The minimum load was 0.1 kN and the load reversal frequency was in the interval 20–30 Hz. The up and down method [27,28] was used to determine the fatigue limits, with the runout condition set at  $2 \times 10^6$  cycles. Stress amplitudes employed in the fatigue testing were 100–350 MPa.

Strain controlled fatigue testing [29] was also performed to obtain the cyclic stress–strain curves and determine the degree of hardening of the materials. The tests were done using the Multiple Step Test method (MST) [30,31] with fully reversed strain cycles. At 280 °C the strain amplitude was initially set to 0.1% and increased in steps of 0.1% when saturation was observed. For the test at 480 °C, an amplitude sequence of 0.42, 0.58 and 0.75% was used. In both

cases the strain rate was 2 mm s<sup>−1</sup>.

## 3. Physical properties

Six types of specimens were tested at three temperatures and each specimen was assigned an identification number based on the test temperature, the manufacturing method (F: Forged; R: Rolled), specimen orientation (L: Longitudinal – along the rolling direction; T: Transverse), and surface quality (P: Electropolished; U: Unpolished).

The results from the tensile and the fatigue tests, and metallographic examination are presented in the following sections.

### 3.1. Density

Densities of powder metallurgical products can vary significantly depending on the method of production and the densification treatments used. For pure tungsten at 20 °C, based on pycnometric measurements, the density has been reported as  $19.25 \pm 0.004$  Mg m<sup>−3</sup> [32]. This value is in excellent agreement with the theoretical density value calculated for the body-centered cubic form of tungsten using a lattice parameter value of 0.31652 nm reported in Ref. [33].

In this work, density measurements were carried out using a Mettler Toledo Precision Balance equipped with a Density Kit. For the rolled and forged specimens used in this study, the density values were determined to be 19.2303 and 18.8802 Mg m<sup>−3</sup> respectively. These values represent the average of three measurements with different samples at 23.1 °C. The corresponding porosities were estimated to be 0.1 and 1.92% respectively.

### 3.2. Hardness

Hardness measurements, both macro and micro, were carried out on room temperature specimens. Macrohardness tests were performed using a Sematic Durometer, and micro hardness tests using a Knoop diamond indenter mounted on a Leica DMRME light optical microscope. The average macrohardness was observed to be slightly above 40 HRC for all samples except for the forged unpolished ones (35.8 HRC). These have the lowest minimum value, the lowest average and the largest scatter, which could indicate relatively rough surfaces. The rolled, unpolished specimens oriented in the transverse direction were marginally harder than the rest. Micro hardness values for all the samples were in the range 460–583 KHN.

### 3.3. Surface examination

The surfaces of all the test pieces were examined in an optical microscope prior to testing. All of the surfaces were characterized by cracks, machining stripes and pores. The electropolished surfaces were slightly smoother, although there was a large variation in the quality of polishing. The room temperature forged, unpolished specimens were associated with very rough surfaces with deep stripes and relatively large holes (>100 µm in diameter). The high temperature forged and polished pieces (HFP) had a relatively more even surface, but still contained plenty of pores (Fig. 2). The room temperature polished tungsten oriented in the rolling direction (RLP) proved to have the best surface finish. The grains were visible in these specimens, as shown in Fig. 2b. These elongated grains were approximately 400 µm × 100 µm. The surfaces of a high temperature rolled and polished oriented in the rolling direction (HLP) and a room temperature polished specimen oriented in the transverse direction (RTP) are also displayed in the figure. The latter showed relatively more longitudinal cracks.

**Table 1**  
Impurity elements in tungsten.

Element	Max. content (in ppm)
O	50
Mo	30
Fe, C	10
Ca	8
As	7
Ni, Mg, Cr, Al	5
V, Sb, Ti, Mn, S, Co	4
Sn, Cu, Bi, Cd, Pb	1
Si	0.56
K	0.13

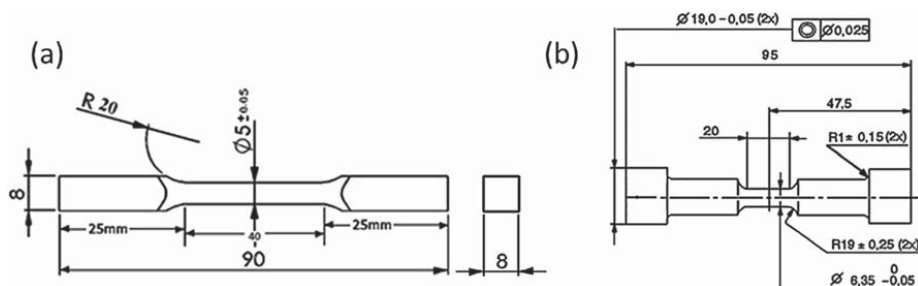


Fig. 1. (a) Room and (b) High temperature test specimens (dimensions in mm).

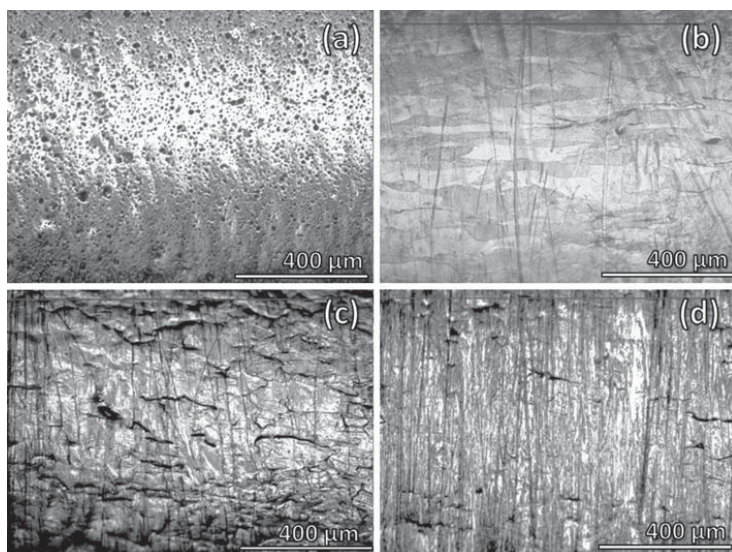


Fig. 2. Microscopic examination of the polished forged and rolled specimens before testing (a) HFP (b) RLP (c) RTP (d) HLP.

## 4. Results and discussion

### 4.1. Tensile testing

Stress–strain curves from the tests performed in tension are shown in Figs. 3–5.7. Mean values of the Ultimate Tensile Strength (UTS) for rolled and forged tungsten are summarized in Table 2.

As expected, the data from room temperature tests (Fig. 3) show the brittle nature of pure tungsten, with almost no ductility observed before failure. Rolled (7) and forged (4) specimens were tested at this temperature. The difference in tensile strength between forged specimens with polished and unpolished surfaces was not observed to be significant. A close examination of the sample surfaces showed that the specimens had roughly the same amount of pores, scratches and cracks, suggesting that the polishing was not performed satisfactorily. Mean values of UTS and Young's modulus for the forged material were found to be 510 MPa and 340 GPa respectively.

For the rolled specimens, specimen orientation appeared to be more important than the surface condition. However, polished

specimens showed significantly better tensile behavior relative to the unpolished specimens. The mean UTS values were determined to be 673 MPa and 458 MPa in the rolling and transverse directions, respectively. The total strain at 25 °C was observed to be in the range of 0.11–0.21%. In view of the large difference in UTS values for different orientations, rolled specimens with longitudinal orientation were chosen for fatigue testing. As the irradiated specimens are known to be very brittle, it was thought that testing of unirradiated specimens at room temperature would give some idea about the fatigue behavior of brittle tungsten with extremely low ductility.

At 280 °C (Fig. 4), a decrease in tensile strength and an increase in ductility were noted relative to those observed at room temperature. The total strain for the rolled specimens was in the range of 0.15–0.30%, as compared to 0.35–1.77% for the forged specimens which also showed a slight decrease in the UTS. The variation could be due to the testing temperature being close to the DBTT for tungsten.

A substantial increase in ductility was observed at 480 °C (Fig. 5). One of the forged and polished specimens showed a total strain of over 25%. However, a second specimen of the same sort

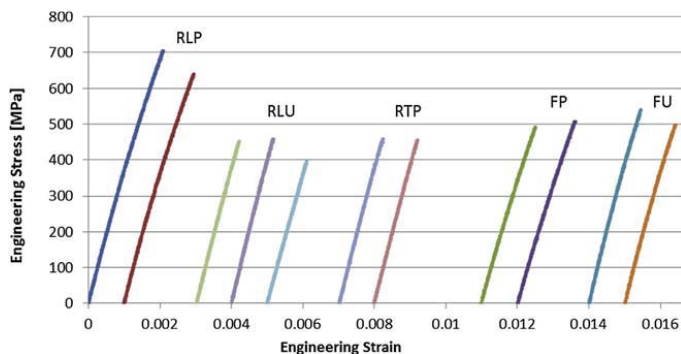


Fig. 3. Tensile data for rolled and forged specimens at 25 °C.

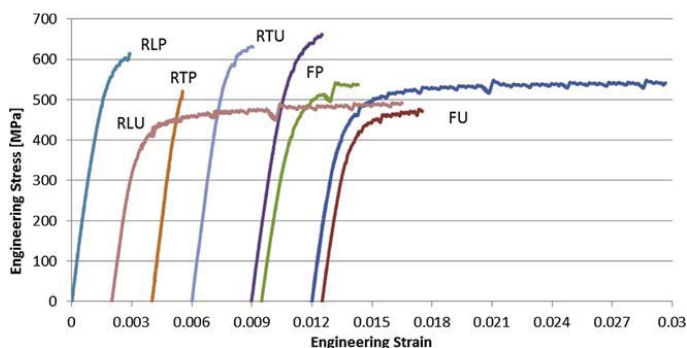


Fig. 4. Tensile data for rolled and forged tungsten at 280 °C.

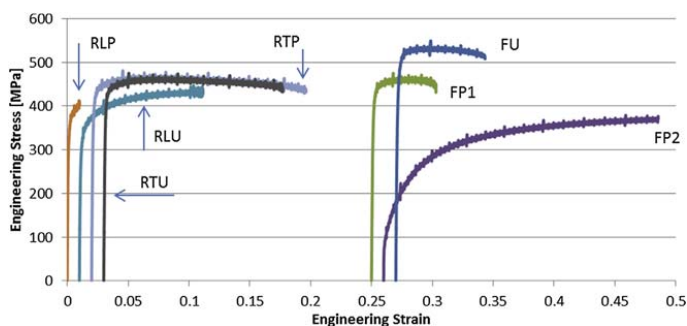


Fig. 5. Tensile data for rolled and forged tungsten at 480 °C.

tested under the same conditions exhibited less ductility, indicating a variation in the quality of the specimens used. Fractographic studies (Fig. 6) showed cleavage fracture to a larger extent in the specimen with lower ductility.

Fig. 7 shows a comparison of the stress–strain curves for the polished specimens oriented in the rolling direction and the polished forged specimens, at three temperatures. At room temperature, the rolled specimen has a higher UTS value, but it is the other way around at 280 °C. However, the most noticeable difference is

the total strain associated with forged tungsten.

The scatter in the results may be explained by the uneven surface for both the polished and unpolished specimens. A rough surface has a lot of stress concentration points where cracks can be initiated. Density variations in forged specimens could also contribute to the scatter in experimental data. For the rolled as well as forged material, Young's modulus data obtained from tensile tests were in the range 316–401 GPa. The effect of temperature was not significant in the range 25°–480 °C, but the forged material was

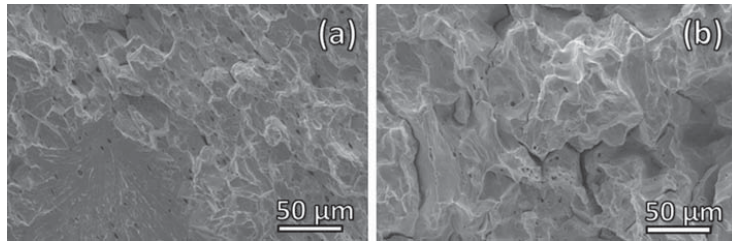


Fig. 6. Fracture surfaces of forged and polished tungsten specimens which failed at 480 °C. (a) & (b) correspond to FP1 and FP2 in Fig. 5.

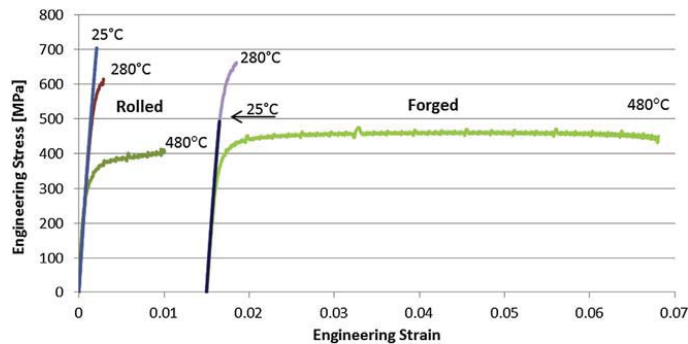


Fig. 7. Tensile data for polished rolled and forged tungsten at 25°, 280°, and 480 °C.

Table 2

Summary of UTS values obtained at different temperatures.

		Mean ultimate tensile strength [MPa]					
		25 °C		280 °C		480 °C	
		U	P	U	P	U	P
R	L	503 (397–571)	673 (640–705)	588 (495–681)	593 (571–615)	447	450
	T		458 (456–459)	633	522	475	481
F		519 (498–540)	500 (493–507)	507 (472–542)	540 (537–542)	550	525 (363–537)

generally associated with a relatively lower stiffness. The UTS values obtained at different temperatures are shown in Table 2.

#### 4.2. Stress-controlled fatigue experiments

In the present study, fatigue data were obtained from a total of 12 different sets of stress-controlled experiments. More than 20 specimens were tested in some of the sets, while only a few were tested in others. While the minimum number of specimens required for different types of tests are specified by ASTM E739-10 [36], the number of specimens used in this work and the replication

rates for the different sets of experiments are given in Table 3.

The results for sets with less than six specimens are considered to be not statistically reliable and are not discussed further. The percent replication rate is good for most of the other sets except for FU at 280 °C, as well as RLU at 480 °C. However, the results give a good indication of fatigue behavior under these conditions. Table 4 presents a summary of the endurance limits obtained in this study. Wöhler diagrams corresponding to data obtained at the ambient and elevated temperatures are presented in Figs. 8 and 9.

At room temperature, there is a large variation in fatigue data for RLU. These specimens were associated with the highest runout

Table 3

Minimum number of specimens and replication rates in this study.

	25 °C						280 °C				480 °C	
	RLU	RLP	FU	FP	RTP	RTU	RLP	RLU	FP	FU	RLU	FP
No. of different stress levels	13	7	5	5	3	3	6	2	7	11	6	6
No. of tested specimens	22	16	12	12	3	3	9	2	9	12	6	9
Replication rate [%]	41	56	58	58	0	0	33	0	22	8	0	33



**Table 4**  
Endurance limits and maximum stress amplitudes at runout for rolled and forged tungsten specimens at different temperatures.

Stress amplitudes [MPa]							
Sample				Endurance limit	No. of tests	Highest runout <sup>a</sup>	
25 °C	R	T	U	150.0	3	150.0	
			P	137.5	3	137.0	
		L	U	150.0	22	337.5	
	P		237.5	16	300.0		
	F	U	175.0	9	200.0		
		P	125.6	12	170.6		
280 °C	R	L	U	300.0	2	300.0	
			P	252.5	12	290.0	
		F	U	242.5	12	300.0	
	F	P	212.5	9	250.0		
		R	L	U	150.0	6	150.0
		F	P	175.0	9	187.5	

<sup>a</sup> Corresponds to  $2 \times 10^6$  cycles.

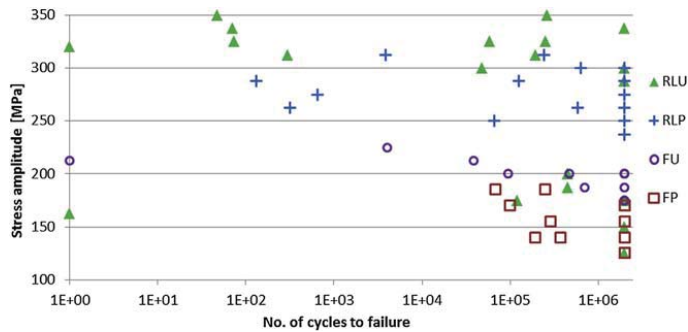


Fig. 8. Wöhler diagram for rolled and forged tungsten at 25 °C.

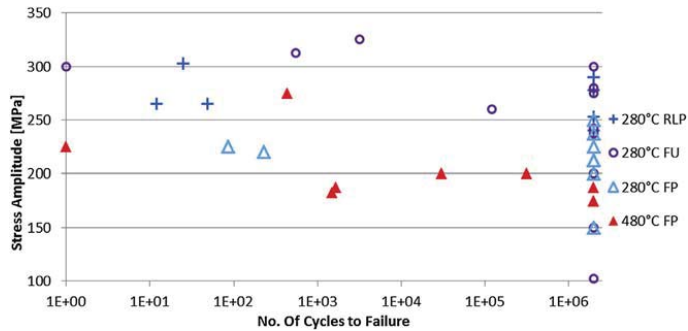


Fig. 9. Wöhler diagram for rolled and forged tungsten at 280° and 480 °C.

stress (337.5 MPa), as well as one of the lowest endurance limits (150 MPa). The scatter for the polished counterpart was relatively less and about half of the tested specimens failed at stress amplitudes between 237.5 and 312.5 MPa. Data for FU were lower relative to the RLP specimens, but more consistent. The 50% failure range for these specimens was within 25 MPa, as compared to 75 MPa for the RLP specimens. Somewhat unexpectedly, the endurance limit for FP (125.6 MPa) was the lowest, even lower than that of FU (175 MPa). This could be due to the fact that some of the FP test pieces fractured in the shoulder region having a radius of curvature, suggesting the presence of weak spots which originated

probably during machining or electropolishing of the specimens. At 280 °C the behavior of RLP and FU specimens were quite similar and the endurance limits were determined to be 252.5 and 242.5 MPa respectively. At this temperature, the specimens generally performed the best and the experimental data showed limited scatter. At 480 °C, the endurance limit for FP (175 MPa) was observed to be 50 MPa higher than at room temperature. It is quite difficult to predict the fatigue behavior of a material, if tests at a given stress amplitude can result in both immediate failure and runout. For example, such data were obtained for the FU specimens at 300 MPa and is typical even for the other types of test

pieces. Instantaneous failures can be due to defective specimens with cracks on the surface or inside. This highlights the importance of proper surface treatment and good quality control. With brittle materials like tungsten, a certain amount of defects and scatter is inevitable. However, this should be kept to a minimum with the right manufacturing methods. A good example of the effect of polishing is seen in the case of rolled specimens at room temperature. The difference in the endurance limit between the polished and unpolished specimens is almost 90 MPa.

#### 4.3. Strain-controlled fatigue experiments

Strain-controlled fatigue tests were performed in order to understand the cyclic hardening behavior of pure tungsten. Assuming Ramberg–Osgood material behavior [34], the cyclic stress–strain curve is expressed as:

$$\varepsilon_a = (\sigma_a/E) + (\sigma_a/K')^{1/n'}$$

where  $\varepsilon_a$  is the strain amplitude,  $K'$  is the cyclic strength coefficient and  $n'$  is the cyclic strain hardening exponent. The method has been described in the introduction section.

Both rolled and forged tungsten exhibited virtually no plasticity at room temperature and it was not possible to evaluate the cyclic behavior from the data obtained. The specimen used at 280 °C was of RLU type. The initial strain level was set to 0.1% and increased in step of 0.1% when saturation was reached. Failure occurred after 22 cycles at the 4th level. From the stabilized hysteresis loop, the cyclic strength coefficient and the strain hardening exponent were determined as 1297 MPa and 0.108, respectively. A comparison between a monotonic tensile test of the same type of specimen and the stress levels of the hysteresis loop shows that the material undergoes marginal cyclic hardening. A forged and polished tungsten specimen showed a similar behavior at 480 °C. The strain levels used in this experiment were 0.42%, 0.58% and 0.75%. At the last level, the specimen only survived 9 cycles. The strength coefficient and the strain hardening exponent for this sample were calculated to be 771 MPa and 0.09 respectively. Fig. 10 shows a comparison of hysteresis data from the strain-controlled fatigue test and a monotonic tensile test at 480 °C.

#### 4.4. Fractography

Fracture surfaces of 18 rolled as well as forged tungsten specimens in the polished as well as unpolished condition were studied in the scanning electron microscope after fatigue testing at various

loads and temperatures. Fig. 11 presents fractographs for the rolled specimens. All these specimens failed in a brittle manner, more so at room temperature and show the characteristic chevron pattern with beach mark ridges.

The difference in fracture behavior between specimens oriented in the rolling and transverse directions is shown in Fig. 11(a) and (b). The test specimen oriented in the transverse direction shows a more brittle fracture with virtually no plasticity. Crack propagation is relatively easier in this specimen where cleavage fracture dominates. From Fig. 11(c), it is seen that the RLU specimen is associated with more ductility and some contribution from intergranular fracture. Fig. 11(d) shows that transgranular fracture dominates even at 280 °C, but displays some ductile areas and intergranular fracture. A feather pattern on a grain of tungsten is also clearly seen in this image.

The fracture surfaces of forged (unpolished) tungsten specimens which failed at 25° and 280 °C are shown in Fig. 12. Both the test pieces showed a number of pores, but exhibited different modes of brittle fracture. The grain sizes in the two specimens were observed to be dissimilar, with the high temperature specimen having smaller grains (~30 µm in diameter). It is interesting to see that some of the grains are completely detached, resembling loose gravel. This indicates a problem during sintering and the specimen failed soon after loading and did not show any sign of fatigue.

Fig. 13(a) and (b) show a comparison of the fracture surfaces of forged, unpolished samples at 25° and 480 °C. Both transgranular and intergranular fracture are observed in both cases, the former dominates at 25 °C. At the higher temperature, the fracture surface is characterized by a relatively smoother surface and deformation of the grains.

Fig. 13(c) and (d) compare the fracture surfaces of forged and rolled samples at 480 °C. The elongated grains are clearly seen in the rolled specimen and the fracture surface is showing a lot of deformation. Transgranular fracture can be clearly seen on the forged specimen surface, while delamination is observed in the rolled specimen. However, areas showing ductility and cleavage fracture can be seen in the case of the forged material.

## 5. Conclusions

Fatigue and tensile properties of forged and rolled tungsten have been studied at ambient and elevated temperatures. There is a wide scatter in data primarily due to the brittle nature of tungsten, but is also affected by the surface condition, volume fraction porosity, grain orientation, manufacturing method and specimen

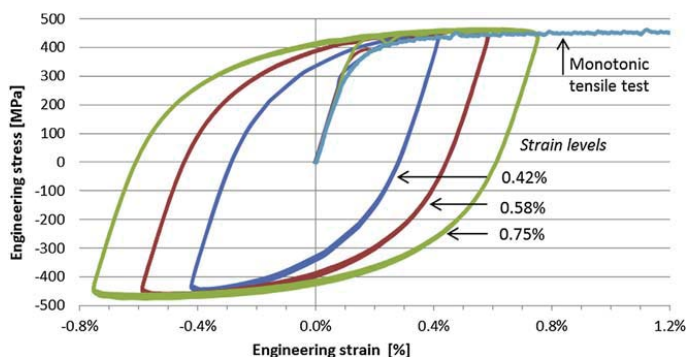
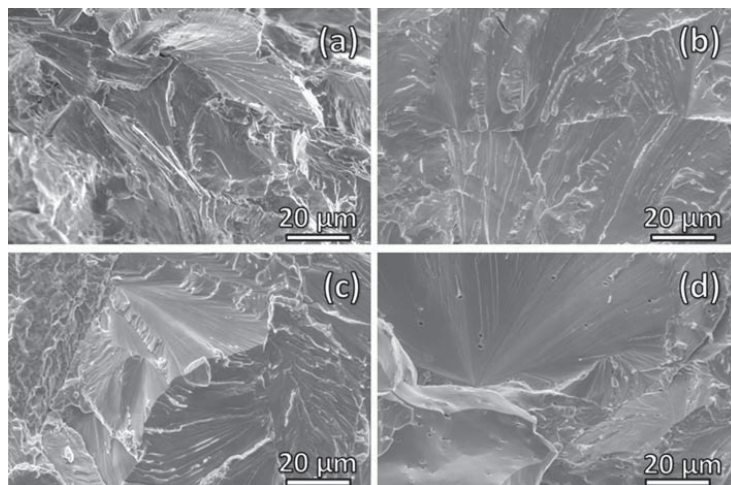
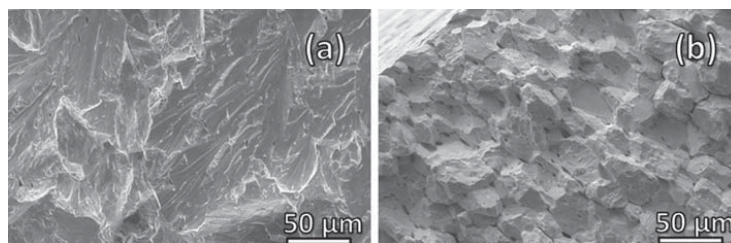


Fig. 10. Comparison between a strain controlled fatigue test and a monotonic tensile test of forged polished tungsten at 480 °C.



**Fig. 11.** Fracture surfaces of rolled specimens which failed after fatigue testing at different stress amplitudes and temperatures (a) RLP (25 °C, 175 MPa, 120841 cycles), (b) RTP (25 °C, 163 MPa, 136219 cycles), (c) RLU (25 °C, 200 MPa, 448951 cycles), (d) RLP (280 °C, 302.5 MPa, 25 cycles).



**Fig. 12.** Fracture surfaces of forged specimens after fatigue testing (a) FU 25 °C, 200 MPa, 473984 cycles; (b) FU 280 °C, 312.5 MPa, 545 cycles.

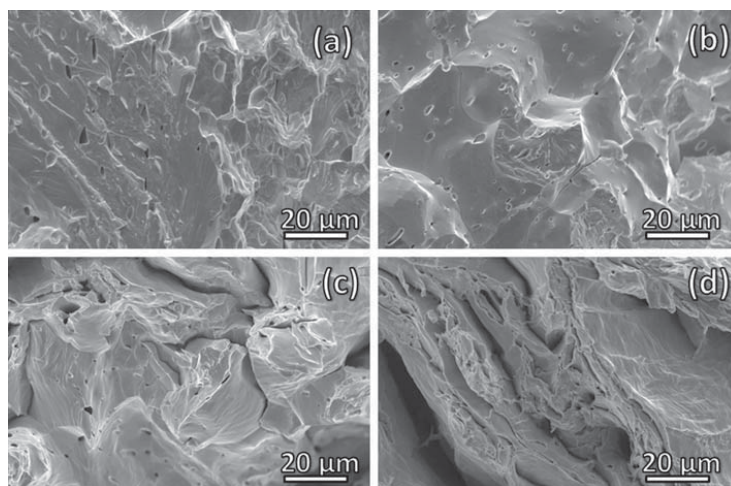


**Fig. 13.** Fracture surfaces of forged specimens at different temperatures and a rolled specimen which failed at 480 °C. (a) FP 25 °C, 156 MPa, 286335 cycles; (b) FP 280 °C, 220 MPa, 226 cycles; (c) FP 480 °C, 187.5 MPa, 1675 cycles; (d) RLU 480 °C, 250 MPa, 22392 cycles.



preparation. All the specimens showed brittle behavior at room temperature, with very little or no ductility. At 280 °C, most of the specimens were observed to be in the ductile regime, with improved fatigue properties. The rolled specimens showed relatively higher fatigue limits (237.5 MPa at 25 °C and 252.5 MPa at 280 °C for RLP specimens), higher density and slightly higher average hardness compared to the forged samples. In general, the specimens showed more ductility at 480 °C, with the strain controlled tests showing a marginal cyclic hardening effect.

In this work, UTS values obtained at room temperature varied from 397 to 705 MPa. Much higher UTS values of 793–1630 MPa have been reported by Foster and Stein [3]. In the same study, a fatigue limit of 772 MPa was determined from bending tests of very small samples (0.5 mm thick) at complete stress reversal. A 20% elongation was reported by Wronski and Chilton [6] for polycrystalline cast tungsten at 420 °C while Zhang et al. [15] reported a value of 1.5% at room temperature for specimens oriented in the rolling direction, as compared to values of 0.11–0.21% from this work.

In the present study, strain levels determined at 480 °C were in the range 1–17.6% for rolled specimens and 0.2–25% for the forged ones. These results are not easily compared with previous data due to differences in specimen size, sample preparation, production routes, and testing methods. The scarcity of fatigue data on pure tungsten is another issue. In the most relevant study to date, Schmunk et al. [11] conducted tensile and low-cycle fatigue tests on cross-rolled tungsten at room temperature and 815 °C. The fatigue experiments at the elevated temperature were run in fully reversed strain control. The room temperature specimens were run in load control at 1 Hz due to their brittleness. Two tests were terminated after 500,000 cycles without failure, corresponding to the stress ranges  $\pm 206.8$  and  $\pm 275.7$  MPa respectively. It may be noted that fatigue loading in the present study was in the tensile regime and the tests were terminated without failure only after  $2 \times 10^6$  cycles.

Even low levels of radiation damage can increase the DBTT for tungsten to >400 °C [35]. At 0.1 dpa, failure of tungsten in the brittle regime has been reported at 500 °C [36]. Data on the brittle behavior of unirradiated tungsten at low temperatures obtained in this study is therefore useful to the design of the ESS target wheel. However, much more work needs to be done in order to understand the behavior of tungsten during the operation of the target. Testing of irradiated samples is essential in this regard. In addition, attempts should be made to improve the quality of tungsten specimens and the test procedures to minimize the spread in experimental data.

## Acknowledgments

The authors are thankful to Zivorad Zivkovic, Sofie Borre, Andreas Löfberg and Kumar Babu Surreddi for invaluable

assistance in the experimental work. Research funding and support from the European Spallation Source (ESS, Lund) is gratefully acknowledged.

## References

- [1] S. Peggs, ESS Conceptual Design Report, Feb 6, 2012. ISBN: 978-91-980173-0-4.
- [2] F.F. Schmidt, H.R. Ogden, Defence Metals Information Center Report no.191, Ohio, Columbus, September 27, 1963.
- [3] L.R. Foster, Jr., B.A. Stein, NASA Tech. Note D-1592, January 1963.
- [4] P. Beardmore, D. Hull, J. Less Common Met. 9 (1965) 168–180.
- [5] A.S. Argon, S.R. Maloof, Acta Met. 14 (1966) 1449–1462.
- [6] A.S. Wronski, A.C. Chilton, Scr. Met. 3 (1969) 395–400.
- [7] H. Braun, K. Sedlatschek, J. Less Common Met. 2 (1960) 277–291.
- [8] P.L. Raffo, J. Less Common Met. 17 (1969) 133–149.
- [9] K. Farrell, A.C. Schaffhauser, J.O. Stiegler, J. Less Common Met. 13 (1967), 141–155\*, 548–558\*.
- [10] R.H. Forster, A. Gilbert, J. Less Common Met. 20 (1970) 315–325.
- [11] R.E. Schmunk, G.E. Korth, J. Nucl. Mater. 103 & 104 (1981) 943–948.
- [12] S.S. Manson, Exper. Mech. 5 (1965) 193–226.
- [13] C.L. Briant, E.L. Hall, Met. Trans. A 20 (1989) 1669–1686.
- [14] A. Giannattasio, S.G. Roberts, Philos. Mag. 87 (2007) 2589–2598.
- [15] Y. Zhang, A.V. Ganeev, J.T. Wang, J.Q. Liu, I.V. Alexandrov, J. Mater. Sci. Eng. A 503 (2009) 37–40.
- [16] D. Rupp, S.M. Weygand, J. Nucl. Mater. 386–388 (2009) 591–593.
- [17] D. Rupp, S.M. Weygand, Philos. Mag. 90 (2010) 4055–4069.
- [18] B. Gludovatz, S. Wurstler, T. Weingärtner, A. Hoffman, R. Pippan, Phil. Mag. 91 (2011) 3006–3020.
- [19] J. Reiser, M. Rieth, B. Dafferner, S. Baumgärtner, R. Ziegler, A. Hoffman, Fusion Eng. Des. 86 (2011) 2949–2953.
- [20] Q. Yan, X. Zhang, T. Wang, C. Yang, C. Ge, J. Nucl. Mater. 442 (2013) S233–S236.
- [21] E. Gaganidze, D. Rupp, J. Aktaa, J. Nucl. Mater. 446 (2014) 240–245.
- [22] V. Krsjak, S.H. Wei, S. Antusch, Y. Dai, J. Nucl. Mater. 450 (2014) 81–87.
- [23] X. Zhang, Q. Yan, S. Lang, M. Xia, C. Ge, J. Nucl. Mater. (2015), <http://dx.doi.org/10.1016/j.jnucmat.2015.04.001>.
- [24] S. Wurstler, N. Baluc, M. Battabyal, T. Crosby, J. Du, C. García-Rosales, A. Hasegawa, A. Hoffmann, A. Kimura, H. Kurishita, R.J. Kurtz, H. Li, S. Noh, J. Reiser, J. Riesch, M. Rieth, W. Setyawan, M. Walter, J.-H. You, R. Pippan, J. Nucl. Mater. 442 (2013) S181–S189.
- [25] ASTM E8/E8M-13a, Standard Test Methods for Tension Testing of Metallic Materials, ASTM International, West Conshohocken, PA, 2013. [www.astm.org](http://www.astm.org).
- [26] ASTM E739-10, Standard Practice for Statistical Analysis of Linear or Linearized Stress-life (S-N) and Strain-life ( $\epsilon$ -N) Fatigue Data, ASTM International, West Conshohocken, PA, 2010. [www.astm.org](http://www.astm.org).
- [27] R. Pollak, A. Palazotto, T. Nicholas, Mech. Mater. 38 (2006) 1170–1181.
- [28] S.-K. Lin, Y.-L. Lee, M.-W. Lu, Int. J. Fatigue 23 (2001) 75–83.
- [29] ASTM E606/E606M-12, Standard Test Method for Strain-controlled Fatigue Testing, ASTM International, West Conshohocken, PA, 2012. [www.astm.org](http://www.astm.org).
- [30] J. Polák, M. Hájek, Int. J. Fatigue 13 (1991) 216–222.
- [31] J. Polák, M. Klesnil, P. Lukáš, Mater. Sci. Eng. 28 (1977) 109–117.
- [32] E. Lassner, W.-D. Schubert, Tungsten – Properties, Chemistry, Technology of the Element, Alloys and Chemical Compounds, Kluwer Academic/Plenum, New York, 1999.
- [33] CRC Handbook of Chem. & Phys., 95<sup>th</sup> ed., 2014–2015 online, sec.12.05\_86.
- [34] S. Suresh, Fatigue of Materials, second ed., 1998. Cambridge.
- [35] F. Ullmaier, F. Carsughi, Nucl. Instrum. Methods Phys. Res. B 101 (1995) 406–421.
- [36] I.V. Gorynin, V.A. Ignatov, V.V. Rybin, S.A. Fabrisiev, V.A. Kazakov, V.P. Chakin, V.A. Tsykanov, V.R. Barabash, Y.G. Prokofyev, J. Nucl. Mater. 191–194 (1992) 421–425.

# PAPER II

J. Habainy, A. Lövberg, S. Iyengar, Y. Lee, Y. Dai

**Fatigue properties of tungsten from two different processing routes**

*Journal of Nuclear Materials*, vol. 506, 2018, pp. 83-91

Reproduced with permission from Elsevier





# Fatigue properties of tungsten from two different processing routes



Jemila Habainy<sup>a, b, \*</sup>, Andreas Löfberg<sup>b</sup>, Srinivasan Iyengar<sup>a, b</sup>, Yongjoong Lee<sup>a</sup>, Yong Dai<sup>c</sup>

<sup>a</sup> European Spallation Source ESS ERIC, Box 176, 22100 Lund, Sweden

<sup>b</sup> Division of Materials Engineering, Lund University, Box 118, 22100 Lund, Sweden

<sup>c</sup> Paul Scherrer Institut, 5232 Villigen PSI, Switzerland

## ARTICLE INFO

### Article history:

Received 29 November 2016

Received in revised form

28 July 2017

Accepted 26 October 2017

Available online 31 October 2017

### Keywords:

Fatigue limit

Tungsten

Spallation material

## ABSTRACT

Fatigue failure is a distinct possibility in spallation targets like tungsten, subjected to cyclic thermo-mechanical loading caused by beam trips and beam pulses. In this study, the tensile and fatigue properties of pure tungsten from two different processing routes have been determined at room temperature. The specimens tested were sintered, rolled and annealed (RA), as well as sintered and HIPed tungsten (SH).

Tensile tests showed low total strain (~0.25%) and negligible plastic strain for both specimens. However, the UTS for rolled specimens (~1 GPa) was much higher relative to the HIPed material (567 MPa). As tungsten is very brittle, fatigue testing was done primarily under stress-control, using the staircase method and a near zero stress ratio. For the rolled and HIPed materials, fatigue limits (no specimen failure up to  $2 \cdot 10^6$  load cycles) were determined to be 350 MPa and 180 MPa, respectively. In addition, results from strain-controlled multiple-step testing (strain ratio ~0) indicated a slight relaxation in stress for the HIPed material while the rolled specimens showed a purely elastic response.

The implication of fatigue test results for spallation target design is discussed.

© 2017 Elsevier B.V. All rights reserved.

## 1. Introduction

The European Spallation Source (ESS) facility is currently under construction in Lund and scheduled to deliver its first neutrons by 2019. The neutrons are produced through a spallation process where the target material is subjected to a high energy and high power, pulsed proton beam. The pulse frequency is 14 Hz with a duration of 2.86 ms. The energy and power levels are 2 GeV and 5 MW, respectively, and each pulse deposits 357 kJ in the target. The target is designed as a 36-sector wheel, rotating in sync with the beam pulse. Each sector consists of  $8 \times 3 \times 1 \text{ cm}^3$  sized blocks of tungsten, separated by helium cooling channels.

The choice of pure tungsten as the spallation material offers a large total neutron yield due to its high atomic weight and density. Other attractive properties of tungsten are the high melting point (~3400 °C) and good thermal conductivity. However, the brittle nature of tungsten and a ductile-to-brittle transition temperature (DBTT) that is well above room temperature puts the structural

integrity of the target at risk.

Cyclic thermo-mechanical loading caused by beam trips and beam pulses can drive the temperatures in the tungsten blocks momentarily up to a maximum of 500 °C. Stresses due to beam pulse induced temperature changes are calculated to be in the range of 44–110 MPa, giving a maximum stress amplitude of 33 MPa [1]. The loss of structural integrity due to thermal cycling may lead to a non-optimal cooling flow configuration, which would create a hot spot in the target. An increase of the temperature in the tungsten will lead to a higher rate of diffusion driven release of radioactive isotopes.

Any dust produced during vibrations of the target wheel will be filtered and will not lead to a cooling channel blockage. Furthermore, experiments dedicated to assessing the dust production rate, using a vibrating test stand with tungsten blocks in steel cassettes, show that the dust collected after the experiment only contains steel from the cassettes [2].

The lifetime of the target is estimated to be about 5 years, which corresponds to approximately  $4 \cdot 10^7$  pulses and  $2 \cdot 10^6$  beam trips per each target segment [3]. The fatigue life of tungsten strongly depends on the quality of the material, as well as the processing and surface conditions. A good understanding of the effect of these factors on the fatigue properties of pure tungsten is therefore

\* Corresponding author. European Spallation Source ESS ERIC, Box 176, 22100 Lund, Sweden.

E-mail address: [jemila.habainy@ess.se](mailto:jemila.habainy@ess.se) (J. Habainy).

essential while designing the target.

### 1.1. Previous studies

An extensive review of the available literature on fatigue in tungsten was made in conjunction with a recently published article on the fatigue properties of pure tungsten at different temperatures [4]. It shows that there are very few studies on stress-controlled fatigue testing of pure tungsten. Many papers focus on the mechanical properties of tungsten [5–8], some on the effects of alloying additions [9,10], and others on the causes of the DBTT shift [11–13]. The only other study on the fatigue properties of tungsten was published in 1981. Schmunk and Korth [14] used cross-rolled tungsten in both as-received and recrystallized condition to test the tensile and low-cycle fatigue properties at room temperature and at 815 °C. Data for the recrystallized tungsten showed a relatively lower fatigue limit at both temperatures. The room temperature tests had to be carried out under load control, due to negligible plasticity. The high temperature tests could however be performed under strain control.

The room temperature tests in Habainy et al. [4] showed that the fatigue limits of tungsten in the rolled condition were higher (however with large scatter) than those for the forged specimens. The orientation of the rolled specimens was shown to be significant and the fatigue limit corresponding to  $2 \cdot 10^6$  cycles was observed to be  $\sim 237$  MPa in the rolling direction as compared to  $\sim 137$  MPa in the transverse direction. The forged specimens had a minimum fatigue limit of  $\sim 125$  MPa.

Gludovatz et al. [15] showed that size and shape of the grains, as well as the degree of deformation and dislocation density, have a greater impact on the fracture behavior of tungsten, than grain boundary impurities. HIPed material in their study had a higher grain boundary dislocation density due to the elongated grain structure, which seems to have outweighed the negative effect on fracture toughness caused by the grain boundary impurities found in the sintered material.

## 2. Materials and methods

In the present study, tungsten specimens in the sintered, rolled and annealed (RA) as well as sintered and HIPed (SH) conditions have been used. The RA specimens were oriented along the rolling direction. All the specimens were supplied by PLANSEE Metall GmbH, Austria.

The DBTT for tungsten is relatively high, reportedly starting from 250° for hot rolled tungsten and about 350 °C for hot forged [16]. Gorynin et al. [17] have reported that the irradiation of tungsten to a damage level around 0.1 dpa pushes the DBTT to above 500 °C, which is close to the operating temperature of the ESS target. Damage levels in the target are estimated to reach 2 dpa per year, meaning that a newly commissioned target would become brittle already after a month of operation. It was therefore decided to carry out fatigue testing in this work at room temperature, in the brittle regime of tungsten.

The specimens used in this study are tested in the as-received condition. The impurity content is shown in Table 1. The specimen geometry, which is the same for both tensile and fatigue tests, is shown in Fig. 1. According to specifications from the supplier the surface roughness in the gauge section is below 1.6  $\mu\text{m}$ . Prior to testing, each specimen was examined using an optical microscope. All surface defects and their positions, including machining stripes and marks from damage during handling, were noted. The microstructure was examined after a polishing procedure followed by etching with Murakami's reagent, in accordance with ASTM E407 [18]. The average grain size of the material was measured using the

**Table 1**  
Impurity elements in tungsten.<sup>a</sup>

Element	Typical max. value [ppm]	Guaranteed max. value [ppm]
Al	1	15
Cr	3	20
Cu	1	10
Fe	8	30
K	1	10
Mo	12	100
Ni	2	20
Si	1	20
C	6	30
H	0	5
N	1	5
O	2	20
Cd	1	5
Hg	0	1
Pb	1	5

<sup>a</sup> PLANSEE Metall GmbH, Austria.

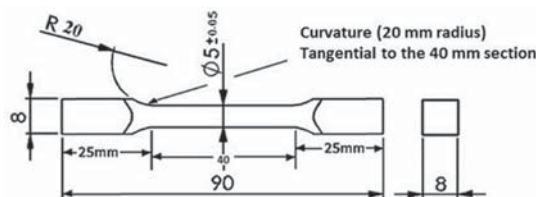


Fig. 1. Specimen geometry.

intercept method described in ASTM E112-13 [19]. Lines of equal length are randomly drawn over the micrograph, and the average number of grain boundary intercepts gives an estimation of the grain size.

### 2.1. Tensile and fatigue testing

The tensile and fatigue tests were carried out in a MTS servo-hydraulic load frame with a maximum capacity of 250 kN, using an Instron 8500 control system. The tensile tests were carried out in accordance with the ASTM E8M standard [20] for testing metallic materials. According to ASTM E8M, for materials with an expected elongation of less than 5%, the strain rate should be set at  $0.015 \pm 0.006$  mm/mm/min. Taking into account the gauge length of the specimen, an elongation rate of 0.6 mm/min has been used in this study.

Due to the brittleness and low plasticity exhibited by tungsten at room temperature, fatigue testing was carried out primarily under stress-control. In these tests only tensile stresses were applied ( $S_{\min} = 5$  MPa, for all tests). This provides a more conservative estimate of the fatigue limit, as cracks generally do not propagate during compressive loading. However, crack growth can still occur during loading in compression if residual tensile stresses are present [21].

Since the brittle nature of the specimens eliminates any significant difference in true vs. engineering stress-strain, all tensile and fatigue data in this paper are presented in the latter form.

At ESS the frequency of the pulsed beam will be 14 Hz. As the target is rotating, and is divided into 36 sectors, the resulting thermo-mechanical load on each section will occur at a  $14/36 = 0.39$  Hz. Running a test of  $2 \cdot 10^6$  cycles would require more than 1400 h, in order to reduce the time a higher frequency of 25 Hz was chosen for all the stress-controlled fatigue tests in this work.

The staircase method (also known as the up-and-down method) [22] was chosen for determining the fatigue limit and its statistical variations. Specimens surviving  $2 \cdot 10^6$  cycles without failure were considered runouts. This limit corresponds to the estimated number of beam trips during the suggested lifetime of the target. The staircase method uses a simple procedure in which a specimen is tested at a given starting stress until failure or runout. If the specimen fails at a given stress amplitude the stress level for the next specimen is decreased. If there is a run out ( $2 \cdot 10^6$  cycles) the stress level is instead increased [23]. The results from the staircase testing are analyzed using the maximum likelihood estimation (MLE), assuming a normal distribution of the threshold stress. It is generally agreed that MLE provides a good estimate of the mean fatigue limit. It was previously thought that the staircase method required a large sample size (40–50 specimens or more). However, Brownlee et al. [24] have shown that the method is fairly reliable for sample sizes as small as 5 to 10, and this is widely recognized in literature. According to common practice, the initial stress level should be set at 35–50% of the UTS [25].

The deformation response of tungsten in the low cycle fatigue (LCF) regime was studied by strain-controlled testing using the multiple-step method. Each step included 50 cycles with a fully reversed or a negative strain ratio. In view of the limited number of specimens available for fatigue testing, this method was useful for getting data over a range of strains. The multiple-step method is schematically shown in Fig. 2. LCF testing was done at a constant frequency of 1 Hz and a maximum of  $10^4$  cycles ( $2 \cdot 10^4$  reversals). The cyclic variation in strain followed a saw-tooth waveform, which was generated using Instron Waverunner software.

### 3. Results and discussion

#### 3.1. Surface condition

The surface condition of both types of tungsten was observed to be reasonably good, with only a few shallow machining stripes or other surface defects being visible. SH materials were noted to be generally more porous, making it difficult to get a very smooth surface on these specimens. Typical surfaces in the gauge section of SH and RA tungsten specimens are shown in Fig. 3.

##### 3.1.1. Pore morphology

The distribution of pores in a material subjected to mechanical loading is important since pore clusters (near or at the surface) can act as stress concentration sites for the initiation of fatigue cracks. Pores would also lower the effective load-bearing area resulting in a lower tensile strength. The shape of the pores is also an important factor which affects fatigue life - an irregular shape is more

detrimental than a perfectly round shape.

The pore shape can be characterized using a form factor  $f_{shape}$  [26,27] which is defined as:

$$f_{shape} = 4\pi A/P^2 \quad (1)$$

where 'A' and 'P' represent the area and perimeter of the pore. A value of unity for the form factor corresponds to a completely rounded pore. Using the image processing software ImageJ to analyze the micrographs, the variation of shape factor with pore size was studied. Fig. 4 shows the relationship for the SH specimen, with about 4.3% porosity. As seen in the figure, smaller pores tend to be spherical, large pores are irregular probably due to a combination of several smaller pores. Only pores larger than  $0.7 \mu m^2$  were quantified in order to avoid bias resulting from resolution where very small pores are only a few pixels in size. At the resolution used here,  $1 \mu m$  corresponds to approximately 9–10 pixels.

#### 3.2. Microstructure

Fig. 5a shows the microstructure of a SH tungsten specimen. It is seen that the pores (the black dots in the image) are uniformly distributed in the microstructure. Fig. 14 in the fractography section of this paper also illustrates the pore distribution in the SH material. The variation in grain size is shown in Fig. 5b. The size is in the range 10–85  $\mu m$ , with an average around 30  $\mu m$ .

The RA specimen has very large, thin and interlocking grains, some as long as 1000  $\mu m$ . These grains are clearly visible to the naked eye after polishing and etching. The surface image shown in Fig. 6a was obtained after etching with Murakami's reagent for over 200s and reveals details within the large grains which indicate a subgrain structure. Fig. 6b shows the effect of rolling using a tri-planar micrograph. The top view of this micrograph shows the rolling plane. In the literature, subgrain structure of rolled tungsten has been observed by Gludovatz et al. [28], Briant et al. [29], as well as Rieth et al. [30].

#### 3.3. Density

The densities of four SH and four RA specimens were determined using the Archimedes Buoyancy method. The average porosity was estimated by comparing the results to the reported density of pure tungsten at 20 °C, which is 19.3 g/cm<sup>3</sup> [31]. The average density and porosity of SH and RA tungsten are presented in Table 2. As expected, RA tungsten is significantly denser than SH, and the value for the SH specimen is in good agreement with the reported porosity of 4% for HIPed tungsten [15]. A minimum density of 19.0 g/cm<sup>3</sup> has been specified for the tungsten bricks in the spallation target. This would correspond to a maximum porosity of 1.55%.

#### 3.4. Hardness

Microhardness measurements were performed using a load of 400 g and a dwell time of 15s. The results showed that the RA tungsten specimens were relatively harder, with an average Vickers hardness number of 508 VHN. The corresponding value for the SH specimens was determined to be 389 VHN. However, it may be noted that the pores are fine and well distributed in SH specimens, which makes it difficult to obtain indentations not affected by the pores.

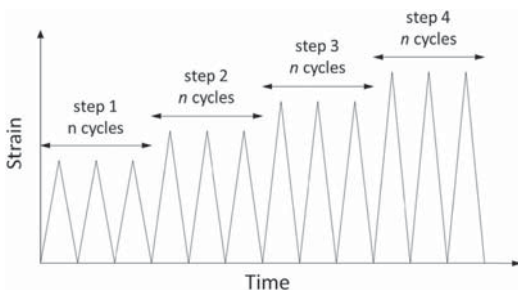


Fig. 2. Multiple-step strain-controlled fatigue testing.

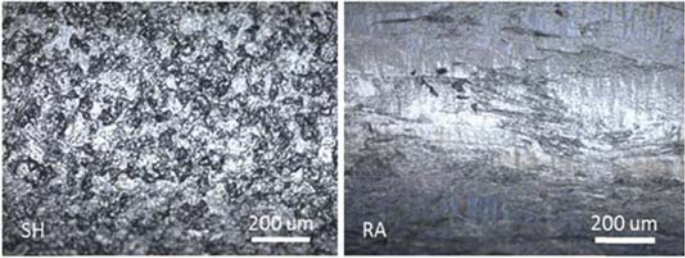


Fig. 3. Images of typical specimen surfaces (SH: sintered and HIPed, RA: sintered, rolled, and annealed).

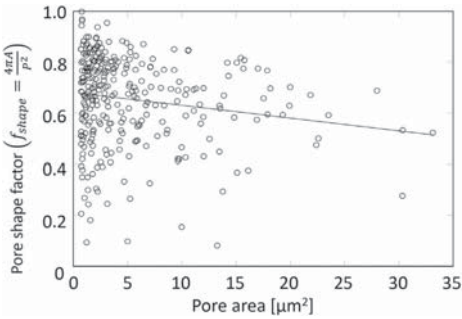


Fig. 4. Pore shape vs pore size in the SH specimens.

3.5. Tensile tests

Engineering stress-strain diagrams corresponding to the monotonic tensile response shown by two SH and one RA specimens are presented in Fig. 7. The experimental data are summarized in Table 3. It is seen that both types of specimens display negligible plasticity. The average ultimate tensile strength of the SH specimens is around 40% lower relative to the RA specimen. The SH specimens also display lower Young's modulus values, which can be explained by the higher porosity of the materials [32].

3.6. Stress-controlled fatigue testing

Fatigue data from constant stress amplitude tests are usually presented in a Wöhler plot where the stress amplitude  $S_a$ , for fully reversed loading, is plotted against the number of cycles to failure ( $N_f$ ). In this work, all the tests have been carried out in the tensile regime with the minimum stress at 5 MPa.

The first SH fatigue specimen, SH4, was tested at an initial stress

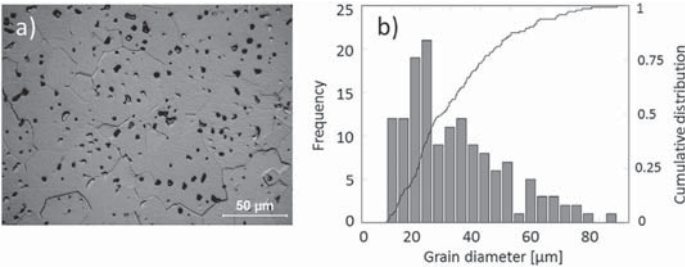


Fig. 5. a) Microstructure and b) grain size distribution in the SH specimen.

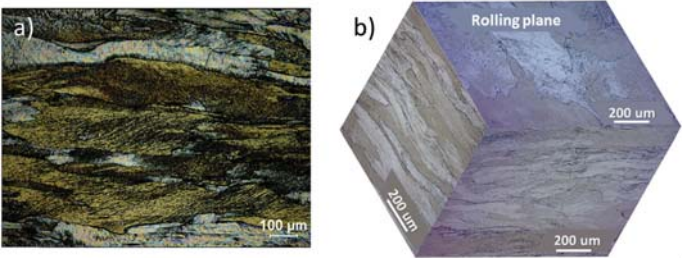
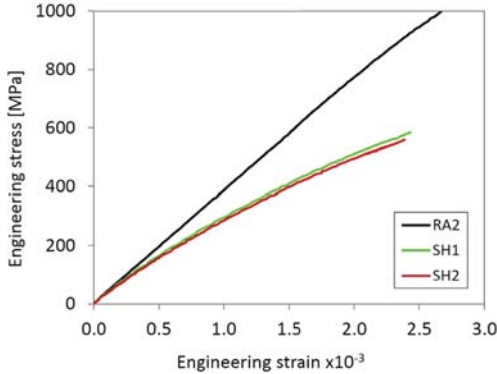


Fig. 6. Optical image of the RA specimen a) surface perpendicular to the rolling direction, b) Triplanar micrograph, showing the rolling plane.



**Table 2**  
Average density at 20 °C.

Specimen	Density [g/cm <sup>3</sup> ]	Porosity [%]
SH	18.475	4.28
RA	19.208	0.48



**Fig. 7.** Tensile testing of SH and RA specimens at room temperature.

**Table 3**  
Tensile test data at room temperature.

Property	SH1	SH2	RA2
Young's Modulus [GPa]	323	332	393
UTS [MPa]	560	573	998
Porosity [%]	4.21	4.37	0.92

amplitude of 180 MPa and resulted in a runout. The stress amplitude was then ramped up in several steps until the specimen failed at 250 MPa. This was done in order to determine the fatigue strength using the least number of specimens. A similar approach was adopted for RA specimens. Data for the runout specimen SH4 at 180 MPa were used in staircase testing between the data for specimens SH9 and SH10. The last fatigue specimen, SH19, was used to get an additional data point in the higher stress regime. A few of the RA runouts were tested again at higher stress amplitudes. These results are not included in the staircase testing and the data is not used for determining the fatigue limit. The results serve only as an indication of the fatigue behavior at higher stresses. Fig. 8 shows S-N data for SH as well as RA specimens. The data from staircase testing are summarized in Table 4.

The Basquin equation [33] for the high cycle, low strain regime can be expressed as:

$$S_a = \text{Stress Amplitude} = \Delta S / 2 = S'_f (2N_f)^b \quad (2)$$

where  $S'_f$  and 'b' are the fatigue strength coefficient and exponent, respectively.  $2N_f$  corresponds to the number of stress cycles to failure. This equation can be modified to take into account the effect of mean stress ( $\sigma_m$ ) and is written as:

$$S_a = (S'_f - S_m) (2N_f)^b \quad (3)$$

Regression analysis of fatigue data for the SH specimens led to the relationship,

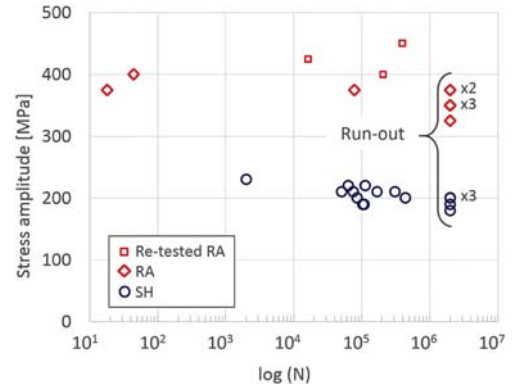


**Fig. 8.** S-N diagram for SH and RA specimens.

$$S_a = 376.94 \times (2N_f)^{-0.0501} \quad (4)$$

A similar relationship could not be derived for the RA specimens due to negligible plasticity and the relatively large experimental scatter involved. However, a one-sided confidence band could be calculated for the fatigue limit. Table 5 presents the mean fatigue limit and standard deviation for SH and RA specimens. Although the single specimen approach was effective in determining the initial stress-level for staircase testing, it should be preferably avoided. Specimen RA5 was initially tested at a stress-level corresponding to the fatigue ratio from previous results [4] and subsequently stepped up in relatively small increments until failure.

The replication rate of fatigue data is 62.50% for SH and 55.55% for RA. According to ASTM guidelines [25], SH specimens fall within the range of allowable data for design, whereas RA specimens are in the research and development regime.

Several specimens from the RA population were rejected due to failure at the grips. This problem had been previously observed for highly brittle, rolled tungsten specimens when using serrated wedge grips. In this study, it was found that the orientation of the specimen during mounting played a critical role; when gripped in the plane perpendicular to the rolling direction, the indentation from the wedge grips initiated cracks which propagated along the grain boundaries. In some cases, such a crack would travel along the entire grip surface, causing delamination. This issue was not as pronounced when the specimen was gripped in the same plane as the rolling direction. However, a number of specimens still failed and had to be rejected. In an attempt to avoid this problem, an aluminum sleeve was placed on the specimen head for protection from indentations. Unfortunately, this caused the specimens to glide in the sleeve at higher stresses. All the RA specimens showed grip damage to varying extents. An example of this is presented in the figures below (Fig. 9a–c). The SH material did not show any damage from such indentations, and no SH specimen was rejected. Additionally, there were no obvious signs of failure originating directly from the machining marks observed in the optical microscope prior to testing.

### 3.7. Strain-controlled fatigue experiments

In fully reversed straining at  $\pm 0.15\%$  and a strain rate of  $10^{-3} \text{ s}^{-1}$ , the SH specimen showed rapid initial hardening for the first 20 cycles, as can be seen in Fig. 10 below. This was followed by a short



**Table 4**  
Summary of staircase test data for SH and RA specimens.

Specimen	$S_a$ [MPa]	$S_{max}$ [MPa]	$N_f$ (Cycles)	Specimen	$S_a$ [MPa]	$S_{max}$ [MPa]	$N_f$ (Cycles)
SH4	180	365	Runout	RA5	325	655	Runout
SH5	230	465	2013	RA7	350	705	Runout
SH6	220	445	112514	RA9	375	755	18
SH7	210	425	170053	RA10	350	705	Runout
SH8	200	405	85874	RA11	375	755	Runout
SH9	190	385	108398	RA15	400	805	44
SH10	190	385	Runout	RA16	375	755	78020
SH11	200	405	Runout	RA18	350	705	Runout
SH12	210	425	75370	RA20	375	755	Runout
SH13	200	405	Runout				
SH14	210	425	310985				
SH15	200	405	Runout				
SH16	210	425	51097				
SH17	200	405	444943				
SH18	190	385	104094				
SH19	220	445	63725				

**Table 5**  
Mean fatigue limit and standard deviation [MPa].

Material	$S$	$\sigma$
SH	185	26.4
RA	371	13.3

period of saturation and even marginal softening. After this, the specimen hardened gradually until failure after 90 cycles. Fig. 11 shows the stress response of the SH specimen during the first cycle in comparison with a cycle at saturation. The strength in tension, 400 MPa, during the first cycle is significantly lower than in compression, 490 MPa.

Since the RA specimens show very little plasticity, any strain controlled cyclic testing would result in a purely elastic response. The stress-strain response for cycle 1 and cycle 50, in the first step of multi-step testing of specimen RA17, show no significant differences. The completely elastic behavior can be seen in Fig. 12. The strain-controlled multiple-step test of specimen RA17, Fig. 13, shows a purely elastic response for all the steps until failure in step 4. Furthermore, the material is cyclically stable in each step and the observed changes in the stress range were negligible.

3.8. Fractography

The fracture surfaces of tungsten specimens were examined using a Scanning Electron Microscope (Philips XL 30 ESEM). It was observed that, in general, the SH specimens fractured

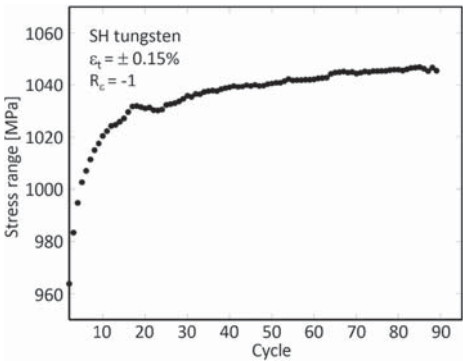


Fig. 10. Hardening of the SH specimen during a strain-controlled fatigue test.

predominantly in an intergranular manner. Larger grains showed a higher frequency of cleavage fracture, while smaller grains tended to remain intact.

SH specimens are associated with a porosity of about 4.3% and are likely to contain microcracks initiated at pores and inclusions. Catastrophic failure occurs due to the growth and coalescence of such microcracks [34] and as such, SH specimens should have a lower fatigue limit relative to RA specimens. The RA specimens tested in this work exhibited low ductility and anisotropic behavior.

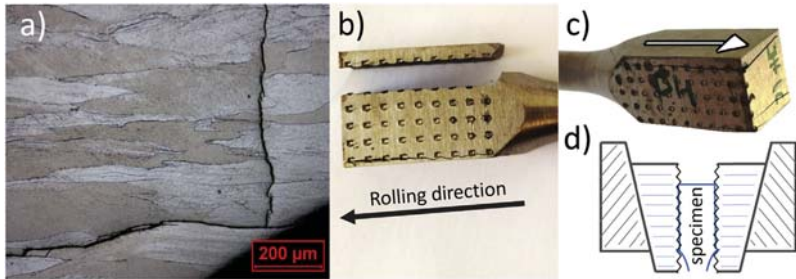


Fig. 9. a) A micrograph showing crack propagation in the RA specimen, initiated by grip indentations. Fig. 9b and c) shows large cracks and complete delamination, the arrows indicate the major rolling direction. Fig. 9d shows an illustration of the serrated wedge grips that are used in the fatigue and tensile tests.

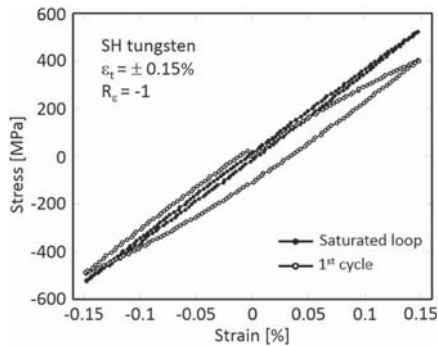


Fig. 11. Stress-Strain relationship during the initial and later stages of testing.

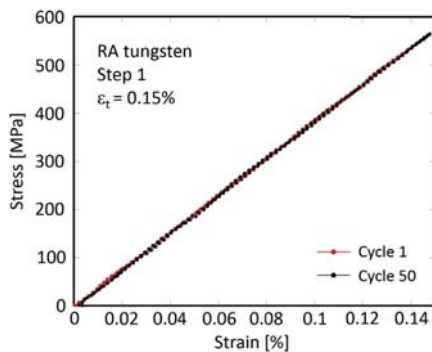


Fig. 12. The elastic response of specimen RA17 during the 1st and 50<sup>th</sup> cycle of step 1.

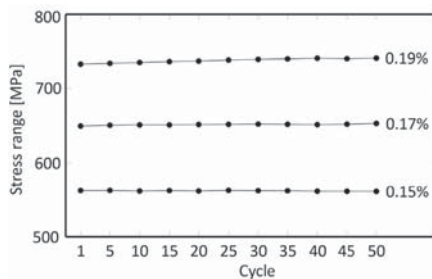


Fig. 13. The variation of stress with cyclic strain. The values at the end of each curve indicate the strain range at that step.

Typical SEM images of the fracture surfaces of SH and RA specimens are presented in Figs. 14–18.

All the RA specimens exhibited transcrystalline brittle failure. This behavior was observed both in the monotonic tensile test and fatigue samples. The large size of the grains (max. 1000  $\mu\text{m}$  in length, with an aspect ratio of about 10) suggests that intergranular failures are unlikely. Further, the grains on the fracture surface do not show any sign of local deformation (Figs. 16 and 17). The transcrystalline nature of the failure in RA specimens can be clearly seen in these images.

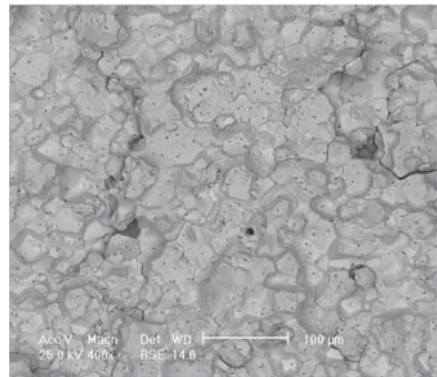


Fig. 14. Predominantly intergranular fracture in specimen SH14.

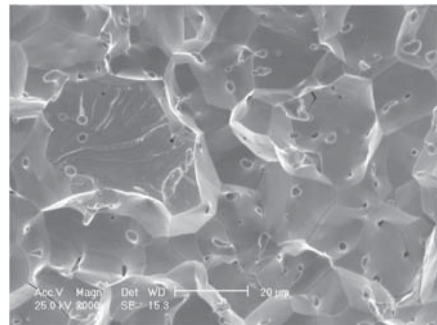


Fig. 15. Mixed inter- and transgranular failure in specimen SH2 after a tensile test.

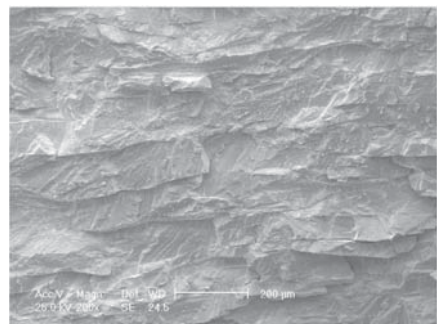


Fig. 16. SEM image of specimen RA10, showing transgranular cleavage.

The fracture surface shown in Fig. 18 suggests that the elongated grains contain subgrains and the specimen could fail through intergranular subgrain fracture.

### 3.9. Current work and target operating conditions

The stress amplitudes employed in the present work are much larger than the stress amplitudes induced by the beam pulse and

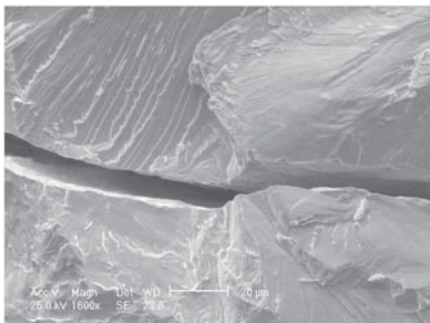


Fig. 17. Fracture surface showing river lines commonly observed in brittle failures.

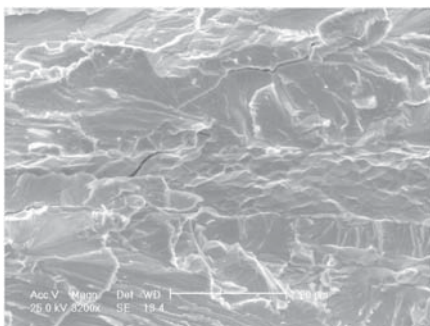


Fig. 18. SEM image of fracture surface of RA2, showing subgrains.

correspond better to the beam trips associated with stress amplitudes of about 110 MPa [1]. However, it has been reported in literature [17,35] that the ultimate tensile strength of an irradiated tungsten specimen could be as low as 60 MPa. Although the metallurgical condition of the tested material is not clearly stated in this paper, the low UTS value is a cause for concern while using pure tungsten targets. It may be noted that the tungsten target at ISIS operates at a maximum stress of 202 MPa [36], but is clad with tantalum. The HIPing process used for cladding introduces compressive residual stresses in tantalum which help in holding the tungsten structure together. It has also been reported that tantalum retains its ductility up to a high irradiation dose [37].

#### 4. Summary and conclusions

RA tungsten specimens used in this study were characterized by very large, elongated and flat interlocking grains (max. 1 mm long, aspect ratio ~10), a high tensile strength (998 MPa), and mean fatigue strength of 371 MPa.

Microstructural examination of the SH specimens showed grain size variation in the range 10–85  $\mu\text{m}$ , with an average size of ~30  $\mu\text{m}$ . Porosity in the specimens was ~4.3%, with most of the pores being relatively round (<5  $\mu\text{m}^2$ ) and evenly distributed in the material. The average UTS value was 567 MPa, while the mean fatigue strength was determined to be 185 MPa.

Microhardness measurements showed that RA specimens were much harder (508 VHN) than the SH specimens (389 VHN). Fractographic studies showed that SH tungsten fails in a predominantly intergranular manner and the monotonic tensile test specimens

were found to have a slightly higher percentage of transgranular cleavage. On the other hand, RA specimens showed pure transgranular cleavage which could be attributed to the long and interlocking nature of the grains.

In strain-controlled tests at zero strain ratio, stress relaxation phenomenon was observed in the case of SH specimens. The relaxation in mean stress continued until no plastic strain was observed in a cycle. In fully reversed straining ( $\pm 0.15\%$ ), there was a rapid initial hardening phase which was followed by a slower and gradual hardening of the specimen until failure.

Results from this work and literature data on irradiated tungsten present an important design guideline for the ESS target, which is to reduce the maximum tensile stress to a low level. The design requirement set for the tungsten blocks in the ESS target wheel is a maximum mean stress of 100 MPa, with a maximum stress amplitude of 50 MPa. The shape and size of the tungsten blocks has been chosen to meet these requirements. Simulations show that with the current design of the blocks ( $8 \times 3 \times 1 \text{ cm}^3$ ) the maximum mean stress will be below 100 MPa.

#### Acknowledgements

The authors are thankful to Zivorad Zivkovic for invaluable assistance in the experimental work. Research funding and support from the European Spallation Source (ESS, Lund) is gratefully acknowledged.

#### References

- [1] A. Aguilar, M. Magan, I. Herranz, F. Sordo, T. Mora, R. Vivanco, G. Bakedano, J. Aguilar, L. Mena, M. Mancisidor, J.L. Martinez, Equipment Specification Document: Spallation Material, Report No. ESS-0058358, September 16, 2016.
- [2] E. Abad, F. Sordo, Vibration Tests, Technical Report No. ESS-0055645, European Spallation Source ERIC, 2017.
- [3] S. Peggs, R. Kreiser (Eds.), ESS Technical Design Report, April 2013, ISBN 978-91-980173-2-8.
- [4] J. Habainy, S. Iyengar, Y. Lee, Y. Dai, Fatigue behavior of rolled and forged tungsten at 25°, 280° and 480°C, J. Nucl. Mater. 465 (2015) 438–447.
- [5] A.S. Wronski, A.C. Chilton, The effects of temperature and pressurization on the tensile and compressive properties of polycrystalline cast tungsten, Scr. Metall. 3 (1969) 395–400.
- [6] F.F. Schmidt, H.R. Ogden, DMIC Report 191: the Engineering Properties of Tungsten and Tungsten Alloys, 1963.
- [7] D. Rupp, S.M. Weygand, Loading rate dependence of the fracture toughness of polycrystalline tungsten, J. Nucl. Mater. 417 (1–3) (2011) 477–480.
- [8] V. Krsjak, S.H. Wei, S. Antusch, Y. Dai, Mechanical properties of tungsten in the transition temperature range, J. Nucl. Mater. 450 (1–3) (Jul. 2014) 81–87.
- [9] P.L. Raffo, Yielding and fracture in tungsten and tungsten-rhenium alloys, J. Less-Common Met. 17 (1969) 133–149.
- [10] H. Braun, K. Sedlatschek, On the influence of small additions of nonmetals and metals on the sintering, working and the mechanical properties of tungsten, J. Less-Common Met. 2 (1960) 277–291.
- [11] K. Farrell, A.C. Schaffhauser, J.O. Stiegler, J. Less-Common Met. 13 (1967) 141–155.
- [12] A. Giannattasio, S.G. Roberts, Strain-rate dependence of the brittle-to-ductile transition temperature in tungsten, Philos. Mag. 87 (17) (2007) 2589–2598.
- [13] Y. Zhang, A.V. Ganeev, J.T. Wang, J.Q. Liu, I.V. Alexandrov, Observations on the ductile-to-brittle transition in ultrafine-grained tungsten of commercial purity, Mater. Sci. Eng. A 503 (1–2) (2009) 37–40.
- [14] R.E. Schmunk, G.E. Korth, Tensile and low-cycle fatigue measurements on cross-rolled tungsten, J. Nucl. Mater. (1981) 943–948 vol. 103 & 104.
- [15] B. Gludovatz, S. Wurster, T. Weingartner, A. Hoffmann, R. Pippan, Influence of impurities on the fracture behaviour of tungsten, Philos. Mag. 91 (22) (2011) 3006–3020.
- [16] T. Shen, Y. Dai, Y. Lee, Microstructure and tensile properties of tungsten at elevated temperatures, J. Nucl. Mater. 468 (2016) 348–354.
- [17] I.V. Gorynin, V.A. Ignatov, V.V. Rybin, S.A. Fabritsiev, V.A. Kazakov, V.P. Chakin, V.A. Tsykanov, V.R. Barabash, Y.G. Prokofyev, Effects of neutron irradiation on properties of refractory metals, J. Nucl. Mater. 191–194 (1992) 421–425.
- [18] ASTM E407: standard practice for microetching metals and alloys, in: Annual Book of ASTM Standards, vol. 3, 2007.
- [19] ASTM E112–E113: Standard Test Methods for Determining Average Grain Size, ASTM International, West Conshohocken, PA, 2013.
- [20] ASTM E8/E8M: standard test methods for tension testing of metallic materials 1, Annu. B. ASTM Stand. 4 (2010) 1–27 no. C.
- [21] N.A. Fleck, C.S. Shin, R.A. Smith, Fatigue crack growth under compressive

- loading, *Eng. Fract. Mech.* 21 (1) (1985) 173–185.
- [22] W.J. Dixon, A.M. Mood, A method for obtaining and analyzing sensitivity data, *J. Am. Stat. Assoc.* 43 (241) (1948) 109–126.
- [23] R. Pollak, A. Palazotto, T. Nicholas, A simulation-based investigation of the staircase method for fatigue strength testing, *Mech. Mater.* 38 (12) (2006) 1170–1181.
- [24] K.A. Brownlee, J. Hodges Jr., M. Rosenblatt, The up-and-down method with small samples, *J. Am. Stat. Assoc.* 48 (262) (1953) 262–277.
- [25] American Society for Metals, *ASM Handb. Mech. Test.* 8 (1985).
- [26] N. Chawla, T. Murphy, K. Narasimhan, M. Koopman, K. Chawla, Axial fatigue behavior of binder-treated versus diffusion alloyed powder metallurgy steels, *Mater. Sci. Eng. A* 308 (2001) 180–188.
- [27] N. Chawla, X. Deng, Microstructure and mechanical behaviour of porous sintered steels, *Mater. Sci. Eng. A* 390 (2005) 98–112.
- [28] B. Gludovatz, S. Wurster, A. Hoffmann, R. Pippan, A study into the crack propagation resistance of pure tungsten, *Eng. Fract. Mech.* 100 (Mar. 2013) 76–85.
- [29] C.L. Briant, E.L. Hall, The microstructure of rolled and annealed tungsten rod, *Metall. Trans. A* 20 (9) (1989) 1669–1686.
- [30] M. Rieth, A. Hoffmann, Influence of microstructure and notch fabrication on impact bending properties of tungsten materials, *Int. J. Refract. Met. Hard Mater.* 28 (6) (2010) 679–686.
- [31] D.T. Hurd, “Tungsten” in *Metals Handbook, Volume 1, Properties and Selection of Metals*, American Society for Metals, Metals Park, Novelty, Ohio, 1961.
- [32] K.K. Phani, S.K. Niyogi, Young’s modulus of porous brittle solids, *J. Mater. Sci.* 22 (1987) 257–263.
- [33] S. Suresh, *Fatigue of Materials*, second ed., Cambridge University Press, Cambridge, 2004, pp. 223–226.
- [34] G.S. Upadhyaya, *Powder Metallurgy Technology*, Cambridge International Science Publishing, Cambridge, 1997.
- [35] H. Ullmaier, F. Carsughi, Radiation damage problems in high power spallation neutron sources, *Nucl. Instrum. Methods Phys. Res. B* 101 (1995) 406–421.
- [36] P. Loveridge, D. Wilcox, Thermo-Mechanical Analysis of ISIS TS2 Spallation Target, 5th High Power Targetry Workshop, Fermilab, May 21, 2014.
- [37] J. Chen, H. Ullmaier, T. Flossdorf, W. Kühnlein, R. Duwe, F. Carsughi, T. Broome, Mechanical properties of pure tantalum after 800 MeV proton irradiation, *J. Nucl. Mater.* 298 (2001) 248–254.



# PAPER III

J. Habainy, S. Iyengar, K. B. Surreddi, Y. Lee, Y. Dai

**Formation of oxide layers on tungsten at low oxygen partial pressures**

*Journal of Nuclear Materials*, vol. 506, 2018, pp. 26-34

Reproduced with permission from Elsevier





Contents lists available at ScienceDirect

## Journal of Nuclear Materials

journal homepage: [www.elsevier.com/locate/jnucmat](http://www.elsevier.com/locate/jnucmat)

## Formation of oxide layers on tungsten at low oxygen partial pressures

Jemila Habainy<sup>a, b, \*</sup>, Srinivasan Iyengar<sup>a, b</sup>, Kumar Babu Surreddi<sup>c</sup>, Yongjoong Lee<sup>a</sup>, Yong Dai<sup>d</sup><sup>a</sup> European Spallation Source ESS ERIC, Box 176, 22 100, Lund, Sweden<sup>b</sup> Div. of Materials Engineering, Lund University, Box 118, 22 100 Lund, Sweden<sup>c</sup> Materials Science, Dalarna University, SE-791 88 Falun, Sweden<sup>d</sup> Paul Scherrer Institut, 5232 Villigen PSI, Switzerland

## ARTICLE INFO

## Article history:

Received 31 January 2017

Received in revised form

15 September 2017

Accepted 11 December 2017

Available online 14 December 2017

## Keywords:

Tungsten

Oxidation

Spallation target

## ABSTRACT

This work focuses on the oxidation of tungsten in inert gas atmospheres containing oxygen and moisture. It is particularly relevant for the European Spallation Source where the tungsten target is cooled by purified helium gas and the 5 MW proton beam can raise the maximum target temperature beyond the threshold for oxidation. Tungsten discs were oxidized isothermally at 400° to 900 °C for 2 h in pure helium and helium mixed with oxygen and water vapor, with varying partial pressures up to 500 Pa. Tungsten was oxidized even with a small amount of oxygen ( $\leq 5$  ppm) present in industrially pure helium. Non-isothermal oxidation of tungsten foils was carried out in water vapor ( $\sim 100$  Pa), *in situ* in an environmental scanning electron microscope. On specimens oxidized in inert gas containing water vapor (2 h,  $p_{H_2O} \sim 790$  Pa), Auger electron spectroscopy studies confirmed the presence of a thin oxide layer (40 nm) at 400 °C. At 500 °C the oxide layer was 10 times thicker. A dark, thin and adherent oxide layer was observed below 600 °C. Above this temperature, the growth rate increased substantially and the oxide layer was greenish, thick and porous. Oxide layers with varying stoichiometry were observed, ranging from  $WO_3$  at the surface to  $WO_2$  at the metal–oxide interface. For comparison, oxidation of tungsten alloys in He–5% $O_2$  was studied. The implications of this work on the design and operation of the helium loop for cooling the target are discussed.

© 2017 Elsevier B.V. All rights reserved.

## 1. Introduction

This study focuses on the oxidation behavior of alloyed and unalloyed tungsten at elevated temperatures, in a helium atmosphere containing small amounts of oxygen and moisture present as impurities. This is of particular interest to the European Spallation Source (ESS) which has chosen to use unalloyed tungsten as the spallation material. The target is designed as a rotating wheel carrying tungsten bricks of the size  $80 \times 30 \times 10$  mm. The rotation is synchronized with the 14 Hz pulse of the 2 GeV proton beam. The duration of each beam pulse is 2.86 ms with a 62.5 mA beam current, providing 5 MW time averaged beam power to the target with a 4% duty factor. The heat generated in tungsten from the beam/material interaction is cooled by active helium flow, with the

maximum temperature in the target reaching 450 °C. Although helium is an inert gas, the incidental presence of small amounts of oxygen and moisture can lead to oxidation and erosion of the target.

The spallation process produces a large amount of radioactive isotopes, fast neutrons and highly penetrating gamma radiation [1], thus making safety issues a top priority. One particularly important issue is the formation of highly volatile, radioactive tungsten hydroxides which can potentially be released into the surroundings under accidental conditions. Such a major event could be triggered by overheating of the target, caused for example by an incidentally over-focused beam [2]. If the higher beam intensity is not corrected in time, it can cause the target vessel to lose its function of helium coolant confinement, which would expose the overheated tungsten to an oxidizing environment, and allow for the release of radioactive isotopes in forms of gas, aerosol and volatiles. A similar incident can occur in the case of loss of coolant in the target. Since the decay heat in the tungsten will drive the temperature up, engineering efforts have been made to secure a passive cooling path to

\* Corresponding author, European Spallation Source ESS ERIC, Box 176, 22 100, Lund, Sweden.

E-mail address: [jemila.habainy@ess.se](mailto:jemila.habainy@ess.se) (J. Habainy).



keep the tungsten below the onset temperature of tungsten oxide sublimation [3].

### 1.1. Present work

The main objective of this study is to understand the oxidation characteristics of unalloyed tungsten in gaseous atmospheres and temperatures of relevance to ESS, during normal as well as off-normal operating conditions. The design lifetime of the target wheel is five years under 5 MW beam power. During normal operation, the tungsten will reach temperatures above 400 °C, which is close to the temperature at which the rate of oxidation becomes significant. The helium loop for the target cooling has a purification system to keep the oxygen and moisture levels low; however, there is a risk that even a small impurity level of oxygen and vapor could be enough to oxidize the tungsten. For an efficient design of the target primary cooling loop, it is important to understand the oxidation characteristics of tungsten in such gaseous environments. It is also important to identify the temperature at which the oxide transitions from the adherent and protective type to the porous, non-protective one with a significantly higher growth rate.

Although oxidation of tungsten at high temperatures has been studied extensively by Gulbransen and co-workers [4–9] and most recently by Greene and Finrock [10,11], these studies are restricted to oxygen and steam-rich atmospheres. There is not much information in the literature on the oxidation of tungsten at low oxygen partial pressures and at relatively low temperatures. Hence, the present study was taken up to gather oxidation data for unirradiated unalloyed tungsten (400°–900 °C) in inert gas mixtures containing small amounts of oxygen ( $p_{O_2}$ : 0.5 Pa to 5.1 kPa) or steam ( $p_{H_2O}$ : 100–790 Pa). For purposes of comparison, the oxidation behavior of a few tungsten alloys has also been studied in this work.

### 1.2. Literature review

Tungsten is characterized by a high density, extremely high melting point and good strength at high temperatures. However, a major drawback is its poor resistance to oxidation which limits the use of uncoated tungsten as a structural material at elevated temperatures. Tungsten is oxidized even at relatively low temperatures [12], and the rate of oxidation becomes significant above 600 °C [13]. At even higher temperatures the oxide becomes volatile. The oxidation process is relatively complex, owing to the wide range of oxides formed with varying stoichiometries, and to the volatility of the oxide. Consequently, the results reported in the literature on the kinetics, composition and structure of tungsten oxides vary widely [14].

A phase diagram for the W–O system [15] is presented in Fig. 1. The diagram shows the presence of stoichiometric oxides ( $WO_2$  and  $WO_3$ ) and a number of non-stoichiometric oxides corresponding to the formula  $WO_{3-x}$  where  $0 < x < 1$ . The composition and stability of the non-stoichiometric oxides are strongly dependent on the partial pressure of oxygen. Despite the large number of oxides found in the W–O system, the most commonly encountered ones are  $WO_2$ ,  $WO_{2.72}$  ( $W_{18}O_{49}$ ),  $WO_{2.9}$  ( $W_{20}O_{58}$ ) and  $WO_3$  [8,16].

The oxides exhibit colors from yellow to green to dark blue;  $WO_3$  (yellow),  $W_{20}O_{58}$  ( $WO_{2.9}$ , dark blue),  $W_{18}O_{49}$  ( $WO_{2.72}$ , violet) and  $WO_2$  (chocolate brown). The color changes are related to a loss of oxygen in the original  $WO_3$  structure, generating an additional valence state and cation to cation charge transfer between  $W^{6+}$  and a reduced ion [17,18].

#### 1.2.1. The different stages of oxidation

The oxidation of tungsten proceeds through several distinct

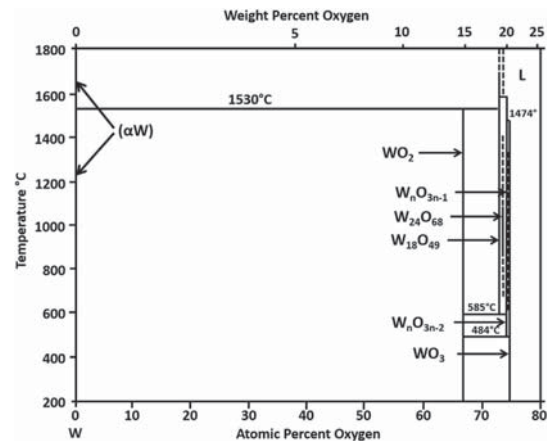


Fig. 1. The W–O system [15].

steps which are governed by different mechanisms. The initial oxidation is phase boundary controlled, with no diffusional effects assuming no limitation on oxygen transport in the gas phase. During the initial stages of oxidation, for thin oxide layers (2–4 nm) and low temperatures (<400 °C), the oxide growth rate follows the logarithmic law [19]. At slightly higher temperatures and thicker oxide layers, the parabolic law governs the oxide growth. A protective film is formed and the rate is limited by the diffusion of  $O^{2-}$  ions through the oxide scale. At this stage, the oxide layer on tungsten is often very thin, adherent and protective, thus limiting further oxidation. Different compositions have been reported for this layer, such as  $WO_2$  [5],  $WO_{2.75}$  [20], and  $WO_{2.72}$  [8,13].

The second stage of oxidation has been observed between 500° and 700 °C, involving the growth of the dark layer as well as the formation and growth of a bright yellow oxide layer. The yellow oxide consists of  $WO_3$  which is usually found in the outermost layer where the oxygen content is the highest. Oxygen ion vacancies play an important role in the growth of  $WO_3$ . Sikka and Rosa [21] confirmed this view with oxidations experiments in which Pt-wire markers moved from the oxide/metal interface toward the oxide/gas interface, showing the inward diffusion of oxygen ions through the oxide. Cifuentes et al. [22] observed that the oxidation was initially controlled by the formation of a continuous  $W_{18}O_{49}$  layer which cracked eventually, leading to a higher oxidation rate and linear kinetics. Thick and columnar  $WO_{2.92}$  formed on the cracked  $W_{18}O_{49}$  layer, followed by the formation of the yellow  $WO_3$  layer on top.

The next stage of the oxidation process occurs when the  $WO_3$  has covered the surface of the thin dark film. Being porous, not particularly adhesive and having a Pilling-Bedworth ratio of 3.35, this oxide creates high stresses causing the oxide layer to crack and thus exposing new surface to the oxygen. The non-protective nature of  $WO_3$  results in a linear oxidation rate.

#### 1.2.2. Reaction with steam and oxide sublimation

At higher temperatures, the oxide becomes volatile. The onset temperature is related to pressure, moisture and oxygen content of the gas, gas flow rate, and oxide film thickness [7,10,11,23]. The lowest reported onset temperature for sublimation of tungsten oxide (in 100% steam) is in the range 700°–800 °C [11]. Numerous reports suggest that any moisture content in the atmosphere will enhance the volatility and speed up the oxidation process [24], as

well as affect the onset temperature [25]. Greene and Finfrock [10,11] state that the vaporization of tungsten depends entirely on the presence of steam or water vapor in contact with hot tungsten. The tungsten will oxidize in dry air, but the hydration of  $\text{WO}_3$  to tungstic acid vapor  $\text{WO}_3\cdot\text{H}_2\text{O}$  does not occur. At high temperatures and low steam content, the oxidation rates will be high and the sublimation rate will be low. On the other hand, at high steam contents, the oxidation rate will be suppressed due to lack of free oxygen molecules, but the abundance of steam will enhance the hydration reaction and thus also the sublimation. Greene and Finfrock conducted experiments at 1000 °C with varying air/steam ratios. In 100% air no vaporization was detected, while a steam content of 85% yielded the maximum amount of vaporized oxide. Analysis of the aerosol produced during these experiments revealed a stoichiometry of  $\text{WO}_{2.7}$ , which would indicate that the volatile hydrate consists of both  $\text{WO}_2$  and  $\text{WO}_3$ .

Several studies [4,6,24,25] have found the oxide sublimation rate to be higher than the rate of oxidation somewhere between 1000° and 1300 °C. Above 1300 °C, oxidation follows a linear rate law and the rate increases exponentially with temperature [26]. At these temperatures, the oxygen pressure and gas flow have a significant effect on the oxidation of tungsten and oxide volatility. According to a study by Gulbransen and Andrew [4], a specimen oxidized at 1200 °C at an oxygen pressure of  $10^3$  Pa did not show oxygen pickup, while a specimen at 1000 °C and  $10^4$  Pa gained 14.5 mg/cm<sup>2</sup> in just 10 min.

## 2. Materials and methods

Two types of unalloyed tungsten samples have been used in this work - tungsten discs (20 mm in diameter, 3 mm thick, ~18 g in weight), and tungsten foils (5.5 mm in diameter, 26 µm thick, ~10 mg in weight). The discs were received in electropolished condition from Beijing Tian-Long Tungsten and Molybdenum Co., and the foils and tungsten alloy discs were fabricated by Plansee Metall GmbH, Austria. Both types of the unalloyed tungsten were having a minimum purity of 99.97% W. The alloys had the following alloying elements: D176 – 5% Ni, 1% Fe; D185 – 2% Ni, 1% Fe; IT170 – 7% Ni, 2.5% Cu; IT180 – 3.5% Ni, 1.5% Cu.

Oxidation studies were carried out in different setups, with the bulk of the work done using a TGA (Thermogravimetric Analysis) unit, in which the larger tungsten discs were oxidized under isothermal conditions. A Carbolite STF 15/75/450 vertical furnace was used for heating the sample disc, which was suspended from the bottom hook of a Shimadzu AUW120D microbalance. The balance was placed about a meter above the furnace, with two radiation shields separating them. A Chromalloy O Resistance (Fe75/Cr20/Al5) wire (0.5 mm in diameter) was used to suspend the sample disc. Mass changes could be measured with an accuracy of ±0.01 mg. Initially, the sample disc was placed in the upper furnace region, close to the water-cooled area and the furnace was flushed with helium gas (150 ml/min) for 30 min, at room temperature. The helium was dried before to entering the furnace by passing through three drying towers containing anhydrous calcium chloride. Furnace heating was then started, with continuous flushing by the dry helium gas. The heating period was about 30 min, with deviations depending on the desired temperature for the experiment (400°–900 °C). When the temperature, as indicated by a K-type thermocouple, was stable in the even temperature zone of the furnace, the sample disc was carefully lowered into this zone. The purge gas was then replaced with the oxidizing gas mixture. From this point, the mass change in the sample disc was monitored continuously, every 10 s, up to a maximum of 2 h. After this time, the oxidizing gas flow is replaced with the helium gas and the sample disc is raised up to the cooler regions of the furnace. Then

the sample is removed from the furnace and stored in a desiccator.

The oxidizing gas mixtures used for the tests were He-5% $\text{O}_2$ , He-0.5% $\text{O}_2$ , pure helium (max.  $\text{O}_2$  impurity: 5 ppm) and He-Ar- $\text{H}_2\text{O}$  ( $p_{\text{H}_2\text{O}}$ : 790 Pa). Pure argon gas, with a flow of 50 ml/min, was bubbled through distilled water at room temperature (25 °C), and mixed with the dry helium (150 ml/min) to get the last-named gas mixture. The He- $\text{O}_2$  gas mixtures were supplied by Aga gas company, Stockholm.

Oxidation tests on tungsten foils were carried out in a NETZSCH STA 449 F3 Jupiter Simultaneous Thermal Analysis unit, in which data from differential scanning calorimetry (DSC) and thermogravimetry could be obtained simultaneously. The samples were first weighed in the STA at room temperature and the chamber was closed and evacuated to remove the air. This was followed by flushing with pure and dry argon gas, evacuation and flushing again with argon. This procedure was repeated at least three times to ensure the complete removal of air from the sample chamber. Pure argon gas ( $p_{\text{O}_2} \leq 5$  ppm) was used as the use of helium was associated with drift in the mass change data. The flow of gas in the specimen chamber was 70 ml/min. The foil sample, placed in an alumina crucible, was heated at 5 °C/min to the desired experimental temperature and held at that temperature for 2 h, before cooling to room temperature. After stabilization for 15 min at the desired temperature, the inert gas was partially replaced by pure and dry oxygen to start the oxidation experiment. After the holding time of 2 h, the oxygen supply was cut off and 100% argon flow was resumed and the sample was cooled to room temperature. A correction file from a blank experiment was used to subtract the background noise from the actual results.

Another technique used to characterize the oxidation behavior of tungsten was the in-situ experiment carried out in a hot stage mounted inside an Environmental Scanning Electron Microscope (ESEM). A tungsten foil specimen was heated in a low-pressure environment consisting of only water vapor at a pressure of 100 Pa.

### 2.1. Post oxidation studies

After the oxidation experiments, sample surfaces were studied using Scanning Electron Microscopy (SEM, Philips XL-30 ESEM) and light optical microscopy (LOM). The surface oxides were characterized by X-ray diffraction (XRD) using a vertical Stoe Stadi X-ray apparatus with germanium monochromator, copper tube and linear PSD as the detector in reflective mode. The composition of the oxide scale was studied using Energy-dispersive X-ray spectroscopy (EDS), and Auger Electron Spectroscopy (AES) was used to determine the oxide scale thickness and the elemental distribution in it. For this purpose, a PHI 700 Scanning Auger Nanoprobe with 4 kV  $\text{Ar}^+$  ion sputtering with a sputter rate of 55 nm/min was used. The sputter rate was determined using a  $\text{Ta}_2\text{O}_5$  reference standard, under the same sputtering conditions.

## 3. Results and discussion

### 3.1. TGA studies (disc specimens – 20 mm in diameter, 3 mm thick)

Fig. 3 presents the increase in mass of the tungsten specimen during oxidation in a stream of dry He-0.5% $\text{O}_2$  gas mixture. No mass change is indicated after 2 h at 400 °C, followed by a marginal increase at 500 °C. As the temperature increases, tungsten oxidizes more and more to reach almost 18 mg/cm<sup>2</sup> at 900 °C. The appearance of four of the oxidized specimens is shown in Fig. 2. The oxide layer formed at 522 °C is thin and adherent, at 618 °C it relatively unchanged, but appears to be covered in a very thin layer of the porous type of oxide. At 716 °C the oxidation rate and the thickness of the greenish porous oxide has increased significantly, and at

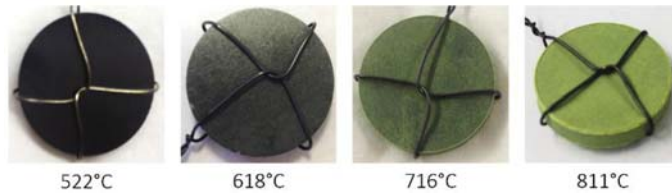


Fig. 2. Tungsten specimens after oxidation in a He-0.5%O<sub>2</sub> gas mixture (2 h).

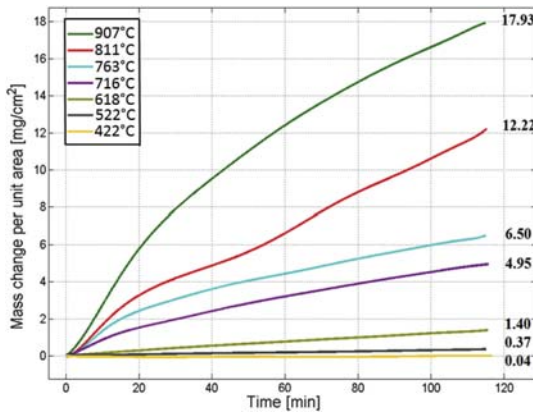


Fig. 3. Oxidation of Tungsten in He-0.5%O<sub>2</sub> gas mixture (2 h).

811 °C the specimen is fully covered by a thick green layer. The mass change curve for the specimen at 811 °C indicates changes in the growth rate during the oxidation, which could be attributed to a decrease in oxide stability and possible oxide spallation.

A number of oxides are normally formed on the surface of tungsten, with WO<sub>2</sub> at the metal-oxide interface and WO<sub>3</sub> at the oxide-gas interface. In between these two oxides, a range of non-stoichiometric oxides (WO<sub>3-x</sub>) are usually present. The color of the oxides depends on the stoichiometry; pure WO<sub>3</sub> is yellow but even very small oxygen deficiencies change the color, e.g. WO<sub>2.98</sub> is blue although there is no significant change in crystal structure. Lower oxides (WO<sub>2.4</sub> to WO<sub>2.7</sub>) shift in colors of red, violet and blue [27].

Fig. 4 shows the oxidation of tungsten in a He-Ar-H<sub>2</sub>O gas mixture. The partial pressure of water vapor in the mixture was 790 Pa. It is seen that the oxidation of tungsten in the presence of small amounts of water is significant, but lower than in the He-0.5% O<sub>2</sub> gas mixture at higher temperatures. This observation reinforces the importance of drying the helium gas coolant in the ESS spallation facility. The appearance of the oxides on these specimens were similar to the ones shown in Fig. 2, although with slightly thinner layers.

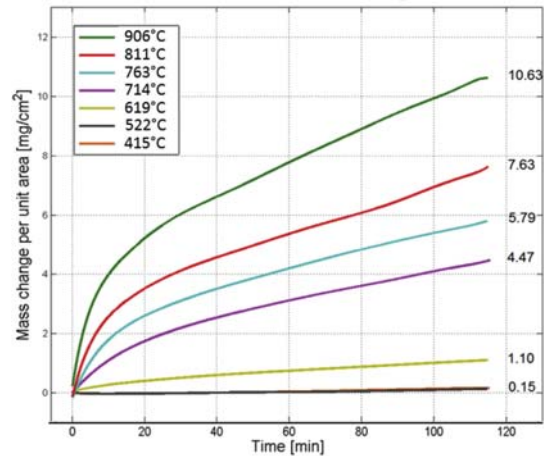


Fig. 4. Oxidation of tungsten in a He-Ar-H<sub>2</sub>O gas mixture (2 h,  $p_{H_2O}$ : 790 Pa).

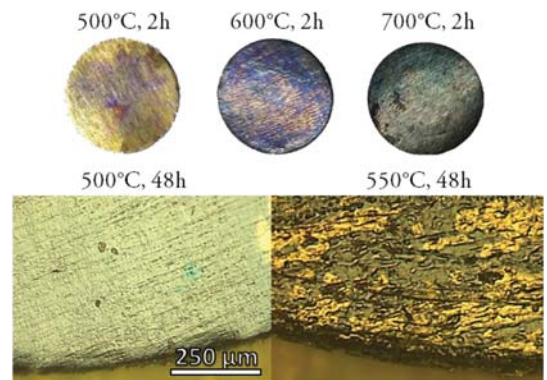


Fig. 5. Surface images of tungsten foils (5.5 mm dia.) after oxidation in argon containing maximum 5 ppm of oxygen.

### 3.2. DSC-STA studies (tungsten foils, 5.5 mm in diameter, 26 µm thick)

These studies were carried out in a stream of dry and pure argon at atmospheric pressure, with oxygen as an impurity, i.e. with an oxygen partial pressure of maximum 5 ppm. Tests were carried out at different temperatures for varying periods of time up to 48 h.

Fig. 5 shows surface images of the oxidized samples. It is seen that the surface of the oxidized specimen is uneven after 48 h at a relatively low temperature of 500 °C. The oxygen impurity in the gas, although in very small amounts, is enough to oxidize the tungsten surface over long periods of time. The oxide layers formed at low temperatures are adherent and protective, but higher

temperatures can lead to relatively thicker and unstable oxide scales. The surfaces of the samples were analyzed using X-ray diffraction, the results are summarized in section 3.4 of this paper.

### 3.3. *In situ* ESEM studies (tungsten foils, 3 mm in diameter, 26 $\mu\text{m}$ thick)

In these studies, the tungsten foil was placed in a hot stage inside the specimen chamber which was flushed repeatedly with water vapor and evacuated to a low pressure of 100 Pa. The specimen was then heated slowly and the changes in surface characteristics were observed continuously. Fig. 6 shows the images of the tungsten surface taken at various temperatures during the heating of the specimen. It is seen that, the changes are not significant up to about 600 °C. Beyond this temperature, even at the low partial pressure of water vapor (100 Pa), oxidation sets in and there is a marked change in surface characteristics. At temperatures above 800 °C, the oxide layer seems to cover the surface almost completely.

### 3.4. X-ray diffraction studies (XRD)

The oxides forming on the surface of the tungsten foil oxidized in pure argon ( $p_{\text{O}_2} \leq 5$  ppm, 2 h) were identified using XRD. These data are shown in Fig. 7, together with the diffractograms.  $\text{W}_{18}\text{O}_{49}$  was observed at 600° as well as at 700 °C.

For comparison, 3 mm thick tungsten discs were oxidized in air for 24 h, at 500° and 600 °C, and the oxide scale was analyzed using XRD. The results show that  $\text{W}_{18}\text{O}_{49}$  dominates at 500 °C. As the temperature is increased to 600 °C, the oxide layer corresponds to the stoichiometric  $\text{WO}_3$ .

### 3.5. Auger electron spectroscopic studies (AES)

Auger electron spectroscopy was used to characterize a number of oxidized samples in order to assess the thickness of the oxide scale, acquire a depth profile and study the variation in stoichiometry of the oxides. Argon ion sputtering, at a rate of 55 nm/min,

was used in between the surface scans to create the depth profile. In order to clean the surfaces prior to examination, a short ion sputtering treatment was carried out. Scans after this pre-sputtering showed that in all cases only a small amount of carbon, present as an impurity, was removed.

AES is normally used for studying very thin layers, therefore, only specimens oxidized at 400°, 500° and 600 °C (2 h) could be examined. The measurement of a sample oxidized at 714 °C (He-Ar- $\text{H}_2\text{O}$ ) was discontinued at a sputter depth of 6.6  $\mu\text{m}$  due to time constraints. This sample was instead examined in a scanning electron microscope with energy-dispersive X-ray spectroscopy (EDS). Fig. 8 presents data from the oxide thickness measurements. The thickness is taken at the midpoint of the slope where the atomic concentration of oxygen drops, see e.g. Fig. 9, bottom right graph.

The average oxide thickness of the He-Ar- $\text{H}_2\text{O}$  specimen oxidized at 415 °C is 35 nm, whereas that of the He-0.5% $\text{O}_2$  specimen (422 °C) is 60 nm. At 522 °C the oxide layer of the He-Ar- $\text{H}_2\text{O}$  specimen is around 520 nm thick, and at 619 °C it is ten times thicker. At 714 °C, the scale is so thick that it cannot be measured by AES. Figs. 9–11 show the surfaces of the He-Ar- $\text{H}_2\text{O}$  specimen before and after ion sputtering, as well as the corresponding graphs of the atomic concentration of tungsten and oxygen, as a function of depth.

The SEM images in Fig. 9 show the surfaces before and after the oxide scale is removed. AES measurements were made on a spot  $\sim 1\text{ mm}^2$  in area. The graph to the left is the differentiated AES spectra obtained from the blue box shown in the left SEM image, prior to ion sputtering. It shows mainly tungsten, oxygen and a small amount of carbon impurity. The lower right graph displays the atomic concentration of tungsten and oxygen as a function of depth. It reveals an oxide scale thickness of about 35 nm.

AES results for the 522 °C specimen (He-Ar- $\text{H}_2\text{O}$ ) are presented in Fig. 10. After 10 min of argon ion sputtering, bare tungsten surface is reached. This corresponds to an oxide scale thickness of 520 nm.

Fig. 11 shows images of the 619 °C (He-Ar- $\text{H}_2\text{O}$ ) specimen surface, during different stages of ion sputtering. The energy spectrum

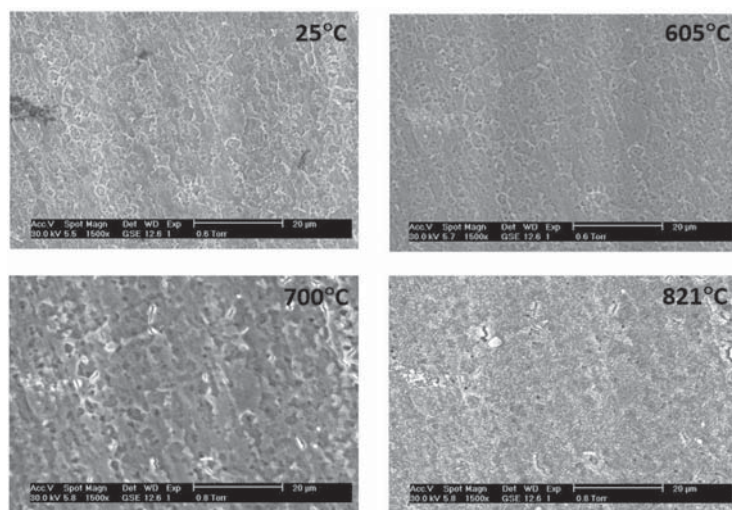


Fig. 6. SEM images of the tungsten surface at various temperatures during heating and oxidation *in situ* in a hot stage ( $p_{\text{H}_2\text{O}}$ : 100 Pa).



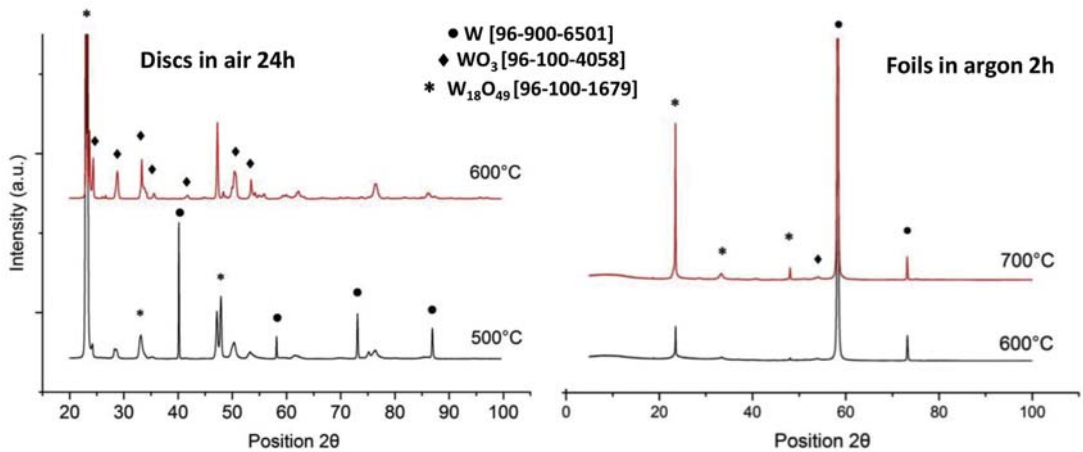


Fig. 7. XRD data on the oxides present on tungsten foil surfaces at different temperatures.

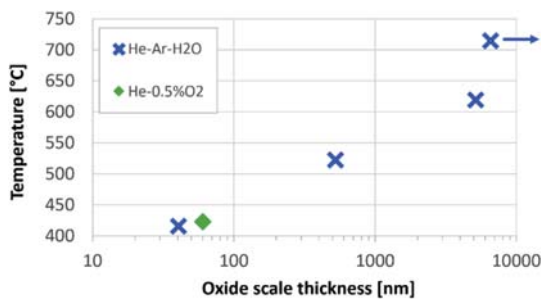


Fig. 8. Oxide scale thickness measured by AES.

is not presented, but is similar to the spectra from the previous specimens, pointing to the existence of only tungsten, oxygen and carbon.

The oxide scale on this sample is significantly thicker, reaching a value of about 5.2  $\mu\text{m}$ . The oxide scale proved to be more difficult to remove, resulting in an uneven surface as seen in the images above.

### 3.6. Energy-dispersive X-ray spectroscopy (EDS)

The specimen oxidized at 714 °C in He-Ar-H<sub>2</sub>O was analyzed using EDS. This specimen was covered by a thick porous oxide scale, as seen in the SEM image presented in Fig. 12. The numbers in the images mark the positions of the EDS analysis. The analysis was made in a Zeiss Ultra 55 field emission gun SEM (FEG-SEM), using an EDS system from Oxford Instruments. The calibration was done

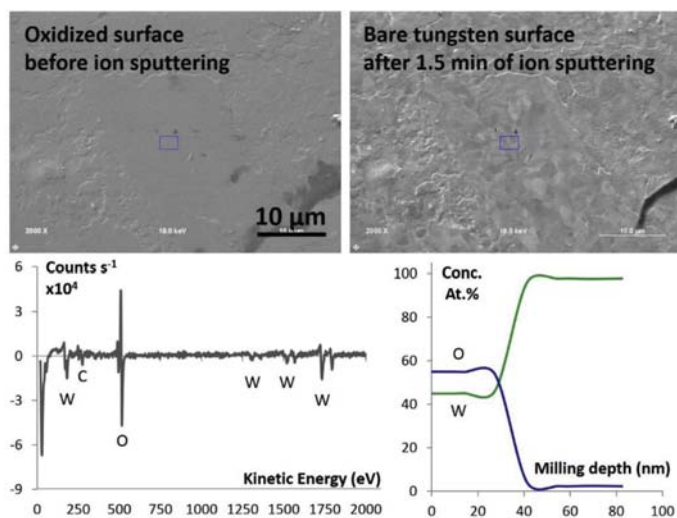


Fig. 9. AES data for the sample oxidized at 415 °C in a He-Ar-H<sub>2</sub>O gas mixture ( $p_{\text{H}_2\text{O}}$ : 790 Pa, 2 h).

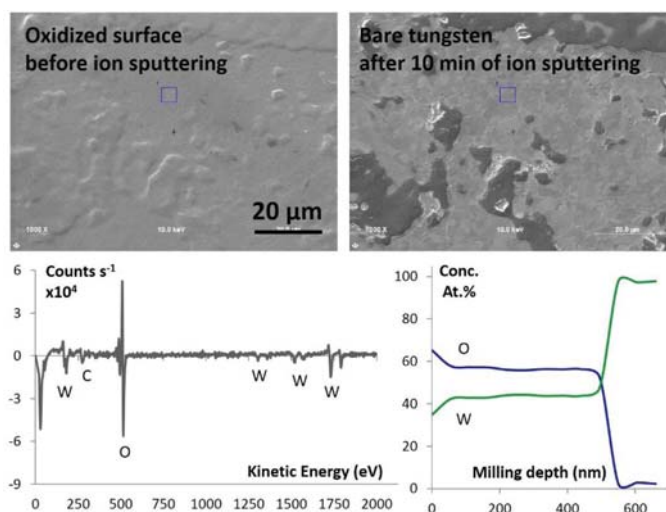


Fig. 10. AES results from the sample oxidized at 522 °C in He-Ar-H<sub>2</sub>O.

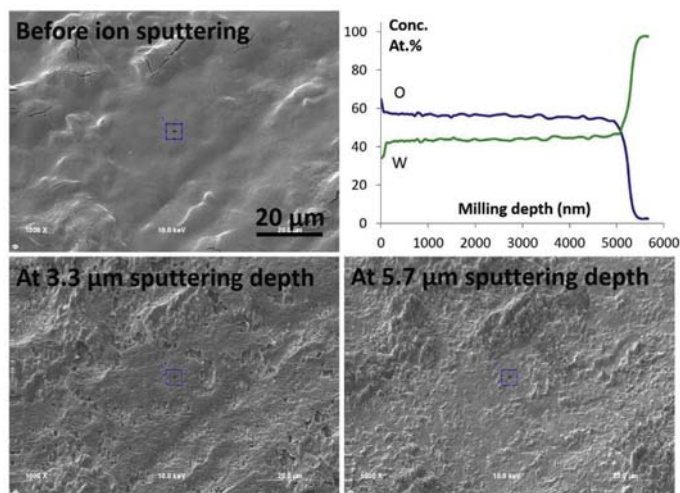


Fig. 11. AES results from the sample oxidized at 619 °C in He-Ar-H<sub>2</sub>O.

using silica and metallic tungsten.

The orange square marks the position (no. 6 in Table 1) of the image presented in Fig. 13. The oxide scale of this sample was much thicker than that of the samples discussed previously. The oxide had cracked and the opening allowed oxygen to reach the bare tungsten easily, leading to a faster oxidation rate. At this stage, the oxidation corresponded to a linear rate law.

Fig. 13 shows an image of the area chosen for the majority of EDS measurements. This area contains a crack in which different spots were examined. In order to study the composition of the oxide scale, EDS analysis was performed on the top surface of the oxide scale, and on the walls and in the bottom of the crack. Numbers 1–5 in the image mark the positions for the analysis. The results from

the measurements are summarized in Table 1.

From the above table, it is evident that the oxide scale indeed consists of a series of oxides, with stoichiometries ranging from close to WO<sub>2</sub> to WO<sub>3</sub>.

### 3.7. Oxidation of tungsten and its alloys in He-5%O<sub>2</sub> gas mixture

Keeping in view the target material and the gaseous atmosphere in the ESS spallation facility, the focus of the present study has been on the oxidation of unalloyed tungsten in inert gas atmospheres containing small amounts of oxygen. However, for purposes of comparison, a few experiments were conducted for studying the oxidation of some tungsten alloys and unalloyed tungsten in a

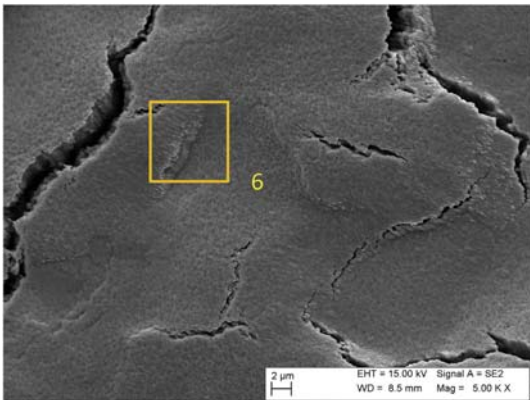


Fig. 12. SEM image of the surface of the 714 °C (He-Ar-H<sub>2</sub>O) specimen. (EDS analysis in the non-sputtered area).

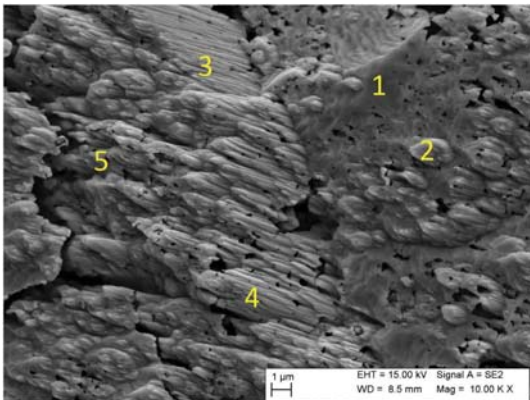


Fig. 13. Close up of the surface of the 714 °C (He-Ar-H<sub>2</sub>O) specimen. The positions of the EDS measurements are marked 1–5.

Table 1

EDS analysis of the oxide scale (714 °C, He-Ar-H<sub>2</sub>O gas mixture).

Position	at.% O*	at.% W**	O/W
1	73.06	26.94	2.71
2	67.23	32.77	2.05
3	75.36	24.64	3.06
4	70.24	29.76	2.36
5	71.75	28.25	2.54
6	71.96	28.04	2.57

\*K-lines, \*\*M-lines.

relatively oxygen-rich, He-%O<sub>2</sub> gas atmosphere.

Fig. 14 shows mass change data for tungsten and its alloy D176, as a function of time at temperatures between 800° and 1000 °C. It is seen that unalloyed tungsten oxidizes much less than D176 at all temperatures. This is probably due to the presence of 5% Ni and 2.5% Fe in the alloy.

The oxidation behavior of tungsten alloys D185, IT170 and IT180 are compared at 800 °C in Fig. 15. It is apparent that D185 oxidizes the least, due to the low nickel and iron contents in the alloy.

Maximum oxidation occurs in the alloy IT170 which contains 7% Ni and 2.5% Cu.

Results from these experiments show that unalloyed tungsten has much better resistance to oxidation, relative to its alloys.

#### 4. Conclusions

The oxidation behavior of tungsten in inert gas atmospheres, with small amounts of impurities such as oxygen and moisture, has been studied in the temperature interval 400° to 900 °C. Oxidation of tungsten was monitored using TGA and DSC. Non-isothermal, *in situ* experiments inside an ESEM showed that, in an atmosphere of water vapor at a pressure of 100 Pa, tungsten foils are oxidized at temperatures above 600 °C. In argon gas with a maximum oxygen partial pressure of 5 ppm, a thin and adherent oxide film was observed to form on the surface of tungsten specimens even at 500 °C. XRD analysis of specimens oxidized in argon showed the presence of W<sub>18</sub>O<sub>49</sub>. Analysis of the samples oxidized in air indicated that a transition from the W<sub>18</sub>O<sub>49</sub> oxide to WO<sub>3</sub> took place between 500° and 600 °C.

Fig. 16 shows a summary of the final mass changes of the specimens oxidized using the TGA setup. The mass gain is relatively low below 600 °C in both atmospheres, but above this temperature it increases significantly. The oxide thickness of the He-Ar-H<sub>2</sub>O specimens was estimated using Auger electron spectroscopy. Between 415 °C and 619 °C the thickness of the oxide scale increases roughly ten times with every 100 °C increase in temperature; from 60 nm to 5.2 μm. Energy dispersive X-ray spectroscopy studies on the sample oxidized at 714 °C showed presence of a series of oxides, varying in stoichiometry from WO<sub>2</sub> to WO<sub>3</sub>.

For the operation of the ESS spallation facility, it is important to note that tungsten can be oxidized in environments with low oxygen partial pressures at temperatures as low as 400 °C. The nominal operation temperature of the tungsten bricks in the target will be below 500 °C, and it is expected that the oxide formed will be of the protective type. However, considering that the tungsten will be cooled by a massive helium flow with a flux of 3 kg/s at 1.1 MPa, surface erosion of the oxide scale was a concern. With this in view, erosion experiments were performed in order to study the adhesion of the oxide formed on tungsten at 500 °C [28]. The sample, pre-oxidized for 1 h in a He-0.5%O<sub>2</sub> gas mixture, showed no signs of erosion caused by the helium jet. Still, the spalling of the oxide layer due to beam pulse and beam trip induced thermal cycling, and fatigue, during five years of target lifetime, remains an issue. Also of concern is the possibility of tungsten oxide sublimation in accidental cases such as over-focused beam combined with loss of helium confinement. To minimize such risks, the target primary cooling loop will be purified and the impurity levels will be monitored during operation.

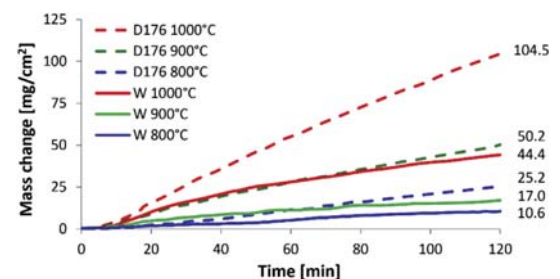


Fig. 14. Oxidation of Tungsten and D176 alloy in He-5%O<sub>2</sub> gas mixture.

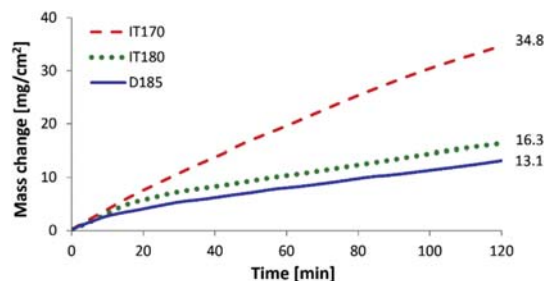


Fig. 15. Oxidation of tungsten alloys at 800 °C in He-5%O<sub>2</sub> gas mixture.

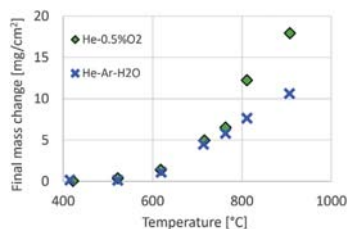


Fig. 16. Final mass change for the unalloyed tungsten discs as a function of temperature.

## Acknowledgements

The authors are thankful to Christopher Nilsson and Dr. Hossein Sina for invaluable assistance in the experimental work. Research funding and support from the European Spallation Source (ESS, Lund) is gratefully acknowledged.

## References

- [1] S. Peggs, et al., ESS Technical Design Report, ESS-doc-274, ESS-0016915, European Spallation Source ERIC, April 23, 2013.
- [2] Y. Lee, M. Hartl, Materials Handbook, Technical Report ESS-0028465, European Spallation Source ERIC, July 28, 2017.
- [3] J. Harborn, System Definition – SOLUTION Target Helium Cooling Systems, Technical Report ESS-0012527, European Spallation Source ERIC, September 14, 2017.
- [4] E.A. Gulbransen, K.F. Andrew, Kinetics of oxidation of pure tungsten from 500° to 1300 °C, *J. Electrochem. Soc.* 107 (7) (1960) 619–628.
- [5] J.W. Hickman, E.A. Gulbransen, An electron diffraction study of oxide films formed on Molybdenum tungsten, and alloys of Molybdenum, tungsten and nickel, *Trans. AIME* 171 (1947) 371–388.
- [6] E.A. Gulbransen, K.F. Andrew, F.A. Brassart, Kinetics of oxidation of pure tungsten, 1150°–1615 °C, *J. Electrochem. Soc.* 111 (1) (1964) 103–109.
- [7] E.A. Gulbransen, W.S. Wysong, Thin oxide films on tungsten, *Met. Technol.* XIV (1947) 611–627.
- [8] P.E. Blackburn, K.F. Andrew, E.A. Gulbransen, F.A. Brassart, Oxidation of Tungsten and Tungsten Based Alloys, WADC TR 59-575 Part II, Arlington, 1961.
- [9] E.A. Gulbransen, High-temperature oxidation of tungsten, molybdenum and carbon, *Nature* 198 (4875) (1963) 82–83.
- [10] G.A. Greene, C.C. Finfrock, Generation, transport, and deposition of tungsten-oxide aerosols at 1000 °C in flowing air/steam mixtures, *Exp. Therm. Fluid Sci.* 26 (8) (2002) 917–929.
- [11] G.A. Greene, C.C. Finfrock, Vaporization of tungsten in flowing steam at high temperatures, *Exp. Therm. Fluid Sci.* 25 (2001) 87–99.
- [12] A. Warren, A. Nylund, I. Olefjord, Oxidation of tungsten and tungsten carbide in dry and humid atmospheres, *Int. J. Refract. Met. Hard Mater.* 14 (5–6) (Jan. 1996) 345–353.
- [13] E.A. Kelleff, S.E. Rogers, The structure of oxide layers on tungsten, *J. Electrochem. Soc.* 110 (6) (1963) 502–504.
- [14] V.Y. Ivanov, Y.P. Nechiporenko, L.N. Yefimenko, M.I. Yurchenko, High Temperature Oxidation Protection of Tungsten (NASA Technical Translation), National Aeronautics and Space Administration, Washington, D. C., 1969.
- [15] H.A. Wriedt, The O-W (Oxygen-Tungsten) system, *Bull. Alloy Phase Diagr.* 10 (1989) 368–384.
- [16] J.P. Bonnet, J. Nowotny, M. Onillon, I. Sikora, Surface electrical properties of tungsten oxides in equilibrium with the gas phase, *Oxid. Met.* 13 (3) (1979) 273–282.
- [17] M. Weil, W.-D. Schubert, The Beautiful Colors of Tungsten Oxides, Tungsten Newsletter, International Tungsten Industry Association, June 2013.
- [18] R. Tilley, Color and Optical Properties of Materials, John Wiley, London, 2000.
- [19] N. Birks, G.H. Meier, F.S. Pettit, Introduction to the High-temperature Oxidation of Metals, second ed., Cambridge University Press, New York, 2006.
- [20] W.W. Webb, J.T. Norton, C. Wagner, Oxidation of tungsten, *J. Electrochem. Soc.* 103 (107–111) (1956).
- [21] V.K. Sikka, C.J. Rosa, The oxidation kinetics of tungsten and the determination of oxygen diffusion coefficient in tungsten trioxide, *Corrosion Sci.* 20 (1980) 1201–1219.
- [22] S.C. Cifuentes, M.A. Monge, P. Pérez, On the oxidation mechanism of pure tungsten in the temperature range 600–800 °C, *Corrosion Sci.* 57 (Apr. 2012) 114–121.
- [23] J.L. Sabourin, R.A. Yetter, High-temperature oxidation kinetics of tungsten–water reaction with hydrogen inhibition, *J. Propul. Power* 27 (5) (2011) 1088–1096.
- [24] E. Lassner, W.-D. Schubert, Tungsten Properties, Chemistry, Technology of the Element, Alloys, and Chemical Compounds, Kluwer Academic/Plenum Publishers, New York, 1999.
- [25] J.L. Sabourin, Doctoral Dissertation “High Temperature Heterogenous Reaction Kinetics and Mechanisms of Tungsten Oxidation”, 2010.
- [26] R.A. Perkins, D.D. Crooks, Low-pressure, high-temperature oxidation of tungsten, *J. Met.* 13 (7) (1961) 490–493.
- [27] G.R. Smolik, R.J. Pawelko, R.A. Anderl, D.A. Petti, Oxidation and Volatilization from Tungsten Brush High Heat Flux Armor during High Temperature Steam Exposure, 2000.
- [28] P. Nilsson, J. Klingmann, J. Habainy, S. Iyengar, Y. Lee, U. Odén, Tungsten Erosion in Helium – Experimental Results from ETHel” – Presented at ICANS XXII, 22nd Meeting on Collaboration of Advanced Neutron Sources, 27–31 March 2017 (Oxford, England).





# PAPER IV

J. Habainy, Y. Dai, Y. Lee, S. Iyengar

**Thermal diffusivity of tungsten irradiated with protons up to 5.8 dpa**

*Journal of Nuclear Materials, vol. 509, 2018, pp. 152-157*

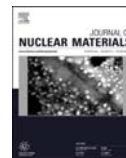
Reproduced with permission from Elsevier





Contents lists available at ScienceDirect

## Journal of Nuclear Materials

journal homepage: [www.elsevier.com/locate/jnucmat](http://www.elsevier.com/locate/jnucmat)

## Thermal diffusivity of tungsten irradiated with protons up to 5.8 dpa

Jemila Habainy<sup>a, b, \*</sup>, Yong Dai<sup>c</sup>, Yongjoong Lee<sup>a</sup>, Srinivasan Iyengar<sup>a, b</sup><sup>a</sup> European Spallation Source ESS ERIC, Box 176, 22 100, Lund, Sweden<sup>b</sup> Div. of Materials Engineering, Lund University, Box 118, 22 100, Lund, Sweden<sup>c</sup> Paul Scherrer Institut, 5232 Villigen PSI, Switzerland

## ARTICLE INFO

## Article history:

Received 24 April 2018

Received in revised form

26 June 2018

Accepted 26 June 2018

Available online 28 June 2018

## Keywords:

Tungsten

Irradiation effects

Spallation target

Thermal diffusivity

Thermal conductivity

## ABSTRACT

Thermal properties of pure tungsten, irradiated in the Swiss neutron spallation source at the Paul Scherrer Institut, have been studied in the temperature range 25–500 °C. Disk-shaped specimens were prepared from a tungsten sheet which was irradiated with high energy protons and spallation neutrons. The specimens tested in this work received total damages of maximum 3.9 and 5.8 dpa at average irradiation temperatures of 115 and 140 °C, respectively. The thermal diffusivity of the irradiated tungsten was measured using the conventional flash method. For both specimens, the results show a significant decrease in thermal diffusivity after irradiation. Relative to unirradiated tungsten, the irradiated samples show thermal diffusivity values which are 28–51% lower, depending on temperature. Annealing of the irradiated specimen of 3.9 dpa at 1000 °C for 1 h resulted in a slight recovery of thermal diffusivity. In addition, thermal conductivity values were calculated from the thermal diffusivity data.

© 2018 Elsevier B.V. All rights reserved.

## 1. Introduction

Pure tungsten has been selected as the target material at the European Spallation Source (ESS) facility, which is currently under construction in Lund, Sweden [1]. The decision is based on the high neutron yield of tungsten, which stems from its high atomic mass and high density. Despite having been used as target material at other spallation facilities for many years, the data on the properties of high energy proton and spallation neutron irradiated tungsten are scarce. At ESS, the target will be subjected to a high power and high energy proton beam. The pulsed proton beam with a duty cycle of 4% and a repetition rate of 14 Hz delivers 357 kJ per pulse to the tungsten. The target consists of about seven thousand bricks of pure tungsten with dimensions  $80 \times 30 \times 10 \text{ mm}^3$ , separated by 2 mm wide channels for the gaseous helium coolant. The bricks are placed on a 2.5 m diameter, rotating wheel. The rotation of the target wheel distributes the beam energy and the radiation damage over a larger volume of the spallation material.

During the 5-year lifetime of the target, the maximum displacement damage in tungsten would be about 10 dpa. With this displacement damage dose rate, the ductile-to-brittle transition

temperature (DBTT) of tungsten will increase to above the target operating temperature after only a few weeks of full 5 MW operation. The radiation induced brittle behavior of pure tungsten and potential loss of structural integrity during target operation is a point of concern. Three-point bending tests performed on tungsten specimens irradiated in a target of the Swiss Spallation Neutron Source (SINQ) to doses in the range 1.3–3.5 dpa, have shown virtually zero ductility at temperatures up to 500 °C [2]. The radiation induced embrittlement of tungsten, in combination with the high power pulsed beam is considered as one of the main contributions to potential target failure. The proton beam, pulsed at 14 Hz with a duty factor of 4%, is expected to give rise to cyclic thermo-mechanical stresses in the tungsten, possibly leading to fatigue failure at stresses far below the yield stress [3].

The calculated maximum temperature and equivalent stress in the ESS target during operation are 445 °C and 110 MPa, respectively [4]. These calculations are based on thermo-mechanical data of unirradiated pure tungsten. The temperature and secondary thermal stress in tungsten is largely determined by its thermal conductivity. However, the radiation induced degradation of thermal properties of tungsten in spallation target environment is not known. Nevertheless, there is an indication of degradation of thermal conductivity of tungsten under neutron radiation in reactor environments. The neutron radiation induced decrease of thermal conductivity is caused by rhenium transmutation due to

\* Corresponding author, European Spallation Source ESS ERIC, Box 176, 22 100, Lund, Sweden.

E-mail address: [jemila.habainy@ess.se](mailto:jemila.habainy@ess.se) (J. Habainy).

low energy neutron capture and displacement damage. While the spallation material is bombarded by high energy protons and fast neutrons, it is also exposed to thermal neutrons moderated by hydrogen-rich moderators and water coolants. Therefore, it is expected that the thermal conductivity of tungsten in the ESS target will decrease due to the formation of irradiation induced transmutation products such as rhenium, and due to displacement damage, although the extent of degradation is still not fully understood.

There are few existing studies on neutron irradiation effects on thermal properties of tungsten-rhenium alloys. Tanabe et al. [5] studied the effect of different rhenium content in tungsten-rhenium alloys on the thermal diffusivity in the temperature range 300–1000 K. It was observed that thermal diffusivity of pure tungsten decreases with increasing temperature, whereas the alloys, having 5–25 wt% rhenium, do not show a sharp change in thermal diffusivity as a function of temperature. Alloys with relatively higher rhenium content show a marginal increase in thermal diffusivity, beyond a certain temperature. The calculated thermal conductivity from the experimentally determined thermal diffusivity was compared to the one derived from electrical resistivity data using Wiedemann-Franz law. This law assumes that thermal conductivity of a metal is determined by the kinetics of electron transport, excluding phonon transport effects. The analysis of the difference between the two values indicated that the degradation of thermal conductivity with higher contents of rhenium is mainly due to the electron contribution.

In a study on electrical resistivity of neutron irradiated tungsten and tungsten-rhenium alloys, Hasegawa et al. [6] irradiated specimens in a fast reactor (JOYO) and in a mixed spectrum reactor (HFIR) to obtain different amounts of rhenium as the transmutation product. In both reactors the displacement damage was 1 dpa, and the irradiation temperatures were similar: 500 °C at HFIR and 600 °C at JOYO. Because of the high flux of thermal neutrons at HFIR, the rhenium production rate is higher due to neutron capture followed by beta decay. At HFIR, pure tungsten is expected to change to W-5Re-0.5Os after 1 dpa, and at JOYO the rhenium content is expected to be less than 0.03%. The resulting difference in the increase of electrical resistivity between the two equivalent specimens, after irradiation, is almost 50%, which should be mainly due to different radiation induced rhenium alloying. The observed loss of electrical conductivity can be related to the loss of thermal conductivity, in part, by Wiedemann-Franz law.

The effect of neutron irradiation on thermal diffusivity of pure tungsten and some tungsten-rhenium alloys has been studied by Fujitsuka et al. [7]. The specimens were irradiated in JMTR at 60 °C to thermal and fast neutron fluences of  $1.03 \times 10^{20}$  and  $3.37 \times 10^{19}$  n/cm<sup>2</sup> ( $E > 1$  MeV), respectively. The thermal diffusivities were measured at temperatures up to 700 °C. Pure tungsten showed a decrease in thermal diffusivity with increasing temperature, both before and after irradiation. At room temperature, thermal diffusivity of the irradiated pure tungsten specimen is approximately 15% lower. The addition of rhenium (5–25 wt%) significantly lowers the diffusivity of all the alloys compared to that of pure tungsten, also after irradiation. With an addition of only 5 wt% rhenium, thermal diffusivity at room temperature drops by nearly 50% compared to that of the pure tungsten. After irradiation thermal diffusivity of the W-5% Re alloy is only marginally changed.

To summarize, the data from the reviewed neutron irradiation studies of tungsten indicate a decrease of thermal diffusivity in the range of 15–50%, showing a clear dependence on the amount of rhenium present. The rhenium content makes the electron effect more dominant, while the displacement damage accounts for the phonon effect. However, the radiation environment of tungsten as a spallation target material is different from the reactor

environments. The high energy protons interact with materials in different ways than neutrons and the tungsten is also exposed to fast secondary neutrons with a kinetic energy of up to an order of 1 GeV. In this work, we present results from thermal diffusivity measurements of pure tungsten irradiated at the Swiss Spallation Neutron Source (SINQ). The specimens are irradiated by a mixed flux of high energy primary protons and fast secondary neutrons up to a displacement damage dose of 5.8 dpa.

## 2. Experimental

### 2.1. Material and specimens

Two slices of  $1 \times 10 \times 100$  mm were cut from the cross-section of a 1 cm thick cross-rolled tungsten plate, with a purity of 99.9 wt% tungsten. The average grain sizes were in the range 17–25  $\mu$ m. From these two slices, several small plates of  $1 \times 8 \times 30$ –50 mm were cut and irradiated in Target-7 of SINQ at the Paul Scherrer Institut (PSI). These plates were irradiated with high energy protons and spallation neutrons up to doses of about 28 dpa. This irradiation campaign took place during the years 2007–2008, as a part of the fifth SINQ Target Irradiation Program (STIP-V). After the irradiation, several disk-shaped specimens, with a diameter of 6 mm, were cut from the plates using electro-discharge machining (EDM). Due to the high activity of the irradiated tungsten, only two of the lowest doses could be used for measurements in this study. The specimens received doses of 3.9 dpa with 158 appm He at an average irradiation temperature of 115 °C, and 5.8 dpa with 245 appm He at an average irradiation temperature of 140 °C. The irradiation temperature is nearly linearly dependent on the proton beam current received by the target. The variation of the current, and thus the temperature, during the irradiation of the STIP V specimens is estimated to  $\pm 15\%$  around the average values.

The main transmutation product in the irradiated specimens is expected to be rhenium, which is produced in tungsten by thermal neutron capturing ( $n, \gamma$ ) followed by beta decay ( $\beta^-$ ). Natural tungsten consists largely of the isotopes W184 (30.7%) and W186 (28.6%). The ( $n, \gamma$ ) cross-section of thermal neutrons with a typical kinetic energy of 0.025 eV is 1.62 barn for W184 and 37.9 barn for W186. The calculated maximum thermal neutron flux in the SINQ target is  $1.5 \times 10^{13}$  n/cm<sup>2</sup>/s/mA [8] and the accumulated beam charge on the SINQ Target 7 is 9.83 Ah. This leads to an estimation of the rhenium fraction in this tungsten material to be approximately 2%.

The irradiated tungsten specimens were mechanically polished on both sides in several steps, finishing with standard colloidal silica suspension. In addition, two unirradiated tungsten reference specimens, polished and unpolished, were also used. The unpolished specimen was used to study the effect of surface roughness and emissivity differences on the signal-to-noise ratio during measurement. The average thicknesses were measured using a point-type micrometer. All the specimens were around 1 mm thick and 6 mm in diameter. The disks were then cleaned with acetone in an ultrasonic bath, carefully dried and coated with Graphit-33 carbon spray (Kontakt Chemie) on both sides. All the disks, except the unpolished reference tungsten, were coated. The graphite coating serves three purposes - increase the absorption of the flash energy to equate the input energy to the deposited energy in the sample, improve the emission of infrared radiation to the detector, and homogenize the surfaces of the test samples and the references used for specific heat determination.

To validate the measurements, two types of standard specimens, alumina and molybdenum, were tested together with the tungsten

specimens. The tests were performed in 100 °C steps, starting from room temperature going up to 500 °C. Argon with a flow of 150 ml/min was used as the protective gas. The design of the sample holder allowed for all the specimens to be tested simultaneously under the same conditions. After the first round of measurements, the irradiated tungsten disk with 3.9 dpa damage dose was annealed at 1000 °C for 1 h and remeasured at 25, 300 and 500 °C. All thermal diffusivity values reported in this work correspond to an average of five measurements under the same conditions.

## 2.2. Flash method

Thermal diffusivity was determined using a conventional flash method, described in detail in ASTM documents E1461-13 *Standard Test Method for Thermal Diffusivity by the Flash Method* [9], and E2585-09 *Standard Practice for Thermal Diffusivity by the Flash Method* [10]. A commercial Netzsch LFA 467 Light Flash apparatus with a xenon lamp and an InSb IR-detector was used for the measurements. The xenon lamp acts as the flash source, subjecting the specimens to a short duration, high intensity energy pulse. The energy is absorbed on the front surface of the specimen, and the resulting temperature rise on the rear is recorded by the detector. The thermal diffusivity is obtained from the specimen thickness  $L$  and  $t_{0.5}$ , which is the time required to reach half of the maximum temperature on the rear surface. For adiabatic conditions, thermal diffusivity  $\alpha$  ( $\text{m}^2/\text{s}$ ) is calculated using the following relationship [11]:

$$\alpha = \frac{0.138785 L^2}{t_{0.5}} \quad (1)$$

In this work, the thermograms describing the heat propagation through the sample are fitted automatically using existing models in Netzsch's analysis software Proteus. Various heat transfer models with corrections for e.g. radial heat loss can be chosen for the best fit, from which the half time  $t_{0.5}$  can be determined.

The flash method was introduced by Parker et al., in 1961 [11]. The original model which is applicable only in ideal conditions with adiabatic boundaries and a one-dimensional heat flow was later modified by Cape and Lehman [12] to also take heat losses into account. The Cape-Lehman model is currently the default standard model in version 7.1 of the Netzsch-Proteus LFA software [13]. The

standard model assumes full pulse energy absorption on the front face of the specimen, followed by a thermal wave travelling through the specimen to the back side, i.e. only conductive heat is considered here. Two additional models can be chosen to analyze the thermograms, the transparent model and the penetration model. The transparent model is used when the material is transparent, diathermic and optically thin. As opposed to the standard model, the transparent model also includes radiative heat transfer within the specimen. In a thermogram this is evidenced by an instantaneous increase of the thermal signal in the detector curve. The transparent model is a modified version of a solution suggested by Mehling et al., in 1998 [14], but here the radiative heat transfer coefficient has been separated from the heat loss coefficient in order to improve the fit in the Proteus software. For measurements of slightly porous materials the third model, the penetration model, is most suitable. It is based on work by McMasters et al. [15] and describes how the pulse energy is absorbed over a thin layer of the specimen, rather than solely on the surface. The penetration of the flash is taken as the mean free path of a photon in the material, resulting in an exponentially decaying temperature distribution within the specimen. The penetration model was found to provide more accurate thermal diffusivity data of the tungsten specimens, compared to the standard model and the transparent model, as described in Section 3.3.

## 2.3. Thermal conductivity calculations

The thermal conductivity  $\lambda$  ( $\text{W}\cdot\text{m}^{-1}\cdot\text{K}^{-1}$ ) is derived according to the following equation

$$\lambda = \alpha \cdot C_p \cdot \rho \quad (2)$$

where  $\alpha$  ( $\text{m}^2/\text{s}$ ) is the measured thermal diffusivity,  $C_p$  ( $\text{J}\cdot\text{kg}^{-1}\cdot\text{K}^{-1}$ ) the specific heat, and  $\rho$  ( $\text{kg}/\text{m}^3$ ) the mass density. The specific heat can be determined in the LFA using a standard material specimen with known specific heat, together with the irradiated tungsten. Provided that the surfaces of the specimens are coated in precisely the same manner, the specific heat can be calculated from the difference in maximum temperature between the specimens resulting from the same pulse energy.

The density of unirradiated tungsten was measured to be 19.11 g/cm<sup>3</sup>, which gives a relative density of 99.03%. The irradiated specimens could not be measured due to the high activity. However, transmission electron microscopic studies of the tungsten samples irradiated under similar conditions could not detect any bubbles or cavities within its resolution limits [16]. This indicates that the radiation induced swelling of the tungsten specimens should be marginal, and the density of the irradiated specimens should be essentially the same as that of unirradiated one.

## 3. Results and discussion

### 3.1. Thermal diffusivity

#### 3.1.1. Unirradiated tungsten

Data obtained from thermal diffusivity measurements are presented in Fig. 1. Thermal diffusivity values for the unirradiated tungsten are plotted together with data on the thermal diffusivity of pure tungsten presented by Touloukian et al. [17]. The values are in excellent agreement, confirming that the preparation of the specimens, the measurement itself, and the subsequent data analysis were performed in a correct manner. Thermal diffusivity of the unirradiated tungsten, in the temperature interval 25–500 °C, can be expressed using a polynomial fit given below.

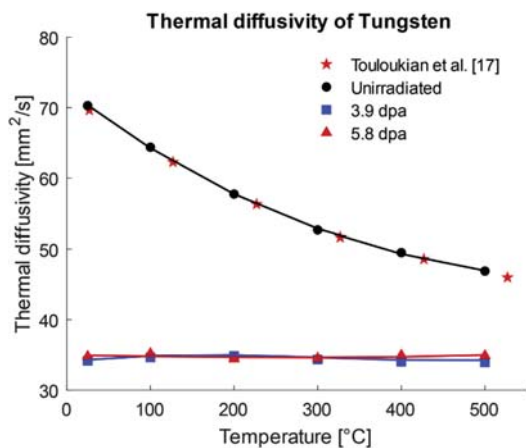


Fig. 1. Thermal diffusivity of irradiated tungsten at 25–500 °C.

$$\alpha_{\text{ref}} = 72.625 - 9.3617 \times 10^{-2} T + 1.0392 \times 10^{-4} T^2 - 3.8694 \times 10^{-8} T^3 \quad (3)$$

Thermal diffusivity,  $\alpha_{\text{ref}}$ , is expressed in  $\text{mm}^2/\text{s}$  and the temperature,  $T$ , in  $^{\circ}\text{C}$ . Thermal diffusivity data obtained for the molybdenum reference sample, which was tested simultaneously, also showed very good agreement (deviation  $< 1\%$ ) with reported standard thermal diffusivity values. Unfortunately, the signal at temperatures 25, 100 and  $200^{\circ}\text{C}$  was distorted and no data for the molybdenum sample could be obtained at these temperatures. This also means that the specific heat for the irradiated tungsten could not be obtained during the experiment as it requires data from the simultaneous measurement of a standard sample with known specific heat.

### 3.1.2. Irradiated tungsten

Thermal diffusivities of the two irradiated specimens are also presented in Fig. 1. The results show that irradiation at SINQ greatly reduces the thermal diffusivity of tungsten. At room temperature, the average thermal diffusivity is around  $35 \text{ mm}^2/\text{s}$  for both specimens, which is a 50% reduction relative to the reference specimen. At higher temperatures, up to  $500^{\circ}\text{C}$ , the thermal diffusivity of the unirradiated tungsten decreases to  $47 \text{ mm}^2/\text{s}$ , whereas the values for the irradiated specimens remain nearly constant at around  $35 \text{ mm}^2/\text{s}$ . The temperature independence of the irradiated tungsten thermal diffusivity is similar to the one reported by Tanabe et al. [5], corresponding to the thermal diffusivities of unirradiated tungsten alloys containing 5.3–9.8% rhenium. The reported thermal diffusivity of the W-9.8% Re alloy in the temperature interval  $27\text{--}500^{\circ}\text{C}$  is around  $25 \text{ mm}^2/\text{s}$ , and that of the W-5.3% Re is in the range  $30\text{--}34 \text{ mm}^2/\text{s}$ . These values are lower by 48–62% relative to their thermal diffusivity measurements on unalloyed tungsten at room temperature.

The irradiation-induced degradation of thermal diffusivity of tungsten is believed to be the result of both displacement damage and compositional changes due to transmutations. As discussed above, an addition of 5% rhenium causes a significant drop in thermal diffusivity, even without irradiation induced displacement damage. Tungsten with smaller additions of rhenium, i.e. 1–2% which is closer to the estimated rhenium content in the present work, has been shown to have a lower thermal diffusivity compared to pure tungsten [18]. Depending on the test temperature ( $25\text{--}200^{\circ}\text{C}$ ), the thermal diffusivity of the W-1%Re alloy is 10–20% lower, and that of the W-2%Re alloy is 20–30% lower.

In an attempt to isolate the effect of displacement damage from the effect of compositional changes, an experiment was set up where heavy ions of energy below the Coulomb barrier were used to irradiate pure tungsten foils up to four different fluences [19]. The irradiation was carried out at GSI Helmholtzzentrum Darmstadt, using a pulsed beam of gold ions with a kinetic energy of 4.8 MeV/u and a particle flux of  $4 \times 10^9 \text{ ions/cm}^2/\text{s}$ . Thermal diffusivity of the irradiated specimens was measured in-plane using the flash method. The results indicate a decrease in thermal diffusivity with an increase of the accumulated fluence. At the highest fluence,  $2 \times 10^{13} \text{ ions/cm}^2$ , the thermal diffusivity had decreased by approximately 10%.

### 3.1.3. Post-irradiation annealing

The 3.9 dpa specimen was annealed at  $1000^{\circ}\text{C}$  for 1 h in 1 Pa vacuum. It was wrapped in a tantalum foil to protect it from oxidation. The unirradiated reference specimen was annealed together with the 3.9 dpa specimen, and both were re-measured

together with the molybdenum standard specimen and the unpolished, uncoated tungsten specimen, at temperatures 25, 300 and  $500^{\circ}\text{C}$ . All three unirradiated specimens showed thermal diffusivity values consistent with the previous measurement. However, thermal diffusivity of the irradiated specimen showed partial recovery. At room temperature, it had increased by  $37\text{--}47 \text{ mm}^2/\text{s}$ , and at  $500^{\circ}\text{C}$ , it had increased by  $19\text{--}41 \text{ mm}^2/\text{s}$ . The results of the measurements before and after annealing are presented in Fig. 2.

The microstructure of the irradiated tungsten, originating from the same piece as the specimens used in the present study, has been previously examined by Horvath et al. [16]. The effect of post-irradiation annealing at different temperatures was studied as well. The unirradiated tungsten was found to have dislocations up to tens of microns in length, whereas the specimens irradiated up to doses of 1.4 and 3.5 dpa, contained mostly defect clusters and dislocation loops of a few nanometers. The dislocation density of the unirradiated material was observed to be around  $1.6 \times 10^{13} \text{ m}^{-2}$ . Apart from the irradiation defect clusters, neither cavities nor rhenium-rich precipitates were observed in the irradiated specimens. Annealing at  $900^{\circ}\text{C}$  for 1 h resulted in a reduction of the number of defect clusters and dislocation lines by factors of 6 and 2, respectively, while the defect clusters grew from an average size of  $2 \text{ nm}\text{--}5 \text{ nm}$ . Meanwhile, cavities of  $1\text{--}2 \text{ nm}$  sizes appeared. It is believed that they grew from invisible helium-vacancy clusters. The small defect clusters, including the invisible helium-vacancy clusters, contribute to the reduction of the thermal diffusivity of irradiated tungsten. This part of the reduction can be largely recovered by annealing at high temperatures.

### 3.2. Thermal conductivity

In order to derive the thermal conductivity of the irradiated specimens from the measured thermal diffusivity, reliable data on the density and specific heat of tungsten in the temperature interval  $25\text{--}500^{\circ}\text{C}$  are needed. Reference values of these properties, as well as reported thermal diffusivity and conductivity of pure unirradiated tungsten are summarized in Table 1.

Values for the specific heat capacity and the thermal conductivity are taken from Lee et al. [20], where data from several sources have been compiled into analytical expressions of these properties. Thermal diffusivity and density at the specified temperatures is

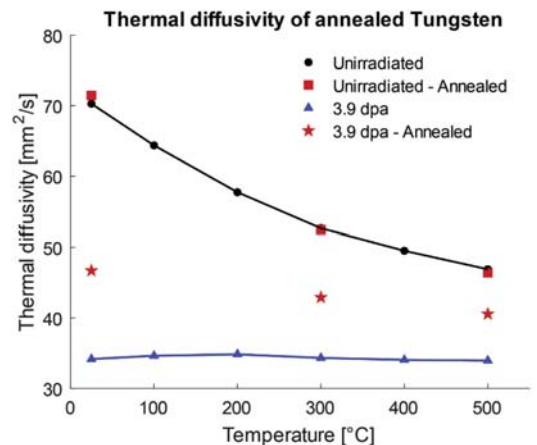


Fig. 2. Thermal diffusivity of annealed tungsten at  $25\text{--}500^{\circ}\text{C}$ .

**Table 1**

Reference data for pure unirradiated tungsten in the temperature range 25–500 °C.

Temp. (°C)	Density [21] (g/cm <sup>3</sup> )	Spec. heat capacity [20] (J·kg <sup>-1</sup> ·K <sup>-1</sup> )	Ther. diffusivity [17] (mm <sup>2</sup> /s)	Ther. conductivity [20] (W·m <sup>-1</sup> ·K <sup>-1</sup> )
25	19.297	129.13	69.8	172.29
100	19.279	131.56	64.3	164.75
200	19.254	134.74	57.9	155.53
300	19.229	137.85	52.8	147.21
400	19.204	140.89	49.4	139.76
500	19.178	143.86	46.7	133.11

estimated using data from Touloukian et al. [17] and Hurd et al. [21], respectively. For the thermal conductivity calculations presented in Table 2, the temperature dependent density in Table 1 was adjusted to account for the 1% porosity of the specimens.

As the specific heat of the irradiated tungsten could not be measured in the present work, thermal conductivities of these specimens have been calculated based on the assumption that the specific heat capacity does not change significantly with irradiation. The same is assumed for the density. The latter assumption is partly justified by the transmission electron microscopic studies of the tungsten samples irradiated in similar conditions [16], which showed no sign of irradiation induced swelling. Published data on irradiation induced changes in the density of tungsten are difficult to find. However, neutron irradiation induced swelling in tungsten has been reported to reach a maximum of 0.22 vol% at a temperature of 430 °C [22]. It is therefore believed that using unirradiated tungsten density data in the calculation of the thermal conductivity of the irradiated tungsten will have a negligible influence on the results. Thermal conductivity data for irradiated tungsten are presented in Table 2.

Roedig et al. [23] presented the thermal conductivities of tungsten irradiated by fast neutrons to doses of 0.2 and 0.6 dpa. The thermal diffusivity was measured using the flash method and the specific heat capacity was measured using a differential scanning calorimeter. The authors briefly mention that the specific heat has increased after the irradiation but do not present this data nor specify the magnitude of the increase. However, they do conclude that the decrease in thermal diffusivity is more distinct and has a larger contribution to the total irradiation induced degradation of thermal conductivity. For the temperatures 20, 100 and 400 °C the reported thermal diffusivities are 152, 146, and 128 W m<sup>-1</sup> K<sup>-1</sup> respectively at 0.2 dpa and 134, 127, and 117 W m<sup>-1</sup> K<sup>-1</sup> respectively at 0.6 dpa.

### 3.3. Methodology and sources of error

The thermogram of each pulse was fitted separately in Netzsch's software Proteus, and they were tested against all three basic models (Standard, Transparent and Penetration), to find the most suitable one. The calculation range of each pulse was set manually to increase the accuracy of the fit by removing the spike at the

beginning of the signals. The spike is an induction-caused electrical potential from the trigger pulse of the flashlight [24]. For correct measurements, the selected calculation range should correspond to 10–12 half times and be in total 0.01–200 s [25]. Special care must be taken with thin samples where there is a risk of superposition of the spike and the signal from the actual heat propagation through the specimen. According to ASTM E2585-09 [10], the thickness of the specimen should be such that the half time  $t_{0.5}$  falls within the 10–1000 ms range.

In this work, the thermograms of the tungsten specimens were evaluated using the Penetration model. The Transparent model tends to underestimate the maximum temperature which leads to a lower half time and thus a slightly higher thermal diffusivity value, although, the difference in the accuracy of the fit was not very far from that of the Penetration model. The Standard model gave the poorest fit for all samples and temperatures. It overestimated the maximum temperature and underestimated the heat losses. For most of the thermograms the  $R^2$  of the fit calculated by the Penetration model was in the range 0.92–0.96. The half time was approximately 4 ms for the irradiated specimens and 2–3 ms for the unirradiated one, depending on the test temperature. Based on the half times, the samples are thinner than what is suggested by the ASTM. Nevertheless, the purpose of these guidelines is ultimately to bring the experimental data as close as possible to the ideal solution, which alternatively can be achieved as well by selecting the smallest possible pulse width, choosing the best model for analysis, and setting the calculation range with care. In a recent publication on the validation of miniature test specimens for use in the LFA [26], reasonable thermal diffusivity values were obtained for tungsten samples of 3 mm diameter and 0.5 mm thickness. The LFA model used for their measurements, a Netzsch LFA-467 Hyper Flash, is the same as the one used in this work. The Hyper Flash feature allows for the regulation of the pulse width in the range 20–1200 µs, where the shortest pulse can measure tungsten samples down to 0.31 mm thickness. In our work, a pulse width of 600 µs was used for all the measurements.

However, thin samples require much greater care during coating. Guidelines by Netzsch suggest three layers of graphite coating, but for the specimens used in this work it proved to be too excessive. As soon as the surface of the specimen was fully covered, thermal diffusivity results were not correct. The standard tungsten and molybdenum specimen would sometimes reach only 20% of the expected value, even when coated only once. Correct results could be obtained once the coating was applied extremely sparsely, at most resembling a very fine layer of dust. The same issue was reported in the previously mentioned publication. The graphite spray recommended by Netzsch, Graphit-33, reportedly results in a layer of thickness up to 10 µm, even after only one application [27]. This leads to inaccurate results for thin and highly conductive specimens. Akiyoshi et al. [26] resolved the problem by using a graphene nanoplatelets containing agent instead, which creates a very thin, sparsely coated surface.

Initially, there were also some concerns associated with the

**Table 2**

Calculated Thermal conductivity, based on reference data for the density and specific heat of pure unirradiated tungsten.

Thermal conductivity (W·m <sup>-1</sup> ·K <sup>-1</sup> )				
Temp. (°C)	Unirr.	3.9 dpa	5.8 dpa	3.9 dpa - Annealed
25	173	84	86	115
100	162	87	88	—
200	148	90	88	—
300	138	90	91	113
400	133	91	94	—
500	128	93	95	111



effect of the high residual dose of the irradiated specimens on the infrared InSb sensor in the LFA. The specimens which were tested in this work had a gamma dose rate of about 2 mSv/h at a distance of 10 cm. This conservatively translates to 2 mGy/h in the sensor. During the measurement which took about 10 h, the total accumulated gamma dose in the sensor was estimated to be 20 mGy. In Pickel et al. [28], the conservative dose limit of an InSb sensor under 14 MeV neutron irradiation is reported to be  $3 \times 10^{11}$  n/cm<sup>2</sup>. This dose limit translates to 1.3 Gy, which is two orders of magnitude higher than the accumulated dose in the photovoltaic InSb sensor used in the LFA. Though the material damage mechanism under neutron and gamma irradiation might differ, the two orders of magnitude of safety margin was deemed large enough to guarantee that the accuracy of the sensor is not affected by the gamma radiation emitted from the tungsten. This was confirmed by post-measurement calibration tests.

#### 4. Conclusions

Thermal diffusivity of proton and spallation neutron irradiated tungsten has been determined in the temperature range 25–500 °C. The specimens were irradiated up to doses of 3.9 and 5.8 dpa. Due to the irradiation, around 2% rhenium is expected to have formed as a transmutation product.

Thermal diffusivity of the irradiated specimens attained a value of around 35 mm<sup>2</sup>/s, independent of test temperature and dose. Compared to thermal thermal diffusivity of the unirradiated specimens this value is 51% and 28% lower at 25 and 500 °C, respectively.

The degradation of thermal diffusivity after irradiation is a result of both displacement damage and compositional changes due to transmutations. The specimens in the present study showed similar thermal diffusivity values despite being irradiated to two different doses. This implies that the rhenium content, which should be similar in both specimens, is responsible for the main contribution to the total thermal diffusivity decrease. Consistent with reviewed literature, an addition of only a few percent of rhenium results in a drastic decrease of thermal diffusivity at room temperature.

In the present study, an attempt was made to separate the effect of displacement damage and rhenium transmutation on the degradation of thermal diffusivity. Annealing at 1000 °C for 1 h resulted in a partial recovery of the thermal diffusivity of the 3.9 dpa specimen. At room temperature, it had increased by 37% to a thermal diffusivity of 47 mm<sup>2</sup>/s, and at 500 °C it had increased by 19%–41 mm<sup>2</sup>/s. The higher post-annealing thermal diffusivity is believed to be a result of the recovery of the radiation induced displacement damage.

In future studies, the thermal diffusivity of tungsten specimens with higher irradiation doses than presented here will be analyzed. An attempt to measure the specific heat of irradiated tungsten will be made. The mechanisms behind the radiation induced degradation of the diffusivity is still to be understood. Further investigations involving the studies of microstructural defects and its correlation with the electron and phonon transport kinetics will be made, which are responsible for the radiation induced change of thermal conductivity.

#### Data availability

The raw/processed data required to reproduce these findings cannot be shared at this time due to technical or time limitations.

#### Appendix A. Supplementary data

Supplementary data related to this article can be found at

<https://doi.org/10.1016/j.jnucmat.2018.06.041>.

#### References

- [1] S. Peggs, R. Kreier, C. Carlile, et al., ESS Technical Design Report, ESS-doc-274, ESS-0016915, European Spallation Source ERIC, April 23, 2013.
- [2] B. Horvath, J. Habainy, Y. Lee, Y. Dai, A study of hardening effect in pure tungsten after irradiation in a mixed spectrum of high energy protons and spallation neutrons and after post-irradiation annealing, in: Presented at the 18th International Conference on Fusion Reactor Materials (ICFRM-17), Aomori, Japan, November 5–9th, 2017.
- [3] J. Habainy, A. Löfberg, S. Iyengar, Y. Lee, Y. Dai, Fatigue properties of tungsten from two different processing routes, J. Nucl. Mater. 506 (2017) 83–91.
- [4] A. Aguilar, M. Magan, I. Herranz, F. Sordo, T. Mora, R. Vivanco, G. Bakedano, J. Aguilar, L. Mena, M. Mancisidor, J.L. Martinez, Equipment Specification Document: Spallation Material, Report No. ESS-0058358, September 16, 2016.
- [5] T. Tanabe, C. Eamchotchawalit, C. Busabok, S. Taweethavorn, M. Fujitsuka, T. Shikama, Temperature dependence of thermal conductivity in W and W-Re alloys from 300 to 1000 K, Mater. Lett. 57 (2003) 2950–2953.
- [6] A. Hasegawa, T. Tanno, S. Nogami, M. Satou, Property change mechanism in tungsten under neutron irradiation in various reactors, J. Nucl. Mater. 417 (2011) 491–494.
- [7] M. Fujitsuka, B. Tschiiya, I. Mutoh, T. Tanabe, T. Shikama, Effect of neutron irradiation on thermal diffusivity of tungsten-rhenium alloys, J. Nucl. Mater. 283–287 (2000) 1148–1151.
- [8] L. Zanini, A. Aiari, A Neutron Booster for the SINQ Neutron Source Using Thin Fissile Layers, No. INIS-xa-09N0647, International Atomic Energy Agency (IAEA), 2009.
- [9] ASTM Standard E1461-13, Standard Test Method for thermal Diffusivity by the Flash Method, ASTM International, 2013.
- [10] ASTM Standard E2585-09, Standard Practice for thermal Diffusivity by the Flash Method, ASTM International, 2015.
- [11] W.J. Parker, R.J. Jenkins, C.P. Butler, G.L. Abbott, Flash method of determining thermal diffusivity, heat capacity, and thermal conductivity, J. Appl. Phys. 32 (1961) 1679–1684.
- [12] J.A. Cape, G.W. Lehman, Temperature and finite pulse-time effects in the flash method for measuring thermal diffusivity, J. Appl. Phys. 34 (1963) 1909–1913.
- [13] Netzsch-Proteus LFA-software, Version 7.1, Software Help Manual, accessed 2018.03.07.
- [14] H. Mehling, G. Hautzinger, O. Nilsson, J. Fricke, R. Hofmann, O. Hahn, Thermal diffusivity of semitransparent materials determined by the laser-flash method applying a new analytical model, Int. J. Thermophys. 19 (1998) 941–949.
- [15] R.L. Masters, J.V. Beck, R.B. Dinwiddie, H. Wang, Accounting for penetration of laser heating in flash thermal diffusivity experiments, J. Heat Tran. 121 (1999) 15–21.
- [16] B. Horvath, Y. Dai, Y. Lee, Annealing effect on the microstructure of tungsten irradiated in SINQ target, J. Nucl. Mater. 506 (2018) 19–25.
- [17] Y.S. Touloukian, C.Y. Ho, Thermophysical properties of matter – the TPRC data series, in: Thermal diffusivity, vol. 10, Purdue University, 1974.
- [18] F. Hofmann, D.R. Mason, J.K. Eliason, et al., Non-contact measurement of thermal diffusivity in ion-implanted nuclear materials, Sci. Rep. 5 (2015) 16042, <https://doi.org/10.1038/srep16042>.
- [19] J. Habainy, A. Prosvetov, Y. Lee, P. Simon, Y. Dai, S. Iyengar, M. Tomut, Radiation induced changes in thermal, electrical and dynamic response properties of tungsten foils under pulsed heavy ion beam, in: Presented at the 16th International Conference on Plasma-facing Materials and Components for Fusion Applications (PFMC-16), Neuss/Düsseldorf, Germany, May 16–19th, 2017.
- [20] Y. Lee, M. Hartl, Materials Handbook, Technical Report ESS-0028465, European Spallation Source ERIC, July 28, 2017.
- [21] D.T. Hurd, “Tungsten” in metals handbook, in: Properties and Selection of Metals, vol. 1, American Society for Metals, Metals Park, Novelt, Ohio, 1961.
- [22] J. Matolich, H. Nahn, J. Moteff, Swelling in neutron irradiated tungsten and tungsten-25 percent rhenium, Scripta Metall. 8 (1974) 837–842.
- [23] M. Roedig, W. Kuehnlein, J. Linke, D. Pitzer, M. Merola, E. Rigal, B. Schedler, E. Visca, Post irradiation testing of samples from the irradiation experiments PARIDE 3 and PARIDE 4, J. Nucl. Mater. 329–333 (2004) 766–770.
- [24] P. Schoderböck, H. Klocker, L.S. Sigl, G. Seeber, Evaluation of the thermal diffusivity of thin specimens from laser flash data, Int. J. Thermophys. 30 (2009) 599–607.
- [25] Operating Instructions, HyperFlash Apparatus LFA 467 Manual, NETZSCH, 2015.
- [26] M. Akiyoshi, R. Kasada, Y. Ishibashi, et al., Validation of miniature test specimens for post-irradiation thermal diffusivity measurement, Fusion Eng. Des. (2018), <https://doi.org/10.1016/j.fusengdes.2018.03.008>.
- [27] Y. Ishibashi, S. Yanagi, O. Tsukamoto, Y. Shinoda, J. Blumm, New black coating method for flash measurements with graphene nanoplatelets containing agent, in: Proc. of the 37th Japan Symposium on Thermophysical Properties, Okayama, Japan, November 28–30th, 2016.
- [28] J.C. Pickel, A.H. Kalma, G.R. Hopkinson, C.J. Marshall, Radiation effects on photonic imagers – a historical perspective, IEEE Trans. Nucl. Sci. 50 (2003) 671–688.

# PAPER V

J. Habainy, Y. Dai, Y. Lee, S. Iyengar

**Mechanical properties of tungsten irradiated with high energy protons  
and spallation neutrons**

*Submitted to Journal of Nuclear Materials, July 2018*

Reproduced with permission from Elsevier



# Mechanical properties of tungsten irradiated with high energy protons and spallation neutrons

Jemila Habainy<sup>1,2,3</sup>, Yong Dai<sup>2\*</sup>, Yongjoong Lee<sup>1</sup> and Srinivasan Iyengar<sup>1,3</sup>

<sup>1</sup>European Spallation Source ESS ERIC, Box 176, 22 100, Lund, Sweden

<sup>2</sup>Paul Scherrer Institut, 5232 Villigen PSI, Switzerland

<sup>3</sup>Div. of Materials Engineering, Lund University, Box 118, 22 100 Lund, Sweden

## Abstract

In this work, 3-point bending tests and micro-hardness measurements were performed on pure tungsten irradiated with high energy protons and spallation neutrons in a target of the Swiss Spallation Neutron Source (SINQ). The samples were irradiated to doses in the range of 1.3-3.5 dpa, with 37-140 appm He, at temperatures 75-110 °C. During the three-point bending tests performed at temperatures up to 500 °C, all the irradiated specimens fractured in the elastic regime at stresses much below those of for the unirradiated reference specimens. The micro-hardness measurements indicate significant irradiation induced hardening under all irradiation conditions. Observations of the fracture surfaces using scanning electron microscopy show brittle fracture behaviour in general, whereas detailed features depend strongly on the irradiation dose and testing temperature.

**Key words:** Tungsten, spallation target, irradiation effects, mechanical properties, 3-point bending test

## 1. Introduction

Tungsten is currently used as a target material in neutron spallation sources such as ISIS Neutron and Muon source, and Los Alamos Neutron Science Center (LANCE). It has also been chosen as the target material at the European Spallation Source (ESS), which is currently under construction in Lund, Sweden. Tungsten provides a high neutron production yield thanks to its high density and high atomic mass, and is largely available commercially. In addition, tungsten has a high melting point and high thermal conductivity, which makes it a favorable material option for use in high power spallation targets.

However, there are concerns about its low ductility, high ductile-to-brittle transition temperature (DBTT), and irradiation-induced embrittlement [1-7], in using tungsten as spallation target material. Despite being used in spallation targets for many years, the changes in material properties of proton and spallation neutron irradiated tungsten is barely understood and there is a scarcity of literature on the subject. The present work is an effort to obtain data on the mechanical properties and the fracture behavior of pure tungsten, which is irradiated by high energy protons and spallation neutrons.

The data obtained in this work is of particular interest to the ESS, where the rotating tungsten target will receive a high radiation damage dose from a 2 GeV and 5 MW pulsed proton beam, during its 5-year lifetime [8]. The ESS target consists of helium cooled spallation volume made of tungsten, contained in a wheel shaped target vessel made of stainless steel. The target wheel with a diameter of 2.6 meters is segmented in 36 equal parts. The spallation volume in each of the 36 segments consists of 186 tungsten bricks with a dimension of  $8 \times 3 \times 1$  cm<sup>3</sup>. The target wheel rotates at a frequency of 0.39 Hz, which is synchronized to the 14 Hz repetition rate of the 2.86 ms long proton beam pulse.

Upon full commissioning with 5 MW beam power, beam pulses and occasional beam trips will induce cyclic thermo-mechanical loading in the tungsten bricks, which can drive the temperature in the target up to a maximum of 500 °C, and lead to stresses in the bricks up to a maximum of 110 MPa [9]. The maximum temperature and stress variances in a tungsten brick during single pulse is calculated to be approximately 100 °C and 70 MPa, respectively. Although the tungsten is not a structural material of the target, it is important to keep the mechanical integrity of the bricks, in order to keep the helium cooling channels intact and the

radioactive transmutation elements retained. Mechanical failure of a tungsten brick may lead to a partial blockage of the 2 mm wide helium cooling channel between it and an adjacent tungsten brick, which could create a hot spot in the target and increase the rate of diffusion driven release of radioactive isotopes [10].

The DBTT of unirradiated tungsten and its dependence on the fabrication route and purity of the material, as well as the method for determining the DBTT and specimen size, have been discussed extensively elsewhere [11-18]. Most of the reported DBTT are within the temperature range defined by 200-350 °C, though the exact value varies widely depending on experimental conditions. The tensile tests data of irradiated tungsten in fission reactor environment suggests that the DBTT of pure tungsten is higher than 500 °C at a displacement damage dose of above 0.1 dpa [6]. At 5 MW proton beam on the ESS target, the tungsten bricks could get maximum 2 dpa per year. This means that the DBTT of the tungsten bricks will rise above the maximum operation temperature of 500 °C in less than a month of operation.

This work is a part of the project that is dedicated to understanding of the mechanical and thermal properties of tungsten spallation material under ESS target environments. Early investigations focused on the unirradiated reference tungsten under conditions relevant to normal ESS operation, which include the bending properties in the operation temperature range [15], the effect of fabrication route on the microstructure, DBTT and tensile behaviour [17], the fatigue behaviour at different temperatures and its dependence on the processing route [16, 18], and the formation of oxide layers at low oxygen partial pressures [19]. Recently, studies on tungsten specimens irradiated at SINQ Target-7 have been carried out, where the specimens were annealed at different temperatures (post irradiation) and observed using a transmission electron microscope (TEM) [20]. The effect of irradiation and the subsequent heat treatment on the density of defects was discussed. Tungsten specimens from the same irradiation campaign were also used for thermal diffusivity studies [21]. Measurements showed that the thermal diffusivities of 3.8 and 5.9 dpa specimens, tested in the temperature range 25-500 °C, were 28-51% lower relative to that of the unirradiated tungsten. In the present work, pure tungsten from the same irradiation campaign has been tested in 3-point bending at temperatures up to 500 °C, and the effect of high energy proton and spallation neutron irradiation on flexural strength and hardness is investigated.

## 2. Experimental

### 2.1 Materials

Slices of 1 mm thickness and 60 mm length were cut from a plate of 10 mm thickness commercially pure (99.9% purity) tungsten using an electro-discharging machine (EDM), then milled to  $1 \times 8 \times 60 \text{ mm}^3$  size for irradiation. The material is cross-rolled with the average grain sizes in the three directions 25, 20 and 17  $\mu\text{m}$ , respectively. The length of the slices is parallel to the rolling direction of the plate. The irradiation was conducted during 2007 and 2008 at the Paul Scherrer Institut (PSI) in the fifth campaign of the SINQ Target Irradiation Program (STIP-V). Figure 1 below shows one of the STIP-V specimen rods containing a tungsten slice. The slice was positioned in the right half of the rod. The centre of the Gaussian shaped beam located at the left part of the slice, where the tungsten material received a total dose of 28 dpa with 1300 appm He and 7200 appm H at an average irradiation temperature of 550 °C. The corresponding values for the right end of the slice are 1.3 dpa, 37 appm He, 310 appm H and 75 °C. The irradiation dose was calculated using the MCNPX code and the irradiation temperature was simulated with the ANSYS code, as in the case of the previous STIP irradiation experiments [22,23].

During unpacking the specimen rods in the hot-cell, the tungsten slices were broken into shorter pieces. Nevertheless, in total 31 specimens, including miniature bend bars and tensile specimens and 6 mm diameter discs, could still be extracted by EDM cutting. Due to the high activity of the material, only a few of the lowest dose specimens could be tested so far. The six bend bars ( $1 \times 2 \times 8 \text{ mm}^3$  size) studied in this work are of doses 1.3-3.5 dpa, with 37-140 appm He and 310-810 appm H and irradiated at temperatures 75-110 °C. Before testing, they were mechanically polished in several steps, finishing with a standard colloidal silica suspension to even out the surface roughness due to EDM cutting.

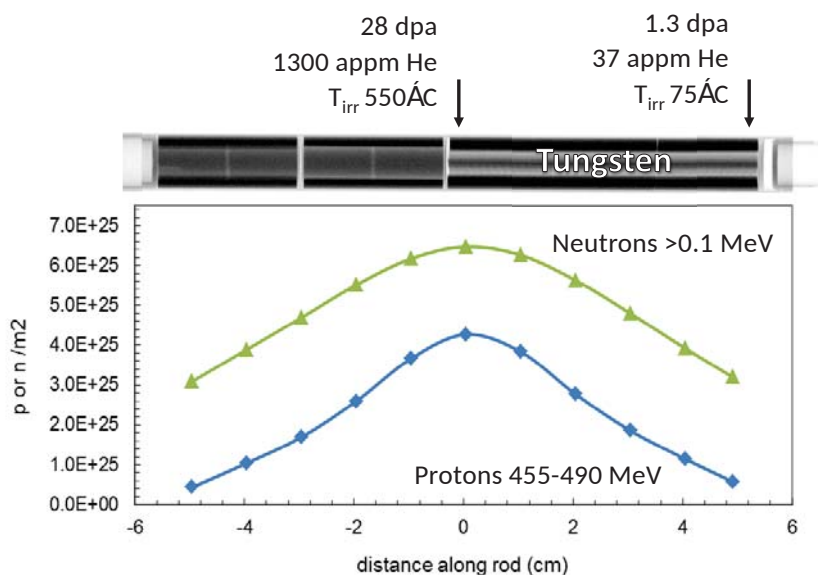


Fig. 1 The upper image depicts the rod containing the tungsten slice. The lower graph shows the fast neutron and proton fluences as a function of distance along the rod.

## 2.2 Experimentals

Both hardness measurements and 3-point bending tests were performed on the same samples. Before bending tests, hardness (HV0.5) was measured using a Vickers hardness tester with a 0.5 kg load and 15 s dwell time. Afterwards, 3-point bending tests were conducted on a Zwick universal test machine with a load capacity of 10 kN at a constant crosshead travel speed of 0.1 mm/min. The load was applied in the long transvers direction of the samples during testing. The 3-point bending method is advantageous for characterizing mechanical behaviour of materials using few and relatively small specimens. This is particularly useful when working with very limited amounts of highly active material, as in the case of this study. The ASTM standard E2769-16: Standard Test Method for Elastic Modulus by Thermomechanical Analysis Using Three-Point Bending and Controlled Rate of Loading [24], can be used for determining the elastic modulus of materials with maximum strains below 3%. The flexure strength, i.e. the maximum stress prior to fracture, is determined using the following equations:



$$\sigma = \frac{3FL}{2bd^2} \quad (1)$$

$$\epsilon = \frac{6Dd}{L^2} \quad (2)$$

where  $\sigma$  is the fracture stress (MPa),  $F$  is the maximum load (N) prior to fracture,  $L$  is the support span (mm),  $b$  is the specimen width (mm),  $d$  is the specimen thickness (mm),  $D$  is the deflection (mm), and  $\epsilon$  is the strain.

Out of the 6 bend samples, only 3 were successfully tested and resulted in useful and reliable data. The doses and their corresponding test temperatures for these 3 specimens were as follows: 1.8 dpa – 350 °C, 2.1 dpa – 400 °C, and 1.4 dpa – 450 °C. In order to collect data over a wider temperature range, the remains of the broken samples, were used as new bend bars with the dimensions  $1 \times 2 \times 4 \text{ mm}^3$ , i.e. half the length of the original ones. The doses and testing temperatures of these bend bars were the following: 1.3, 2.1, and 3.5 dpa – 25 °C, 1.8 dpa – 350 °C, 2.1 dpa – 400 °C, 1.4 dpa – 450 °C, and 2.6 dpa – 500 °C.

After bend testing, the fracture surfaces were observed using scanning electron microscopy (SEM). The SEM images are presented in the following section together with the hardness and bending test data.

### 3. Results and discussion

#### 3.1 3-point bending testing

Data obtained from the 3-point bending tests were converted into engineering stress and strain using the equations presented in section 2.2. The results are summarised in Fig 2. The strain and fracture stress of the unirradiated reference tungsten increased with increasing temperature. At 450 °C, the strain corresponding to a fracture stress of 1171 MPa was nearly 15%, whereas at 25 °C, the unirradiated specimen fractured already at 570 MPa in the elastic regime. The DBTT seems to be around 350 °C. The irradiated specimens on the other hand, remain brittle fracture and without any plastic deformation regardless of the irradiation dose and testing temperature. At 25 °C, the average fracture stress of the irradiated tungsten is 304 MPa. The difference in dosage among the 25 °C specimens (between 1.3 and 3.5 dpa) does not seem to affect the fracture behaviour much. As the testing temperature increases, the

fracture stress also increases. The 2.6 dpa specimen tested at 500 °C fractured at a stress of 548 MPa, which is very similar to the behaviour of the unirradiated 25 °C specimen.

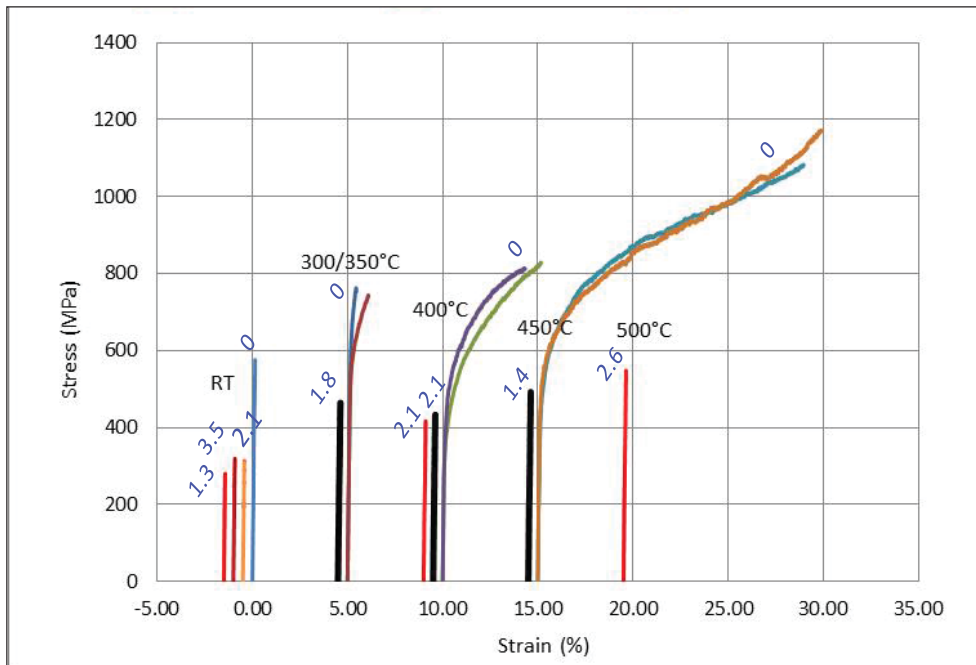


Fig. 2 Stress-strain diagram displaying results from the 3-point bending testing. The data are grouped according to the testing temperature with a shift of 5% on the x-axis. The numbers nearby the curves indicate the irradiation dose (dpa).

### 3.2 Hardness

Hardness measurements were performed on the reference specimens and on the specimens irradiated to 1.3, 1.4, 2.1, and 3.5 dpa. The results are presented in Fig. 3, plotted together with data from Maloy et al. [7].

The average microhardness of the unirradiated tungsten is 400 HV. Already at an irradiation damage of 1.3 dpa the hardness increases by 51%, and at 3.5 dpa the increase is 68%. The microhardness measurements presented by Maloy et al. [7], were performed on tungsten irradiated by 800 MeV protons in the temperature range of 50-160 °C, with 50-320 appm He. The hardness of these specimens is, however, slightly lower in comparison.

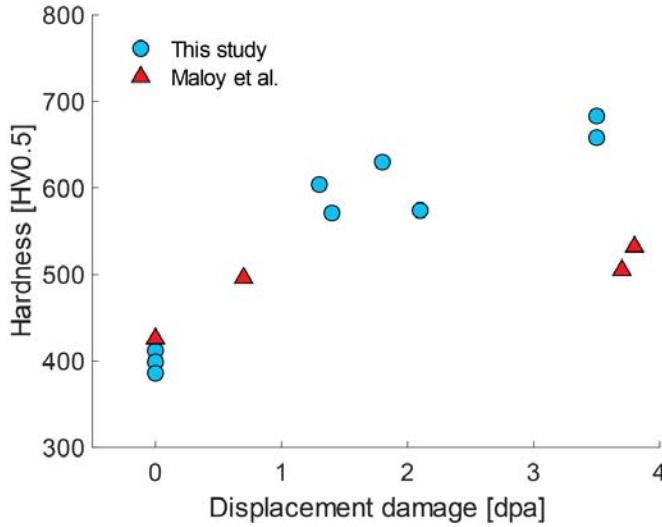


Fig. 3 Hardness of tungsten as a function of irradiation damage. The results obtained in this work are compared to data from Maloy et al. [7] where tungsten was irradiated with 800 MeV protons.

### 3.3 Fractography

After 3-point bending testing the fractured specimens were observed in a SEM. Fig. 4 presents a comparison of two unirradiated specimens, tested at 25 °C and 450 °C, respectively. The specimen tested at the lower temperature shows no sign of plastic deformation, which is consistent with the bending test results, presented in section 3.1. The specimen tested at 450 °C, above the DBTT, displays a significant amount of plasticity. The side surface shows numerous cracks and slip bands (Fig. 4d). The specimen tested below the DBTT fractured in a mixed trans- and intergranular fracture mode (Fig. 4e). whereas the high temperature specimen fractured mainly in an intergranular mode (Fig. 4f).

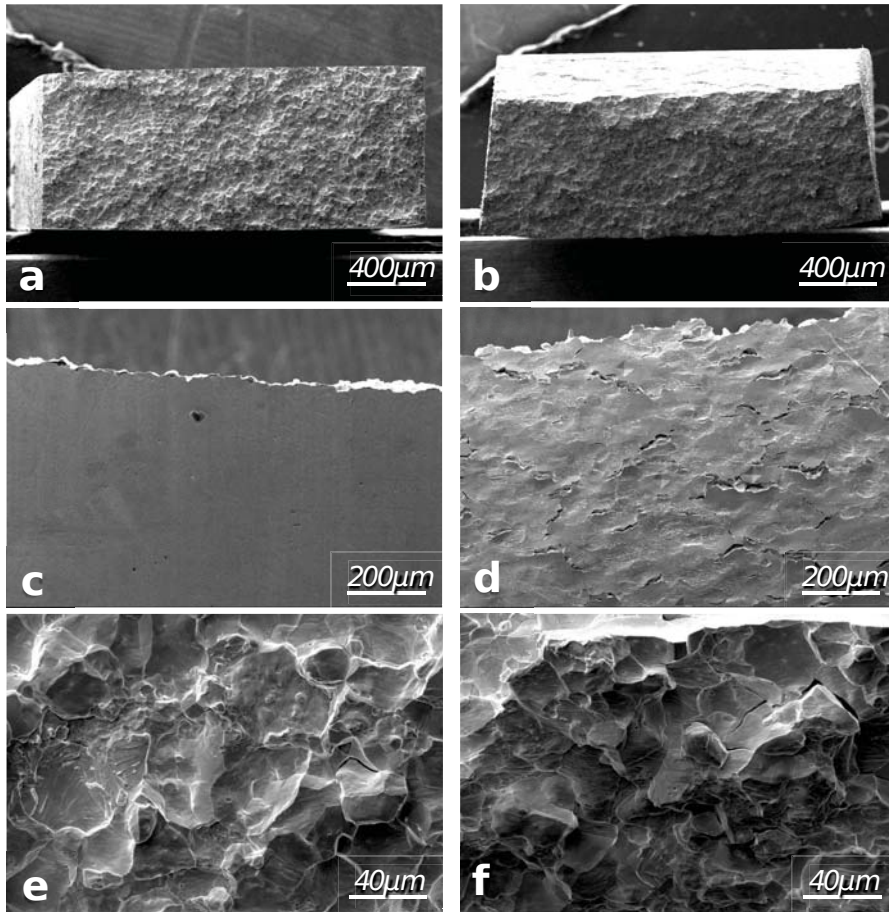


Fig. 4 SEM images of the fractured unirradiated tungsten specimens. The images to the left show a specimen tested at 25 °C, which fractured in a brittle manner. The images to the right show a specimen tested at 450 °C, which is above the DBTT, as is confirmed by the large amount of plastic deformation. Images *a*, *b*, *e*, and *f* show the fracture surfaces. Images *c* and *d* show the side surfaces.

Figure 5 presents the fractographs of two specimens irradiated to 1.3 and 3.5 dpa and tested at 25°C. Both specimens fractured in mixed transgranular and intergranular mode. The fracture surface of the 1.3 dpa specimen (Fig. 5a and 5c) looks like the unirradiated specimen tested at 25°C (Fig. 4e), but with a higher portion of transgranular fracture. The fracture surface of the 3.5 dpa specimen (Fig. 5b and 5d) looks quite different from that of the 1.3 dpa one, with the intergranular mode dominating. One may also notice that the grain surfaces of the 1.3 dpa

specimen are generally smooth, while those of the 3.5 dpa specimen are having many small facets.

Figure 6 exhibits the fracture surfaces of two specimens of 1.4 dpa and 2.6 dpa and tested at 450° and 500°C, respectively. The overall fracture characteristics of these two samples resemble those of specimens tested at 25°C (Fig. 5). The lower dose specimen shows again a mixed transgranular and intergranular fracture mode. However, slip bands can be seen everywhere on the surfaces of the grains. The 2.6 dpa specimen shows an interesting feature. The low magnification image (Fig. 6b) indicates that the fracture should be transgranular type, because the fracture surface is smooth or flat, whereas the high magnification image (Fig. 6d) depicts intergranular fracture, with tiny grain surfaces, rather facets shown in Fig. 5d, on large grain surfaces, as seen in the insert in the figure.

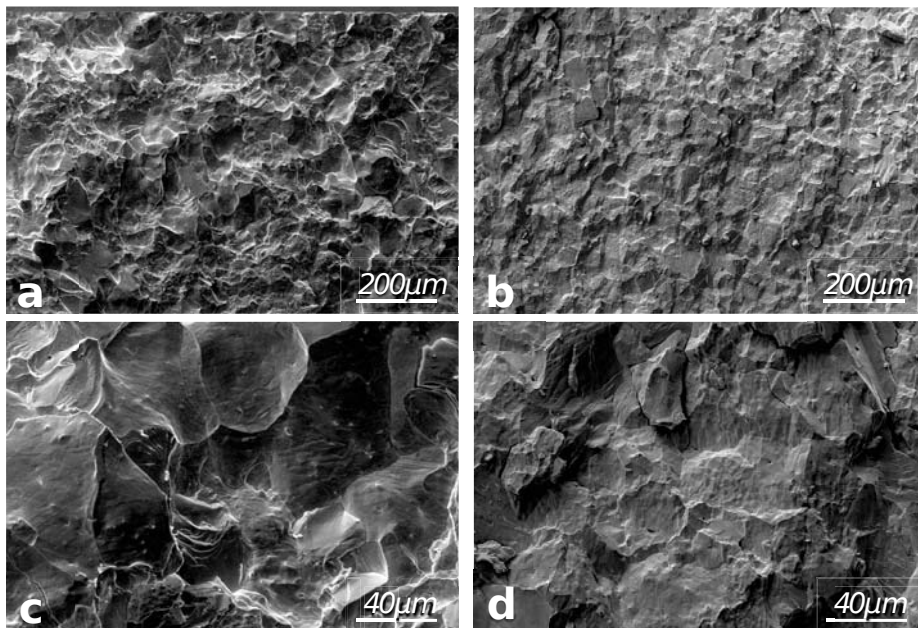


Fig. 5 SEM images of the fracture surfaces of tungsten specimens irradiated to 1.3 dpa (images *a* and *c*) and 3.5 dpa (images *b* and *d*), tested at 25 °C.

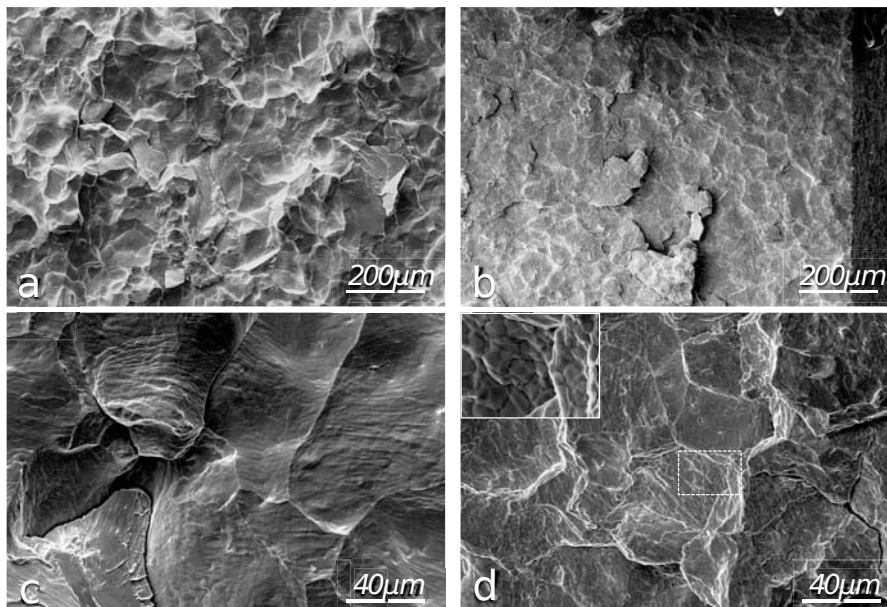


Fig. 6 SEM images of the fracture surfaces of tungsten specimens irradiated to 1.4 dpa and tested at 450°C (images *a* and *c*) and 3.5 dpa and tested at 500°C (images *b* and *d*).

#### 4. Discussion

Effect of neutron irradiation on the mechanical properties of tungsten has been studied since 1950s. However, not many data could be found in open publications. The reason might be that tungsten is brittle at room temperature and its DBTT increases quickly after irradiation, which make mechanical testing of irradiated tungsten rather difficult, particularly at irradiation doses above 1 dpa. In the 1960s and 70s some low dose ( $<1$  dpa) irradiation experiments were performed on pure tungsten materials. For example, Rau et al. [1] irradiated commercially pure (99.98%) tungsten in ORR (Oak Ridge Research Reactor) at  $\sim 70^\circ\text{C}$ . Tensile testing at  $400^\circ\text{C}$  showed that specimens irradiated to fast neutron fluence of  $3.9 \times 10^{23} \text{ n/m}^2$  ( $E > 0.1 \text{ MeV}$ , the corresponding dose is about 0.01 dpa) and higher were fractured essentially without plastic deformation. Meanwhile, large hardening effect was detected as the increase of yield stress or ultimate tensile strength. In another case, Younger et al. [3] found the DBTT of tungsten increased rapidly with irradiation dose. After irradiation at about  $120^\circ\text{C}$  to  $1.5 \times 10^{24} \text{ n/m}^2$  ( $E > 1 \text{ MeV}$ ), the transition temperature derived from tensile testing increased from  $315^\circ\text{C}$  of the unirradiated specimens to about  $795^\circ\text{C}$ , with a shift by  $480^\circ\text{C}$ . At the lower bound of the transition, the specimens failed with zero ductility, although the testing temperatures were



much higher than the irradiation temperature. At higher irradiation doses,  $\geq 1 \times 10^{25}$  n/m<sup>2</sup>, Gorynin et al. [5] found that W and some W-alloys were all brittle at irradiation and testing temperature below 700°C. In this work, for the specimen of the lowest dose the fast ( $E > 0.1$  MeV) neutron fluence is about  $2.3 \times 10^{25}$  n/m<sup>2</sup>, and in addition, the high energy (average energy is 470 MeV) proton fluence is about  $1.1 \times 10^{24}$  n/m<sup>2</sup>. The displacement dose is much higher than the neutron irradiation doses as mentioned above. Hence, it is not surprising to see the brittle fracture of the specimens when they were tested at temperatures up to 500°C.

As observed by many authors that neutron spectra play an important role in the irradiation effect of tungsten. The early results obtained by Rau et al. [1] from tensile and creep tests on Cd-shielded and unshielded tungsten specimens irradiated to a fast neutron fluence of  $3.8 \times 10^{23}$  n/m<sup>2</sup> ( $E > 1$  MeV) showed a marginally lower strength and a greater degree of embrittlement (lower total elongation or creep rupture life), although no microstructural differences could be seen in the TEM. This means the thermal neutron fluence,  $2.3 \times 10^{24}$  n/m<sup>2</sup>, did not play an important role in the irradiation induced hardening and even improved ductility to some extent. This early observation contradicts recent results obtained by Hasegawa et al. [25,26], which demonstrated, due to high production rates of Re and Os from thermal neutrons, irradiation of tungsten in HFIR with mixed spectrum neutrons induced a stronger hardening effect as compared to irradiation in JOYO with fast neutrons. Figure 7 presents a comparison of the hardening effect observed under different irradiation conditions: 1) irradiations in HFIR and JMTR at temperatures between 90 and 850°C with mixed spectrum neutrons [26], 2) in JOYO at temperatures between 400 and 850°C with fast neutrons [26], 3) in SINQ Target-7 at low temperatures between 85 and 110°C with high energy protons and spallation neutrons, and 4) at LANCE at temperatures between 60 and 250°C with 800 MeV protons [7]. The differences among the four data sets are clear. The differences may be attributed to different purities (99.9 – 99.999%), different crystalline structures (single- and poly-crystalline structures), different helium/hydrogen contents ( $\sim 0/0$  – 1900 appm He/10300 appm H), and wide irradiation temperature ranges (60 – 850°C), while the main cause seems to be the effect of the irradiation spectrum, or the rhenium production and perhaps precipitation as well [25-28]. The production of rhenium by 800 MeV protons is about 15 appm per dpa, which is much lower than that in HFIR irradiation case,  $\sim 34000$  appm per dpa, or even in JOYO irradiation case,  $\sim 520$  appm per dpa [28]. In the SINQ irradiation case, since there is a thermal neutron spectrum [22], the rhenium production should be greater than that of 800 MeV protons, but perhaps lower than that of fast neutron irradiation, because

for tungsten a large part (>60%) of displacement damage is contributed by high energy protons. In the tungsten target of ESS, the rhenium production after 5 years target lifetime at 5 MW beam operation is calculated to be a maximum of 0.4 at-%, namely about 400 appm per dpa. Therefore, the rhenium effect may not be so pronounced.

It should be mentioned that the hardening effect in the present series of specimens will be further studied with the specimens of higher doses. The rhenium production and clustering will be quantitatively analyzed with different techniques.

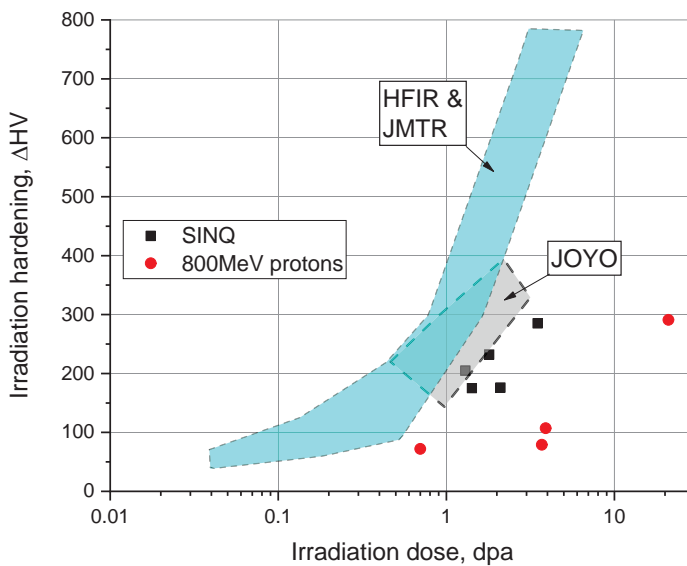


Fig. 7 Irradiation dose dependence of pure tungsten irradiated in different irradiation facilities. The data bands of HFIR/JMTR and JOYO are taken from [26].

The observation of fracture surfaces of neutron irradiated tungsten samples is quite limited up to date. The early work performed by Younger et al. depicted that, after irradiation with fast ( $E > 1$  MeV) neutrons to  $10^{24}$  n/m<sup>2</sup> at 204°, 316° and 371°C (400°, 600° and 700°F) and tensile tested at the same temperatures, the specimens (with a gauge section of 4.83 mm diameter and 25.4 mm length) showed brittle intergranular fracture. The specimens of the same dose irradiated and tested at 149°C (300°F) exhibited transgranular fracture. Unfortunately, there



is no detailed information available. Transgranular brittle fracture was also observed by Saito et al. [29] on tungsten irradiated in SINQ Target-4 to higher doses ( $>8$  dpa) and tensile tested at room temperature, in which all specimens fractured in the elastic regime.

The present results show a strong dependence of fracture behavior on irradiation dose and testing temperature. For unirradiated or 1.3/1.4 dpa specimens, the fracture is typically mixed transgranular and intergranular, with a general trend of increase in intergranular fracture with increasing testing temperature. For specimens tested at 450°C, slip bands were observed on the grain surfaces of both unirradiated and 1.4 dpa specimens, which indicate some amount of plastic deformation taking place inside the grains. At higher doses, 2.6 and 3.5 dpa, the fracture surfaces are flat, which reflects a very brittle cleavage fracture. The crack propagation path should be mainly through the original grains, namely in a transgranular manner. However, the small facets (Fig. 5d) or tiny grain surfaces (Fig. 6d) suggest that the fracture is a kind of intergranular type. As shown in [16] and [18], intergranular fracture was observed along boundaries of small grains or subgrains. EBSD (Electron backscatter diffraction) analysis [30] demonstrated that there is a subgrain structure in the hot-rolled tungsten (the RA samples of [19]). The subgrains have sizes typically between 0.5 and 2  $\mu\text{m}$  and many subgrain boundaries are with angles greater than  $10^\circ$ . Therefore, in the 2.6 and 3.5 dpa specimens, the crack propagation should be mainly along subgrain boundaries. This is different from that observed by Saito et al. in higher dose specimens, where the feature was transgranular cleavage fracture with river patterns and no intergranular fracture was observed. The reason may be associated with the production and purity of the tungsten materials in different studies. This issue will be investigated in the future using the different tungsten materials irradiated in STIP-VI and STIP-VII.

As for the significance of the present work to the ESS application, the results show that in the ESS operation conditions, the fracture stress of the tungsten bricks may be 200 MPa or higher. This is higher than that induced by beam pulses and beam trips, in the range of 44-110 MPa [8]. However, it does not guarantee that the tungsten bricks would not fail during the operation, because crack propagation under a cyclic stress condition is easier.

## 5. Summary and conclusion

Cross-rolled commercially pure tungsten was irradiated in SINQ Target-VII during the period 2007-2008, as a part of the STIP-V irradiation campaign. The samples were exposed to both high energy proton and spallation neutrons, accumulating radiation damage in the range of 1.3-28 dpa with 37-1300 appm He, at irradiation temperatures of 75-550 °C. Due to the high activity of the tungsten, only specimens of low dose, i.e. 1.3-3.5 dpa, were studied. In order to estimate the DBTT and investigate the fracture behaviour of irradiated tungsten, three-point bending tests were performed at temperatures up to 500 °C. The results showed that at all doses and temperatures, the specimens have virtually zero ductility and fail at stress levels much below those of the reference specimens. The hardness measurements demonstrate a strong irradiation-induced hardening effect in all samples.

## Acknowledgement

Mr. Roger Brun and the operators of the Hot-cell Experiment Group at PSI are acknowledged for their help on sample preparation. Dr. Kumar Babu Surreddi at Dalarna University, Sweden provided the EBSD information for the rolled tungsten used in previous work [19]. Yong Dai also thanks Dr. Xuejun Jia at Chinese Spallation Neutron Source for providing the tungsten material.

## References

- [1] R.C. Rau, J. Moteff, R.L. Ladd, Comparison of microstructure with mechanical properties of irr tungsten, J. Nucl. Mater. 24 (1967) 164-173.
- [2] C.L. Younger and G.N. Wrights, Effect of  $10E+20$ -neutron-per-square-centimeter irradiation on embrittlement of polycrystalline tungsten, NASA Technical Note (TN D-4611), 1968.
- [3] C.L. Younger and G.N. Wrights, Effect of reactor irradiation on ductile-brittle transition and stress-strain behavior of tungsten, NASA Technical Note (TN D-5991), 1970.
- [4] J.M. Streichen, Tensile properties of neutron irradiated TZM and tungsten, J. Nucl. Mater. 60 (1976) 13-19.
- [5] I. V. Gorynin, V. A. Ignatov, V. V. Rybin, S. A. Fabritsiev, V. A. Kazakov, V. P. Chakin, V. A. Tsykanov, V. R. Barabash, Y. G. Prokofyev, Effects of neutron irradiation on properties of refractory metals, J. Nucl. Mater. 191-194(1992) 421-425.
- [6] H. Ullmaier, F. Carsughi, Radiation damage problems in high power spallation neutron sources, Nuclear Instruments and Methods in Physics Research B 101 (1995) 406-421.
- [7] S. A. Maloy, M. R. James, W. Sommer Jr., G. J Willcutt Jr., M. Lopez, T. J. Romero, M. B Toloczko, The effect of 800 MeV proton irradiation on the mechanical properties of tungsten at room temperature and at 475 °C, J. Nucl. Mater. 343 (2005) 219-226.
- [8] R. Garoby et al. The European Spallation Source Design, Phys. Scr. **93** (2018) 014001.
- [9] A. Aguilar, M. Magan, I. Herranz, F. Sordo, T. Mora, R. Vivanco, G. Bakedano, J. Aguilar, L. Mena, M. Mancisidor, J.L. Martinez, Equipment Specification Document: Spallation Material, Report No. ESS-0058358, European Spallation Source ERIC, September 16, 2016.
- [10] Y. Lee, M. Hartl, Materials Handbook, Technical Report ESS-0028465, European Spallation Source ERIC, July 28, 2017
- [11] K. Farrell, A. C. Schaffhauser, J. O. Stiegler, Recrystallization, grain growth and the ductile-brittle transition in tungsten sheet, J. Less Common Met. 13 (1967) 141-155.

- [12] R. H. Forster, A. Gilbert, The effect of grain structure on the fracture of recrystallised tungsten wire, *J. Less Common Met.* 20 (1970) 315-325.
- [13] R. E. Schmunk, G. E. Korth, Tensile and low-cycle fatigue measurements on cross-rolled tungsten, *J. Nucl. Mater.* 104 (1981) 943-947.
- [14] Y. Zhang, A. V. Ganeev, J. T. Wang, J. Q. Liu, I. V. Alexandrov, Observations on the ductile-to-brittle transition in ultrafine-grained tungsten of commercial purity, *J. Mater. Sci. Eng. A*, 503 (2009) 37-40.
- [15] V. Krsjak, S. H. Wei, S. Antusch, Y. Dai, Mechanical properties of tungsten in the transition temperature range, *J. Nucl. Mater.* 450 (2014) 81-87.
- [16] J. Habainy, S. Iyengar, Y. Lee, Y. Dai, Fatigue behaviour of rolled and forged tungsten at 25°, 280° and 480 °C, *J. Nucl. Mater.* 465 (2015) 438-447.
- [17] T. Shen, Y. Dai, Y. Lee, Microstructure and tensile properties of tungsten at elevated temperatures, *J. Nucl. Mater.* 468 (2016) 348-354.
- [18] J. Habainy, A. Löfberg, S. Iyengar, Y. Lee, Y. Dai, Fatigue properties of tungsten from two different processing routes, *J. Nucl. Mater.*, vol. 506, pp. 83-91, 2018
- [19] J. Habainy, S. Iyengar, K. B. Surreddi, Y. Lee, Y. Dai, Formation of oxide layers on tungsten at low oxygen partial pressures, *J. Nucl. Mater.* 506 (2018) 26-34.
- [20] B. Horvath, Y. Dai, Y. Lee, Annealing effect on the microstructure of tungsten irradiated in SINQ, *J. Nucl. Mater.* 506 (2018). 19-25.
- [21] J. Habainy, Y. Dai, Y. Lee, S. Iyengar, Y. Lee, Thermal diffusivity of tungsten irradiated with protons up to 5.8 dpa, *J. Nucl. Mater.* 509 (2018) 152-157.
- [22] Y. Dai and G.S. Bauer, Status of the first SINQ Irradiation Experiment, STIP-I, *J. Nucl. Mater.* 296 (2001) 43-53.
- [23] Y. Dai, X. Jia, R. Thermer, D. Hamaguchi, K. Geissmann, E. Lehmann, H.P. Linder, M. James, F. Gröschel, W. Wagner, G.S. Bauer, The Second SINQ Target Irradiation Program, STIP-II, *J. Nucl. Mater.* 343 (2005) 33-44.

- [24] ASTM Standard E2769-16, Standard test method for elastic modulus by thermomechanical analysis using three-point bending and controlled rate of loading, ASTM International, 2016
- [25] Akira Hasegawa, Makoto Fukuda, Takashi Tanno and Shuhei Nogami, Neutron irradiation behavior of tungsten, *Materials Transactions*, Vol. 54, No. 4 (2013) 466-471
- [26] Makoto Fukuda, N.A.P. Kiran Kumar, Takaaki Koyanagi, Lauren M. Garrison, Lance L. Snead, Yutai Katoh, Akira Hasegawa, Neutron energy spectrum influence on irradiation hardening and microstructural development of tungsten, *J. Nucl. Mater.* 479 (2016) 249-254.
- [27] Xunxiang Hu, Takaaki Koyanagi, Makoto Fukuda, N.A.P. Kiran Kumar, Lance L. Snead, Brian D. Wirth, Yutai Katoh, Irradiation hardening of pure tungsten exposed to neutron irradiation, *J. Nucl. Mater.* 480 (2016) 235-243.
- [28] Chen-Hsi Huang, Mark R. Gilbert, Jaime Marian, Simulating irradiation hardening in tungsten under fast neutron irradiation including Re production by transmutation, *J. Nucl. Mater.* 499 (2018) 204-215.
- [29] S. Saito, Mechanical properties of W alloys and pure Ta irradiated at SINQ target-4, presented at 11<sup>th</sup> International Workshop on Spallation Materials Technology, 6 November 2012, Ghent, Belgium.
- [30] Kumar Babu Surreddi, private communication.

# PAPER VI

J. Habainy, Y. Lee, K. B. Surreddi,  
A. Prosvetov, P. Simon, S. Iyengar, Y. Dai, M. Tomut

**A study of ion beam induced damage in tungsten  
for high power target applications**

*Submitted to the Journal of Nuclear Instruments and  
Methods in Physics Research Section B, August 2018*

Reproduced with permission from Elsevier



# Study of heavy ion beam induced damage in tungsten for high power target applications

J. Habainy<sup>a,b,\*</sup>, Y. Lee<sup>a</sup>, K. B. Surreddi<sup>c</sup>, A. Prosvetov<sup>d</sup>, P. Simon<sup>d</sup>,  
S. Iyengar<sup>a,b</sup>, Y. Dai<sup>e</sup>, M. Tomut<sup>d</sup>

<sup>a</sup>European Spallation Source ESS ERIC, SE-221 00, Lund Sweden

<sup>b</sup>Lund University, SE-221 00 Lund, Sweden

<sup>c</sup>Dalarna University, SE-791 88 Falun, Sweden

<sup>d</sup>GSI Helmholtz Centre for Heavy Ion Research, D-64291 Darmstadt, Germany

<sup>e</sup>Paul Scherrer Institute, CH-5232 Villigen PSI, Switzerland

## Abstract

The spallation material at ESS is pure tungsten, which is cooled by gaseous helium flow. To study the behaviour of tungsten under dynamic beam conditions, pure tungsten specimens have been irradiated at the M3-beamline of the UNILAC facility at GSI Helmholtz Centre for Heavy Ion Research. Tungsten specimens of two thicknesses, 26  $\mu\text{m}$  and 3 mm, were exposed to pulsed uranium and gold ion beams for fluences up to  $7.5 \times 10^{13}$  ions/cm<sup>2</sup> at 4.8 MeV/nucleon. Nanoindentation tests were performed on the cross section of the irradiated 3 mm sample, and microhardness was measured on the top surface. The measured data are compared with the calculated damage values, and a correlation between the radiation induced damage and the observed mechanical property is presented. Thermal diffusivities of foil samples, irradiated up to four different fluences, were measured with a Laser Flash Apparatus (LFA). The observed changes in the mechanical and thermal properties of irradiated tungsten were used to estimate the changes of operational temperature and mechanical stresses in the ESS target material with the progress of radiation damage, using coupled thermal and mechanical



simulations. From the pulsed beam induced dynamic oscillations of thin tungsten specimens, information on fatigue properties of tungsten under irradiation was drawn. In addition to pure tungsten, oxidised tungsten samples were also irradiated. This is to investigate the stability of the adhesive oxide layer under pulsed beam conditions, which would be formed due to oxygen impurities in the helium cooling loop. The irradiated oxide scale was examined using Auger Electron Spectroscopy (AES) and Scanning Electron Microscopy (SEM).

**Keywords:** Tungsten, Spallation target, Heavy ion irradiation, Radiation damage

*\*Corresponding author Email address: jemila.habainy@ess.se (J. Habainy)*

*Manuscript submitted to Nuclear Inst. and Methods in Physics Research B September 26, 2018*

## 1. Introduction

The European Spallation Source (ESS) selected pure tungsten as the spallation target material, which is cooled by gaseous helium flow [4]. The spallation volume consists of 6696 tungsten bricks with dimensions of  $80 \times 30 \times 10 \text{ mm}^3$ , which are separated by 2 mm wide helium cooling channels. These tungsten bricks are confined within the wheel-shaped target vessel made of stainless steel. A top view of the target geometry, with an illustration of the tungsten brick layout in a single segment is shown in Fig. 1.

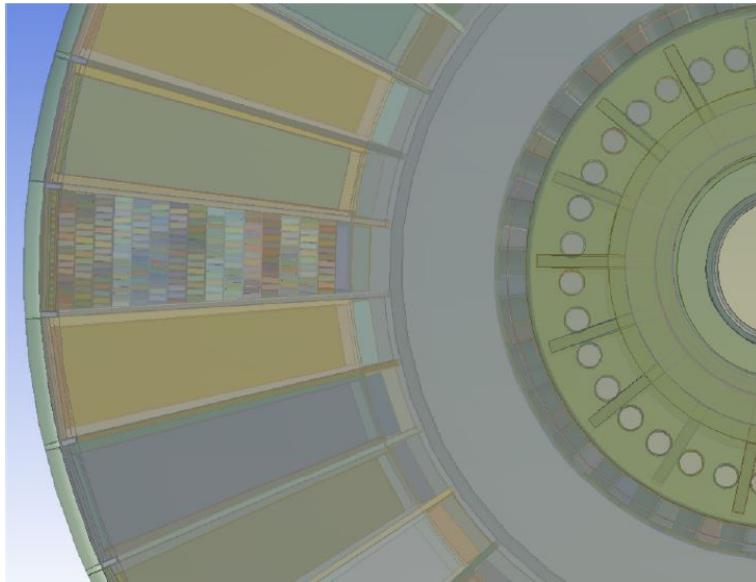


*Figure 1 A top view of the target geometry with an illustration of the tungsten brick layout in a single segment. The picture is taken from the ESS internal design report on the target vessel [1], with the courtesy of ESS-Bilabo.*

The target rotates with a frequency of 0.39 Hz to distribute the thermal loads and radiation damage caused by the high intensity proton beam. Upon full commissioning, the ESS linac will deliver a 2 GeV pulsed proton beam with a repetition rate of 14 Hz and a pulse length of 2.86 ms to the target. The maximum beam current on the target will be 62.5 mA, loading 357 kJ per pulse to the tungsten. During the 5-year lifetime of the target the maximum

proton beam induced displacement damage in the tungsten is estimated to be 10 dpa. Beam pulses and occasional beam trips will cause cyclic thermo-mechanical loading of the bricks, which in combination with the radiation induced embrittlement of tungsten poses a risk of premature failure of the target. For example, broken tungsten pieces could block a cooling channel, creating a local hot spot in the structural parts of the target vessel. The subsequent temperature increase could also result in a higher rate of diffusion driven release of radioactive isotopes and a higher rate of oxidation as well, in the presence of oxygen impurity in the helium coolant [8]. A good understanding of the changes in the physical, mechanical and thermal properties of pure tungsten induced by pulsed beam irradiation is therefore important for the reliable operation of the ESS target. In the present work, pure tungsten specimens have been irradiated with a pulsed heavy ion beam with the purpose of studying changes in thermal and dynamic response properties of tungsten with progressive irradiation damage. Though its damage mechanism differs from that of the high energy proton beam, the heavy ion beam used for irradiating tungsten specimens could induce radiation hardening of tungsten at a relatively low ion fluence. The results obtained from the performed post-irradiation examination confirms and complements the study of the proton irradiated tungsten specimens at PSI [6,7]. The dynamic mechanical response to the beam pulses was analysed using a transient mechanical and thermal simulation software. In addition to pure tungsten, oxidised samples were irradiated in order to investigate the oxide adhesion under a pulsed beam.

## **2. Irradiation Setup**

### **2.1. Specimens for irradiation**

For irradiation, disk shaped specimens made of pure tungsten were prepared in two different thicknesses, 3 mm for the thick ones and 26  $\mu\text{m}$  for the thin ones. The diameter of the disks was 20 mm for both thicknesses. The thick specimens were fabricated by Beijing Tian-Long Tungsten & Molybdenum Co., Ltd., China, and the thin specimens by Plansee Metall GmbH, Austria. Among the thick samples, one specimen was pre-oxidised in air at 500 °C for 24 hours, to study the dynamic beam pulse effects on a mildly oxidised layer on the tungsten surface. The specimens were mounted on an aluminium sample holder and fixed with copper spring washers, as shown in Fig. 2. A stripe of graphite coating was made on the sample for online infrared (IR) temperature measurements. To measure the beam pulse induced dynamic vibration of the samples, a small reflective tape is attached on the downstream side of the samples for laser doppler velocimetry (LDV). The beam spot size was set to approximately 10×10 mm<sup>2</sup>.

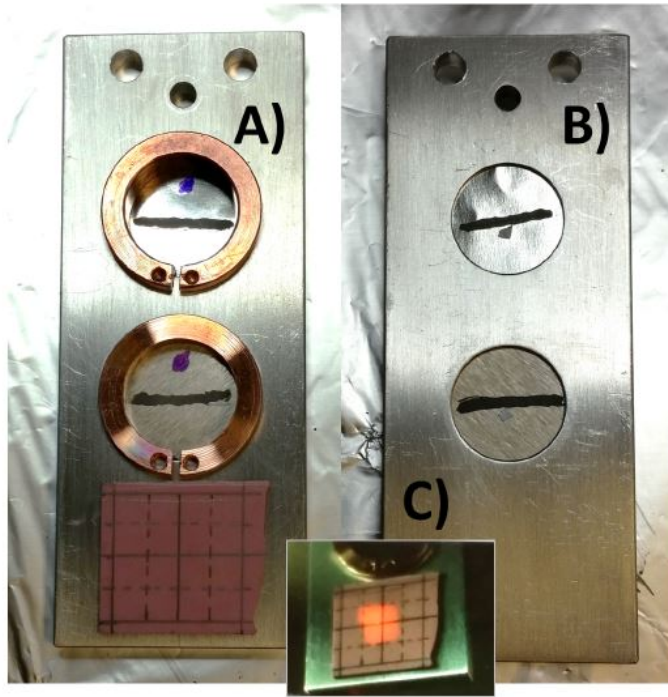


*Figure 2 Aluminium sample holders. Beam upstream side (A) showing two specimens attached with copper spring washers (1). Beam downstream side (B) showing a thin and a thick specimen with a graphite stripe for the IR temperature monitoring, and a small piece of reflective tape for LDV measurement. The image of the beam footprint on the luminescence target is shown in (C).*

## **2.2. Irradiation conditions**

Irradiation of the tungsten specimens was carried out at the M3-beamline of the UNILAC facility at GSI Helmholtz Centre for Heavy Ion Research, Darmstadt, Germany. Pulsed uranium ion beam with a kinetic energy of 4.8 MeV/nucleon was used to study the dynamic response of tungsten. The repetition rate of the uranium beam was 1 Hz with a pulse length of 150  $\mu$ s. Each pulse had an ion intensity of  $7.5 \times 10^9$  U-ions/cm<sup>2</sup>/pulse. The gold beam

with kinetic energy of 4.8 MeV/nucleon was used to study the potential degradation of thermal diffusivity of tungsten induced by radiation damage. The time averaged ion flux of the gold beam was  $5.0 \times 10^9$  Au-ions/cm<sup>2</sup>/s. Table 1 lists the applied beam conditions and performed in-situ monitoring (ISM) and post irradiation examinations (PIE) for the irradiated tungsten specimens.

*Table 1 Applied beam conditions and performed in-situ monitoring (ISM) and post irradiation examinations (PIE). In the sample ID, "Thick" represents 3 mm thickness and "Thin" the 26 mm thickness. The label "Ox" represents the pre-oxidised sample, while "U" and "Au" represent the used ions for irradiation.*

Sample ID	Ion type	Fluence [ions·cm <sup>-2</sup> ]	ISM	PIE
Disc_Thick_U	U	$7.5 \cdot 10^{13}$	IR/LDV	AES/Hardness/SEM
Disc_Thick_Ox_U	U	$5.0 \cdot 10^{12}$	IR/LDV	AES/SEM
Disc_Thin_U	U	$7.5 \cdot 10^{13}$	IR/LDV	SEM
Disc_Thin_Au_1	Au	$1.0 \cdot 10^{11}$	-	LFA
Disc_Thin_Au_2	Au	$1.0 \cdot 10^{12}$	-	LFA
Disc_Thin_Au_3	Au	$5.0 \cdot 10^{12}$	-	LFA
Disc_Thin_Au_4	Au	$2.0 \cdot 10^{13}$	-	LFA

### 2.3. Quasi-static thermal and mechanical load

The quasi-static thermal and mechanical loads in the thick tungsten specimens induced by pulsed uranium beam were calculated using ANSYS Workbench [9]. The observed beam spot size on the sample was a rectangular area with a dimension of  $10 \times 10$  mm<sup>2</sup>, with a uniform distribution of the beam current. The particle transport code FLUKA [10,11] was used to calculate the heat deposition in the tungsten sample. Figure 3 shows the temporal development of maximum temperature of the uranium irradiated tungsten specimen at an ion flux of  $7.5 \times 10^9$  U-ions/cm<sup>2</sup>/pulse. Also shown in the figure

is the von Mises stress configuration at the peak of the twentieth pulse. Note that the variance in maximum temperature per pulse is 54 °C and that of the maximum von Mises stress is 122 MPa. These values lie in the comparable ranges of the operational stress and temperature of the ESS target at 5 MW full power operation, despite the significantly lower beam energy and power of the heavy ion beam used for this study. For reference, the temperature and stress variances per single pulse in the tungsten bricks in the ESS target are about 74 °C and 56 MPa, respectively, as summarised in Table 2 in Sec. 7. However, the temperature and thermal stress comparisons are valid only in the volume where beam interacts with the material. The 2 GeV proton beam at ESS penetrates through the 30 mm long tungsten brick, creating a uniform temperature profile in the beam direction. The maximum temperature gradient is seen in the vertical direction, where the beam intensity varies the most. As a result, the tensile stress in the vertical direction accounts for the maximum equivalent stress in the tungsten bricks of the ESS target. For this reason, the tungsten bricks for the ESS target will be manufactured such that the vertical direction is aligned with the rolling direction in which the tungsten texture exhibits highest tensile strength. On the contrary, the 4.8 MeV heavy ion beam is stopped within 20  $\mu\text{m}$  depth in the tungsten specimen, as shown in Fig. 4. This creates a stiff temperature gradient on the surface region of the tungsten specimen. As a result, the maximum shear stress in the surface region accounts for the maximum equivalent stress in the tungsten specimen. As the rolled direction of the tungsten specimen is transversal to the beam direction, the shear stress might cause fracture or delamination of the rolled material.

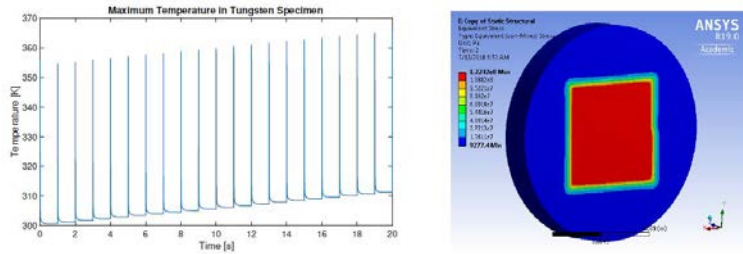


Figure 3 The temporal development of maximum temperature of uranium irradiated tungsten specimen and the von Mises stress configuration at the peak of the twentieth pulse.

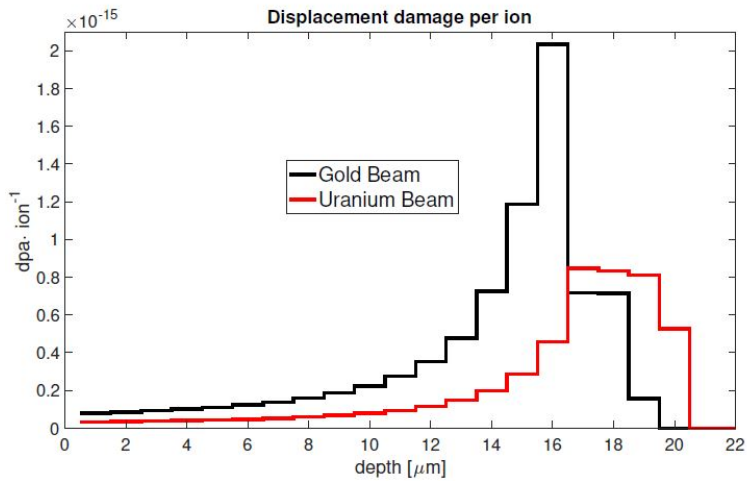


Figure 4 The one-dimensional dpa configurations per single ion, for the uranium and gold beam cases.

## 2.4 Radiation damage

The ion beam energy 4.8 MeV/nucleon used for irradiation of tungsten specimens is below the Coulomb barrier. As it does not induce nuclear reaction in the tungsten atoms, the used beam condition can simulate the displacement radiation damage effect only. Other radiation damages expected in the spallation material at ESS, which are caused by gas production and solid transmutations, cannot be obtained with this low energy beam. On the



contrary, this low energy ion beam irradiation campaign is useful to make a focused study of the atomic displacement damage effect in tungsten properties only, separated from other nuclear reaction induced damage effects. In interpreting displacement damage caused by slow heavy ion, care must be taken in assessing the microchemical and microstructural changes due to irradiation. While heavy ions produce damage in large clusters, protons will produce damage as isolated Frenkel pairs or in small clusters [12].

The displacement damage in the tungsten specimens was calculated by FLUKA. Figure 4 shows the one-dimensional configurations of the dpa values per single ion, for the uranium and gold beam cases. The radiation damage caused by 4.8 MeV/nucleon beam is confined within the surface area, with a depth of about 20  $\mu\text{m}$ . At a maximum uranium beam fluence of  $7.5 \times 10^{13}$  ions/ $\text{cm}^2$  for Disc Thick U, the displacement damage in the sample varies from 0.0024 dpa in the beam upstream surface to 0.063 dpa at the Bragg peak. The average one dimensional dpa for the 20  $\mu\text{m}$  is calculated to be 0.018 dpa. For the used ion beam flux of  $7.5 \times 10^9$  U-ions/ $\text{cm}^2/\text{s}$ , the average damage rate is  $1.8 \times 10^{-6}$  dpa/s. At a maximum gold beam fluence of  $2.0 \times 10^{13}$  Au-ions/ $\text{cm}^2$  for Disc Thin Au 4, the displacement damage in the sample varies from 0.0016 dpa in the beam upstream surface to 0.041 dpa at the Bragg peak. The average one dimensional dpa for the 19  $\mu\text{m}$  is calculated to be 0.008 dpa. For the used ion beam flux of  $5.0 \times 10^9$  Au-ions/ $\text{cm}^2/\text{s}$ , the average damage rate is  $2.0 \times 10^{-6}$  dpa/s. For reference, the tungsten bricks in the ESS target will get maximum 2.6 dpa annual dose at 5 MW operation [13]. This corresponds to maximum damage rate of  $1.4 \times 10^{-7}$  dpa/s. This is comparable to the damage rate in the ion beam irradiated samples, within an order of magnitude. As the stopping range of the 2 GeV proton beam is much longer than the depth of a single tungsten brick, the displacement damage in

the tungsten brick is uniform in the beam direction. The average displacement damage of 0.01 obtained in the irradiated sample is far below that of the ESS target. Furthermore, the large variance of the dpa values in 20  $\mu\text{m}$  thin region makes it difficult to study the displacement damage induced changes of bulk material properties. Nevertheless, the radiation damage induced degradation of the mechanical properties of pure tungsten is manifest already at a neutron dose of 0.1 dpa [14]. This indicates that the radiation induced hardening effect could be studied in the Bragg peak region of the irradiated specimens, where the maximum displacement dose reaches quite close to 0.1 dpa. Indeed, the radiation hardening effects in the damaged region are observed from micro- and nanoindentation tests as presented in Sec. 3.

### **2.5 Beam induced radiation hardening**

Microhardness was measured on the irradiated surface of the 3 mm thick specimen, Disc Thick U, using a CSM instruments Micro Combi Tester with a load of 500 g. As tungsten is a hard material, a relatively higher load was used to have measurement values with reasonable statistical errors while not penetrating the 20  $\mu\text{m}$  thin damaged layer. Three areas were chosen within the irradiated spot and milled down to 6, 9, and 12  $\mu\text{m}$  depths using Auger Electron Spectroscopy (AES). The hardness was subsequently measured in these spots. The results of the test are shown in Fig. 5. The horizontal bar at each measurement point shows the penetration depth of each indentation, which is about 5  $\mu\text{m}$ .

In addition to microhardness, nanohardness of the irradiated thick specimen was measured in its cross section, to obtain a more accurate correlation between the dpa and the hardness. As the maximum ion penetration depth is only 20  $\mu\text{m}$ , determining the hardness profile in-depth is challenging. In order to fit as many indentations as possible, the specimen was sectioned at an angle

so that the surface area of the irradiated volume could be increased. The cross section used for nanohardness measurements was polished after mounting, to a mirror finish quality. Fig. 6 shows a schematic drawing of the indentation plane. The indentations were placed 15  $\mu\text{m}$  apart in 8 rows, with 10 indentations per row. The hardness was measured using a Berkovich nanoindenter, for depths from 3.5 to 51.5  $\mu\text{m}$ . A load of 50 mN was used, which resulted in a displacement of approximately 500 nm into the surface. The results of the nanoindentation test is shown in Fig. 7. The plastic zone affected by indentation is much larger than the indentation itself [15]. Assuming a plastic zone of three times the indentation depth, each data point shown in the figure is an average value over a depth of 1.5  $\mu\text{m}$ .

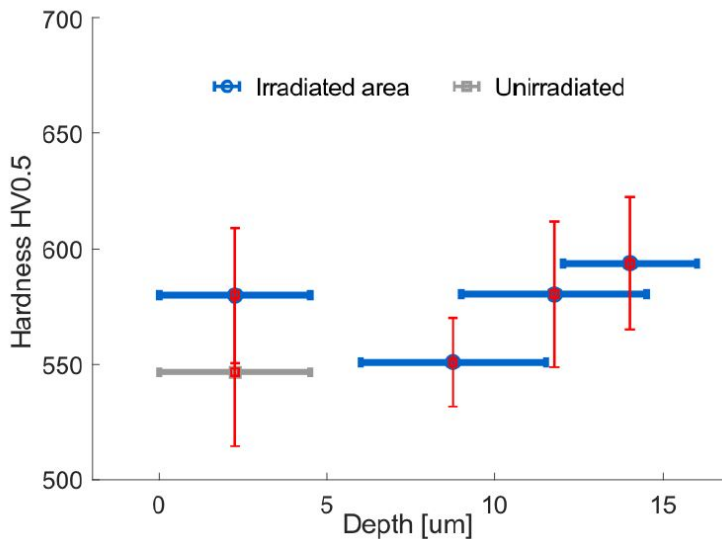


Figure 5 Microhardness of the uranium ion irradiated thick specimen. The horizontal bar represents the penetration depth of the indenter. The load was 500 g. The vertical bar shows the standard deviation for an average of ten measurement at each depth.

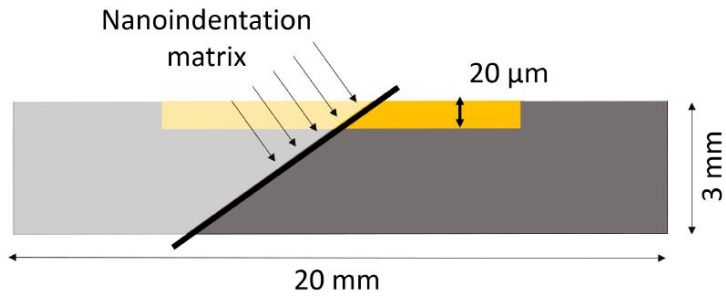


Figure 6 Schematic drawing of the side view of the uranium ion irradiated thick specimen. The yellow top layer represents the irradiation damaged area. Hardness measurements were performed on the plane marked with the black line.

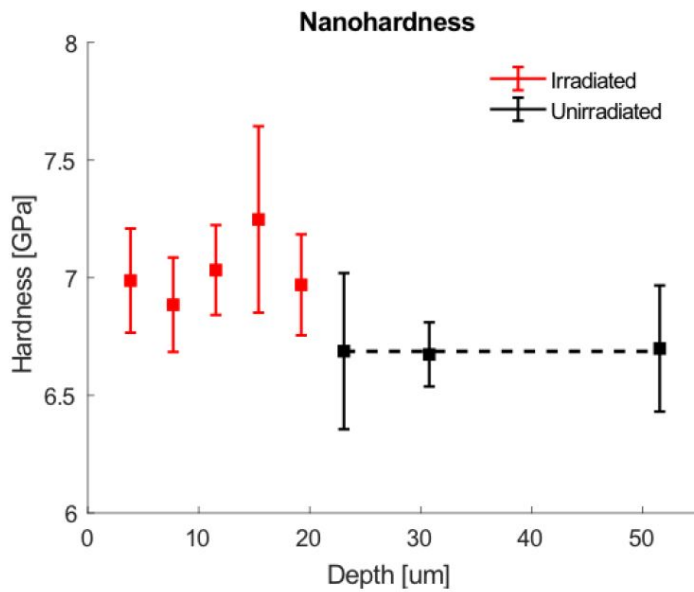


Figure 7 Nanohardness measured in the cross section of the uranium ion irradiated thick specimen. The black dotted line represents the average hardness at depths beyond the range of the irradiation ions.

Figures 5 and 7 indicate irradiation induced hardening in the tungsten. Comparing the two data points within 10  $\mu\text{m}$  depth from the surface, where the displacement damage is less than 0.01 dpa, the hardness measured closer to the surface is slightly higher for both methods. This could be explained by residual stresses in the top surface, which is a result of hot rolling not followed by stress relieving during production. Except the data point closest to the surface, the microhardness measurements show a tendency of increasing hardness with depth. Radiation hardening effect is observed in the surface area, by comparing the hardness values measured on the irradiated and unirradiated surfaces. The average hardness in the irradiated area has increased from approximately 550 to 580 HV0.5 due to irradiation. The nanoindentation data also shows the general tendency of increasing hardness with depth, up to the Bragg peak.

During the microhardness tests, the applied load and penetration depth are recorded in real time. The increase in stiffness was estimated based on results from the Micro Combi Tester, which records the applied load as a function of indentation depth. The relative stiffness was taken as the change in slope of the load-depth curves, just after the unloading, as described in Ref. [16]. Compared to the reference stiffness measured on the unirradiated surface at 0  $\mu\text{m}$ , average stiffnesses at the depth of 0  $\mu\text{m}$  and 12  $\mu\text{m}$  in the irradiated were 15% and 14%. higher.

### **3. Dynamic response and fatigue**

The pulsed uranium beam on the thin specimen Disc\_Thin\_U should induce dynamic vibration. Figure 8 shows the calculated maximum principal and minimum principal stresses at the central node of the thin sample, which is activated by 150  $\mu\text{s}$  long beam pulse with the ion intensity  $7.5 \times 10^9$  U-

ions/cm<sup>2</sup>/pulse. Implicit time marching with 5  $\mu$ s time step was used for the dynamic simulations, suppressing the vibration modes with frequencies higher than 200 kHz. The pulse impact on the sample excites vibration modes of different frequencies. The mode with an approximate frequency of 7 kHz provided the largest stress variance. For the simulation, a quarter of three-dimensional model was used, with symmetric boundary conditions. Mesh resolution of 2  $\mu$ m was used for the 26  $\mu$ m sample thickness. As only a quarter of the geometry was used, due to the limitation of the available computational power, non-symmetric vibration modes were not captured. The pulsed uranium beam induced visible dynamic vibrations in the thin tungsten specimen, Disc Thin U were attempted to be measured using LDV. The surface velocity of the centre of the 26  $\mu$ m thin specimen was measured at a frequency of 128 kHz, which corresponds to a time resolution of 7.8  $\mu$ s. With this time resolution, many of the stress wave modes travelling at the speed of sound within the boundaries of the irradiated specimen could not be captured. Besides the insufficient data collection frequency, uncontrolled surface smoothness of the target area resulted in a failure in obtaining meaningful data.

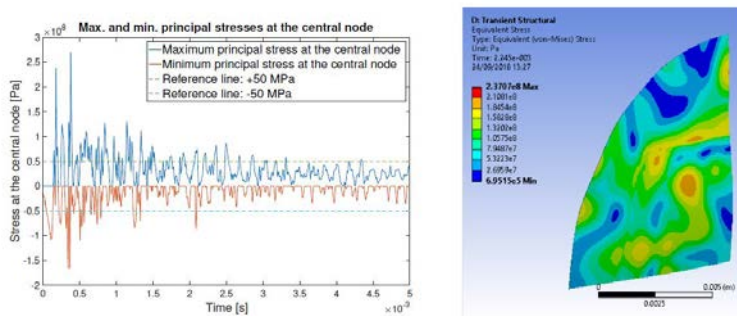


Figure 8 Calculated maximum principal and minimum principal stresses at the central node of the thin sample, which is activated by 150 ms long beam pulse with the ion intensity  $7.5 \times 10^9$  U-ions/cm<sup>2</sup>/pulse (left) and a snapshot of the von Mises stress configuration at 2.245 ms after the start of a beam pulse (right).

Nevertheless, the LDV measurement provided information about the time scale for the stress wave damping after each pulse. The velocity amplitude damped away after 5 ms at a lower fluence level of  $5 \times 10^{11}$  U-ions/cm<sup>2</sup>, whereas the one at a higher dose of  $4 \times 10^{13}$  U-ions/cm<sup>2</sup> did not suffer from damping. This could be attributed to the loosening of the sample holder with the progress of radiation. At a lower dose with a tight sample holding, the beam pulse induced stress wave is damped away by surrounding structure. At a higher dose with loosened sample holding caused by number of accumulated vibrations, the stress wave propagation is confined within the sample geometry, with the sample edge providing a virtual free vibration condition.

Assuming an average stress wave damping time scale of 15 ms after each beam pulse and 7 kHz vibration frequency, the centre of the irradiated specimen experiences about 100 cycles per pulse with a stress variance of 100 MPa, as shown in Fig. 8. For the total 10,000 pulses on the specimen Disc Thin U, it corresponds to applying about 1 million fatigue cycles with a stress amplitude of 50 MPa. After the irradiation, SEM images were taken on the surface of the specimen, where no cracks were observed. This agrees with the fatigue limit of pure tungsten studied in Ref. [17].

#### **4. Radiation damage and thermal diffusivity**

Four of the tungsten foils were irradiated with a gold ion beam up to the fluences of  $1 \times 10^{11}$ ,  $1 \times 10^{12}$ ,  $5 \times 10^{12}$ , and  $2 \times 10^{13}$  ions/cm<sup>2</sup>. Together with a reference specimen, these foils were used for thermal diffusivity studies. Thermal diffusivity was measured at room temperature, using a laser flash apparatus (LFA) and an in-plane sample holder. The surface of the LFA specimens were blackened with graphite spraying, with a couple of light

passes at 20 cm distance from the surface. The total film thickness is estimated to be about 10  $\mu\text{m}$ , according to product description. No effort was given to measure the uniformity and exact thickness of the coating layer. Due to very thin specimen thickness, the graphite layer caused uncertainties in measuring the exact thermal diffusivities of pure tungsten. Therefore, only the relative change in displacement dose dependent thermal diffusivity of the coated specimens is presented. The decrease of thermal diffusivity of the coated tungsten foils irradiated with the gold ion beam is shown in Fig. 9. The measured values were normalised to the thermal diffusivity measured with unirradiated reference foil specimen. Irradiation up to a fluence of  $1 \times 10^{11}$  ions/ $\text{cm}^2$  did not affect the thermal diffusivity. Fluences of  $1 \times 10^{12}$ ,  $5 \times 10^{12}$ , and  $2 \times 10^{13}$  ions/ $\text{cm}^2$  caused a slight decrease, with the highest fluence resulting in a decrease in thermal diffusivity of approximately 12%, relative to the unirradiated tungsten foil. For reference, the gold beam fluence of  $2 \times 10^{13}$  ions/ $\text{cm}^2$  corresponds to average displacement damage of 0.006 dpa over the entire 26  $\mu\text{m}$  thickness of the irradiated specimen. The maximum damage at the Bragg peak at this fluence is calculated to be 0.04 dpa. The decrease of thermal diffusivity shown in Fig. 9 should be mainly due to the displacement damage. This is consistent with the observed thermal diffusivity degradation of tungsten which is irradiated by primary protons and secondary neutrons at PSI [7]. In the mixed field of protons and neutrons, both the displacement damage and solid transmutation contribute to the change of thermal diffusivity. Figure 9 shows that a low level of displacement damage could induce a large degradation of tungsten thermal diffusivity.



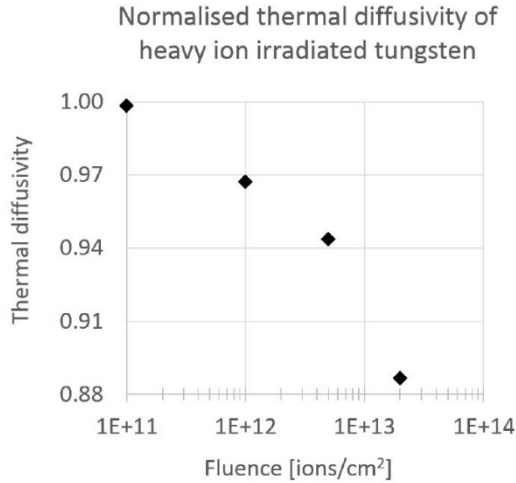


*Figure 9 Relative change in thermal diffusivity of tungsten as a function of fluence.*

## 5. Damage in the oxidised surface

Though the tungsten bricks are cooled by purified helium gas flow, a certain amount of oxygen impurities are invariably present in the loop. At the operational temperature of the tungsten bricks, which could reach 500 °C, oxide layers might form on the tungsten surface [8]. For safe operation, it is important to know whether the tungsten oxide debris could be released into the helium loop. An experiment dedicated to assessing the erosion rate of the tungsten oxide layer did not show any sign of loss of tungsten oxide layer due to the impinging helium jet flow [4]. However, dynamic effect from the pulsed beam on the spalling of the tungsten oxide layer has not yet been studied. For this reason, an oxidised tungsten specimen has been irradiated by pulsed uranium beam to observe the consistency of the oxide layer under irradiation. An image of the oxidised thick specimen after irradiation is presented in Fig. 10. The specimen was pre-oxidised at 500 °C in air. This

caused the formation of an oxide scale with varying stoichiometry ranging from  $\text{WO}_2$  at the metal-oxide interface, to  $\text{WO}_3$  at the surface [8]. The outermost oxide is porous, green, and thick, while the innermost oxide is dark, thin and adherent. After the irradiation, there is a clear mark in the centre of the specimen, corresponding to the size and shape of the ion beam. The colour of the surface within the area has shifted from green to dark grey, indicating the removal of the outer, porous oxide layer.

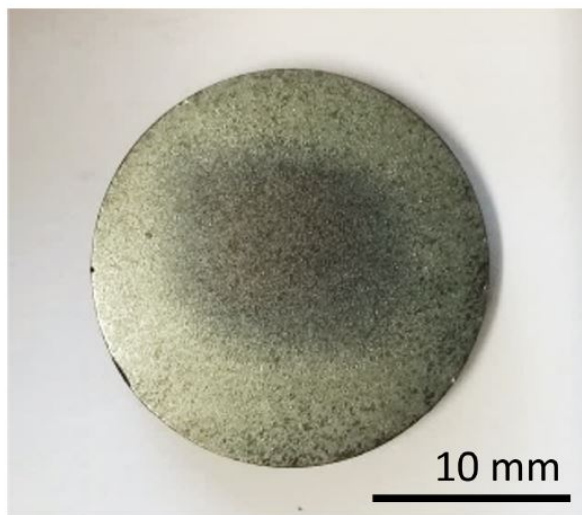


*Figure 10 Image of the oxidised thick specimen after irradiation. The darker area in the centre appeared due to the irradiation and indicates the position and shape of the beam spot.*

SEM images of the  $10 \times 10 \text{ mm}^2$  beam spot area reveal a damaged oxide layer, as shown in Fig. 11. A large number of flakes from the porous outer layer of the oxide have been removed, exposing the more adhesive oxide layer underneath. This could be due to the pulsed beam induced thermal fatigue fracture at the tungsten oxide surface. In addition, the oxide layer was examined with AES. A PHI 700 Scanning Auger Nanoprobe with 4 kV  $\text{Ar}^+$  ion sputtering was used to characterise the remaining oxide layer in the

irradiated area. The oxide layer thickness was estimated by a depth profile using ion sputtering. The sputtering rate of 55 nm/min was determined with a Ta<sub>2</sub>O<sub>5</sub> reference standard, used under the same sputtering conditions. The measured depth of the oxide layer in the irradiated area is on average 1.3 µm, and the one measured outside the beam region is 2.4 µm. This indicates that about 1.1 µm of the oxide layer was removed by the pulsed beam. Elemental analysis showed that only tungsten and oxygen are present in the oxide scale, in both the irradiated and non-irradiated areas. Figure 12 shows one of the elemental analyses performed in the beam spot of the thick specimen. The analysis was done on the top surface, before the ion sputtering was started. Also shown is one of the depth profiles, where the thickness of the oxide scale is approximately 1.3 µm.

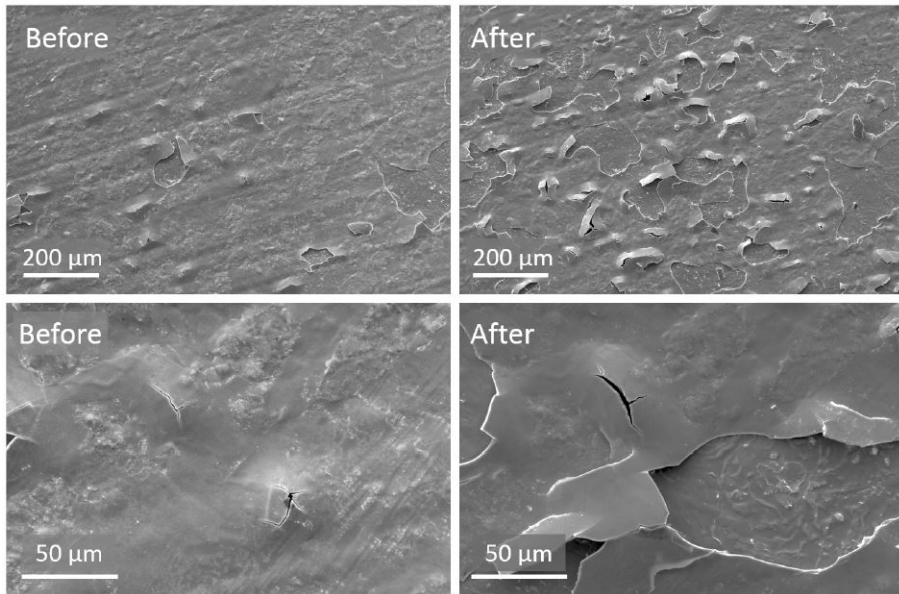


Figure 11 SEM images of the oxidised thick specimen before and after irradiation. The images are taken near the centre of the disk where the oxide layer has been damaged by the beam.

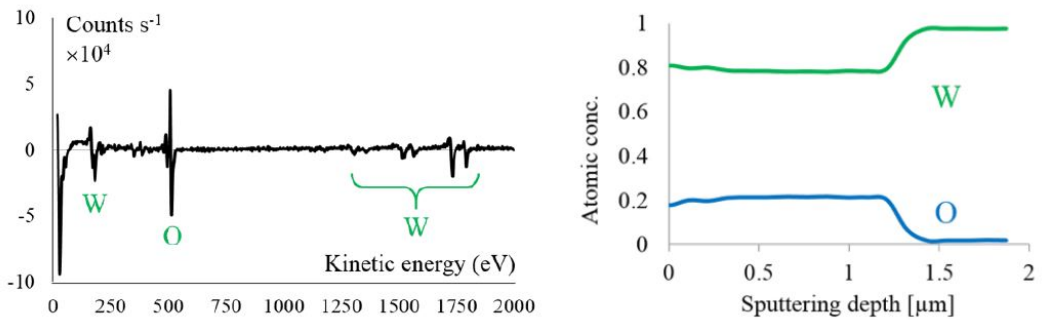


Figure 12 Elemental analysis at the beam spot of the oxidised thick specimen after irradiation (left) and depth profile taken at the beam spot of the irradiated oxidised thick specimen (right).

## **6. Implications of the observed radiation damage effects on the ESS target**

In order to assess the impact of observed radiation induced materials hardening and thermal diffusivity degradation on the operational conditions of the ESS target, heat deposition calculations using FLUKA and coupled flow, thermal and structural mechanics simulations using ANSYS Workbench are made. While a full target model was used for heat deposition calculations, a partial model shown in Fig. 13 is used for the ANSYS simulations. This model represents a matrix of tungsten bricks with three layers in the beam direction and four columns in the transverse direction, which is located in the middle section of a target segment. Also shown is the beam profile on the target used for heat deposition calculations. The toy model represents upstream part of a quarter radial fraction of tungsten bricks. The mass flux of the helium coolant in the target cooling loop is 2.85 kg/s at 1.1 MPa, which converts to 19.79 g/s for this toy model. The inlet temperature used was 400 K. Shear stress transport model was used to calculate the heat exchange between the tungsten bricks and the helium flow, with a fine boundary layer mesh resolution. Transient simulation for 8 beam pulses are made, where the initial condition is provided by a calculated steady state configuration. The calculated maximum temperature in a chosen tungsten brick is shown in Fig. 14, for unirradiated and irradiated tungsten with 20% lower thermal conductivity. The case for the 20% lower thermal conductivity is chosen motivated by the 12% thermal diffusivity loss observed in Sec. 5 in a tungsten with a maximum 0.06 dpa of radiation damage. Since the tungsten bricks in the ESS target will be exposed to much higher radiation damage than 0.06 dpa, a higher loss value of 20% than 12% was chosen to represent the case of the ESS target. For the quasi-static structural analyses, the temperature profiles in the tungsten bricks just before (pre-pulse) and

immediately after (post-pulse) the 8th pulse are used. To assess the effect of radiation damage in tungsten, two cases were studied. The material properties of tungsten as compiled in ITER Material Properties Handbook [5] were used to study the case of unirradiated tungsten. A 20% higher stiffness and a 20% lower thermal conductivity were assumed for the irradiated tungsten. As the displacement damage in the tungsten bricks in the ESS target wheel will suffer from a much higher dpa dose than the one in the irradiated sample, higher than the observed 15% stiffness increase in Sec. 3 was taken for the study of the combined effects of radiation induced degradation of thermal and mechanical properties. Table 2 compiles the results of the analyses.

The temperature and the stress values shown are the ones for the tungsten bricks in the second row. This row was chosen because the tungsten bricks are surrounded by fully developed flow as in the real target case. On the contrary, the flow pattern in the third row has an open outflow region, which is different from the actual target case. Figure 15 shows the calculated post-pulse temperature and stress configuration of a single brick from which the values for Table 2 were drawn. The radiation damage in tungsten could induce a increase of about 8 °C in operational temperature of tungsten at 5 MW beam power. Considering that the tungsten oxidation rate becomes significant at above 500 °C, this increase of temperature does not threaten the target operation in oxidation perspective. However, the radiation damage induced increase in maximum stress is more remarkable. The combined effect of material hardening and thermal conductivity degradation could cause more than 20% increase of maximum thermal stress in tungsten. It has been known that irradiated tungsten suffers from total loss of ductility at the operational temperature range of the ESS target [6]. In particular, the tensile strength of irradiated tungsten with a displacement damage dose of 2 dpa showed 150 MPa in Ref. [14]. The calculated maximum stress 108 MPa of irradiated

tungsten is still below this value. However, considering that the brittle tungsten shows largely scattered statistics in fatigue tests [17] and almost 7000 tungsten bricks are in use for the ESS target, the safety margin in the maximum stress values of irradiated tungsten bricks should be analysed further.

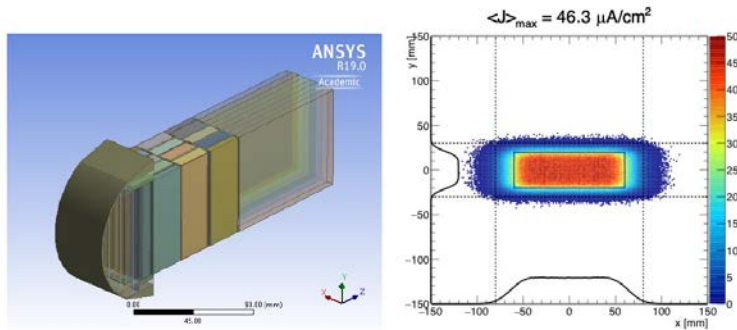


Figure 13 Toy model representing the middle section of a target segment (left) and the beam profile on the target used for heat deposition calculations (right).

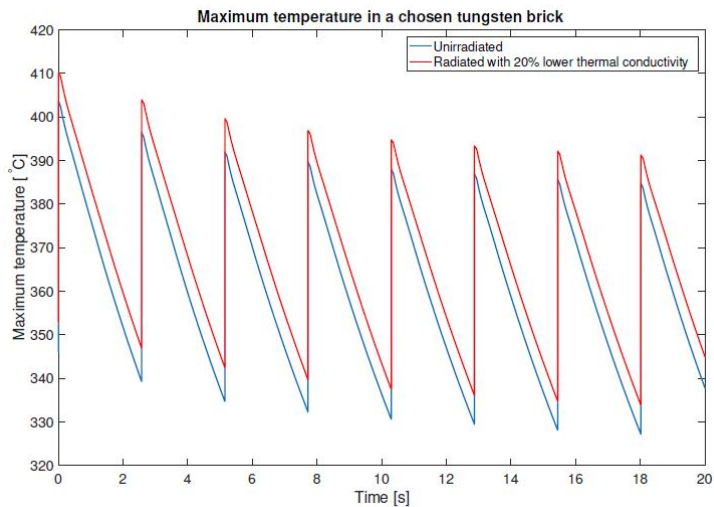


Figure 14 Calculated maximum temperatures in a chosen tungsten brick, for unirradiated tungsten and irradiated one with 20% lower thermal conductivity.

Table 2 Radiation damage effect on operational temperature and maximum von Mises stress in a tungsten brick.

Case	Time	Max. Temp. [°C]	Max. Stress [MPa]
Unirradiated	Pre-pulse	321.3	26.6
	Post-pulse	395.4	82.7
	Variance	74.1	56.1
Irradiated	Pre-pulse	329.3	40.7
	Post-pulse	403.2	107.9
	Variance	73.9	67.2

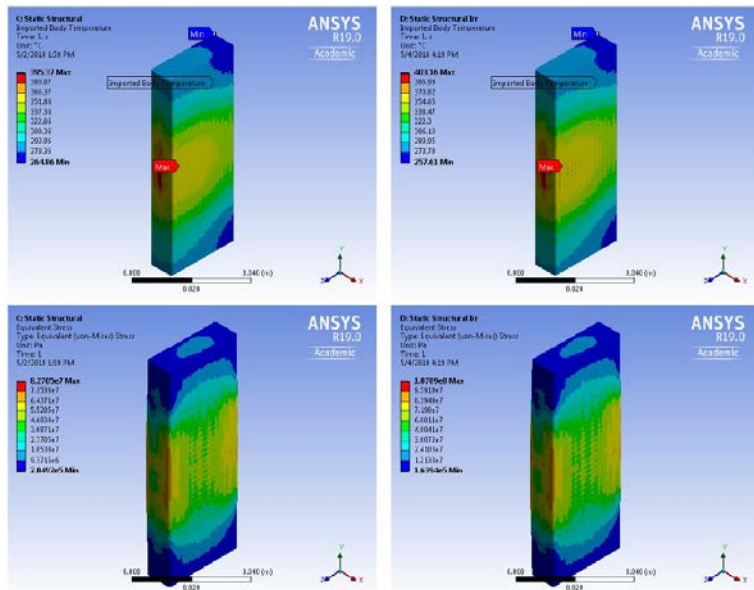


Figure 15 Calculated post-pulse temperature (top row) and stress (bottom row) configuration of single brick. The left and right columns are for the unirradiated and irradiated cases, respectively.



## 7. Conclusions

Tungsten specimens of two thicknesses were irradiated using a pulsed heavy ion beam. The beam pulse induced stress in the tungsten reached 122 MPa in the 3 mm thick specimen and 270 MPa in the 26  $\mu\text{m}$  thin specimen. These applied stresses exceed the expected maximum stress of 83 MPa in the ESS target material, providing an opportunity to study dynamic response of tungsten subject to repeated beam pulse loads. The specimens in this work were tested up to approximately 10,000 pulses. The pulsed beam on the thin specimen caused dynamic stress waves, which resulted in about 1 million load cycles at a stress amplitude approximately of 50 MPa, during the 10 000 beam pulses. The specimen did not show any signs of fatigue failure at the stress variance of 270 MPa. The used heavy ion beam with an energy below Coulomb barrier induced radiation damage mostly in a form of atomic displacements in tungsten. The maximum radiation damage obtained is 0.06 dpa at the Bragg peak located at 20  $\mu\text{m}$  from the beam upstream surface, which is the maximum damage dose in the ESS spallation material approximately after 5 days of 5 MW proton beam operation. Considering that heavy ion induced radiation damage differs in character from that caused by high energy protons, the results obtained in this paper complements the previous study on the proton irradiated tungsten [6,7] Thermal diffusivity and hardness measurements performed on the irradiated specimens indicate an irradiation induced increase in hardness and decrease in thermal diffusivity. In order to estimate the radiation damage effects in the ESS target, coupled flow, thermal and mechanical simulations have been made. The maximum temperature and maximum stress in the tungsten bricks in unirradiated condition and in irradiated condition with 20% higher stiffness and 20% lower thermal conductivity were compared. The calculated results for an irradiated ESS tungsten shows an increase of more than 20% of the maximum

thermal stress, pushing the maximum stress above the design value of 100 MPa. Specifically, the simulated maximum stress of the irradiated ESS tungsten is 108 MPa, which is close to the reported UTS of irradiated tungsten. An oxidised specimen was used to study the effect of the pulsed beam on the adhesion of the oxide scale. SEM imaging and AES confirmed loss of a 1.1  $\mu\text{m}$  thick oxide layer within the irradiated region. The underlying oxide scale showed considerable damage. This indicates that the oxide layer formed during the operation of the ESS target will be released to the cooling loop eventually. For this reason, the design of the target cooling loop purification system at ESS assumes the complete loss of oxide layer on the tungsten bricks, during operation [3]. Under this assumption, the erosion rate of oxide layer from the tungsten bricks in the target wheel is estimated to be 10 g/year, which is taken to be the same as the estimated formation rate of the tungsten oxide layer, for an oxygen impurity of 5 appm in the helium coolant flow in operation.

## Acknowledgements

Dr. Phillipe Spätig at Paul Scherrer Institute is gratefully acknowledged for assistance in the nanohardness measurements.

## References

- [1] L. Mena et al., Design report: Target vessel, Tech. Rep. ESS-0109614, ESS-Bilbao (2018).
- [2] P. Nilsson, Ethel erosion tests, Tech. Rep. ESS-0051445, European Spallation Source ERIC (2016).
- [3] Y. Lee - Editor, ESS Materials Handbook, Tech. Rep. ESS-0028465, European Spallation Source ERIC (2018).
- [4] R. Garoby et al., The European Spallation Source design, Phys. Scr. 93 (014001) (2018) 1–121.
- [5] ITER EDA, ITER Material Properties Handbook, Tech. Rep. ITER Document No. S 74 MA 2, ITER (June 1998).
- [6] J. Habainy, Y. Dai, Y. Lee, S. Iyengar, Mechanical properties tungsten irradiated with high energy protons and spallation neutrons, Journal of Nuclear Materials Submitted.
- [7] J. Habainy, Y. Dai, Y. Lee, S. Iyengar, Thermal diffusivity of tungsten irradiated with protons up to 5.8 dpa, Journal of Nuclear Materials 509 (2018) 152–157.
- [8] J. Habainy, K. B. Surreddi, S. Iyengar, Y. Lee, Y. Dai, Formation of oxide layers on tungsten at low oxygen partial pressures, J. Nucl. Mater. 506 (2018) 26–34.
- [9] ANSYS, Inc., ANSYS Academic Research Workbench, Release 19.0
- [10] A. Ferrari, P. R. Sala, A. Fasso, J. Ranft, Fluka: a multi-particle transport code, Tech. Rep. CERN-2005-10, INFN/TC 05/11, SLAC-R-773 (2005).
- [11] T. T. Böhlen, F. Cerutti, M. P. W. Chin, A. Fasso, A. Ferrari, P. G. Ortega, A. Mairani, P. R. Sala, G. Smirnov, V. Vlachoudis, The Fluka code: Developments and challenges for high energy and medical applications, Nuclear Data Sheets 120 (2014) 211–214.
- [12] G. S. Was, Fundamentals of Radiation Materials Science, no. ISBN 978-3- 540-49471-3, Springer-Verlag, Berlin, Heidelberg, New York, 2007.

- [13] Y. Lee, R. Miyamoto, T. Shea, H. D. Thomsen, The beam conditions on the target and its operational impacts on beam intercepting devices at European Spallation Source, in: 61st ICFA Advanced Beam Dynamics Workshop on High-Intensity and High-Brightness Hadron Beams: Daejeon, Korea, 17-22 June, 2018, 2018.
- [14] H. Ullmaier, F. Carsughi, Radiation damage problems in high power spallation neutron sources, *Nuclear Instruments and Methods in Physics Research B* 101 (1995) 406–421.
- [15] P. Hosemann, D. Kiener, Y. Wang, S. A. Maloy, Issues to consider using nano indentation on shallow ion beam irradiated materials, *Journal of Nuclear Materials* 425 (2012) 136–139.
- [16] W. C. Oliver, G. M. Pharr, Measurement of hardness and elastic modulus by instrument indentation: Advances in understanding and refinements to methodology, *J. Mater. Res.* 19 (1) (2004) 3–20.
- [17] J. Habainy, A. Löfberg, S. Iyengar, Y. Lee, Y. Dai, Fatigue properties of tungsten from two different processing routes, *Journal of Nuclear Materials* 506 (2018) 83–91.





**LUND**  
UNIVERSITY

Doctoral Dissertation  
ISBN 978-91-7753-844-8 (print)  
ISBN 978-91-7753-845-5 (pdf)